Acoustical Physics, Vol. 46, No. 1, 2000, pp. 1–7. Translated from Akusticheskiĭ Zhurnal, Vol. 46, No. 1, 2000, pp. 5–12.

Specific Features of the Spatial Interference Structure of Acoustic Field in Shallow Sea

D. I. Abrosimov and Yu. V. Petukhov

Institute of Applied Physics, Russian Academy of Sciences,
ul. Ul'yanova 46, Nizhni Novgorod, 603600 Russia
e-mail: petukhov@hydro.appl.sci-nnov.ru

Received June 2, 1998

Abstract—It is shown that in a constant-velocity waveguide, the periodic diffraction focusing of an acoustic field gives rise to a "beam" interference structure in the corresponding spatial regions. © *2000 MAIK "Nauka/Interperiodica".*

It is well known that the sound propagation along an oceanic waveguide is accompanied by a rearrangement of the interference structure of the acoustic field [1, 2]. This rearrangement is characterized by the minimum $R_{\min}$ and maximum $R_{\max}$ spatial periods and manifests itself as a partial repetition of the characteristic features observed at the distances $0 \le r < R_{\min}$ in the spatial distribution of the field intensity. This effect, in its turn, leads to the diffraction focusing of the field within the corresponding intervals of distances [1, 2]:

$$mR_{\min} \le r \le mR_{\max} \quad (m = 1, 2, \ldots). \tag{1}$$

In relation (1), the characteristic spatial periods are determined by the expressions [1–3]

$$\begin{aligned} R_{\min} &= \min[R_g(l, l+1; l+1, l+2)], \\ R_{\max} &= \max[R_g(l, l+1; l+1, l+2)], \end{aligned} \tag{2}$$

where the quantity

$$\begin{aligned} &R_g(l, l+1; l+1, l+2) \\ &= R_{l,l+1}R_{l+1,l+2}/|R_{l,l+1} - R_{l+1,l+2}| \end{aligned} \tag{3}$$

represents the period of the rearrangement of the interference structure formed by the neighboring pairs of modes with the corresponding interference periods

$$\begin{aligned} R_{l,l+1} &= 2\pi/(k_l - k_{l+1}), \\ R_{l+1,l+2} &= 2\pi/(k_{l+1} - k_{l+2}); \end{aligned} \tag{4}$$

the frequency dependence of the horizontal wave number k_l of mode number l in (4) is determined from the dispersion equation for a given waveguide.

We note that here (as in [1, 2]), by analogy with the diffraction images of periodic structures in optics [4], the diffraction focusing of acoustic field in waveguides means the formation of the corresponding zones of intense acoustic illumination. The spatial period of such a focusing fundamentally depends on the wavelength [1, 2, 4], which makes it different from the refraction focusing [5]: for the latter, the dependence of the spatial period on the wavelength is determined by only a small diffraction correction to the ray approximation [6–9].

In deep-water oceanic waveguides with the underwater sound channel opened to the surface (near which the sound velocity is less than at the bottom), the diffraction focusing of the acoustic field leads to a periodic spatial rearrangement of the far zones of acoustic illumination and a corresponding diffraction focusing of the mode beams at characteristic distances (1) [1, 2, 10]. These phenomena are best observed in the case of the excitation of only one mode beam (see [10]) giving rise to a single maximum in the dependence of the product of the amplitudes of neighboring modes on their number at the source depth [1–3].

From expressions (1)–(4) it is evident that similar phenomena [1, 10] should also be observed in constant-velocity waveguides [11–15]. In some cases (see [5, 11–14]), such waveguides can model the conditions of sound propagation in shallow-water oceanic waveguides. Hence, it is possible to use them for describing the specific features of the spatial interference structure of acoustic field in shallow sea.

The purpose of this paper is the theoretical study of the effect of the diffraction focusing of an acoustic field on the formation of its spatial interference structure in a constant-velocity waveguide. The latter is modeled by a homogeneous liquid layer overlying a homogeneous liquid halfspace. The layer is characterized by the thickness H, the sound velocity c, and the density ρ, and the halfspace is characterized by the sound velocity c_b and the density ρ_b.

To obtain the approximate analytical dependences for $R_{l,l+1}$, $R_g(l, l+1; l+1, l+2)$, $R_{\min}$, and $R_{\max}$ in the form that is convenient for estimating the corresponding values and generalizing the results of numerical simulation, we first consider a constant-velocity waveguide with an absolutely hard bottom at $z \ge H$. In

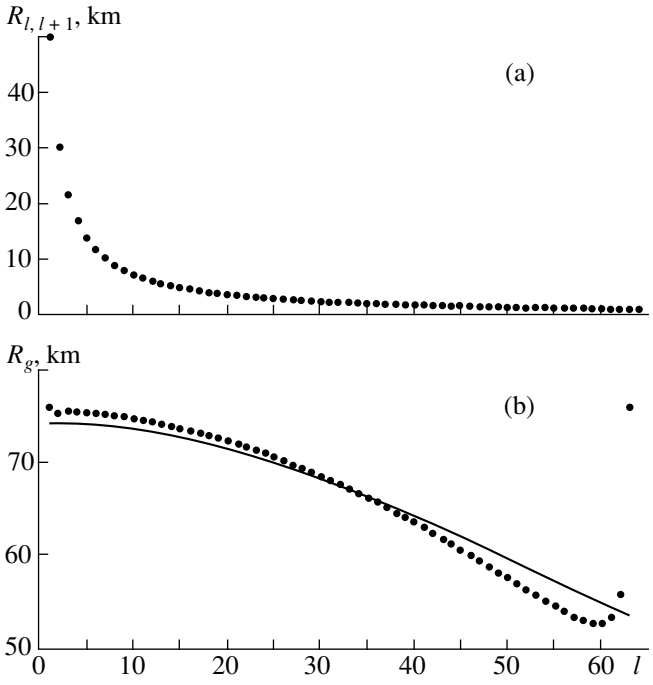

Fig. 1. Dependences of the spatial periods of (a) the interference of neighboring modes $R_{l,\,l+1}$ and (b) the rearrangement of the interference structure of the field of neighboring pairs of modes $R_g = R_g(l, l+1; l+1, l+2)$ on the mode number l. The solid line corresponds to approximate dependence (6).

this case, restricting our consideration to the modes of interest with small grazing angles, we expand the known expression (see [5]) for the horizontal wave numbers of such a waveguide in the series

$$k_l = k\sqrt{1 - x_l^2} \approx k\left(1 - \frac{1}{2}x_l^2 - \frac{1}{8}x_l^4\right) \tag{5}$$

correct to the term of the fourth order of the small quantity $x_l \ll 1$, where

$$x_l = \pi(l - 1/2)/kH \quad (l = 1, \ldots),$$

$k = \omega/c$, $\omega = 2\pi f$, and f is the frequency of the CW acoustic signal.

Then, from expressions (3)–(5), we obtain the approximate dependences

$$R_{l,\,l+1} \approx \frac{D/l}{1 + \dfrac{\lambda}{8D}(4l^2 + 1)},$$
$$R_g(l, l+1; l+1, l+2) \approx \frac{D}{1 + \dfrac{\lambda}{8D}(12l^2 + 12l + 5)}, \tag{6}$$

where

$$D = 4H^2/\lambda \tag{7}$$

and $\lambda = 2\pi/k$ is the sound wavelength. Substituting dependence (6) in expressions (2), we determine the values of the characteristic spatial periods of the diffraction focusing of acoustic field in the waveguide under study:

$$R_{\min} \approx D/\left(1 + \frac{\lambda}{8D}(12L_0^2 + 12L_0 + 5)\right),$$
$$R_{\max} \approx D/\left(1 + \frac{29}{8}\frac{\lambda}{D}\right). \tag{8}$$

Here, L_0 is the limiting number of modes with small grazing angles. This number satisfies the natural condition $1 \ll L_0 < L - 2$, where $L = 2H/\lambda + 1/2$ is the total number of excited modes.

Because the diffraction focusing of the field is most pronounced in the case of a multimode propagation of acoustic waves [1, 2, 14], we assume that $\lambda/H \ll 1$, and using expression (8), we obtain a relation coincident with that presented in [14]:

$$R_{\max} \approx D. \tag{9}$$

Expressions (8) and (9) allow one only to estimate the dimensions of the spatial regions (1) where the diffraction focusing of the acoustic field strongly affects the formation of its spatial interference structure in a constant-velocity waveguide. However, to study the specific features of the interference structure that are caused by the diffraction focusing, it is necessary to numerically calculate the distribution of the intensity of acoustic field $J(r, z)$ both along the horizontal distance r and with the depth z on the basis of the mode theory [5], for the given conditions of sound propagation.

Therefore, to illustrate the characteristic features of the dependences $R_{l,\,l+1}$, $R_g(l, l+1; l+1, l+2)$, and $J_0(r, z) = rJ(r, z)$, we present the results of the corresponding numerical calculations in Figs. 1 and 2. The results were obtained for the following conditions of sound propagation: $H = 300$ m, $c = 1.45 \times 10^3$ m/s, $\rho = 10^3$ kg/m^3, $c_b = 1.7 \times 10^3$ m/s, and $\rho_b = 1.6 \times 10^3$ kg/m^3, and for the frequency $f = 300$ Hz of sound generated by a point source located at the depth $z_s = 4.5$ and 9 m. The spatial distribution of the acoustic field intensity $J_0(r, z)$ normalized with allowance for the geometric divergence is shown by shading, with the dynamical range 15 dB (see Fig. 2).

The analysis of the results of numerical simulation (see Figs. 1–3) offers the following conclusions:

First, the quantities $R_{\min}$ and $R_{\max}$ (2), the values of which are calculated by approximate expressions (8) with sufficient accuracy (see Fig. 1), truly determine the boundaries of the spatial regions (1) of the diffraction focusing of acoustic field in the oceanic waveguide under study. Here, we have $R_{\max} > \max[R_{l,\,l+1}] = R_{1,\,2}$ (see Fig. 1), in contrast to the waveguide with an absolutely hard bottom where an inverse relation is valid.

Second, in the spatial regions (1) corresponding to the manifestation of the effect of diffraction focusing, specific interference "spots" form a characteristic structure of lines of higher field intensity. This structure

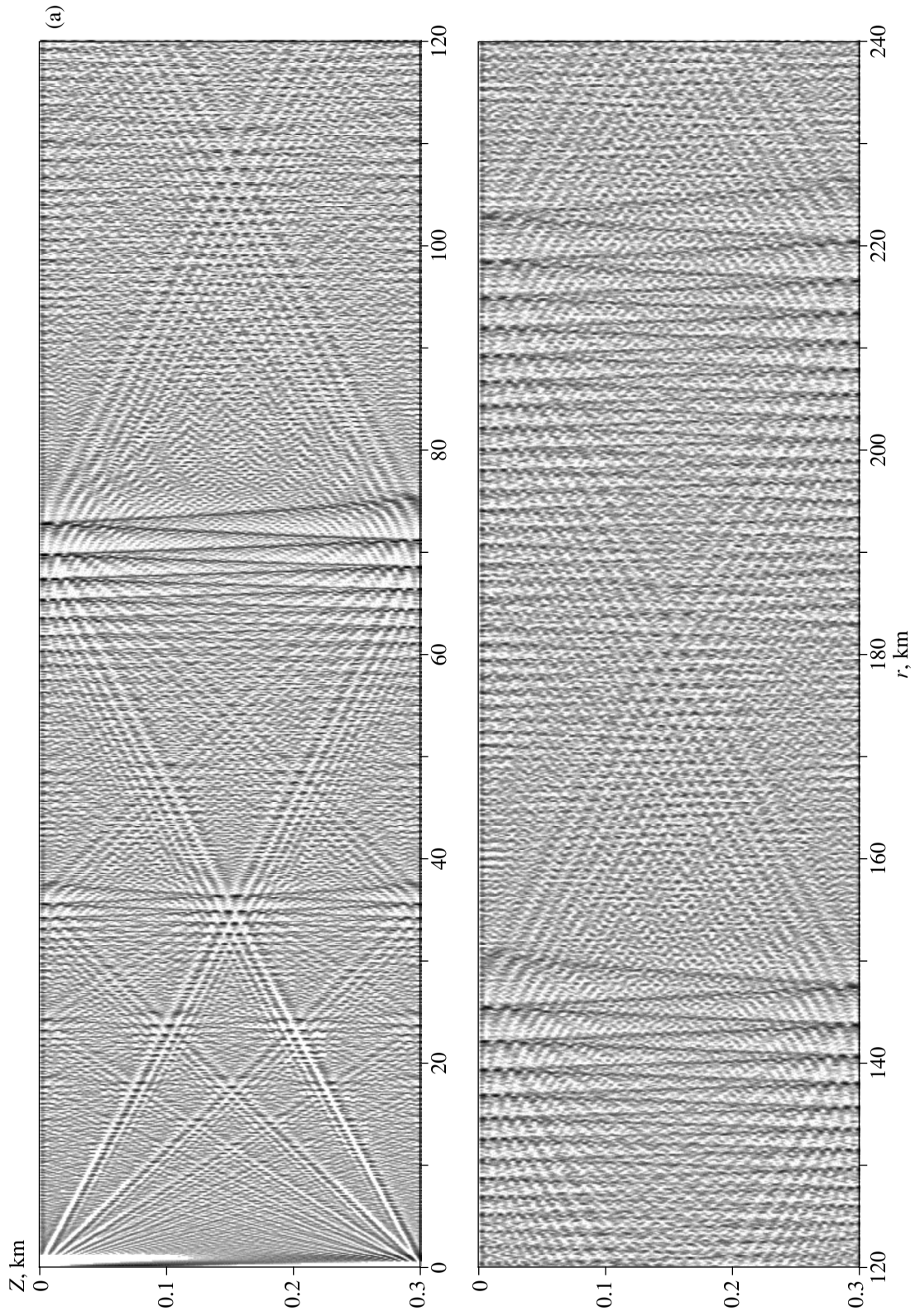

Fig. 2. Distribution of the normalized intensity of acoustic field $J_0(r, z)$ along the horizontal distance r and with the depth z. The distribution is shown by shading; the dynamical range is 15 dB, the frequency is $f = 300$ Hz, and the source depth is $z_s =$ (a) 4.5 and (b) 9 m.

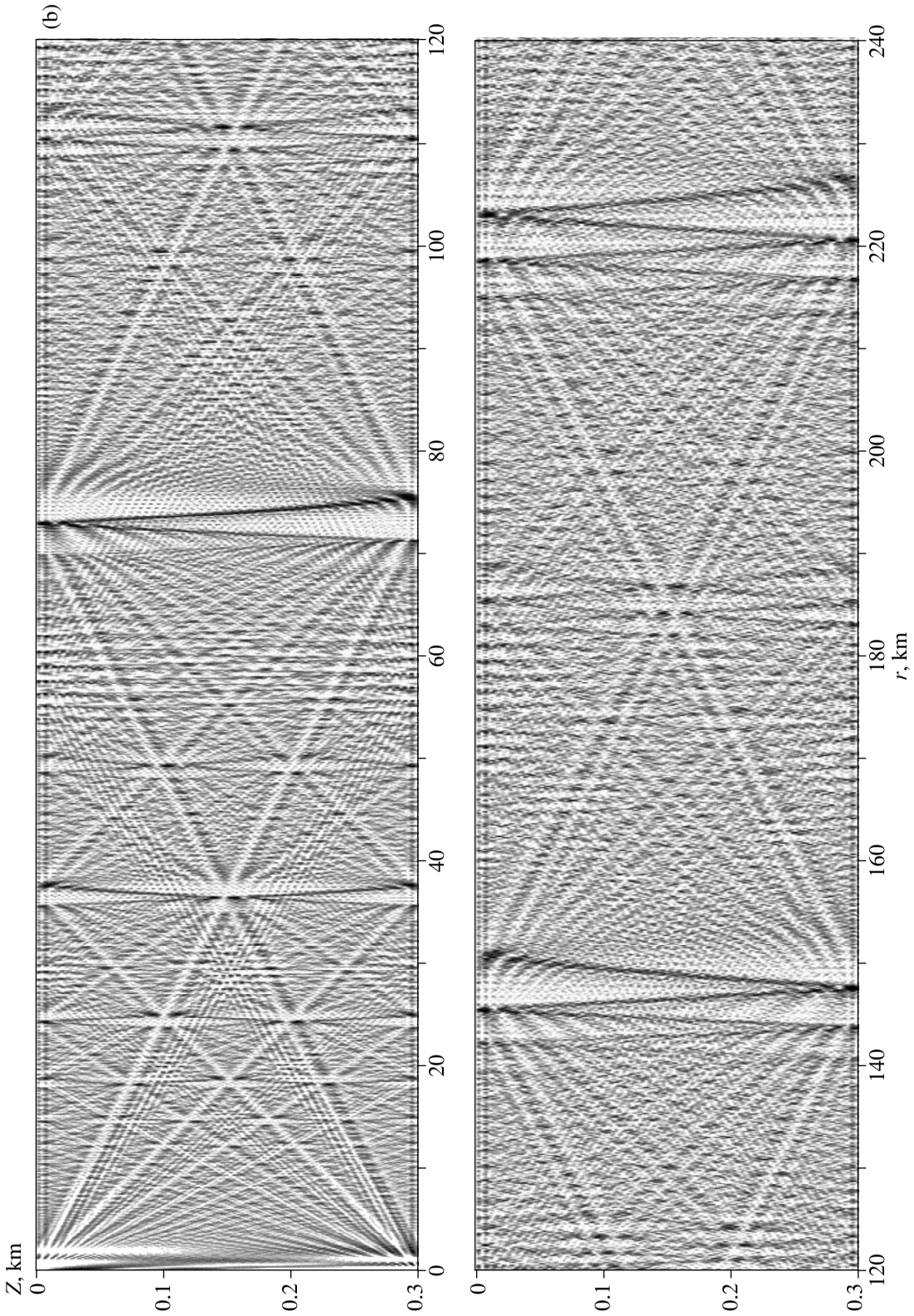

Fig. 2. (Contd.)

corresponds to a "beam" multiply reflected from the boundaries of the water layer so that the angle of the beam incidence increases with every reflection. As the number m of the spatial region of the diffraction focusing of acoustic field increases, the number of clearly defined reflections of such a "beam" also increases (see Fig. 2).

Third, with increasing source depth, the spatial region corresponding to a clearly defined "beam" structure of the acoustic field considerably decreases in every interval of horizontal distances (1) (see Fig. 2). The latter fact is explained by the increase in the number of the excited mode beams [3] corresponding to the maxima in the dependence of the product of the neighboring mode amplitudes $B_{l,\,l+1}$ on their number at the source depth $z = z_s$ (see Fig. 3). Therefore, as in [10], the most clearly defined "beam" structure of the interference lines is observed in the case of the excitation of a single beam of maximum width (see Figs. 2, 3).

Naturally, with decreasing sound frequency, the spatial regions corresponding to the manifestation of the aforementioned specific features of the interference structure of the field $J(r, z)$ will be narrowed, because the quantities $R_{\max}$, $R_{\min}$, and $\Delta R = R_{\max} - R_{\min}$ decrease (see (7), (8), and [1, 2, 10]). In addition, as a result of a decrease in the total number of excited modes L, the effects of the diffraction focusing will be less pronounced in the spatial interference structure on the background of the energy sum of modes in $J(r, z)$. However, with a simultaneous increase in the source depth under the conditions that the quantity kz_s remains constant and only one mode beam is excited [3], the interference structure of acoustic field in a constant-velocity waveguide will, on the whole, reproduce its characteristic features, but on a correspondingly decreased scale in r. This inference is confirmed by the numerical calculations of the dependence $J_0(r, z)$ at f = 150 Hz and z_s = 9 m (Fig. 4). The dependence exhibits the same characteristic features as those observed at f = 300 Hz and z_s = 4.5 m (see Fig. 2a), but now they occur at two times smaller horizontal distances.

Thus, the described theoretical studies show that in a constant-velocity waveguide, as in the case of the underwater sound channel [1, 10], the effect of periodic spatial rearrangement of far zones of acoustic illumination is possible. It is found that the appearance of such zones is caused by the diffraction focusing of the field, and this focusing leads to the formation of a "beam" interference structure of the acoustic field in the corresponding spatial regions.

In closing, we dwell on the qualitative estimate of the effect of the absorption of acoustic energy in a constant-velocity waveguide on the diffraction focusing of sound field.

Evidently, the inclusion of this effect will lead to an exponential decrease in the mode amplitudes with distance, hence, to an additional decrease in the total intensity of acoustic field compared with the decrease caused by the geometric divergence of the wavefront [16–18]. The latter fact will hinder the observation of the effects of diffraction focusing of acoustic field at long distances, i.e., at $m \gg 1$ (see (1)). However, because of the dissipation loss, the attenuation with distance will be maximum for the modes of relatively high numbers $l > L_1$ ($L_1 < L_0$) [16–18], i.e., the modes that make practically no contribution to the diffraction focusing of acoustic field at the distances $r \approx mR_{\max}$ (see (6)–(8)) and form only the background for its manifestation. Since, at these distances, the main contribution to the diffraction focusing of acoustic field is made by the modes of relatively low numbers $l \le L_1$, one can expect that at some conditions, the presence of the dissipation loss will even lead to a relative enhancement of the effect of diffraction focusing in the corresponding intervals of distances:

$$mR_g(L_1, L_1 + 1;\ L_1 + 1, L_1 + 2) \le r \le mR_{\max}. \quad (10)$$

For the multimode propagation $L \gg 1$ (which is the case of interest), we can obtain the limitation on the maximum value of kH for the distances satisfying condition (10). We use the fact that for the modes of relatively low numbers (with small grazing angles), the following expression for the exponential factor E characterizing the attenuation of these modes with distance is valid [16–18]:

$$E = \exp(-\alpha_l^2 \sigma r / H). \quad (11)$$

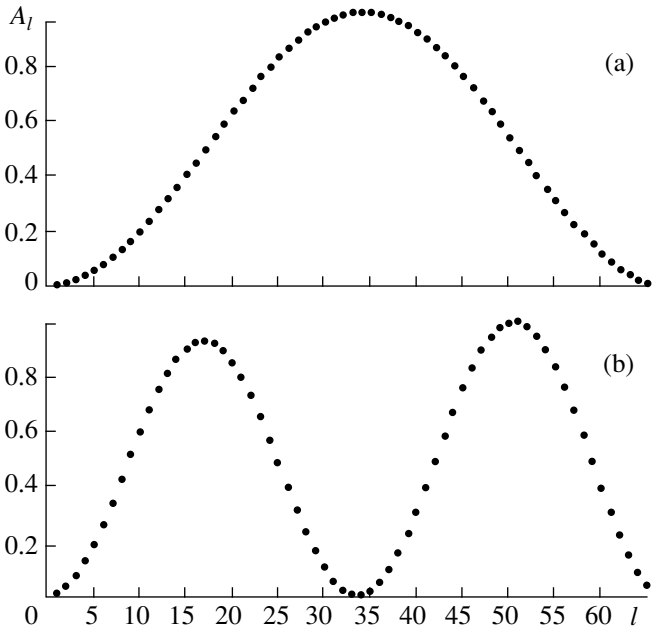

Fig. 3. Normalized dependences of the product of neighboring mode amplitudes $A_l = B_{l,\,l+1}/B$ on their number l at the source depth $z = z_s$, at f = 300 Hz; z_s = (a) 4.5 and (b) 9 m; $B = \max[B_{l,\,l+1}]$.

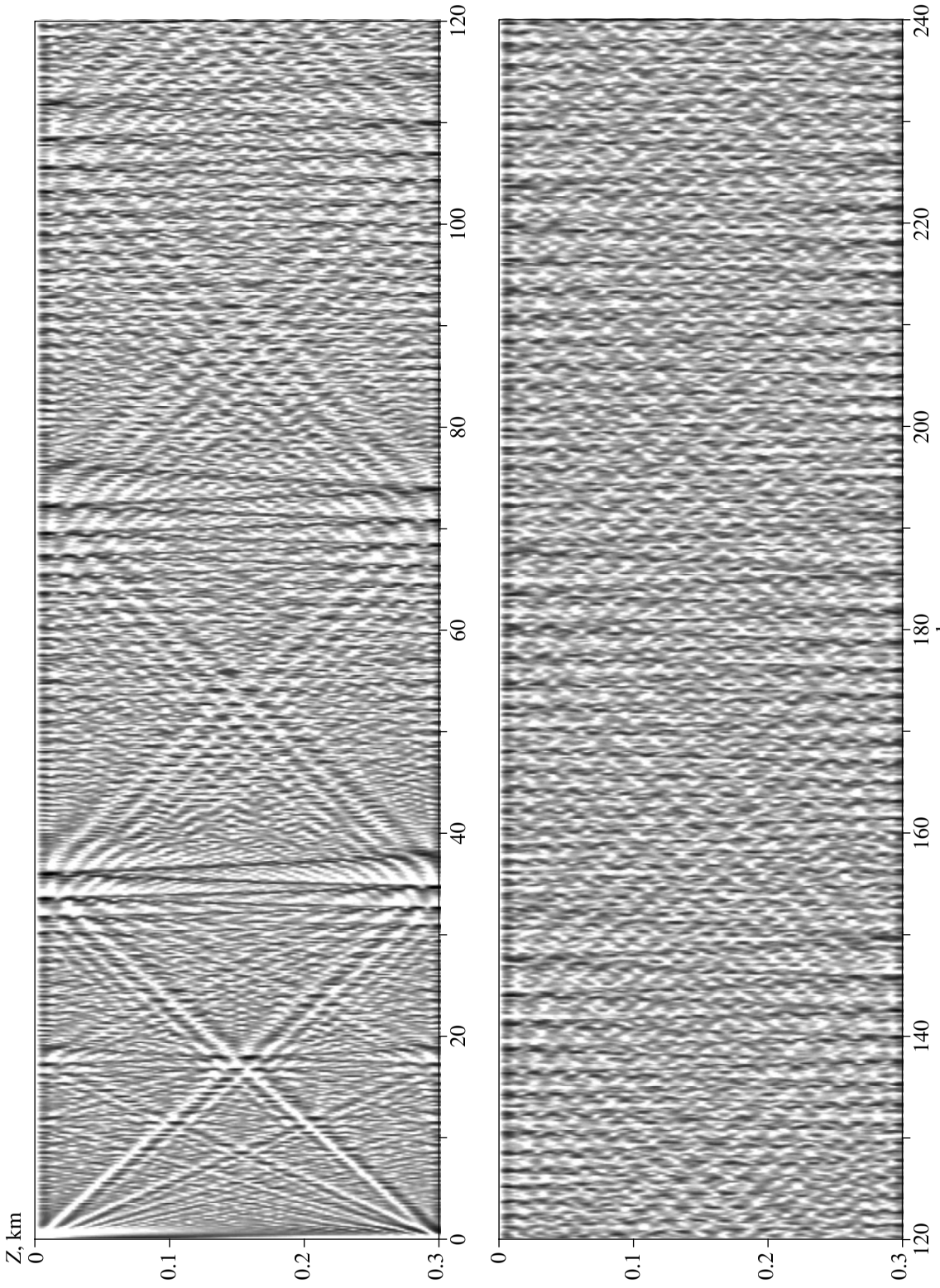

Fig. 4. Distribution of the normalized intensity of acoustic field $J_0(r, z)$ along the horizontal distance r and with the depth z. The distribution is shown by shading; the dynamical range is 15 dB, $f = 150$ Hz, and $z_s = 9$ m.

Here:

$$\alpha_l = \frac{\pi l}{kH} \ll 1, \quad \sigma = \frac{\rho_b}{\rho}\frac{n_i n_r}{(1-n_r^2)^3},$$

$$n_r = \mathrm{Re}(c/c_b), \quad n_i = \mathrm{Im}(c/c_b),$$

$$n_i/n_r \ll 1, \quad n_r < 1.$$

For a noticeable manifestation of the diffraction focusing of acoustic field in a constant-velocity waveguide at distances (10), it is necessary that a sufficiently great number of low-number modes ($l \le L_1$) interfere. The limiting number of such modes $L_1 = L/N \gg 1$ makes up some integral part of their total number L; here, $N \ge 2$ is an integer, even or odd, depending on the corresponding value of L. Hence, for all these modes at the corresponding distances $r \approx mR_{\max}$, it is necessary that the absolute value of the exponent in (11) be small compared with unity:

$$\left(\frac{\pi L_1}{NkH}\right)^2 \sigma \frac{mR_{\max}}{H} < 1. \tag{12}$$

This condition corresponds to the inequality $1/e < E < 1$.

Then, at $L \gg 1$, we use the estimate $L \approx kH\sqrt{1-n_r^2}/\pi$ [5] and expression (9) and obtain the condition

$$\frac{\pi}{\sqrt{1-n_r^2}} \ll kH < \frac{\pi}{2\sigma(1-n_r^2)m}N^2. \tag{13}$$

Thus, in constant-velocity waveguides with dissipation losses, the effects of the diffraction focusing of acoustic fields will clearly manifest themselves in the corresponding spatial regions (10) only for the values of kH that satisfy condition (13).

It should be noted that in modeling the formation of the spatial interference structure of acoustic fields in shallow sea, it is necessary to take into account not only the absorption but also other factors such as the stratification of sound velocity in water and sediment layers [19]. A strict description of the effects of these factors on the diffraction focusing of acoustic fields in shallow sea is of particular interest and will be the subject of a special study.

ACKNOWLEDGMENTS

This work was supported by the Russian Foundation for Basic Research (project nos. 96-02-16116a and 98-02-16402) and the Competitive Center of Fundamental Natural Sciences, project no. 97-8.2-78.

REFERENCES

1. Yu. V. Petukhov, Akust. Zh. **42**, 688 (1996) [Acoust. Phys. **42**, 606 (1996)].
2. Yu. V. Petukhov, Preprint No. 443 NIRFI (Radiophysical Inst., Nizhni Novgorod, 1998).
3. D. I. Abrosimov and Yu. V. Petukhov, Akust. Zh. **43**, 437 (1997) [Acoust. Phys. **43**, 373 (1997)].
4. R. F. Edgar, Opt. Acta **16**, 281 (1969).
5. L. M. Brekhovskikh, and Yu. P. Lysanov, *Fundamentals of Ocean Acoustics* (Springer, Berlin, 1982).
6. N. C. Nicholas and H. Uberall, J. Acoust. Soc. Am. **44**, 1259 (1968).
7. N. C. Nicholas and H. Uberall, J. Acoust. Soc. Am. **48**, Part 2, 745 (1970).
8. D. White, J. Acoust. Soc. Am. **46**, 1318 (1969).
9. A. T. Semenov, Akust. Zh. **27**, 315 (1981) [Sov. Phys. Acoust. **27**, 174 (1981)].
10. D. I. Abrosimov and Yu. V. Petukhov, Preprint No. 467, IPF RAN (Inst. of Applied Physics, Russian Academy of Sciences, Nizhni Novgorod, 1998).
11. A. B. Wood, J. Acoust. Soc. Am. **31**, 1213 (1959).
12. A. B. Wood, in *Underwater Acoustics*, Ed. by V. M. Albers (Plenum, New York, 1963; Mir, Moscow, 1965).
13. D. E. Weston, J. Acoust. Soc. Am. **32**, 647 (1960).
14. D. E. Weston, J. Acoust. Soc. Am. **44**, 647 (1968).
15. L. A. Rivlin and V. S. Shil'dyaev, Izv. Vyssh. Uchebn. Zaved., Radiofiz. **11**, 572 (1968).
16. L. M. Brekhovskikh, *Waves in Layered Media* (Academic, New York, 1980).
17. G. A. Grachev, Akust. Zh. **29**, 275 (1983) [Sov. Phys. Acoust. **29**, 160 (1983)].
18. G. A. Grachev and G. N. Kuznetsov, Akust. Zh. **31**, 675 (1985) [Sov. Phys. Acoust. **31**, 408 (1985)].
19. N. R. Chapman, C. T. Tindle, and E. K. Westwood, J. Acoust. Soc. Am. **100**, 3631 (1996).

Translated by E.M. Golyamina

Acoustical Physics, Vol. 46, No. 1, 2000, pp. 100–101. Translated from Akusticheskiĭ Zhurnal, Vol. 46, No. 1, 2000, pp. 116–117.

SHORT COMMUNICATIONS

Two-Dimensional Solitary Waves in a Strained Nonlinear Viscoelastic Medium

G. A. Arshinov, A. I. Zemlyanukhin, and L. I. Mogilevich

Saratov State Technical University, ul. Politekhnicheskaya 77, Saratov, 410054 Russia

Received February 30, 1999

The basic idea of the methods of nonlinear wave dynamics lies in the passage from the initial mathematical model to the known evolutionary equations (or systems of equations) that allow analytical studies. Usually, such a passage is achieved with the help of asymptotic methods [1]. Attempts to obtain more adequate descriptions of wave processes lead to nonintegrable equations the exact solutions of which are in most cases unknown.

The variety of wave phenomena that occur in a continuous medium is determined by the interaction of the effects of nonlinearity, dispersion, and dissipation. Therefore, thin-walled spatial structures are convenient objects for studying strain waves in nonlinear dissipative dispersive media.

Let us consider the evolutionary equation modeling the propagation of a quasi-plane beam of longitudinal waves in a geometrically and physically nonlinear viscoelastic cylindrical shell [2]:

$$\frac{\partial}{\partial\xi}(\psi_\tau + b_1\psi\psi_\xi - b_2\psi^2\psi_\xi + b_3\psi_{\xi\xi} + b_4\psi_{\xi\xi\xi}) = b_5\psi_{\eta\eta}. \quad (1)$$

Here, ψ is the component of the longitudinal strain, and the coefficients b_i characterize the geometric nonlinearity, the physical nonlinearity, the dissipation, the dispersion, and the diffraction divergence, respectively.

Equation (1) generalizes the Kadomtsev–Petviashvili equation, and it is the most general spatially two-dimensional equation of the third order that takes into account the combined effect of the quadratic and cubic nonlinearities and the dissipation.

Exact particular solutions of nonintegrable equations of mathematical physics can be obtained in only a few special cases. Among spatially one-dimensional equations of the third order, only the Korteweg–de Vries–Burgers equation (a particular case of equation (1)) was solved exactly [3]. Hence, a qualitative analysis of equation (1) is important from both mechanical and mathematical points of view.

We seek the solution to equation (1) by using the method proposed by Weiss *et al.* [4] and developed by Kudryashov and Zargaryan [3, 5]. We represent the sought-for solution in the form of a series

$$\psi = \sum_{j=0}^{\infty}\psi_j F^{j-1}, \quad (2)$$

where ψ_j and F are unknown functions of independent variables. Substituting formula (2) in equation (1) and equating the expressions multiplying equal powers of F to zero, we obtain a chain of equalities:

$$\psi_0 = \pm\sqrt{6\frac{b_4}{b_5}}F_\xi, \quad (3)$$

$$\psi_1 = \mp\frac{1}{2}\sqrt{6\frac{b_4}{b_2}}\frac{F_{\xi\xi}}{F_\xi} \mp \frac{b_3}{(6b_2b_4)^{1/2}} + \frac{b_1}{2b_2}. \quad (4)$$

According to expression (2), ψ_1 satisfies the initial equation

$$\frac{\partial}{\partial\xi}(\psi_{1\tau} + b_1\psi_1\psi_{1\xi} - b_2\psi_1^2\psi_{1\xi} + b_3\psi_{1\xi\xi} + b_4\psi_{1\xi\xi\xi}) = b_5\psi_{1\eta\eta}.$$

From equalities (3) and (4), it follows that b_2 and b_4 should be of the same sign.

Setting $U_j = 0$ for $j \geq 2$, we obtain the following form of the transformation for the solutions of equation (1):

$$\psi = \pm\sqrt{6\frac{b_4}{b_2}}\frac{F_\xi}{F} + \psi_1, \quad (5)$$

where ψ_1 is determined from equality (4).

The latter expression allows one to determine the exact solutions of equation (1). This transformation is the one of the Backlund type if F satisfies the system of equations, the simplest of which has the form

$$\frac{F_\tau}{F_\xi} + b_4\{F,\xi\} - b_5\frac{F_\eta^2}{F_\xi^2} = \frac{1}{6}\frac{b_3^2}{b_4} - \frac{1}{4}\frac{b_1^2}{b_2}, \quad (6)$$

where $\{F,\xi\} \equiv \dfrac{F_{\xi\xi\xi}}{F_\xi} - \dfrac{3}{2}\dfrac{F_{\xi\xi}^2}{F_\xi^2}$ is the Schwartz derivative of the function F.

1063-7710/00/4601-0100$20.00

Setting $F = 1 + \exp(k_0\xi + k_1\eta - \omega_0\tau)$, we obtain that equation (6) (as well as other equations of the system) is identically satisfied when the dependence of ω_0 on k_0 and k_1 (the dispersion relation) has the form

$$\omega_0 = \left(\frac{1}{4}\frac{b_1^2}{b_2} - \frac{1}{6}\frac{b_3^2}{b_4}\right)k_0 - \frac{b_4}{2}k_0^3 - b_5\frac{k_1^2}{k_0}. \quad (7)$$

Substituting $F = 1 + \exp(k_0\xi + k_1\eta - \omega_0\tau)$ in transformation (5) with allowance for relation (7), we obtain the exact solution to equation (1):

$$\psi = \pm k_0\sqrt{6\frac{b_4}{b_2}}\tanh\left(\frac{k_0\xi + k_1\eta - \omega_0\tau}{2}\right) \mp \frac{b_3}{(6b_2b_4)^{1/2}} + \frac{b_1}{2b_2}. \quad (8)$$

From relation (7), it follows that solution (8) propagates with the velocity equal to that of linear waves described by the linearized Kadomtsev–Petviashvili equation corresponding to relation (7) in the absence of dissipation:

$$\frac{\partial}{\partial\xi}\left[\psi_\tau + \left(\frac{1}{4}\frac{b_1^2}{b_2} - \frac{1}{6}\frac{b_3^2}{b_4}\right)\psi_\xi + \frac{b_4}{2}\psi_{\xi\xi\xi}\right] = b_5\psi_{\eta\eta}.$$

In the spatially one-dimensional case ($k_1 = 0$), formula (8) describes the class of solutions of equation (1) in the form of travelling profiles. For example, at $k_0 = \frac{b_3}{6b_4} + \frac{b_1}{2(6b_2b_4)^{1/2}}$, a shockwave structure is formed with $\psi = 0$ before the shock front and $\psi = \frac{2b_3}{(6b_2b_4)^{1/2}} + \frac{b_1}{b_2}$ behind the shock front (this solution corresponds to the lower signs in expression (8)).

If we select $k_0^2 = \frac{b_3^2}{3b_4^2} - \frac{b_1^2}{2b_2b_4}$, then, instead of formula (7), we obtain a dispersion relation for the linearized problem without dissipation:

$$\omega_0 = -b_4k_0^3 - b_5\frac{k_1^2}{k_0}.$$

With the substitution $F = 1 - \exp(k_0\xi + k_1\eta - \omega_0\tau)$, from transformation (5) of the Backlund type, we obtain a class of exact singular solutions of equation (1):

$$\psi = \pm k_0\sqrt{6\frac{b_4}{b_2}}\coth\left(\frac{k_0\xi + k_1\eta - \omega_0\tau}{2}\right) \mp \frac{b_3}{(6b_2b_4)^{1/2}} + \frac{b_1}{2b_2}.$$

However, these solutions have no physical meaning. Equation (1) has no soliton-like solutions.

The analysis described above shows that evolutionary equation (1) modeling a wave process in a strained nonlinear viscoelastic medium allows a Backlund-type transformation of the solutions. This transformation makes it possible to construct the classes of exact solutions of equation (1). Among them, the shockwave structures are of particular interest. Thus, the results obtained in this paper provide the necessary basis for further analytical and numerical analysis of non-one-dimensional wave processes in nonlinear dissipative and dispersive media.

REFERENCES

1. V. I. Erofeyev, *Microstructured Solids: Mathematical Models and Wave Processes Analysis* (Intelservice, Nizhni Novgorod, 1996).
2. G. A. Arshinov, A. I. Zemlyanukhin, and L. I. Mogilevich, in *Proceedings of the VIII Session of the Russian Acoustical Society, Nizhni Novgorod, Russia 1998*, p. 7.
3. N. A. Kudryashov, Prikl. Matem. Mekh. **54**, 450 (1990).
4. J. Weiss, M. Tabor, and G. Carnevale, J. Math. Phys. **24**, 522 (1983).
5. N. Kudryashov and E. Zargaryan, J. Phys. A **29**, 8067 (1996).

Translated by E.M. Golyamina

Acoustical Physics, Vol. 46, No. 1, 2000, pp. 102–104. Translated from Akusticheskiĭ Zhurnal, Vol. 46, No. 1, 2000, pp. 118–120.

SHORT COMMUNICATIONS

Contribution of Resonance Structures to the Formation of a Region of Wave Localization in a Randomly Inhomogeneous Medium

M. V. Kurbatov

Andreev Acoustics Institute, Russian Academy of Sciences, ul. Shvernika 4, Moscow, 117036 Russia
e-mail: bvp@akin.ru

Received December 29, 1998

Different aspects of the effect of wave localization were considered in a number of publications [1–4]. For a one-dimensional case of wave incidence on a layer of discrete random inhomogeneities in a medium without absorption, it was found that the region of wave localization tends to half of the layer with an increasing number of inhomogeneities, the amplitude of every inhomogeneity being fixed [5, 6]. It was also found that resonance structures (within which the field far exceeds the incident field) play a crucial role in the formation of the localization region [7, 8]. In this paper, by the method of numerical modeling, it is shown that the localization scale is determined by an extremely small number of realizations with high intensity peaks. In the case described below, this number makes only a fraction of percent of the total number of realizations over which the averaging is performed.

The problem under consideration is the determination of the field in a one-dimensional structure with random inhomogeneities. A harmonic wave $\exp(ikx)$ is incident from the left on a system of discrete inhomogeneities. Each of the latter can be uniformly and independently positioned within an interval equal to the half-wavelength; intervals for different inhomogeneities do not overlap; the average distance between the neighboring inhomogeneities is a. The resulting field formed in a medium with discrete inhomogeneities satisfies the differential equation

$$\varphi''(x) + k^2\left(1 + \mu\sum_{j=1}^{n}\delta(x - x_j)\right)\varphi(x) = 0, \qquad (1)$$

where μ is the amplitude of the discrete inhomogeneities, n is their number, $k = q(1 + i\beta)$ is the wave vector, β characterizes the absorption (at the beginning, we assume that $\beta = 0$), and x_j are the coordinates of the inhomogeneities ($j = 1, 2, \ldots, n$).

To solve the problem numerically, different methods can be used. A method that requires minimum machine time (the necessary time of computation grows only linearly with n) and provides an exact result is the field calculation by the transition matrices. The method is as follows: knowing the field $\varphi(x) = A_m\exp(ikx) + B_m\exp(-ikx)$ between x_m and x_{m+1}, we can determine the field $\varphi(x) = A_{m-1}\exp(ikx) + B_{m-1}\exp(-ikx)$ between x_{m-1} and x_m from the condition of the field continuity at the point x_m and the drop in its first derivative at x_m according to equation (1):

$$\varphi'(x_m + 0) - \varphi'(x_m - 0) + k^2\mu\varphi(x_m) = 0.$$

As a result, we obtain the transition matrix

$$\begin{aligned} A_{m-1} &= A_m(1 - i\varepsilon) - i\varepsilon B_m\exp(-2ikx_{m+1}), \\ B_{m-1} &= B_m(1 + i\varepsilon) + i\varepsilon A_m\exp(2ikx_{m+1}), \end{aligned} \qquad (2)$$

where $\varepsilon = k\mu/2$.

The field transmitted through the system of n inhomogeneities has the form $\varphi(x > x_n) = Ae^{ikx}$, where $A \neq 0$ is some complex number.

The quantity $\varphi_{new}(x) = \varphi(x)/A$ also satisfies equation (1). To determine $\varphi_{new}(x)$, we apply the following method: using matrix (2), we determine $\varphi_{new}(x)$ between x_{n-1} and x_n (assuming that at $x > x_n$, the field is determined by e^{ikx}, i.e., $A_n = 1$ and $B_n = 0$); then, from $\varphi_{new}(x)$ determined at this interval, we obtain $\varphi_{new}(x)$ at $x \in (x_{n-2}, x_{n-1})$, and so on, down to the interval $x < x_1$, where $\varphi_{new}(x < x_1) = A_0e^{ikx} + B_0e^{-ikx}$, i.e., $A = 1/A_0$.

Having determined A and $\varphi_{new}(x)$, we obtain the desired field, i.e., the solution to equation (1). This field has the form $\exp(ikx)$ to the left of the layer, i.e., at $x < x_1$, we have $\varphi(x) = A\,\varphi_{new}(x) = \varphi_{new}(x)/A_0$. We also obtain the average square of the field magnitude after the averaging over the number of possible realizations:

$$\overline{|\varphi(x)^2|} = (1/n)\sum_{i=1}^{n}[\mathrm{Re}^2(\varphi_i(x)) + \mathrm{Im}^2(\varphi_i(x))].$$

The result of numerical modeling is coincident with the analytical dependence obtained by Gazaryan and Gel'fgat [5, 6]. According to this dependence, with $n\varepsilon^2 \longrightarrow \infty$, the localization region tends to half of the layer, and the distribution of the field intensity in the layer tends to a "step" (see Figs. 1, 2, curves *1*).

1063-7710/00/4601-0102$20.00

At first glance, the fact that the localization region does not depend on the dimensions of the inhomogeneities forming the layer seems quite unexpected. For the vast majority of configurations, the localization length decreases with increasing ε. However, according to the results of our theoretical studies [9], there always exist some configurations of inhomogeneities for which the square of the field magnitude inside the layer may far exceed the intensity of the incident wave (the maximum value of this ratio is estimated in [9]). These "resonance" configurations are fairly unstable: they are highly sensitive to the least variations in the coordinates of the inhomogeneities. A numerical analysis was performed for the resonances characterized by the square of the field magnitude inside the layer reaching the values that exceed the incident field intensity by a factor of $\sim 10^7$; the analysis was performed for the case $n = 100$, $\varepsilon = 1$. It was found that when the coordinate of some inhomogeneity varies by a fraction of percent near the resonance, the maximum ratio of the square of the field magnitude inside the layer to the incident field intensity decreases by a factor of $\sim 10^3$.

Thus, with increasing $n\varepsilon^2$, the statistical weight of the resonance configurations sharply decreases, while the field amplification in these structures sharply increases. As a result, the role of a very small number of realizations becomes crucial, so that, in the process of statistical averaging, their contribution to the formation of a "step" becomes decisive.

Let us consider the case $n = 60$, $\varepsilon = 0.9$. The distribution of the square of the field magnitude inside the layer is shown in Fig. 1 (curve *1*). Here, the averaging is performed over 5×10^8 realizations. If we perform the averaging after eliminating 5000 strongest resonances which constitute one thousandth of percent of the total number of realizations, the distribution of the square of the field magnitude inside the layer will be similar to that shown in Fig. 2 (curve *2*), i.e., the localization length will decrease by a factor of two. If we eliminate one percent of the realizations with maximum field amplification inside the layer, the localization length will be equal to 1/10 of the layer length.

The introduction of a weak absorption β has practically no effect on the nonresonance structures, while for sufficiently large numbers *n*, the wave interference that leads to the resonance in the absence of absorption is destroyed, i.e., the energy rather than amplitude summation takes place. According to our results [9], no matter what configuration, the field amplification cannot exceed some quantity depending on ε and β. Suppose that this quantity corresponds to the maximum field amplification in the medium without absorption for a layer containing n_0 inhomogeneities. Then, evidently, in the presence of absorption, the region of wave localization will never contain more than $\sim n_0$ inhomogeneities, no matter how great the number *n*. Thus, at large numbers *n*, the wave localization length sharply decreases with increasing β because of the fast decrease

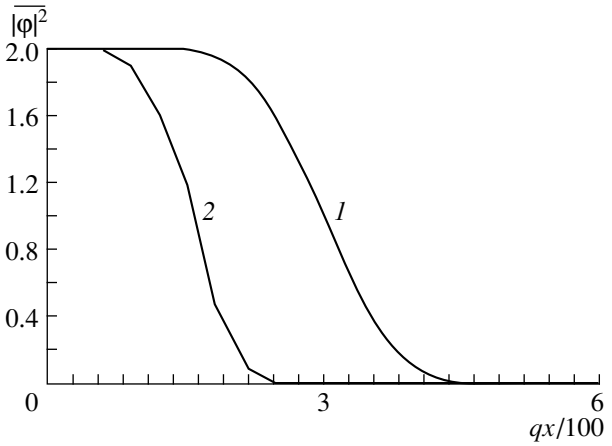

Fig. 1. Distribution of the field intensity along the inhomogeneity structure in a medium without absorption: (*1*) the result of averaging over 5×10^8 realizations (this result is coincident with the analytical dependence (24) from [5]); (*2*) the result of the elimination of 5000 strongest resonances from the previous averaging. The average distance between the inhomogeneities is $a = 10/q$; $n = 60$ and $\varepsilon = 0.9$.

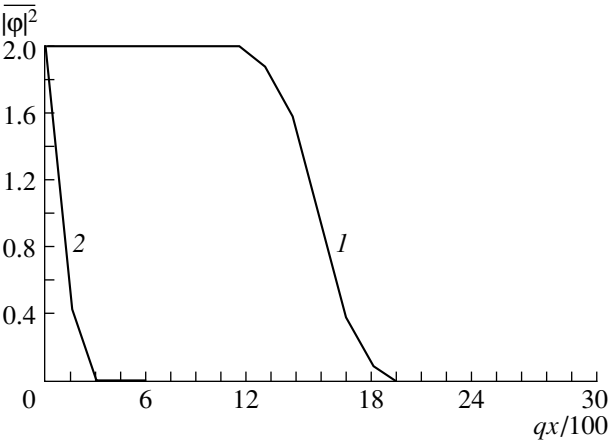

Fig. 2. Distribution of the field intensity along the inhomogeneity structure in a randomly inhomogeneous medium: (*1*) in the absence of absorption and (*2*) in the presence of a weak absorption $\beta = 10^{-5}$. The average distance between the inhomogeneities is $a = 10/q$; $n = 300$ and $\varepsilon = 0.9$.

in n_0. Figure 2 shows the results of the numerical calculation for $n = 300$, $\varepsilon = 0.9$. The average distance between neighboring inhomogeneities is $a = 10/q$. Curve *1* displays the spatial distribution of the square of the field magnitude inside a layer without absorption. In the presence of a weak absorption $\beta = 10^{-5}$, this dependence takes the form of curve *2* (Fig. 2), i.e., the localization region becomes ten times smaller. Note that in a homogeneous medium with such an absorption, the intensity of a wave transmitted through a distance equal to the length of the layer under consideration, $3000/q$, decreases only by 6%.

In closing, we formulate the main results:

(1) in the absence of absorption in a randomly inhomogeneous medium with a large value of $n\varepsilon^2$, the formation of the wave localization region is governed by the resonance structures; if these structures are eliminated from the process of averaging over possible realizations, the localization length sharply decreases;

(2) with the introduction of a weak absorption, the wave localization length at large n becomes much less than the length of half of the layer.

ACKNOWLEDGMENTS

I am grateful to S. A. Rybak for useful discussions. This work was supported by the Russian Foundation for Basic Research (project no. 96-02-16561 and grant no. L-96-15-96608).

REFERENCES

1. M. P. Castanier and C. Pierre, J. Sound Vibr. **183**, 493 (1995).
2. D. M. Photiadias, Appl. Mech. Rev. **49**, 100 (1996).
3. P. D. Cha and C. R. Morganti, AIAA J. **32**, 2269 (1994).
4. P. W. Anderson, Phys. Rev. **109**, 1492 (1958).
5. Yu. L. Gazaryan, Zh. Éksp. Teor. Fiz. **56**, 1856 (1969) [Sov. Phys. JETP **29**, 996 (1969)].
6. V. I. Gel'fgat, Akust. Zh. **18**, 31 (1972) [Sov. Phys. Acoust. **18**, 25 (1972)].
7. V. I. Klyatskin and A. I. Saichev, Usp. Fiz. Nauk **162**, 161 (1992) [Sov. Phys. Usp. **162**, 135 (1992)].
8. V. I. Klyatskin, *Immersion Method in the Theory of Wave Propagation* (Nauka, Moscow, 1986).
9. M. V. Kurbatov and S. A. Rybak, Akust. Zh. **45**, 370 (1999) [Acoust. Phys. **45**, 326 (1999)].

Translated by E.M. Golyamina

Acoustical Physics, Vol. 46, No. 1, 2000, pp. 105. Translated from Akusticheskiĭ Zhurnal, Vol. 46, No. 1, 2000, pp. 121–122.

CHRONICLE

Nikolaĭ Vladimirovich Studenichnik (On His 70th Birthday)

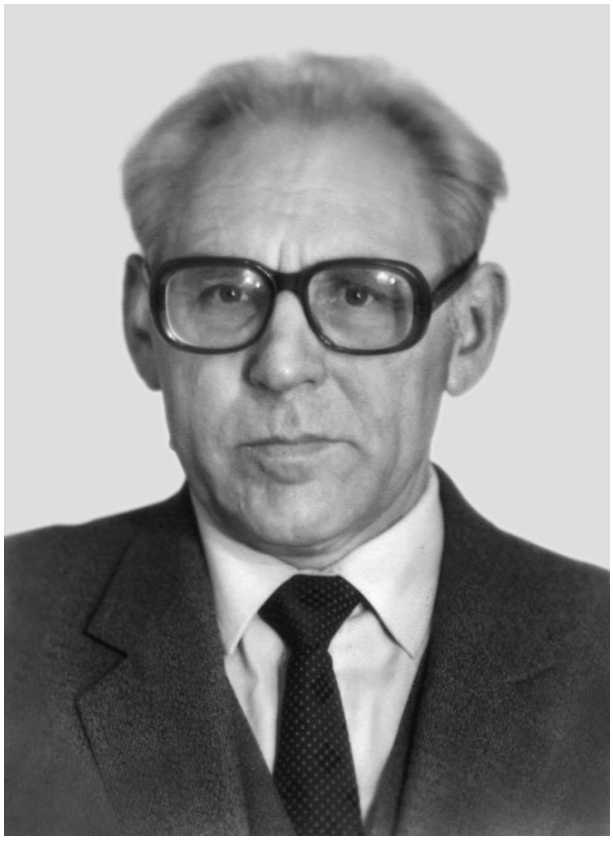

On May 20, 1999, Nikolaĭ Vladimirovich Studenichnik—candidate of physics and mathematics, senior researcher, and one of the eldest staff members of the Andreev Acoustics Institute—turned seventy.

Studenichnik was born in Byten', a small town in the Brest region of Belorussia. After he graduated from the Physicomathematical faculty of the Belorussian State University in 1953, he began working at the Acoustical laboratory of the Lebedev Physical Institute of the Academy of Sciences of the USSR. In 1954, this laboratory was reorganized into the Acoustics Institute of the Academy of Sciences of the USSR.

The first research project carried out by Studenichnik dates back to 1952–1953; at that time he was a fifth-year university student. At the Acoustics Institute, he began to study multielement broadband resonance absorbers. The main scientific activity of Studenichnik is related to the studies of sound fields in underwater waveguides.

The first experiments on the propagation in the underwater sound channel were performed in 1950s in the Black Sea, at the Sukhumi Sea Research Station of the Acoustics Institute of the Academy of Sciences of the USSR. From 1960 onwards, experimental and theoretical studies were carried out by Studenichnik in different water areas of oceans all over the world. He obtained fundamental results on the characteristics of sound fields in underwater waveguides; he also developed new methods for analyzing and processing the experimental data. The main object of his studies was the fine structure of sound fields in waveguides in deterministic conditions in the presence of statistical inhomogeneities. This includes the multiray propagation, the near-surface channel, the nature and identification of the diffraction field and the field of bottom reflections in the open and internal shadow zones in the deep sea and in the wedge-shaped regions of the coastal zone, the geometric dispersion of sound velocity in the underwater sound channel and in shallow sea, the refraction frequency-angular filling of the channel, etc. Studenichnik developed the ray method of the determination of the sound source coordinates in the ocean, as well as the physical foundations and principles of the design of digital multichannel instruments for studying the angular spectra of sound fields in the ocean. He substantially contributed to the classification and generalization of the hydrological-acoustical characteristics of shallow-water and shelf zones of the internal and external seas of the Soviet Union, as well as of a number of shelf zones and the continental slope of the ocean.

The results obtained by Studenichnik by the mid-60s were generalized in his candidate dissertation. In 1966, he received the degree of candidate of physics and mathematics. In 1971, he received the title of senior researcher.

Studenichnik was also involved in scientific–organizational activities. In 1966–1994, he supervised nine comprehensive research projects that were carried out in cooperation with large research groups from different institutions including the academic ones, as well as from universities and industrial organizations. He organized the All-Union Interdepartmental Scientific Seminar on Acoustics of the Shallow Sea and Coastal Shelf of the Ocean. This seminar was a regular event in the 1970s–1980s. Studenichnik is the author of more than 170 scientific reports and papers and the author of six inventions.

Studenichnik took part in the organization of many oceanic expeditions on the research ships belonging to the Acoustics Institute and the Navy.

Today, Nikolaĭ Vladimirovich Studenichnik continues his active work in science. We wish him good health and new scientific achievements.

Translated by E.M. Golyamina

1063-7710/00/4601-0105$20.00

Acoustical Physics, Vol. 46, No. 1, 2000, pp. 106. Translated from Akusticheskiĭ Zhurnal, Vol. 46, No. 1, 2000, pp. 123.

CHRONICLE

L. M. Brekhovskikh Elected Honorary Member of the Acoustical Society of America

Academician Leonid Maksimovich Brekhovskikh was elected Honorary Member of the Acoustical Society of America. He received this title for his pioneering contributions to wave propagation and scattering. The presentation of the diploma and the celebration of Brekhovskikh's new title took place at the Joint Convent of the Acoustical Society of America and the European Acoustical Association in March 1999, in Berlin (Germany).

L. M. Lyamshev Elected Honorary Member of the International Institute of Acoustics and Vibration

Professor Leonid Mikhaĭlovich Lyamshev was elected Honorary Member of the International Institute of Acoustics and Vibration, which unites acousticians from many countries all over the world. Lyamshev was given this title for his outstanding contributions to scientific knowledge in acoustics and vibration. Officially, the new Honorary Member of the International Institute of Acoustics and Vibration was presented to the public at the Sixth International Congress on Sound and Vibration in July 1999, in Copenhagen (Denmark).

1063-7710/00/4601-0106$20.00 © 2000 MAIK "Nauka/Interperiodica"

Acoustical Physics, Vol. 46, No. 1, 2000, pp. 107–108. Translated from Akusticheskiĭ Zhurnal, Vol. 46, No. 1, 2000, pp. 124–126.

INFORMATION

The 15th International Symposium on Nonlinear Acoustics

The 15th International Symposium on Nonlinear Acoustics was held in Goettingen, Germany, on September 1–4, 1999. Professor W. Lauterborn was the chairman of the Organizing Committee of the Symposium. Over 130 papers were presented. The papers covered the following fields: propagation of waves of finite amplitude in liquids and solids, wave propagation in media with essential nonlinearity, interaction of waves of finite amplitude with boundaries and particles, cavitation and luminescence, thermoacoustics, acoustic streaming and Bjerknes forces, industrial and medical applications of nonlinear acoustics, focused high-intensity ultrasound and lithotripsy, and sonochemistry. The invited papers reflect the modern state of nonlinear acoustics relatively fully.

The results of the experiments conducted at the Cavendish Laboratory and the Third Physical Institute of Goettingen University were discussed in the paper by J. Blake and G. Keen (Great Britain) entitled "Single Cavitation Bubble Luminescence." It was established that a strong light emission occurred in the process of an asymmetric collapse of a bubble when a strong high-velocity jet emerged near a solid boundary. An attempt to explain the observed phenomena was made. A calculation of the collapse of a bubble with toroidal geometry was performed on the basis of the modified boundary integral method. It was noted that the considered model can explain some experimental results, including those obtained at Goettingen University.

L. Crum (USA) delivered a paper entitled "Acoustic Hemostasis." Results of multiple purposeful experiments conducted within the framework of a special program were described in detail. This program provided for the investigation of the application of focused ultrasound to the detection and treatment of strong internal hemorrhage, which often leads to a lethal outcome. A real opportunity to apply ultrasound to these purposes was demonstrated. Encouraging results were obtained, which can increase the chances of a patient's ability to survive under extreme conditions of intensive therapy.

A review of the development and the current status of ultrasonic lithotripsy was given in the paper by M. Delius (Germany), "The History of Extracorporeal Shock Wave Lithotripsy." It was noted that the first studies had been performed in the 1950s. Intensive shock waves were produced with the help of electric discharge in a fluid. Quite encouraging results of the application of ultrasonic lithotripsy refer to the early 1970s. Now, ultrasonic lithotripsy is successfully used for treating illnesses connected with the formation of stones in various organs of the human body. It was reported that a new kind of therapy utilizing lithotripsy for affecting "unhealthy tumors" was developed in Germany. Results of its application are as yet unknown.

In the paper entitled "Nonlinear Acoustics and Industrial Applications," J. Gallego-Suares (Spain) considered the effects arising in the process of action of acoustic waves on substances and structures such as radiation pressure, cavitation, acoustic streaming, Bjerknes forces, etc. Utilization of these effects lies in the basis of the development of devices and equipment used in industry. It was noted that in many cases these effects occur simultaneously. Some of them are useful, while other ones interfere. The problem of optimal application of useful effects and suppression of interfering factors must be solved in the process of the development of devices and equipment. Specific examples of devices used in industry were given.

The paper "Acoustic Phase Conjugation" by M. Fink (France) was devoted to reviewing the opportunities to observe the effect of phase conjugation in acoustics and its utilization in practice. Its application to lithotripsy and other fields of medicine, where it is necessary to solve the problem of "targeting" to an object, was discussed. Its application to underwater acoustics and investigating processes of multiple scattering of waves and turbulence was considered.

M. Hamilton, Yu. Il'inskii, and E. Zabolotskaya (USA) presented a paper entitled "Nonlinear Surface Acoustic Waves." The theory of nonlinear surface acoustic waves grounded on the formalism of Hamiltonian mechanics was developed during the last decade, largely due to the efforts of the authors. A review of this theory and its further development was given. A theory of nonlinear Rayleigh waves in isotropic solids was discussed. A system of evolutionary equations in three alternative forms was obtained for the description of these waves. One of these forms is a set of coupled spectral equations, and another one is an integral equation, the solution of which allows one to separate the contributions of the local and nonlocal nonlinearities. The third form is a differential equation involving the Hilbert transforms. Analytical and numerical solutions to these equations provided an opportunity to study the formation of shock waves, the beam diffraction, pulsed transient processes, and the attenuation of nonlinear Rayleigh waves. Specific features of the propagation of nonlinear Stoneley and Scholte waves were considered

1063-7710/00/4601-0107$20.00

recently. The application of evolutionary equations to the investigation of the propagation of nonlinear surface waves in crystals and piezoelectrics was discussed.

The paper by Y. Matsumoto (Japan), "Bubble and Bubble Cloud Dynamics," was devoted to analyzing the processes of the formation and propagation of shock waves in a bubble cloud. The behavior of a single bubble was considered from the point of view of a nonlinear oscillator. Many basic physical processes taking place within the bubble volume and at its boundaries (surfaces) such as diffusion, heat transfer, mass transfer, etc. were taken into account. These effects were considered in the analysis of nonlinear collective oscillations of multiple bubbles in a cloud. Numeric solutions of a set of equations describing these oscillations provided an opportunity to consider the specific features of the formation and propagation of shock waves in a cloud. It was stressed that the amplitude of a shock wave at the center of a cloud may be several hundred times higher than in the case of a collapse of a single bubble due to the collective interaction of bubbles.

The paper by F. Melo (Chile), "Granular Materials and Sound," described the sound propagation in a granular medium. The medium was treated as a set of rigid spheres of equal radius. The contact nonlinearity caused by forces at the contacting boundaries of spheres (Hertz contacts) was considered.

L. Ostrovsky, P. Johnson, and T. Shankland (USA) presented a paper on "The Mechanism of Nonlinear Response in Highly Nonlinear Solids." It is well known that many materials, such as rock, concretions, polymer materials, etc., possess a pronouced elastic nonlinearity, which is many orders of magnitude higher than that of homogeneous gases, liquids, and crystals. Moreover, these materials frequently exhibit hysteretic properties in the process of their deformation. The mechanism of this nonlinearity is extremely complex and can be caused by structural inhomogeneities and defects, i.e., granules, cracks, dislocations, etc. The inhomogeneities may exist as compliant inclusions in a relatively rigid matrix. The authors call this nonlinearity "structural nonlinearity" and materials by the name "mesoscopic nonlinear materials." The paper treated some models of such media and materials and some model equations that allow one to study the propagation of nonlinear waves in these materials.

The paper "Nonlinear Phenomena in Structures with Movable Boundaries" by O. Rudenko (Russia) formulated and discussed some nonlinear problems of wave dynamics, which took into account finite displacements of oscillating boundaries. Such problems are the formation of a sonic boom in the process of supersonic motion of an airfoil with a nonzero cross-section, a high-amplitude vibration of a body in a strongly compressible medium, vibrations of resonance structures, and some problems of the nonlinear wave propagation. The specific features of the propagation of waves and vibrations in considered dynamical structures were discussed. It was demonstrated, for example, that spectral distortions may be caused not only by nonlinear physical properties of a medium, but also by nonlinear interaction of waves with the boundary (radiating surface) performing vibrations of finite amplitude. Part of the paper was devoted to the analysis of the equations of nonlinear acoustics obtained by various authors and at different times for describing the propagation and evolution of nonlinear acoustic waves.

K. Suslick (USA) delivered a paper entitled "Sonochemistry." He noted that chemistry is the interaction of energy and matter. There are many ways of transferring energy to molecules. The application of high-intensity ultrasound opened up new possibilities of controlling chemical reactions. For example, a local pressure of 1000 atmospheres and a temperature increase up to 5000 K may occur during the time of several nanoseconds in the process of a cavitation bubble collapse. Chemical reactions, which normally take place only under extreme conditions, are possible under the effect of ultrasound. Many examples of ultrasound applications in chemical technology were given and discussed.

The paper by G. Swift (USA), "Streaming in Thermoacoustic Engines and Refrigerators" was devoted to an important and rapidly developing field of nonlinear acoustics. Without going into the details of this paper, we note that the efficiency of acoustic refrigerators may reach 40%. Thermoacoustic refrigerators are in operation now.

From the given brief and quite incomplete description of the invited papers, one can see that nonlinear acoustics is developing rapidly. In the 1950s, it was the focus of "curious theoreticians," but now research teams from many countries work on the problems of nonlinear acoustics, and the results of these studies are finding ever more applications.

The 16th International Symposium on Nonlinear Acoustics is planned to be held in Moscow, Russia, in 2002.

L. M. Lyamshev

Translated by M.L. Lyamshev

Acoustical Physics, Vol. 46, No. 1, 2000, pp. 109–111. Translated from Akusticheskiĭ Zhurnal, Vol. 46, No. 1, 2000, pp. 127–130.

INFORMATION

BOOK REVIEW:
Acoustics of Layered Media. I. Plane and Quasi-Plane Waves (1998); *II. Point Sources and Bounded Beams* (1999)

by L. M. Brekhovskikh and O. A. Godin.

Published by Springer Verlag, Berlin

All natural media, including the atmosphere, ocean, and the earth's crust, as well as various technical equipment (ultrasonic filters, lenses, delay lines on surface waves, etc.), are layered structures. As a consequence, an environmental layered model occupies a quite prominent place in the propagation theory of atmospheric and underwater sound, and internal, seismic, and radiowaves. The model itself is continuously refined and complicated; more and more new analytical and numerical methods are developed for the investigation of wave fields in layered media; the number of applied problems solved on the basis of the layered model rapidly increases, and the circle of researchers involved in these studies is expanded. The publication of the second updated edition of the two-volume book *Acoustics of Layered Media* is quite timely. This book sums up the development of the wave propagation theory in layered media within the last 8–10 years that elapsed since the time of its first publication (1990–1992).

The first volume that treats plane and quasi-plane waves underwent only insignificant modifications compared to the first edition: some polishing of the language with the help of Canadian colleques, corrections of misprints in the text and equations, and additional references predominantly to papers and books published in or after 1990 (more than 90 new references). The latter is probably the most important improvement. A few textual changes are also introduced to make the treatment clearer and to connect it closely to recent publications. The structure of the first volume of the second edition (as in the first edition) is the same as the first ten sections of *Akustika sloistykh sred* published in Russian (Nauka, Moscow, 1989) by the same authors with each section of the Russian version becoming a chapter.

Because the review of the first edition of this monograph was not published, it is expedient to give a short description of the content of the second edition. The first volume consists of ten chapters. The first chapter is devoted to the propagation theory of waves with a harmonic dependence on horizontal coordinates and time. The wave equations, boundary and initial conditions, as well as the conditions at infinity, are derived for sound and elastic waves in solids. Of special interest is the derivation of modified wave equations containing no derivatives of the environmental parameters. A wave equation for a moving layered medium is also presented.

Chapter 2 deals with the plane-wave reflection from an interface between two homogeneous media, a plane layer, and an arbitrary number of layers. On the basis of the generalization of the sound wave impedance for moving layered media, the plane-wave reflection from a discretely layered medium of a general type was considered.

Chapter 3 is devoted to the plane-wave reflection from the boundaries of continuously layered media. The cases that allow exact solutions of the one-dimensional wave equation in liquid with continuously stratified density and velocities of sound and current are analyzed. From these solutions, all previously known solutions can be obtained as limiting cases.

In Chapter 4, the plane-wave reflection from the boundaries of discretely layered solids is considered. The expressions for the reflection coefficients characterizing the reflection from elastic halfspace boundaries and a system of solid layers are obtained. It is worth noting the efficient use of the matrix formalism in describing waves in solids, which allows one to avoid the awkwardness of the resulting formulas and make the results more clear and easily representable in an algorithm form.

Chapter 5 is devoted to the reflection of sound pulses. The integral representation of a sound field is obtained, the law of conservation of an integrated pulse is determined, the change of the pulse shape upon a total internal reflection from an interface between two homogeneous media is investigated, and the total reflection of a pulse in continuously layered media is studied.

In Chapter 6, the universal properties of the reflection and transmission coefficients of plane monochromatic waves are determined and analyzed. These properties do not depend on the type of the medium stratification. Relations of symmetry of the reflection coefficients with respect to the inversion of the direc-

1063-7710/00/4601-0109$20.00

tion of wave propagation in liquid are obtained. Some symmetry relations are also proved for solids. Much attention is given to analyzing the singularities (poles and branch points) of the reflection and transmission coefficients, which is very important in the investigation of the field of a point source in a layered medium by decomposing the field into plane waves. A class of layered media is described, for which the reflection coefficient equals unity for a fixed frequency and angle of incidence. This result is of practical significance.

Chapter 7 deals with waves in absorbing anisotropic media. The influence of absorption and dispersion on the wave propagation in liquid and solid media is analyzed. The effects of anisotropy are most significant in solids, in particular, in acoustics of crystals, as well as in seismology. Two cases are considered in detail: the wave propagation in piezoelectrics (including the Gulyaev–Bleustein waves) and elastic waves in transversally isotropic solids (fine-layered media).

Chapter 8 is devoted to geometric acoustics and approximate (mainly, asymptotic) methods of wave field investigations. The central place is given to the WKB method. The necessary and sufficient conditions of the validity of the WKB method are formulated; these conditions are also considered near the turning points and the resonance interaction depths. The difference in the ray patterns in moving and motionless media are analyzed.

In Chapter 9, the sound field in the case of turning horizons and resonance interaction with a flow is studied. Using the reference equation, the authors construct the high-frequency asymptotics of the sound field in the vicinity of turning depths, consider the sound reflection from a "potential barrier," and estimate the accuracy of the asymptotic solutions and their relation to the WKB approximation. The theory of the resonance amplification of sound because of its interaction with a flow is developed in detail for arbitrary separated depths of resonance interaction and turning points. Unfortunately, this interesting effect can be realized neither in the ocean nor in the atmosphere, since the speeds of currents are too small in these media. Possibly, it will be of interest for aeroacoustics, in the studies of sound reflection from a stratified jet.

Chapter 10 deals with the sound reflection from a medium with arbitrarily varying density and speeds of sound and current along the vertical coordinate. The Riccati equation is obtained for the reflection coefficient, and different approximate methods are considered for its solution. A new approach is proposed to the analysis of the plane-wave reflection from a thin (compared to wavelength) inhomogeneous layer. This approach allows the description of some degenerate cases that cannot be treated by the previous methods.

The second volume was subjected to more substantial changes in the second edition as compared to the first volume. This occurred because the second volume deals with more advanced problems, many of which remain at the forefront of recent research. Currently, the interest of researchers is more and more shifted toward two-and three-dimensional inhomogeneous media. The new edition further develops the theory of wave propagation in such complicated environments. As a result, a new large chapter (Chapter 8) and two extended appendices (Appendix B and Appendix C) were added to the second edition, which increased the volume of the book by more than 25%. These additions are based on recent original publications by one of the authors (Godin). It was necessary to add about 360 new references to an already extensive list of the first edition to keep the list of references up to date and to provide the reader with a link to the latest developments.

The second volume consists of eight chapters. In the first chapter, on the basis of the sound field representation as a superposition of plane waves, the authors investigate the reflection and refraction of a spherical wave from a plane interface of media. An integral representation of the reflected field and its uniform asymptotics, which are also valid with allowance for the absorption and relative motion of the bordering media, are derived. The reflection of sound from an impedance surface and a boundary of media with different densities are considered. The reflection from weak boundaries, which is the most complicated case from a theoretical point of view, is investigated in detail.

Chapter 2 is devoted to the reflection of bounded wave beams. Much attention is given to the effect of the beam displacement along the reflecting surface. The authors have developed the exact theory of this phenomenon and analyzed its dependence on various parameters of the problem. Some nonspecular effects accompanying the beam reflection are considered.

Chapter 3 presents the theory of lateral waves. A technique for calculating the lateral waves in layered inhomogeneous media is developed for both a point (omnidirectional) source and a directional source. The physical interpretation of the lateral wave is given, and the regions of its observation are analyzed. The influence of the absorption and medium motion on the lateral wave characteristics is investigated. In the approximation of the small perturbation method, the scattering of lateral waves by a small-scale random roughness of the interface between media is considered. It is shown that for certain conditions, the presence of roughness leads to an increase in the lateral wave intensity.

In Chapter 4, the theory of the sound field of a point source in horizontally stratified liquid media, both moving and motionless, is developed. The wave equation for a nonstationary moving medium is derived. Exact wave equations are obtained for some particular cases: a steady motion, a medium with slow currents, and a motionless medium. The reciprocity relations for sound fields are discussed, and the flow reversal theorem is proved for a moving layered medium. Some exact solutions of the wave equations are obtained for a motionless medium with various vertical sound velocity profiles. The modes generated in a moving medium by a line or a point source are obtained and analyzed.

In Chapters 5 and 6, high-frequency sound fields are considered. The fundamentals of the geometric acoustics method are presented for monochromatic waves in a steady-state three-dimensional inhomogeneous moving medium. The eikonal equation and the radiation transport equation are obtained. Using the reference integrals and reference functions, the uniform and local asymptotics near a simple caustic and a cusp of a caustic are obtained. Some more complicated peculiarities of ray structures are also considered.

Chapter 7 covers the theory of wave propagation in irregular, range-dependent waveguides, which is a much more complicated problem than the wave propagation in an ideal layered medium. The main difficulty is related to the mode interactions in such irregular waveguides and the appearance of modes that propagate in the opposite direction. The authors have significantly developed the theory of coupled modes. The cross-section method based on the concept of the reference waveguide was further developed. The equation of the coupled modes is obtained and its solution by the method of successive approximations is described. Much attention is given to the wave propagation in three-dimensional irregular waveguides. For solving such problems, the method of two-scaled expansions (in ocean acoustics, this approximation is usually called "horizontal rays and vertical modes") is widely used. The method is generalized to the case of a three-dimensional inhomogeneous moving medium. The ray adiabatic invariants are determined, and the flow reversal theorem for modes is proved. The sound field peculiarities in the vicinity of the critical section of a waveguide are analyzed. The ray theory of a sound field in an irregular waveguide with allowance for the medium motion is developed. A new generation of parabolic equations is investigated. The use of these equations allows one to considerably improve the accuracy of the amplitude calculations without sacrificing the phase accuracy. A new class of the parabolic equations generalized to the case of a moving medium provides the fulfilment of the conservation law and the reciprocity principle for the acoustic field in the case of the waveguide propagation

The new Chapter 8 is devoted to the problems of wave reciprocity and wave energy conservation in three-dimensional inhomogeneous moving media. Recently, a remarkable progress in treating this rather difficult problem was achieved. By applying non-typical variables for describing the wave field, the equations of linear acoustics of a moving medium and the boundary conditions were dramatically simplified. As a result, it became possible to derive the reciprocity relations and the wave energy conservation law under rather general assumptions. This approach appears to be suitable for a simultaneous treatment of acoustic and acoustic-gravity waves, as well as waves in incompressible fluids.

Appendix A describes the basis of the method of the reference integrals which are encountered in studying the field of a point source in layered media, pulse propagation in dispersive media, wave diffraction from various bodies, quantum theory of collisions, and other physical problems. Various methods of calculating the reference integral are considered: the method of steepest descent, the saddle point method, and the method of stationary phase. The asymptotics of various reference integrals is investigated.

Appendix B covers the differential equations for coupled-modes in the waveguides with sloping boundaries and medium interfaces. In this case, the derivation of the coupled-mode equations relies on the reciprocity principle rather than the wave equation, which allows one to overcome some mathematical difficulties encountered with the use of a conventional approach. An important result is the evidence that the acoustic field representation as a sum of coupled modes in the waveguide with sloping boundaries is well justified. Thus, a definite answer is obtained to the prolonged discussion (mostly, among English-speaking acousticians) concerned with this problem.

Appendix C is devoted to the analysis of the wave propagation in irregular waveguides on the basis of a new class of parabolic equations. This Appendix is essentially a continuation of Chapter 7. Much attention is given to the problems of the wave reciprocity and the law of wave energy conservation in various physical situations.

On the whole, we should note first of all the fundamental character of this monograph. It provides the most comprehensive and systematic description of the recent theory of wave propagation in layered media. Starting from the first principles, the authors lead the reader to the latest results and the most powerful theoretical techniques currently available in the field of wave propagation in inhomogeneous media. The rigorous manner of the theory description is aptly combined with an analysis of possible applications. From complicated mathematical formulas, the authors try to get physically meaningful effects; mathematical transformations, as a rule, are accompanied by qualitative considerations. The volume of the represented material is vast (above 760 pages). Therefore, it is natural that some sections of the book are represented relatively briefly, and their reading requires certain efforts.

Several sections of the book can be used as the basis for the lecture courses for students and postgraduates on the theory of the propagation of waves of various physical nature in inhomogeneous media. For researchers working in different branches of acoustics, as well as in seismics and electromagnetic wave propagation, the monograph will be a valuable textbook. For the future development of the studies of wave propagation in Russia and some other countries of the former Soviet Union, it would be beneficial to publish this monograph in Russian.

Yu. P. Lysanov

Translated by Yu. P. Lysanov

Acoustical Physics, Vol. 46, No. 1, 2000, pp. 112. Translated from Akusticheskiĭ Zhurnal, Vol. 46, No. 1, 2000, pp. 131.

INFORMATION

Reviewers of Papers Published in vol. 45 of 1999

Alekseev, V.N.
Anisimkin, V.I.
Avilov, K.V.
Bobrovnitskiĭ, Yu.I.
Burov, V.A.
Chaban, A.A.
Chaban, I.A.
Danilov, S.D.
Dubrovskiĭ, N.A.
Erofeev, V.I.
Esipov, I.B.
Frolov, V.M.
Furduev, A.V.
Galkin, O.P.
Golyamina, I.P.
Goncharov, V.V.
Grinchenko, V.T.
Gulin, E.P.
Khokhlova, V.A.
Krasil'nikov, V.A.
Kravtsov, Yu.A.
Krupin, V.D.
Kryazhev, F.I.
Kudryashov, V.M.
Kurtepov, V.M.
Kuz'kin, V.M.
Lapin, A.D.
Lyakhov, G.A.
Lyamshev, L.M.
Lysanov, Yu.P.
Makov, Yu.N.
Mansfel'd, A.D.
Mikhalevich, V.G.
Mironov, M.A.
Molotkov, L.A.
Mozhaev, V.G.
Petnikov, V.G.
Petukhov, Yu.V.
Pikin, S.A.
Postnov, G.A.
Pyatakov, P.A.
Rudenko, O.V.
Rybak, S.A.
Serebryanyĭ, A.N.
Shenderov, E.L.
Shvachko, R.F.
Solov'ev, V.A.
Sorokin, V.N.
Studenichnik, N.V.
Telepnev, V.N.
Tyutekin, V.V.
Urusovskiĭ, I.A.
Virovlyanskiĭ, A.L.
Vovk, I.V.
Volovov, V.I.
Zosimov, V.V.
Zverev, V.A.

The Editorial Board extends its sincere gratitude to all listed reviewers for their active cooperation with the *Akusticheskiĭ Zhurnal.*

1063-7710/00/4601-0112$20.00 © 2000 MAIK "Nauka/Interperiodica"

Acoustical Physics, Vol. 46, No. 1, 2000, pp. 15–20. Translated from Akusticheskiĭ Zhurnal, Vol. 46, No. 1, 2000, pp. 21–27.

Acoustic Intensity of Deep Scattering Layers in Central Atlantic

I. B. Andreeva, N. N. Galybin, L. L. Tarasov, and V. Ya. Tolkachev

Andreev Acoustics Institute, Russian Academy of Sciences,
ul. Shvernika 4, Moscow, 117036 Russia
e-mail: bvp@akin.ru

Received December 27, 1998

Abstract—A computer database is developed for the purposes of quantitatively describing the spatial variability of acoustic inhomogeneities formed in the ocean by deep scattering layers (DSL). The database is now being completed with the results of full-scale measurements carried out during the last few decades. At the moment, the database is completed for the Atlantic Ocean. Using the Central Atlantic as an example, two methods of describing the spatial distribution of the DSL total column strength (intensity) M are tested for the daylight hours and frequencies between 3 and 20 kHz. The first method consists of plotting the isolines of the quantity M on the map of the ocean. Such plots are obtained for six frequencies of the above frequency range; several maps are presented in the paper. The second method is based on the selection of hydrologically homogeneous regions with the subsequent statistical processing of all column strengths M existing in the database for every particular region. The estimates of the mean values and variances of the quantity M for individual regions show that some of these regions can be combined. As a result, the Central Atlantic is divided into four acoustically homogeneous (in the considered parameter) regions that widely differ in the statistical estimates of the column strength and their variances. The corresponding maps and tables with quantitative characteristics are presented. The comparison of the results obtained with the two methods demonstrates their good agreement. © *2000 MAIK "Nauka/Interperiodica"*.

In the last few decades, much attention was given to the acoustics of deep scattering layers (DSL). These layers are of biological nature and intensively scatter acoustic waves in the frequency range from several units to several tens kilohertz. The peak of scientific publications on these problems falls on 1960–1970th. Now, the number of papers dealing with these topics is considerably reduced; however, the interest to the problem remains intact (see, e.g., [1, 2]). Almost all publications on the acoustics of DSL give only fragmentary geographic data providing no general pattern over the whole body of the ocean. Even the excellent paper by Chapman *et al.* [3] presenting the results of measurements over all oceans of the Earth (excluding the Arctic Ocean) gives only sampled data corresponding to several sections.

We studied the sound scattering by ocean inhomogeneities of biological nature for years, and now we set ourselves the task to quantitatively describe the fundamental acoustic characteristics of DSL—the column strength and depths—and to represent these data on the maps over the entire World Ocean for relatively wide ranges of frequencies. To accomplish this task, we collected the maximum body of experimental data on the acoustics of DSL. In addition to published materials, we were able to use archive records from scientific reports of several Russian institutions that carried out full-scale measurements of the DSL characteristics. Among these records, there are the results of our investigations that form nearly half of the collected materials. As a result, we obtained a sufficiently large body of experimental data, which, after some additional processing, can be considered as an integral data bank.

We created a computer database that contains the DSL characteristics together with the corresponding references, geographic coordinates, years, months, and hours, as well as depths of the source/receiver and some information on the measurement techniques. In the database, the fundamental DSL characteristics are the column strength M and the depths of the upper and lower boundaries of every selected layer. The column strength is defined as an integral of the volume backscattering coefficient over the depth. The integration interval either coincides with the interval of depths between the upper and lower boundaries of every layer, or covers all depths where the DSL occur. In the latter case, the obtained quantity is called the total column strength for a given point of the ocean. The column strength M is a dimensionless quantity and is usually measured in decibels relative to unity. The experimental values given in most sources are obtained as a result of averaging over several successive measurements carried out in the same conditions. Our estimates show that their scatter is characterized by a variance of about 1.0–1.5 dB.

The results collected in the database correspond mainly to six frequencies: 3, 5, 7, 10, 15, and 20 kHz. For lower frequencies, the level of scattering from DSL is low (especially, during daylight hours), and the scattered signal does not exceed the noise level. For higher frequencies, the propagation of sounding and scattered

1063-7710/00/4601-0015$20.00 © 2000 MAIK "Nauka/Interperiodica"

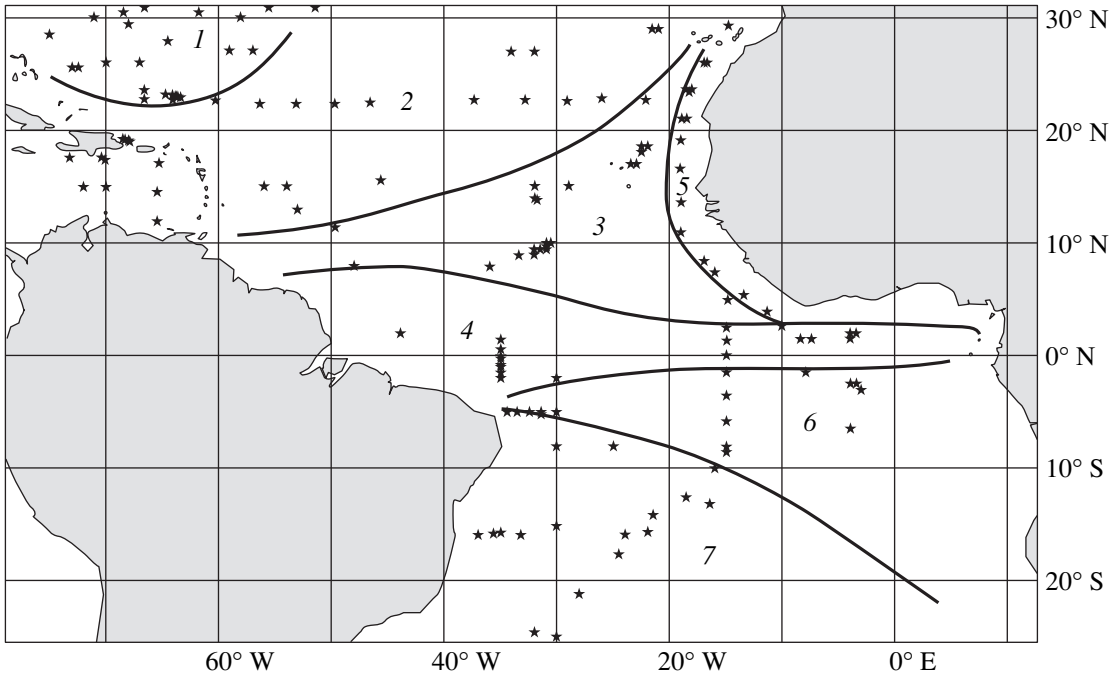

Fig. 1. Map of the hydrological regions of the Central Atlantic and the sites of measurements of the acoustic characteristics of DSL.

signals through absorbing sea water result in large losses, and a possible error in the determination of the absorption coefficient may result in a significant error in the column strength evaluated from the experimental data.

This paper considers the Central Atlantic, for which the database already contains a sufficient body of data on the total DSL strength. All data considered in this paper correspond to daylight hours during which DSL lie at large depths.

We divided the Central Atlantic into seven regions nearly homogeneous in their hydrological characteristics (Fig. 1). Below, we briefly describe these regions.

Region 1 corresponds mainly to the Sargasso Sea; it is characterized by a thick and warm surface layer with uniform temperature and a low biological productivity. **Regions 2 and 7** are hydrologically similar; they form a transition region to mid latitudes and are relatively stable both in dynamics of currents and in water mass structures. They are characterized by a well-developed warm surface layer, a large depth of the discontinuity layer, and a low biological productivity of the upper waters. **Regions 3 and 6** are located in the eastern parts of northern and southern tropics, respectively; they are also similar in their properties. They are characterized by complex hydrodynamic conditions resulting in multiple local frontal zones that are unstable in time and space. **Region 4** extends along the equator; in this region, the Northern and Southern Trade-Wind Currents interact, as well as the Equatorial Current and the countercurrent. This interaction forms a temperature-homogeneous surface layer and forces the discontinuity layer to go downwards. The region is biologically productive, because the Equatorial Current carries a large body of organic matter ascending from ocean depths near the coast of Africa. **Region 5** is the zone where intermediate waters ascend near the coast of Africa, which causes its high biological productivity. The boundaries shown for these regions in Fig. 1 are not strictly fixed and may vary by several degrees depending on many natural factors. In Fig. 1, the asterisks show the points where acoustical measurements used in this paper were carried out.

The averaged distribution of the total column strength M in some considered area of ocean allows at least two representations: (1) in the form of a set of isolines of the quantity M over the area and (2) in the form of confidence intervals for actual average values and variances obtained for this quantity in different parts of the area under consideration. The confidence intervals are evaluated assuming that the DSL characteristics are statistically homogeneous for every region with homogeneous hydrology. Both representations are to be evaluated for each frequency separately. It should be noted that although acoustical measurements in the ocean are numerous, they cover the ocean in a very nonuniform manner; as a result, the estimates of the DSL intensity given below cannot be considered as quite reliable estimates. However, this approach seems to be one of the few approaches that can result in approximate, but nevertheless statistically substantiated quantitative estimates of the distribution of the acoustical properties of DSL over the ocean area.

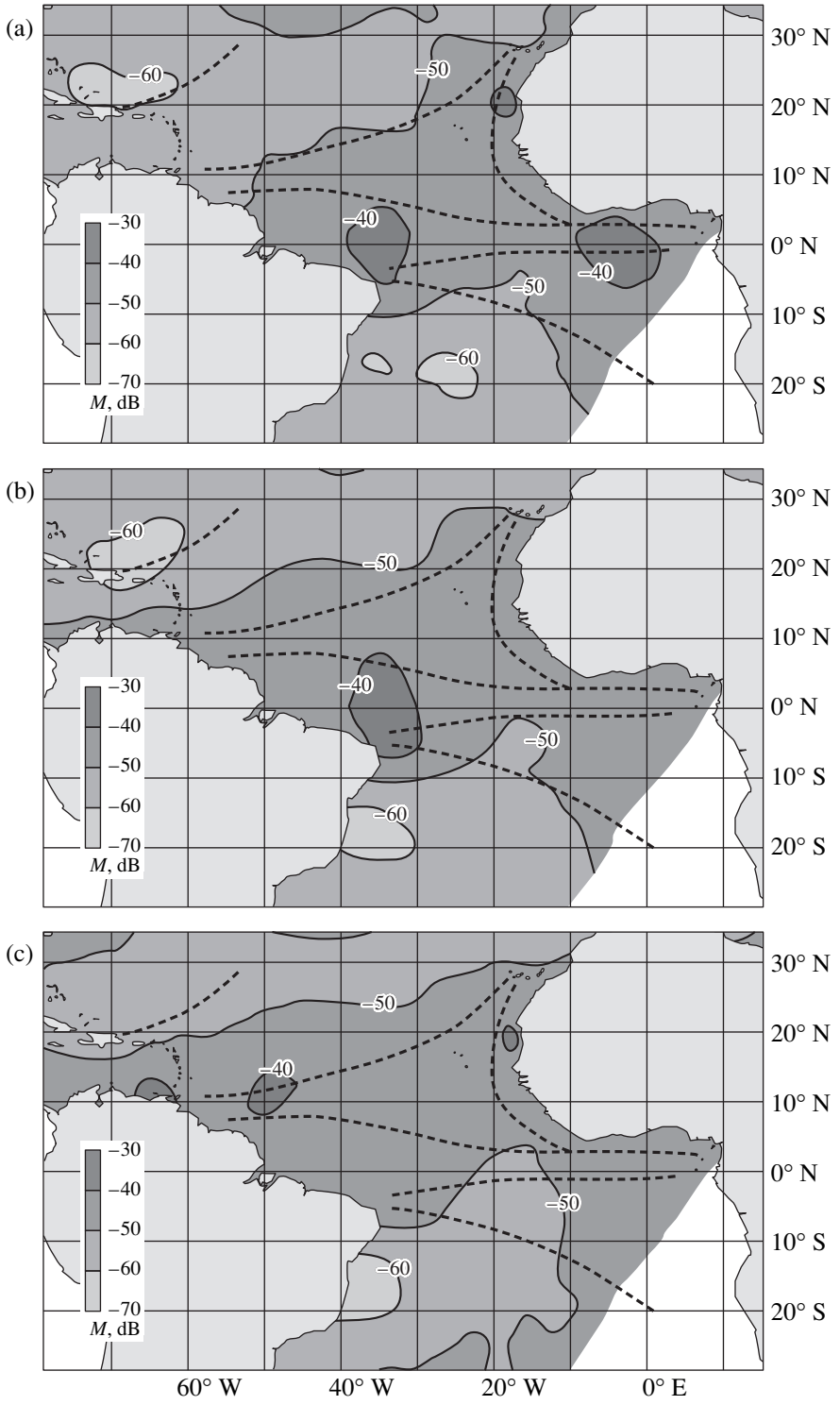

Fig. 2. Maps of isolines of the total column strength for the frequencies (a) 5, (b) 10, and (c) 20 kHz.

Figure 2 shows the total column strength measured for the frequencies 5, 10, and 20 kHz in the form of isolines drawn with the step 10 dB. They were obtained by using the triangular method and linear interpolation between the points. The dashed lines show the boundaries of the regions with homogeneous hydrology (the regions shown in Fig. 1). For each frequency, the isolines are characterized by their own configuration; however, all patterns of the DSL intensity distribution are similar in their general features.

Here, we note some specific features of the column strength distribution shown in Fig. 2. The white spot at

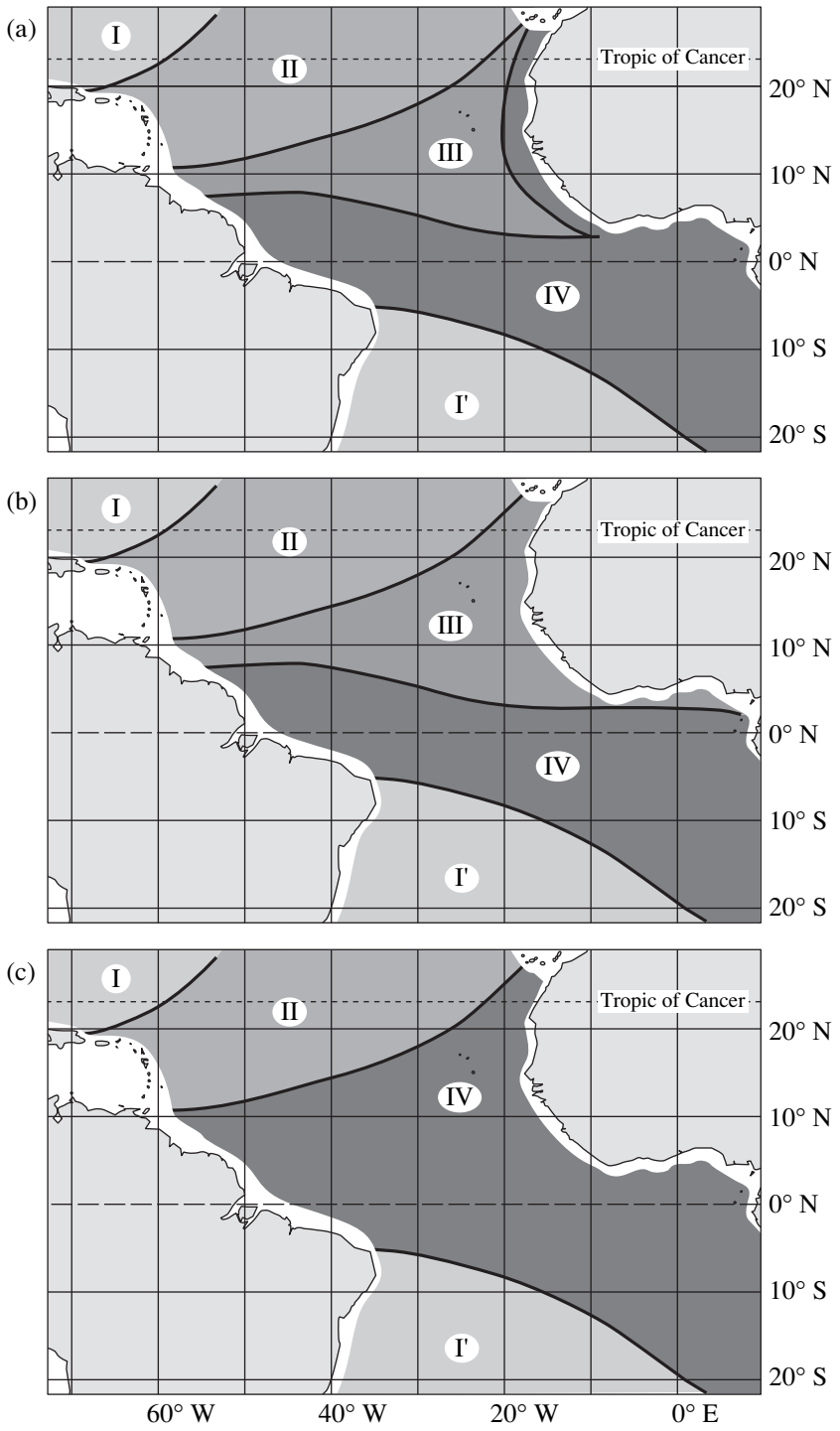

Fig. 3. Central Atlantic regions statistically homogeneous in the total column strength for the frequencies (a) 5, (b) 10, and (c) 20 kHz. The shading intensity qualitatively corresponds to the DSL intensity. The quantitative data are resented in the table.

the southeast correspond to the region for which only scarce data exist in the database. On the map, one can clearly see a zone near the equator, which is relatively rich in scattering layers (especially, for lower frequencies), and relatively poor zones corresponding to the Sargasso Sea in the Northern hemisphere and to the cyclonic circular motion in the Southern hemisphere. In general, the isoline pattern corresponds to the boundaries of the regions with homogeneous hydrology, which is evidence in favor of the hypothesis that hydrological, acoustical, and biological characteristics of the ocean are closely related. The local differences observed for differ-

Evaluated acoustical characteristics of DSL in homogeneous regions of the Central Atlantic

f, kHz	5				10				20			
Point estimates												
Region	$\hat{M}$, dB	$\hat{\sigma}^2$	$\hat{V}$, %	n	$\hat{M}$, dB	$\hat{\sigma}^2$	$\hat{V}$, %	n	$\hat{M}$, dB	$\hat{\sigma}^2$	$\hat{V}$, %	n
I	–60	46	12	38	–60	30	9	34	–56	23	9	15
I'									–58	77	15	16
II	–52	40	12	12	–48	16	8	10	–48	62	17	13
III	–46	16	9	17	–44	24	11	32				
IV	–40	58	19	49	–41	56	18	37	–44	48	16	63
Interval estimates												
Region	$\overline{M}$, dB	$\overline{\sigma^2}$	$\overline{V}$, %		$\overline{M}$, dB	$\overline{\sigma^2}$	$\overline{V}$, %		$\overline{M}$, dB	$\overline{\sigma^2}$	$\overline{V}$, %	
I	–61…–57	28…77	9…15		–62…–58	20…52	7…13		–58…–53	12…57	6…14	
I'									–63…–54	41…201	10…26	
II	–56…–48	20…114	8…22		–51…–45	9…81	6…18		–50…–45	38…162	11…28	
III	–48…–44	9…37	6…14		–46…–43	15…42	8…15					
IV	–42…–38	40…90	15…25		–44…–38	28…98	12…26		–45…–42	36…74	14…21	

ent frequencies—in particular, the positions of the "spots" with $M > -40$ dB and $M < -60$ dB—are presumably caused by the differences in the fauna composition of the DSL [4].

The spatial pattern shown in Fig. 2 is very descriptive; however, it gives no way of estimating the probability confidence of measured column strengths. Such estimates can be obtained using the second approach to the problem. Suppose that the values of the total column strength obtained within every selected region (samples in the database) belong to a single general set. In simultaneous processing of these results, we will assume that errors of all measurements coincide and all measurements have equal statistical weight. Additionally, we checked the hypothesis that the total column strength M is distributed according to the Gaussian law in all regions under consideration. This was done for every frequency using the W-criterion, which is optimum for small samples [5]. For the majority of cases, it was found that there is no reason to reject this hypothesis.

At the first step of the simultaneous processing of data relating to every region and every frequency, we calculated sampling arithmetic means of the column strength (in dB) and the variances of the differences between particular measurements and this mean. In every considered sample, abnormal values (outliers) of M were rejected using a standard procedure of the statistical processing of experimental data. Then, for every pair of regions, we checked the hypothesis that their sampling means and variances of the column strength coincide. If they coincided with a confidence level of 5%, we decided that these samples belong to a single general population; the data corresponding to these regions were combined, and the processing was repeated. For the regions of the Sargasso Sea (region 1) and the southern cyclonic circular motion (region 7), at frequency 20 kHz, the sampling means coincided; but the corresponding variances differed widely. For this reason, regions 1 and 7 could not be combined. Below, we will use the term "acoustically homogeneous regions" for the regions with equal mean values and variances of M at a given frequency.

At every frequency, we selected four acoustically homogeneous regions. The boundaries of these regions (numbers of combined hydrologically homogeneous regions) generally depend on frequency. As an example, Fig. 3 shows the maps with these regions for frequencies 5, 10, and 20 kHz. The table lists the quantitative estimates relating to the column strength for the regions shown in Fig. 3. The upper part of the table presents the estimates of the mean values of $\hat{M}$, the variances $\hat{\sigma}^2$, and the variation coefficients $\hat{\nu}$ obtained for every sample of length n. The lower part of the table presents the approximate 95% confidence intervals of true mean values of the column strength $\overline{M}$, the variances $\overline{\sigma^2}$, and the corresponding intervals for the variation coefficient $\bar{\nu}$.

For all frequencies, the lowest column strengths occur in regions I and I' (the Sargasso Sea and the southern cyclonic circular motion, respectively). The most intense scattering occurs in the zone of coastal

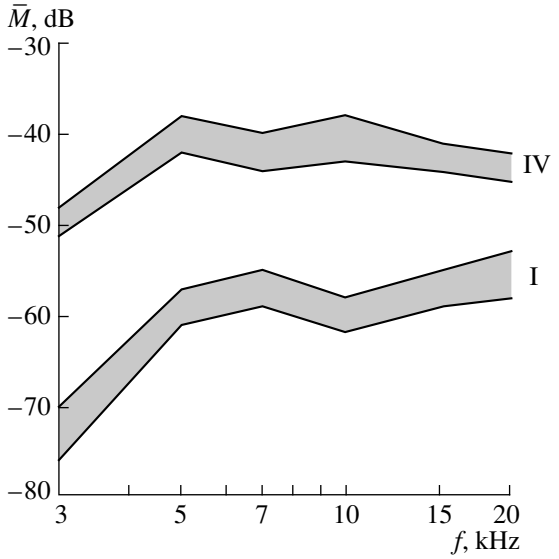

Fig. 4. Interval estimates of the frequency characteristics of the column strength in homogeneous regions I and IV.

upwelling and in the equatorial region (regions III and IV). In region II (northern mid latitudes), the scattering level is intermediate for all frequencies under consideration. This spatial distribution of the DSL intensity is in qualitative agreement with the isoline maps shown in Fig. 2, the hydrological features described above for the corresponding water areas, and does not contradict the map of pelagic regions of the Atlantic Ocean [6].

In Fig. 4, the shaded zones corresponding to 95% confidence intervals represent the frequency characteristics of the column strength $\overline{M}$ for two acoustically homogeneous regions (I and IV) radically different in the total DSL intensity. In plotting these graphs, we used the data on the confidence intervals of $\overline{M}$ for all frequencies used in our processing, including the data for the frequencies 3, 7, and 15 kHz that were not presented in the table. In both cases, the minimum column strength corresponds to the frequency 3 kHz, and the minimum value is below –70 dB for region I. In region IV, this minimum value is higher and approaches –50 dB. The maximum column strength also corresponds to region IV; it occurs at the frequencies 5 and 10 kHz and approaches the level –40 dB. With further increase in frequency, the column strength varies only slightly. In region I, poor in scatterers, this maximum decreases to –55 dB, and in region IV, rich in scatterers, it increases to almost –45 dB. The specific feature of most curves $M(f)$ measured during daylight hours is a radical increase in the column strength observed as the frequency increases from 3 to 5 kHz; this increase is clearly seen in Fig. 4. For other regions shown in Fig. 3, i.e., for the regions with moderate column strengths, the frequency characteristics $M(f)$ lie between the shaded zones shown in Fig. 4.

We hope to continue the studies of the variability of the properties of deep scattering layers in the ocean in two directions: first, we will extend our database to the entire ocean, and, second, we will take fuller advantage of the experimental data contained in the database at the moment. As a result, we will be able to give the most reliable statistical description not only for the scattering intensity of DSL, but also for the DSL depths and their diurnal migration in different regions of the ocean.

ACKNOWLEDGMENTS

This work was supported by the Russian Foundation for Basic Research, project no. 98-05-64849.

REFERENCES

1. P. H. Wiebe, IEEE J. Ocean Eng. **22**, 445 (1997).
2. D. R. McKelvey, J. Acoust. Soc. Am. **103**, 3069 (1998).
3. R. P. Chapman, O. Z. Bluy, R. H. Adlington, *et al.*, J. Acoust. Soc. Am. **56**, 1722 (1974).
4. I. B. Andreeva, Akust. Zh. **45**, 437 (1999) [Acoust. Phys. **45**, 385 (1999)].
5. G. Hahn and S. Shapiro, *Statistical Models in Engineering* (Wiley, New York, 1967; Mir, Moscow, 1969).
6. R. H. Backus and J. E. Craddock, in *Oceanic Sound Scattering Prediction*, Ed. by N. R. Anderson and B. I. Zahuranec (Plenum, New York, 1977), pp. 529–547.

Translated by A.G. Vinogradov

Acoustical Physics, Vol. 46, No. 1, 2000, pp. 21–26. Translated from Akusticheskiĭ Zhurnal, Vol. 46, No. 1, 2000, pp. 28–34.

Measurement of the Correlation Properties of Thermal Acoustic Radiation

A. A. Anosov[1, 2], M. A. Antonov[1], and V. I. Pasechnik[1]

[1] *ELDIS Research Center, Institute of Radio Engineering and Electronics, Russian Academy of Sciences, Starosadskiĭ per. 8, Moscow, 101000 Russia*
e-mail: passechn@bfhome.msk.ru

[2] *Sechenov Medical Academy, Moscow, Russia*

Received December 14, 1998

Abstract—The space correlation function of sound pressures produced by a source of thermal acoustic radiation in the megahertz frequency range is measured by a system of two plane piezoelectric transducers. The source of radiation is an acoustic blackbody radiator represented by a heated strip of material with a large absorption coefficient. The strip is moved along the coordinate x perpendicular to the acoustic axis of the system. The correlated signal periodically varies in the course of the strip motion, and its magnitude is proportional to the difference between the temperatures of the source and the surrounding medium. The space correlation function $R(x)$ is calculated, and the results of the calculation agree well with the experimental data. The problem of the development of a device for correlated signal measurements in passive thermoacoustic tomography is discussed. © *2000 MAIK "Nauka/Interperiodica".*

The information carried by thermal acoustic radiation can be used for measuring the temperature within biological objects [1]. The corresponding technique, namely, the acoustic thermography based on the measurements of the intensity of this radiation by single piezoelectric transducers, provides an opportunity to measure in-depth temperatures with the precision of 0.1 K [1, 2]. At the same time, it was suggested to use a correlation reception of thermal radiation by several piezoelectric transducers operating simultaneously. Such measurements were expected to increase the sensitivity and the resolution of the method [3, 4]. It was demonstrated that such a technique provided an opportunity to determine not only the distribution of the in-depth temperature of objects but also the distribution of the absorption coefficient in them. In its turn, this offers a possibility to develop a passive thermoacoustic tomograph that requires no *a priori* information on the absorption coefficient [5]. The major difficulty is the selection of the corresponding geometry of a pair of detecting transducers and the determination of their characteristic parameters. The first approaches were proposed by Barabanenkov and Pasechnik [6].

At the same time, it is necessary to note that the situation realized in the studies of the correlation properties of thermal acoustic radiation from heated objects is normally absent in the measurements of thermal electromagnetic radiation. In the case of thermal acoustic radiation, the temperature of the source only slightly exceeds the background temperature, while in the second case the difference is essential. Therefore, a special study of this problem is necessary.

We note that experimental correlation measurements of thermal acoustic radiation have not been performed up to now, and theoretical formulas for the simplest experimental situations have not been obtained. This paper is devoted to the experimental determination of the spatial correlation function of the sound pressures produced at two piezoelectric transducers by a source of thermal acoustic radiation, and to the comparison of the experimental results with the theoretical estimates.

The measurements were performed in a basin (*1*) (Fig. 1) with the dimensions $40 \times 28 \times 30$ cm^3. The source of acoustic radiation was a narrow strip (*2*) of width $\Delta = 2$ mm made of a material strongly absorbing ultrasound (plasticine). The strip was heated up to the temperature T by placing it in a dish (*3*) with acoustically transparent windows. The dish was filled with water and equipped with a heater (*4*). Two plane circular piezoelectric transducers (PT_1 and PT_2) were used as the receivers. The radius of the transducers was $a = 5$ mm, and the distance between their centers was $D = 16$ mm. Their temperatures coincided with the temperature T_0 of the basin. The acoustic axes of the piezoelectric transducers were lying in the xz plane and intersected at a distance of ~140 mm from the straight line connecting the centers of both transducers (Fig. 1). Thus, the angle between the acoustic axes was about 6.5°. The strip was positioned in the plane L along the y axis

1063-7710/00/4601-0021$20.00 © 2000 MAIK "Nauka/Interperiodica"

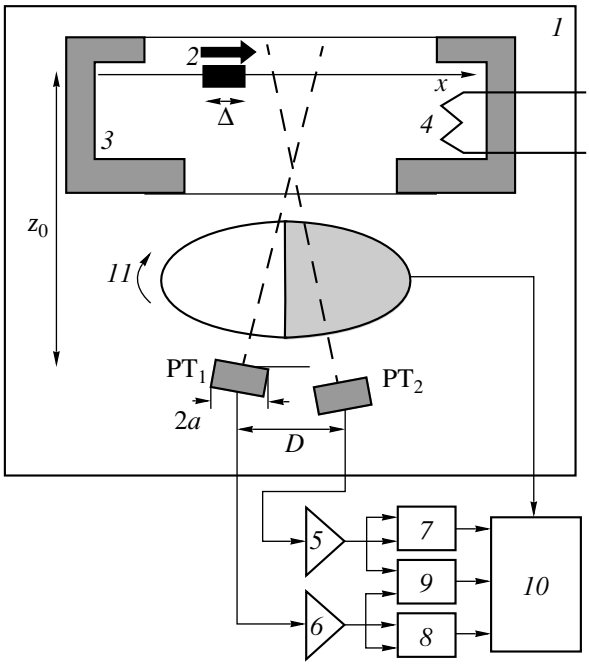

Fig. 1. Schematic diagram of the experiment: (*1*) a basin; (*2*) a plasticine strip of width Δ; (*3*) a dish; (*4*) a heater; (*5*), (*6*) high-frequency amplifiers; (*7*), (*8*), (*9*) multipliers; (*10*) a computer; and (*11*) a chopper. PT_1 and PT_2 are the radiation receivers represented by piezoelectric transducers of radius a with the distance between their centers D; the distance to the source is z_0.

inside the dish at the distance z_0 = 200 mm from the piezoelectric transducers. The strip was moved horizontally (along the x axis) with the step 2 mm, perpendicularly to the acoustic axis of the system (the z axis), i.e., the straight line passing through the point of intersection of the acoustic axes of the piezoelectric transducers and the middle of the line segment connecting the two piezotransducers. The origin of coordinates was located at the point of intersection of the acoustic axis of the system and the plane L. Using a pulsed ultrasonic source, we found that the point lying on the x axis in the plane L at x = 8 mm is equidistant from both piezoelectric transducers.

The piezoelectric transducers were equipped with two quarter-wave layers, loaded to matching transformers, and tuned to the frequency 2.2 MHz (the bandwidth of the amplifiers (*5*) and (*6*) was 200 kHz). The piezoelectric transducers had approximately equal sensitivities. The sound pressures at PT_1 and PT_2—p_1 and p_2, respectively—were transformed into electric signals, which were amplified and fed to the inputs of three multipliers (MLT04 Analog Devices). Two multipliers, (*7*) and (*8*), were used for the determination of the mean squares of pressures measured by each of the piezoelectric transducers—$\langle p_1^2 \rangle$ and $\langle p_2^2 \rangle$, respectively. The third multiplier (*9*) was used to determine the mean value of the product of pressures measured by different piezoelectric transducers, namely, $\langle p_1 p_2 \rangle$. The resulting signals were stored in an IBM-386 personal computer (*10*) via amplifiers with the bandwidth 1–15 Hz (the time of recording 40 s) and an L-154 interface card (L-card SoftWare Lab Limited, Russia). A modulation reception was used to avoid the signal drift: the radiation of the heated plate was periodically interrupted by a chopper (*11*) with the frequency 4 Hz. Thus, the signals from the strip heated with respect to the basin to the temperature ΔT and from the whole basin were recorded ($\Delta T = T - T_0$ = 9.5 K, where T and T_0 are the temperatures of the source and the surrounding medium). A signal reflecting the chopper position was also stored in the computer and used as a reference signal. The process of synchronous detection was performed with the help of the computer. The difference (increment) of the mean intensity values of the correlated signal from the strip and the signal from the whole basin, as well as the increments of the signals from the strip and the whole basin detected by PT_1 and PT_2, were determined. The measurements were repeated four times for each position of the plate.

In order to calibrate the setup in Kelvin degrees, a "blackbody" was placed into the dish. The blackbody was sufficiently large to overlap the apertures of both piezoelectric transducers. The measured signal magnitudes expressed in Kelvin degrees were the increments of the acoustic brightness temperature; e.g., for PT_1, the corresponding increment is $\Delta T_b = T_b - T_0$. The acoustic brightness temperature T_b is the temperature of the blackbody that produces the same radiation flux as the object under investigation [2]. In the case of a blackbody filling the whole aperture of the piezoelectric transducers, we have $\Delta T_b = \Delta T = T - T_0$. In the case of a narrow strip, the acoustic brightness temperature is proportional to its width.

A common modulated high-frequency signal was fed to the input amplifiers instead of the signals from the two piezoelectric transducers in order to calibrate the channel measuring the correlated signal. We also took into account the fact that the mechanical chopper blocked the apertures of both piezoelectric transducers not simultaneously but with a certain shift, which caused a reduction of the correlated signal by 10%. For the sake of uniformity, the correlated signal expressed in Kelvun degrees will be called the increment of the correlated acoustic brightness temperature, ΔT_{bC}.

Figure 2 presents the measurement-averaged dependences of the increment of the correlated acoustic brightness temperature $\Delta T_{bC}(x)$ on the x coordinate (curve *1*) and the dependences of the increments of the acoustic brightness temperature measured by PT_1 and PT_2, $\Delta T_{b1}(x)$ and $\Delta T_{b2}(x)$ (curves *2* and *3*, respectively). One can see that, within the limits of the directivity pattern, the correlated signal varies periodically with the spatial period Λ about 8.5 mm. The signal $\Delta T_{bC}(x)$ is

less in magnitude than the average values of $\Delta T_{b1}(x)$ and $\Delta T_{b2}(x)$.

Let us consider the following model in order to calculate the parameters of the correlated signal and correlation function

$$R(x) = \Delta T_{bC}(x)/\sqrt{\Delta T_{b1}(x)\Delta T_{b2}(x)}. \qquad (1)$$

The source of thermal radiation is a heated long strip 1 lying in the plane L and oriented along the y axis (Fig. 3). The plane L lies at the distance z_0 from the piezoelectric transducers. A strip of the width Δ can move along the x axis. The transducers PT_1 and PT_2 are positioned symmetrically with respect to the acoustic axis of the system, at the distance $\pm D/2$ from it, and rotated relative to each other in such way that the acoustic axis of PT_1 intersects the x axis at the point x_{01}, while the acoustic axis of PT_2 intersects the x axis at the point x_{02}. In the process of measurement in the far wave field, we use the Fraunhofer approximation for a circular piezoelectric transducer [7]. The complex amplitudes of the velocity potentials ϕ_1 and ϕ_2 measured by each piezoelectric transducer are connected with the velocity potential u_0 of a point source located at the distances r_1 and r_2 from the centers of the corresponding piezoelectric transducers:

$$\phi_{1,2} = -\frac{a^2}{r_{1,2}}\frac{J_1(ka\sin\theta_{1,2})}{ka\sin\theta_{1,2}}e^{-jkr_{1,2}}u_0, \qquad (2)$$

where $k = 2\pi/\lambda$ is the wave number, $\lambda = c/f$ is the wavelength, f is the frequency, c is the sound velocity, θ_1 and θ_2 are the angles between the directions from the centers of the piezoelectric transducers PT_1 and PT_2, respectively, to the radiation source and their acoustic axes, and J_1 is the Bessel function of the first order.

In the case of a source in the form of a strip oriented along the y axis and with the center at the point x and width Δ, the complex amplitudes of the velocity potentials at both piezoelectric transducers can be obtained by integrating expressions of the type of formula (2) with respect to the x and y axes. For example, we have for the first of them

$$\phi_1(x) = -a^2\int_{-\infty}^{\infty}dy\int_{x-\Delta/2}^{x+\Delta/2}u_0(\xi, y) \times\left(\frac{1}{r_1}\frac{J_1(ka\sin\theta_1)}{ka\sin\theta_1}e^{-jkr_1}\right)d\xi. \qquad (3)$$

Infinite limits of integration with respect to the variable y are determined taking into account the fact that the plate length along this axis exceeds the transverse dimensions of the characteristic functions of piezoelectric transducers.

We assume that thermal noise is delta-correlated, the thermodynamic temperature of the plate T does not depend on the x and y coordinates, and $r_1 \approx z_0$ in the denominator of the integrand in expression (3). Taking into account the fact that the signal reception is performed by a device with a certain frequency response $S(f)$, we obtain that the quantity $\Delta T_{b1}(x)$ corresponding

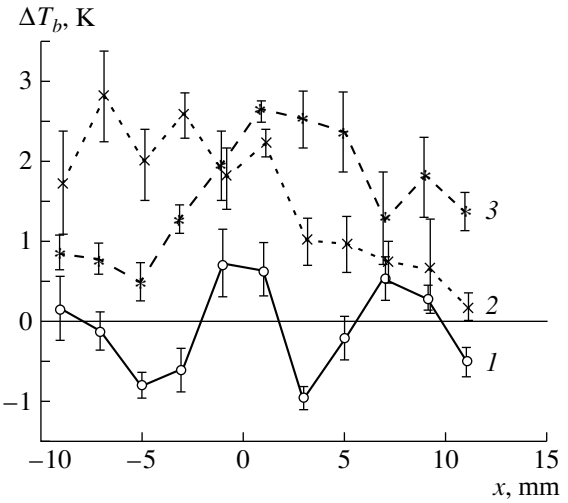

Fig. 2. Increment of the correlated acoustic brightness temperature $T_{bC}(x)$ (curve *1*) and increments of the acoustic brightness temperature measured by PT_1, $T_{b1}(x)$ (curve *2*), and PT_2, $T_{b2}(x)$ (curve *3*), versus the x coordinate; the curves are obtained by averaging over four measurements each.

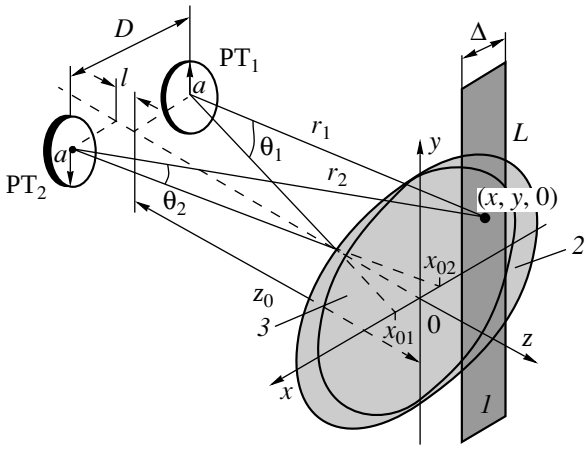

Fig. 3. A scheme for the calculation of the correlation function of thermal acoustic radiation received by two piezoelectric transducers, PT_1 and PT_2, with the radius a and the distance between their centers D. The radiator (*1*) is a strip of width Δ lying in the xy plane; z_0 is the distance from the xy plane to the transducers; r_1 and r_2 are the distances to the point source from the centers of the piezoelectric transducers; θ_1 and θ_2 are the corresponding angles between the axes of the transducers and the rays r_1 and r_2; l is the distance of the displacement of PT_2 along its acoustic axis; x_{01} and x_{02} are the coordinates of intersection of the x axis with the acoustic axes of PT_1 and PT_2; and (*2*, *3*) the lightly shaded areas represent the sections of the planes of characteristic functions by the plane L.

to the signal measured by, e.g., PT_1, has the form

$$\Delta T_{b1}(x) = \Delta T\frac{1}{\pi z_0^2} \times\int_0^\infty S(f)\mathrm{d}f\int_{-\infty}^{\infty}\mathrm{d}y\int_{x-\Delta/2}^{x+\Delta/2}(ka)^2\left(\frac{J_1(ka\sin\theta_1)}{ka\sin\theta_1}\right)^2\mathrm{d}\xi. \quad (4)$$

It is convenient to approximate the frequency response of the receiver $S(f)$ normalized to unity by an expression with the maximum at the frequency f_0 and a transmission bandwidth at the level 3 dB, δf,

$$S(f) = (\delta f/2\pi)(1/((f-f_0)^2+(\delta f/2)^2)). \quad (5)$$

In this case, $\int_0^\infty S(f)\,\mathrm{d}f = 1$. For small angles θ, we replace $\sin\theta$ by its argument, and, in order to calculate integrals of the type of expression (4), we approximate the integrand function by the expression

$$\frac{J_1(ka\sin\theta_1)}{ka\sin\theta_1} = (1/2)e^{-(ka\theta_1)^2/8}. \quad (6)$$

In the Cartesian coordinates, the angle θ_1 is determined according to the formula $\theta_1 \approx \sqrt{(x-x_{01})^2+y^2}/z_0$, where x and y are the coordinates of a point in the plane L. From expression (4) after the integration over the y axis, it follows that the increment of the acoustic brightness temperature has the form

$$\Delta T_{b1}(x) = \frac{1}{2\sqrt{\pi}z_0}\Delta T \times\int_0^\infty S(f)\mathrm{d}f\int_{x-\Delta/2}^{x+\Delta/2}ka\exp(-(ka/2z_0)^2(\xi-x_{01})^2)\mathrm{d}\xi. \quad (7)$$

In the process of measurement, the increments of the acoustic brightness temperature are calibrated with respect to the radiation of the blackbody filling the whole aperture of the piezoelectric transducers. The radiation of a plate of very large width ($\Delta \longrightarrow \infty$) corresponds to this case in expression (7), and, as it follows from this expression, the increment ΔT_{b1} of the acoustic brightness temperature is equal to the increment ΔT of the thermodynamic temperature.

Since the relative transmission bandwidth is small, i.e., $\delta f/f_0 \ll 1$, we can change the wave number k for its average value k_0. Moreover, if the strip width Δ is far less than the characteristic width of the characteristic function at the distance z_0, i.e., $\Delta \ll z_0/k_0a$, we may change the exponent for its value at the point x. Then, we obtain

$$\Delta T_{b1}(x) \approx \Delta T A_1^2(k_0, x), \quad (8)$$

where the quantity $A_1^2(k_0, x) \approx \frac{k_0a\Delta}{2\sqrt{\pi}z_0}\exp(-(k_0a/2z_0)^2(x-x_{01})^2)$ depending on the coordinate and the average value of the wave number is the square of the characteristic function of PT_1.

An analogous expression can be obtained for PT_2:

$$\Delta T_{b2}(x) \approx \Delta T A_2^2(k_0, x), \quad (8a)$$

where

$$A_2^2(k_0, x) \approx \frac{k_0a\Delta}{2\sqrt{\pi}z_0}\exp(-(k_0a/2z_0)^2(x-x_{02})^2)$$

is the square of the characteristic function of PT_2.

In calculating the correlated acoustic brightness temperature for the sound pressures measured by both piezoelectric transducers, it is necessary to take into account the dependence on a coordinate only in the phase factors in the expressions of the type of formula (3) for both piezoelectric transducers. We consider a more general case with one of the piezoelectric transducers (let it be PT_2 for definiteness) is shifted from the point of intersection of the acoustic axes along its own acoustic axis by the distance l (Fig. 3). This case provides an opportunity to take into account the additional propagation difference between the piezoelectric transducers. As a result, the total propagation difference for the point $(x, 0)$ will be $r_1 - r_2 = Dx/z_0 - l$. Taking the characteristic functions from under the integral, we obtain the following expression for the increment of the correlated acoustic brightness temperature:

$$\Delta T_{bC}(x) = \Delta T(A_1(k_0, x)\cdot A_2(k_0, x)) \times\int_0^\infty S(f)\mathrm{d}f\int_{x-\Delta/2}^{x+\Delta/2}\cos(k(D\xi/z_0 - l))\mathrm{d}\xi. \quad (9)$$

Calculating this double integral, we first integrate the fast-variable oscillating function with respect to frequency. After some transformations, we obtain the following formula from expression (9):

$$\Delta T_{bC}(x) = \Delta T A_{12}(k_0, x)\frac{\sin(k_0\Delta D/2z_0)}{k_0\Delta D/2z_0} \times e^{-k_0(\delta f/f_0)|Dx/z_0 - l|/2}\cos(k_0(Dx/z_0 - l)), \quad (10)$$

where $A_{12}(k_0, x) = A_1(k_0, x)A_2(k_0, x)$ is the characteristic function for the correlated signal.

It follows from expression (10) that the envelope of the correlated signal is determined by the product of the characteristic functions of both piezoelectric

transducers. The factor $\frac{\sin(k_0\Delta D/2z_0)}{k_0\Delta D/2z_0} \le 1$ takes into account the loss of correlation with increasing strip width. The exponential factor depending on the relative transmission bandwidth $\delta f/f_0$ takes into account the correlation loss due to the nonmonochromatic structure of the received signal. The quantity ΔT_{bC} depends on the x coordinate almost periodically with the spatial period $\Lambda = \lambda_0 z_0/D$.

As it follows from expressions (8), (8a), and (10), the correlation function $R(x)$ has the form

$$R(x) = \frac{\sin(k_0\Delta D/2z_0)}{k_0\Delta D/2z_0} \times e^{-k_0(\delta f/f_0)|Dx/z_0 - l|/2}\cos(k_0(Dx/z_0 - l)). \quad (11)$$

The amplitude of $R(x)$ is maximum at $x = lz_0/D$, this value being determined by the additional propagation difference between the piezoelectric transducers and the intersection point of their acoustic axes.

Figure 4 shows the calculated increment of the correlated acoustic brightness temperature (curve *1*) and the experimental curve (curve *2*) smoothed out using the cubic interpolation technique. Experimental errors are indicated at the experimental points. In the process of calculation, we used a characteristic function obtained by multiplying our experimental curves (curves *2* and *3* in Fig. 2) for both piezoelectric transducers (the curves were smoothed out by parabolas using the least-square method) and the exponential and periodic factors from expression (10). We selected the value of l in such way that the exponential factor had the maximum value at $x = 8$ mm to comply with the experimental data.

The correlation function $R(x)$ obtained by the division of two noisy signals is determined with a greater error than the value of ΔT_{bC}. Figure 5 presents the theoretical dependence $R(x)$ calculated according to formula (11) for the conditions of our experiment (curve *1*). The experimental points in Fig. 5 are obtained by formula (1) directly from the corresponding experimental data (Fig. 2). Curve *2* is obtained by formula (1) with $\Delta T_{b1}(x)$ and $\Delta T_{b2}(x)$ approximated by second-order polynomials and $\Delta T_{bC}(x)$ approximated using the cubic interpolation technique. A characteristic exponential drop at the distance $\Delta x = z_0\lambda_0/\pi(\delta f/f)D$ can be seen in the theoretical dependence. The calculated spatial period in Figs. 4 and 5 is $\Lambda = 8.5$ mm, which almost coincides with the period measured experimentally. The amplitudes of the correlated signal and the correlation function calculated theoretically coincide on the whole with those measured experimentally.

At the same time, a systematic excess of theoretical values over the experimental data is observed. Let us consider possible reasons for this discrepancy. The first of them can be experimental errors. They are especially large at the edges of the range of the values of x, since,

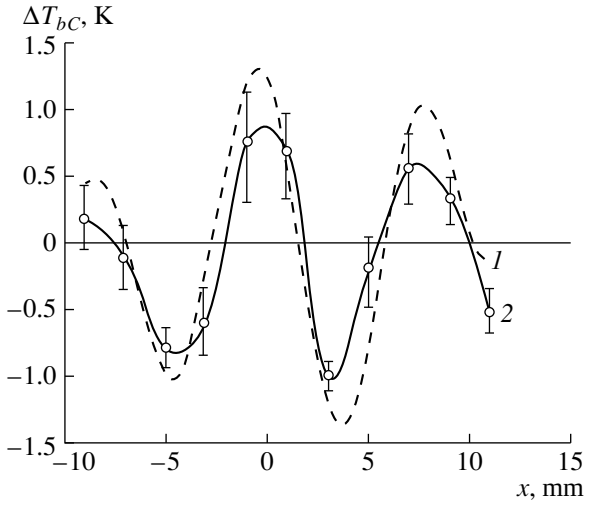

Fig. 4. Dependence of the calculated (curve *1*) and experimental (curve *2*) increments of the correlated acoustic brightness temperature $T_{bC}(x)$ on the x coordinate. The interpolated data of Fig. 2 are used as experimental data. The measurement errors are indicated at the experimental points. The calculation was performed with the following parameters: the width of the heated strip $\Delta = 2$ mm; the distance from the piezoelectric transducers to the strip $z_0 = 200$ mm; $f_0 = 2.2$ MHz; $\lambda_0 = 0.68$ mm; $a = 5$ mm; $D = 16$ mm; $\delta f = 0.2$ MHz; and $l = 0.64$ mm.

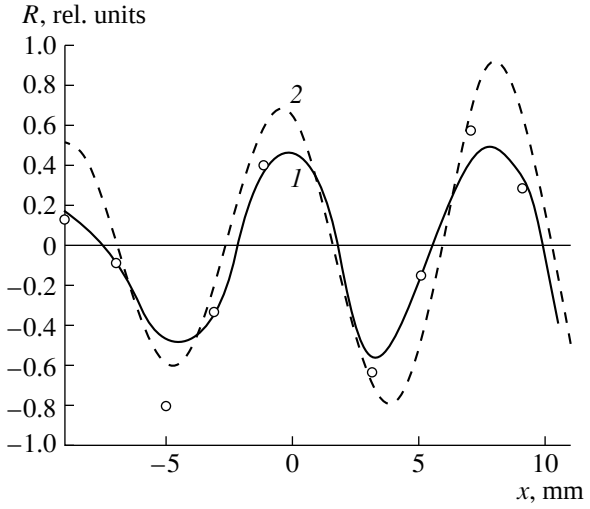

Fig. 5. Calculated (curve *1*) and experimental (curve *2*) values of the correlation function $R(x)$ versus the x coordinate. The points correspond to the calculation by the data given in Fig. 2. For the parameters used in the calculation, see Fig. 4.

in reality, the correlation function can be measured only within the limits of overlapping of the directivity patterns of both piezoelectric transducers, the width of each of them at the level e^{-1} at the distance z_0 being $2z_0\lambda_0/\pi a \approx 18$ mm. The second reason may originate from the specific features of the utilized experimental setup. We used not an isolated heated source, but a dish with heated water containing a body heated by this

water and having a large absorption coefficient; the body was represented by a thin plasticine strip oriented in the direction of both piezoelectric transducers and covered by a metal housing. In this case, thermal acoustic radiation exists inside the dish. The radiation is diffracted by the source. As it is well known from optics [9], the effective cross-section of the radiating strip increases due to this effect. This hypothesis is confirmed by the fact that the acoustic brightness temperatures measured by both piezoelectric transducers are slightly higher than the values calculated by formula (7). By virtue of the design of the utilized blackbody, additional diffraction contribution measured by both piezoelectric transducers apparently cannot be totally correlated. Therefore, the measured correlated signal and the correlation function are less in magnitude than the corresponding theoretical values.

One can see also from Fig. 5, that the correlation coefficient does not reach the values ±1. First, this is connected with the finite width of the strip: as it follows from expression (11), the maximum value of $R(x)$ decreases as the strip expands. And second, this is caused by the diffraction effects discussed above. Thus, the correlation properties of thermal acoustic radiation on the whole can be adequately described by the proposed theory.

Two important conclusions follow from the data obtained in our experiments. The correlated thermal acoustic radiation can be measured experimentally, and the experimental errors can be estimated rationally; this provides an opportunity to develop a passive thermoacoustic tomograph, which does not utilize any *a priori* information on the absorption properties of the medium [5]. At the same time as it follows from the described theory (expressions (10) and (11)), the utilized technique of measuring the thermal acoustic radiation with the help of two piezoelectric transducers positioned at some distance from each other provides an opportunity to separate the correlated part of radiation only from small sources with dimensions comparable to the wavelength. If the source is a relatively large, uniformly heated body with dimensions greater than the aperture of piezoelectric transducers, the total correlated signal obtained by averaging over the whole xy plane vanishes. Thus, under the given experimental geometry, the simple device used in our study cannot serve as a sensor for a passive thermoacoustic tomograph utilizing the correlation properties of radiation [5], and special investigation is needed to develop such a sensor.

We note that, as our experiment shows, the magnitude of the correlated signal, as well as the magnitudes of signals detected by single sensors, was determined by the difference $\Delta T = T - T_0$ of the source temperature T and the receiver temperature T_0. Apparently, this result is caused by the fact that the utilized sensor of the correlated signal, which consists of two separate piezoelectric transducers, gives a zero value in the case of a source with the width exceeding that of the characteristic function. Therefore, the signal source we used can be considered as a source consisting of two parts: a plane with the temperature T_0 and a narrow strip with the temperature $\Delta T = T - T_0$, only the second source producing detectable correlated radiation. This conclusion agrees well with the results obtained for the reception of an uncorrelated signal [8].

In closing, we note that the possibility of using passive measurements of the absorption coefficient in objects seems to be especially promising for biomedical applications, since the methods currently used for these purposes are active ultrasonic ones [10–12].

ACKNOWLEDGMENTS

We are grateful to Yu. N. Barabanenkov, K. M. Bograchev, A. V. Erofeev, and S. A. Ivanov for their assistance.

This study was supported by the Russian Foundation for Basic Research, project no. 98-01-00100.

REFERENCES

1. Yu. V. Gulyaev, E. E. Godik, V. I. Mirgorodskiĭ, *et al.*, in *Acoustic Sensing and Probing. Forth Course of the International School on Physical Acoustics* (World Scientific, Singapore, 1991), pp. 77–95.
2. V. I. Passechnik, Ultrasonics **32**, 293 (1994).
3. R. A. Hessemer, Jr., L. J. Perper, and T. Bowen, U.S. Patent No. 4,416,552 (22 November 1983).
4. V. A. Burov and E. E. Kasatkina, Akust. Zh. **43**, 162 (1997) [Acoust. Phys. **43**, 135 (1997)].
5. V. I. Pasechnik, Akust. Zh. **43**, 563 (1997) [Acoust. Phys. **43**, 485 (1997)].
6. Yu. N. Barabanenkov and V. I. Pasechnik, in *Proceedings of the VI Session of the Russian Acoustical Society: Acoustics at the Threshold of the 21st Century, Moscow, Russia, 1997*, pp. 466–469.
7. S. Kino, *Acoustic Waves, Devices, Imaging and Analog Signal Processing* (Prentice Hall, New York, 1987; Mir, Moscow, 1990).
8. V. I. Pasechnik, Akust. Zh. **39**, 140 (1993) [Acoust. Phys. **39**, 70 (1993)].
9. L. D. Landau and E. M. Lifshits, *Field Theory* (Nauka, Moscow, 1988).
10. N. de Jong and F. J. Ten Cate, Ultrasonics **34**, 587 (1996).
11. J. Brian Fowlkes, J. Acoust. Soc. Am. **101**, Part 2, 3120 (1997).
12. G. A. Gordon, J. Acoust. Soc. Am. **101**, Part 2, 3168 (1997).

Translated by M. L. Lyamshev

Acoustical Physics, Vol. 46, No. 1, 2000, pp. 27–32. Translated from Akusticheskiĭ Zhurnal, Vol. 46, No. 1, 2000, pp. 35–41.

Interference Acoustooptic Technique for Sound Velocity Measurements

S. V. Bogdanov*, I. I. Zubrinov*, E. V. Pestryakov, and V. K. Sapozhnikov***

** Institute of Physics of Semiconductors, Siberian Division, Russian Academy of Sciences, pr. Akademika Lavrent'eva 13, Novosibirsk, 630090 Russia*

e-mail: bogd@isp.nsc.ru

*** Institute of Laser Physics, Siberian Division, Russian Academy of Sciences, pr. Akademika Lavrent'eva 13/3, Novosibirsk, 630090 Russia*

Received August 17, 1998

Abstract—A pulsed interference acoustooptic technique for measuring the phase velocity of sound in solids is described. The technique is an outgrowth of the known long-pulse interference technique. The interference acoustooptic technique retains all advantages of the initial method, and, due to the usage of acoustooptics, it is more precise and provides an opportunity to conduct the measurements of velocities of both longitudinal and transverse waves, in both isotropic and crystalline materials. *© 2000 MAIK "Nauka/Interperiodica".*

INTRODUCTION

The sound velocity is one of the most important characteristics of a material. It is necessary to know it for both the interpretation of physical effects and the calculation of parameters of various systems and devices. The phase velocity of sound in a crystal is the initial quantity for the determination of its elastic [1] and piezoelectric [2, 3] constants. The severe requirements imposed upon the precision of their determination make it necessary to determine the absolute value of sound velocity with a high precision. For example, it is necessary to measure the sound velocity with a relative precision no less than 10^{-4}, which corresponds to the precision of several meters per second, in order to determine the piezoelectric constants of weak piezoelectric materials, which have the electromechanical coupling coefficient $K^2 \le 0.01$, with the precision 10%.

There are many various techniques for measuring the phase velocity of sound. In the majority of cases, they are grounded on either the measurement of the propagation time of an ultrasonic signal over a sample of known dimensions or the determination of the sound wavelength at a known frequency. In the first group of methods, it is necessary to measure the time intervals with high accuracy, while in the second group, precision measurements of frequency are needed. Modern devices for measuring time and frequency provide sufficiently high precision, and they do not restrict the precision of the techniques. (However, it is preferable to use frequency meters.) At the same time, both groups of methods require precise measurements of the sample length, which is rather difficult to perform in practice. It is just the inaccuracy in the determination of the sample length that is the main source of errors. Possibly, the only methods, which do not require the measurements of the sample length, are the acoustooptic methods using light diffraction by ultrasound [4, 5]. Unfortunately, they are suitable only for optically transparent media. These techniques need high-precision measurements of the diffraction angle, which is usually quite small ($\varphi \sim 0.5°$–$1.0°$). The difficulty of high-precision measurements of small angles restricts the capability of the acoustooptic methods in the sound velocity measurements. We should note that an original acoustooptic technique for high-precision measurements of the velocity of elastic surface waves was proposed recently [6, 7].

Both continuous and pulsed modes of sound radiation are used in the sound velocity measurements. For example, the continuous mode is used as a rule in the resonance methods, which are especially efficient for high-precision measurements of small changes of sound velocity [8]. However, currently, the pulsed mode is more widely used, because it has several advantages [9, 10]. According to Truell *et al.* [11], pulsed methods of the sound velocity measurement can be divided into several groups utilizing detected pulses with a discrete delay, radio-frequency pulses with a discrete delay, techniques of pulse autocirculation, and methods of pulsed interference with the interference of high-frequency signals of the filling of reflected sound pulses. From our point of view, methods of pulsed interference and, in particular, the long-pulse method are very precise and at the same time, simple enough [12, 13]. The method we suggest is its outgrowth. In our case, the long-pulse technique is combined with an acoustooptic detection of the interference of ultrasonic waves. This technique retains all advantages of the long-pulse method (a large bandwidth, the absence of errors connected with both diffraction and the necessity to take into account the phase shift in the case of reflection from a transducer, and relatively thin samples) and

1063-7710/00/4601-0027$20.00 © 2000 MAIK "Nauka/Interperiodica"

has several additional ones originating from the utilization of acoustooptics. First of all, this is the applicability of this method to the measurement of sound velocity in anisotropic media. Acoustooptics provides an opportunity to observe directly the signals propagating in a sample and to separate the useful signal from additional ones, thus, determining the resonance frequency and visualizing the whole pattern of propagation of the sound pulse over the sample [14].

INTERFERENCE ACOUSTOOPTIC TECHNIQUE

The suggested method is grounded on the observation of the interference of two or several sound waves, i.e., a wave reflected from the sample surface and another wave that is transmitted through the sample, reflected from its rear surface, and then coming out of the sample. A medium where interfering waves propagate is a solid isotropic buffer. Optically transparent glass is used as such a buffer. A narrow laser beam is transmitted through the buffer across the direction of sound propagation in order to observe the interference of acoustic waves. Light diffraction by sound waves in the buffer is observed. If the sound frequency is changed, the phase shift between interfering waves also changes, and the interference maxima and minima of the resulting wave amplitude are observed. They are detected by the corresponding maxima and minima of the intensity of diffracted light. The character of light diffraction is unimportant for the detection of beating (usually, this is a transient regime from the Raman–Nath diffraction to the Bragg diffraction), and there is no need in fine tuning of the angles of incidence and observation to the changes of sound frequency (the optical system is tuned to the presumed average frequency of the range only once before the beginning of measurements). If the sound frequency changes, only a decrease in the intensity of diffracted light occurs.

The measuring cell for the interference acoustooptic technique is schematically depicted in Fig. 1. Elastic

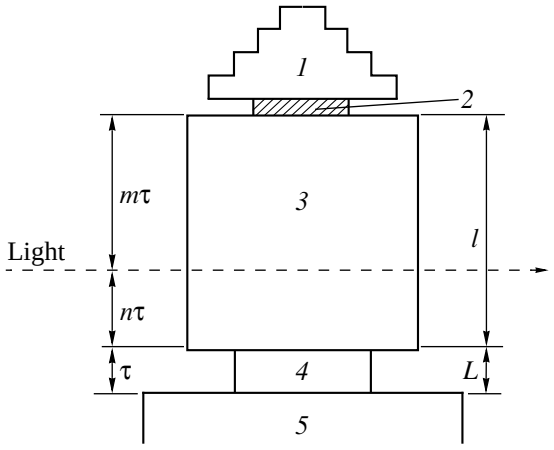

Fig. 1. Measuring cell: (*1*) load, (*2*) transducer, (*3*) buffer, (*4*) sample, and (*5*) base (holder).

waves are excited by a transducer positioned on a buffer. The polarization of the excited wave is determined by the utilized transducer. It is possible that the transducer is positioned not on the buffer but on the sample. In this case, a buffer is necessary only in the process of investigation of opaque samples. However, in the case of such positioning of the transducer, a precise determination of sound velocity is much more difficult, since the phase shift that appears as a result of reflection from the transducer depends on sound frequency. In this case, it is necessary to take into account not only the finite thickness of the transducer [15] but also the conversion of part of the elastic energy into the electric one. Therefore, this version of the technique will not be considered in this paper.

In the case of normal incidence of an elastic wave on a boundary between two media, the wave vectors of the incident, reflected, and transmitted waves lie in a single straight line normal to the boundary. If both media are isotropic (the buffer and the sample are isotropic), waves of different polarization do not arise. However, if a sample is crystalline and the wave vector of the incident wave is oriented arbitrarily with respect to its crystallographic axes, the pattern of the waves excited in the sample will be much more complex. Three waves (a longitudinal wave and two transverse waves) propagate in the sample in the general case. Each of them has its own velocity. The amplitudes of these waves are proportional to the force exciting them. For example, if the incident wave is longitudinal, a quasi-longitudinal wave is dominant in the sample. Since the angle between the displacement direction and the wave vector in a longitudinal wave is small (usually, it does not exceed 5°–10°), the amplitudes of transverse waves correspondingly do not exceed 10–15% of the amplitude of the longitudinal wave, and these waves may be ignored. A longitudinal wave is reflected from the sample–load boundary, arrives at the buffer, and excites longitudinal and transverse waves in it. However, the amplitude of the transverse wave in the buffer again does not exceed 10–15% of the amplitude of the longitudinal wave.

If a transverse wave arrives from the transducer, in the general case it also excites all three waves in a crystalline sample. However, the quasi-longitudinal wave is small. It does not exceed the aforementioned 10–15% of the transverse wave. The ratio of the amplitudes of transverse waves does not depend on the closeness of the polarization of the incident wave to the polarization of the corresponding transverse wave in the sample. In each specific case, we can select such a polarization of the incident shear wave that would coincide or be close enough to the polarization of the transverse wave of interest in the sample. Just this wave is dominant in this case. It is reflected from the sample–base boundary and returns to the buffer. In the buffer, it excites two waves: a dominant transverse wave with the polarization coincident with the polarization of the transverse wave in the sample and a weak longitudinal wave. Thus, when

the polarization of the shear wave incident from the side of the transducer does not exactly coincide with the polarization of the transverse wave in the sample, the polarization of the wave returning to the buffer after reflection and the polarization of the wave reflected from the buffer–sample boundary differ to some extent. However, this difference does not prevent their interference. We note that the presence of waves with different polarizations in the buffer does not restrict the observation of the interference of the waves of interest, since the waves of different polarization also have different velocities and, therefore, different diffraction angles. This provides an opportunity to direct the light diffracted only by the waves of interest to a photodetector. In the pulsed mode, all mentioned waves can be distinguished by the arrival times of their fronts at the line of optical observation.

TECHNIQUE SUBSTANTIATION

Let us consider the wave propagation in the measuring cell assuming for simplicity that the sample is isotropic.

We introduce the notation: L is the sample length, l is the buffer length, V_0 is the sound velocity in the sample, $k_0 = \omega/V_0$ is the wave number in the sample, V is the sound velocity in the buffer, and $k = \omega/V$ is the wave number in the buffer.

For the phase shift caused by the reflection from the boundary, we introduce the notation: a_1 for the buffer–sample boundary, a_2 for the sample–base boundary, a_3 for the sample–buffer boundary, and a_4 for the buffer–transducer boundary.

We assume that the phase shifts $a_{1,2,3}$ do not depend on frequency. The phase shift a_4 depends on frequency, but it is not involved in the described technique.

If we feed a single high-frequency electric pulse of length S to the transducer, a train of ultrasonic pulses of the same length and frequency is excited in the transducer–buffer–sample system because of the sequential reflections from the boundaries. The following pulses are observed in the buffer at the distance x from the transducer (Fig. 1): a pulse U_1 incident from the transducer; a pulse U_2 reflected from the buffer–sample boundary; a pulse U_3 transmitted through the sample twice (a pulse, which penetrated the sample, was reflected from the sample–base boundary, and came out to the buffer); a pulse U_4, which penetrated the sample, passed through the sample four times, and returned to the buffer as a result of sequential reflections from the sample–base and sample–buffer boundaries; and a pulse U_5, which entered the sample, passed through it six times, and returned to the buffer. It is necessary to note that the intensity of acoustic waves substantially decreases in the process of sequential reflections. Therefore, we may ignore the pulse U_5 and all further pulses of the train.

Signals filling all considered pulses have the same frequency, wavelength, and polarization. If pulses overlap, they interfere.

Let us consider the interference of the high-frequency signal filling the pulse U_3 (since this pulse has the largest amplitude of the pulses carrying information on the sample) with the pulse U_2. It is easy to show that their phase difference $\Delta\Phi_{23} = \Phi_2 - \Phi_3$ at the observation line – x is as follows:

$$\Phi_2 = -(2k_1 l - k_1 x) + a_1, \tag{1a}$$

$$\Phi_3 = -(2k_1 l - k_1 x + 2k_0 L) + a_2, \tag{1b}$$

$$\Delta\Phi_{23} = 2k_0 L + a_1 - a_2, \tag{2a}$$

$$\Delta\Phi_{23} = 2\pi f(2L/V) + a_1 - a_2. \tag{2b}$$

We note that the position of the light beam and its diameter do not affect the precision of the measurements, since $\Delta\Phi_{23}$ does not depend on x.

The phase difference consecutively acquires the values $\Delta\Phi_{23} = 2n\pi$ and $(2n + 1)\pi$ as the frequency varies. In this case, the high-frequency signals filling the pulses U_1 and U_2 are either in phase, their amplitudes being added, or in antiphase, their amplitudes being subtracted. Thus, as the frequency varies, changes (beating) of the amplitude of the total pulse U_{23} from minimum $A_{23} = A_2 - A_3$ to maximum $A_{23} = A_2 + A_3$ take place. Correspondingly, beating of the intensity of diffracted light is observed.

Let the nth maximum of the intensity of diffracted light be observed at the frequency f_1,

$$2\pi f_1(2L/V_0) + a_1 - a_2 = 2\pi n, \tag{3}$$

and some mth, $m = n + N$, maximum be observed at the frequency f_2,

$$2\pi f_2(2L/V_0) + a_1 - a_2 = 2\pi m. \tag{4}$$

Thus, if the frequency changes by $\Delta f = f_2 - f_1$, $N = (m - n)$ maxima are observed, these maxima being independent on the phase shift caused by the reflection:

$$\begin{aligned} N - (1/2\pi)[2\pi f_2(2L/V_0) \\ + (a_1 - a_2) - 2\pi f_1(2L/V_0) - (a_1 - a_2)], \end{aligned} \tag{5}$$

$$N = \Delta f(2L/V_0). \tag{6}$$

Knowing the frequency variation Δf and the number of "transmitted" maxima N, it is easy to determine the sound velocity in the sample

$$V_0 = 2L\Delta f/N. \tag{7}$$

An analogous expression can be obtained when we detect not the maxima of the intensity of diffracted light but the minima.

Now let us consider the interference of high-frequency signals filling the pulses U_2 and U_4. It is easy to show that in this case we have

$$\begin{aligned} \Delta\Phi_{24} &= 4k_0 L + a_1 - 2a_2 - a_3 \\ &= 2\Delta\Phi_{23} - (a_1 + a_3). \end{aligned} \tag{8}$$

Table 1. Arrival time of the pulse fronts at the observation line (t_n) and the interval between them (Δt_n)

	t_n	$\Delta t_n = t_n - t_{n-1}$	I_n/I_1
U_1	0	–	1.000
U_2	$2n\tau$	$2n\tau$	0.380
U_3	$2n\tau + 2\tau$	2τ	0.380
U_4	$2n\tau + 4\tau$	2τ	0.146
U_5	$2n\tau + 6\tau$	2τ	0.056
U_6	$2n\tau + 2m\tau$	$2\tau\,(m-3)$	0.190

Thus, when $\Delta\Phi_{23} = 2\pi n$ and U_1 and U_2 are in phase, the phase of the high-frequency signal filling the pulse U_4 relative U_2 is determined only by the phase shift caused by reflections ($a_1 + a_3$). This sum is always equal to π independently of the character of adjoining media, since it is a phase shift between two waves reflected from the same boundary but incident at it from different sides.

Thus, U_2 and U_4 are in antiphase at the frequency at which U_2 and U_3 are in phase. We note that the combinations of U_3 and U_4 and U_4 and U_5 are also in antiphase in this case.

If the length of pulses is small enough, all of them arrive at the line of observation at different times, and the intensity of diffracted light will represent a set of single pulses. However, if the length of pulses is increased, some of them overlap for some time and interfere. If the frequency changes, the beating described above is observed in the range of overlapping of these pulses. If it is possible to perform overlapping of only the pulses U_2 and U_3, the beating U_{23} may be observed in its pure form.

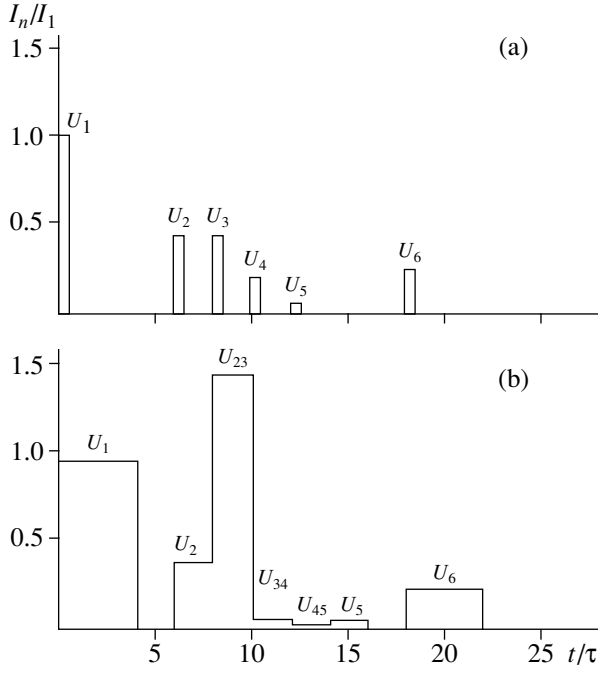

Fig. 2. Schematic diagram of the pulses of diffracted light: (a) at $S = 0.5\,t$, $n = 3$, and $m = 6$; (b) at $V = 2\pi N$, $S = 4t$, $n = 3$, and $m = 6$.

Let us consider the pulsed mode in more detail. We assume that the time interval between two successive pulses from the transducer is large enough and the next train of reflected pulses repeats the previous one. Therefore, it is sufficient to consider only one of them.

Let us denote the pulse travel time (Fig. 1) within the sample, from its one boundary to another, by τ, the travel time between the transducer and the observation line by $m\tau$, and the travel time between the observation line and the sample by $n\tau$.

The values of τ and $\tau_1 = (m + n)\tau$ depend on the dimensions of the buffer and the sample, and on the sound velocity. They do not depend on the position of the light beam (the observation line). However, by changing the position of the light beam, we can change the values of m and n.

Let us monitor the time of arrival of the front of the considered pulses at the observation line τ and the interval Δt between the pulses. We take the instant of arrival of the front of the pulse U_1 from the transducer to the observation line as the zero time. The times of interest are given in Table 1. The relative intensities I_n/I_1 of light diffracted by a given pulse are presented in the last column. These intensities are proportional not to the sound amplitude, but to its intensity. The table gives the values of I_n/I_0 for the coefficients of sound reflection (in intensity) from the buffer–sample, sample–base, and buffer–transducer boundaries $R_{bs} = 1.0$, $R_{sb} = 0.38$, and $R_{bt} = 0.5$, respectively.

Assuming for definiteness that the pulse length $S = 0.5\tau$, $n = 3$, and $m = 6$, we present the intensity of pulses of interest graphically (Fig. 2a).

One can see from Fig. 2a that the length of the incident pulse S must exceed 2τ for the pulses U_2 and U_3 to overlap. In this case, we cannot avoid overlapping of the pulses U_3, U_4, and U_5. Noticeable overlapping of the pulses U_2 and U_3 is observed at $S = 3\tau$. It is necessary that $n \geq 2$ for the pulse U_1 not to overlap with the pulse U_2, and $m \geq 4.5$ for the pulse U_5 not to overlap with the pulse U_6. However, the pulse U_5 is small (as was mentioned earlier), and its coincidence with the pulse U_6 is quite acceptable. Moreover, the presence of the pulse U_6 between the pulses U_4 and U_5, i.e., at $m =$ (2–3), is acceptable for the detection of beating in the range of overlapping of the pulses U_2 and U_3. Thus, the minimum time of sound propagation over the sample is $\min\tau_1 = (4–5)\tau$, and the optimum time is $\tau \geq (7–10)\tau$. These conditions restrict the minimum size of the buffer. Therefore, it is necessary to select a buffer made of material with a small sound velocity. Moreover, it is desirable to have a buffer with a high enough acoustooptic quality factor in order to detect diffracted light with high contrast.

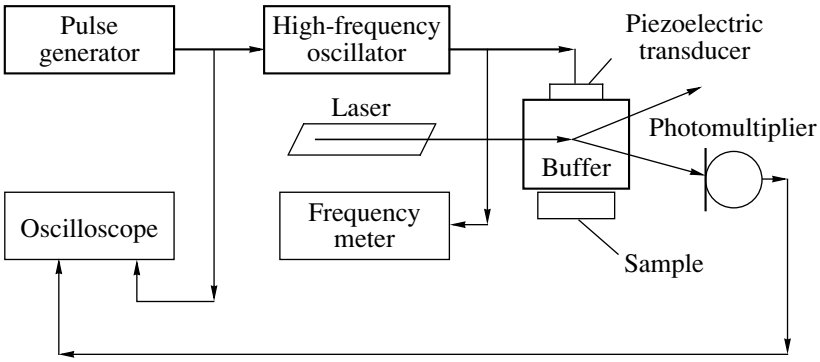

Fig. 3. Experimental setup.

Figure 2b presents a pattern of inphase interfering pulses U_2 and U_3 at $S = 4\tau$, $n = 3$, and $m = 6$. Let us remind ourselves that, under these conditions, the pulses U_3 and U_4, as well as U_4 and U_5, are in antiphase.

REALIZATION OF THE TECHNIQUE

The setup is schematically represented in Fig. 3. Rectangular pulses with the frequency of the filling signal from 25 to 400 MHz and the length 0.5–1000 μs from a G4-143 generator were fed to a transducer. The modulation of the G4-143 generator was performed by a G5-54 generator. The frequency of sinusoidal signals was measured by a Ch3-34A frequency meter with accuracy no worse than 10 Hz. Ultrasonic vibrations excited in the studied sample were detected by the diffraction of light with the wavelength 0.6328 μm from an LG-79/1 helium-neon laser. Diffracted light was detected by an FEU-28 photomultiplier.

The measuring unit consisted of a metal holder with the measuring cell consisting of a transducer with a load, a buffer, and a sample (Fig. 1). A buffer of length $l = 30$ mm was made of F-4 optical glass with the velocity of longitudinal acoustic waves $V = 4100$ m/s, density $\rho = 3.67 \times 10^3$ kg/m^3, and acoustooptic coupling five times higher than that of fused quartz. Transducers made of single-crystal lithium niobate ($LiNbO_3$) of two types (36°Y cut for longitudinal waves and 163°Y cut for transverse waves) were fixed each at its own buffer with the help of an acoustic coupling substance (salol). The acoustic coupling substance was also introduced between the buffer and the sample. Salol was used for transverse waves, and vacuum oil, for longitudinal waves.

The liquid coupling provided an opportunity to change to some extent the coefficient of reflection from the buffer–sample boundary by changing the force of their pressing to each other. The acoustic coupling was not introduced between the transducer and the load, and between the sample and the base. Moreover, a layer of cotton cloth was placed between the sample and the base to provide an almost total reflection of sound from the rear surface of the sample.

The electric contact was established between the metal-coated surfaces of the transducer and the metal-coated surfaces of the buffer and the base where the voltage from a high-frequency oscillator was supplied.

Preliminary visualization of sound in the system provided an opportunity to assemble the measuring cell in such a way that the sound beam did not touch the lateral faces of the sample, and the polarization of the transverse wave in the buffer was close to the polarization of the transverse wave in the sample.

The phase velocity of a plane sound wave in an unbounded space is usually of interest for the determination of the sound velocity in a medium. Therefore, measurement conditions must allow one to determine just this velocity, i.e., it is necessary that a plane acoustic wave propagates in the sample with the sound beam divergence being small (the near Fresnel zone) and the sound beam not touching the lateral faces of the sample.

Thus, the following conditions must be satisfied:

$$a > D \gg \lambda_1, \tag{9a}$$

$$D^2 \gg 1\lambda_1 \quad \text{or} \quad D^2 \gg [2L + 2l - x]\lambda_1, \tag{9b}$$

where D is the smallest dimension of the transducer, λ_1 is the wavelength of the longitudinal wave in the buffer, and a is the smallest dimension of the sample.

These conditions, in their turn, restrict the dimensions of the buffer and the sample, as well as the value of the operating frequency. For example, at $D = 5$ mm, $a =$ 7–8 mm, $L = 5$–10 mm, $l = 30$ mm, and $x = 15$–20 mm, the operating frequency must be no less than $f_0 \geq 50$ MHz.

According to formula (7), the error in the determination of the sound velocity V_0 consists of the error of the determination of the sample length L and the error of the determination of the frequency range $\Delta f = f_2 - f_1$, since N is a an integer number:

$$\delta V_0/V_0 = \delta L/L + \delta(\Delta f)/\Delta f. \tag{10}$$

The error in the determination of Δf consists, in its turn, of the error of determination of the frequencies of the first and last maxima of the diffracted light intensity

Table 2. Measured values of the phase velocity of longitudinal V_L and transverse V_T sound waves in fused quartz

	Frequency band, Δf, Hz	Number of readings, p	Number of beating, N	Longitudinal velocity, V_L, m/s	Transverse velocity, V_T, m/s
1	42246450	25	137	5961	–
2	42245910	25	137	5961	–
3	40096550	25	130	5962	–
4	41949300	25	136	5962	–
5	40091370	25	130	5961	–
6	9761700	10	50	–	3767
7	9758000	10	50	–	3766
	Average values			5961.4 ± 0.5	3766.5 ± 0.7
	Tabular values [1]			5960	3760

$\delta(\Delta f) = \delta f_1 + \delta f_2$. The error δf is determined by the precision of utilized frequency meter δf_0 and the precision of measurement of the frequency of the maximum δf_m: $\delta f = \delta f_0 + \delta f_m$. As was already mentioned, δf_0 is of the order of 10 Hz, and we may ignore it within the whole frequency range. The main error in the determination of Δf is governed by the precision of measurement of the frequencies corresponding to the first and last maxima. With the use of the equipment listed above, δf_m was 3–5 kHz for both f_1 and f_2. Then, $\delta(\Delta f) = 2\delta f_m < 10$ kHz, and $\delta(\Delta f)/\Delta f$ is determined by the realized frequency range Δf. As a rule, common transducers provide an opportunity to observe beating of diffracted light intensity within the frequency range $\Delta f = 30$–50 MHz.

Thus, $\delta(\Delta f)/\Delta f \le 3 \times 10^{-4}$. Since $\delta f_0 \ll \delta f_m$, by repeating the measurements of f_1 and f_2 p times and averaging the results, it is possible to reduce the measurement error; e.g., at $p = 10$, we obtain $\delta(\Delta f)/\Delta f \le 10^{-4}$.

The error in the determination of the sample length L is governed by the precision of the utilized measuring instrument and the quality of the sample fabrication (the deviations from the planar and plane-parallel shape). An IZV-3 optical comparator capable of measuring the length up to 100 mm with the precision not worse than 10^{-3} mm was used. The plane-parallell shape was maintained with the same precision, which constituted $\approx 10^{-2}\lambda$. The sample thickness was measured at five points (at four corners and in the middle of the sample). The measurements of L were repeated 10 times at each point, and the average value was accepted as L.

The sample length was selected proceeding from the preset precision of the sound velocity measurement. At $\delta V_0/V_0 = 3 \times 10^{-4}$ and $\delta(\Delta f)/\Delta f = 10^{-4}$ ($p = 10$), the sample length L must be no less than 5 mm.

The best achievable accuracy of measurement of the sound velocity by the suggested method with the utilized equipment was $\delta V_0/V_0 \approx 10^{-4}$.

The results of measurements of the phase velocity of longitudinal (V_L) and transverse (V_T) waves in a sample of length $L = 9.649$ mm made of fused quartz are given in Table 2. We conducted five independent measurements of V_L and two measurements of V_T. These results demonstrate that the experimental scatter of data on ΔV_L corresponds to the expected accuracy of measurements $\delta V_L/V_L \approx 10^{-4}$.

ACKNOWLEDGMENTS

This work was supported by the Russian Foundation for Basic Research, project no. 97-02-18555.

REFERENCES

1. B. P. Belikov, L. S. Aleksandrov, and T. V. Ryzhova, *Elastic Properties of Rockforming Minerals and Rocks* (Nauka, Moscow, 1970).
2. S. V. Bogdanov, Akust. Zh. **41**, 751 (1995) [Acoust. Phys. **41**, 661 (1995)].
3. S. V. Bogdanov, Akust. Zh. **43**, 304 (1997) [Acoust. Phys. **43**, 260 (1997)].
4. Cl. Schaefer and L. Bergmann, Ann. Phys. **3**, 72 (1948).
5. C. Krischer, Appl. Phys. Lett. **13**, 310 (1968).
6. E. A. Kolosovsky, A. V. Tsarev, and I. B. Yakovkin, IEEE Trans. Ultrason. Ferroelect. Frequency Control **44**, 1219 (1997).
7. E. A. Kolosovskiĭ, A. V. Tsarev, and I. B. Yakovkin, Akust. Zh. **44**, 793 (1998) [Acoust. Phys. **44**, 690 (1998)].
8. C. Jin, Rev. Sci. Instrum. **67**, 271 (1996).
9. L. Godfrey and J. Philip, Solid State Commun. **97**, 635 (1996).
10. V. Rajendran, H. A. Elbatal, and F. A. Khalifa, Indian J. Pure Appl. Phys. **35** (2), 82 (1997).
11. P. Truell, Ch. Elbaum, and B. Chick, *Ultrasonic Methods in Solid State Physics* (Academic, New York, 1969; Mir, Moscow, 1972).
12. H. J. McSkimin, J. Acoust. Soc. Am. **22**, 413 (1950).
13. H. J. McSkimin, J. Acoust. Soc. Am. **34**, 404 (1962).
14. G. W. Willard, Bell Lab. Rec. **25**, 194 (1947).
15. J. Williams and J. Lamb, J. Acoust. Soc. Am. **30**, 308 (1958).

Translated by M. L. Lyamshev

Acoustical Physics, Vol. 46, No. 1, 2000, pp. 33–36. Translated from Akusticheskiĭ Zhurnal, Vol. 46, No. 1, 2000, pp. 42–46.

Acoustic Waves in Thin Plates of Lithium Niobate

I. A. Borodina*, S. G. Joshi, B. D. Zaĭtsev**, and I. E. Kuznetsova***

** Institute of Radio Engineering and Electronics, Russian Academy of Sciences, ul. Zelenaya 38, Saratov, 410019 Russia*
e-mail: kazakov@sfire.saratov.su

*** Marquette University, Milwaukee, WI 53201-1881, USA*

Received September 28, 1998

Abstract—By the example of lithium niobate, the main features of the propagation of antisymmetric (A_0) and symmetric (S_0) Lamb waves and the waves with transverse horizontal polarization (SH_0) in thin piezoelectric plates are theoretically analyzed. The obtained results may be used in the development of signal processing devices, various types of sensors, and chemical and biological instruments on the basis of acoustic waves propagating in lithium niobate plates. © *2000 MAIK "Nauka/Interperiodica".*

Currently, growing interest is being shown in acoustic waves propagating in thin piezoelectric plates [1–7]. This is connected with the possibility of developing a variety of sensors and devices for signal processing with unique features [1–4]. As is known, one of the materials most widely used in acoustoelectronics is lithium niobate, which exhibits a strong piezoelectric effect. The properties of bulk and surface acoustic waves in this material have been much studied. As for the characteristics of acoustic waves in a plate considered as a one-dimensional waveguide, there are only fragmentary data on certain types of waves for particular orientations and directions of propagation [5–9]. The data presented in these papers reveal good prospects for the application of these waves but do not give a full picture of the phenomenon that would allow one to draw definite conclusions regarding the general features of their propagation. Besides, the available information is insufficient for developing specific acoustoelectronic devices. For instance, it is established and experimentally confirmed that the square of the electromechanical coupling coefficient (K^2) for a wave with transverse horizontal polarization (SH_0) in *Y–X* lithium niobate plates may be as high as 36% [8, 9]. But, at the same time, the data on the characteristics of other fundamental modes—the antisymmetric A_0 and symmetric S_0 Lamb waves—are lacking. These modes also have no cut-off frequency, i.e., they can exist at any frequency and plate thickness and may be a source of interference. Therefore, the information on all aforementioned types of waves would allow one to make a justified choice of the plate orientation for obtaining maximum excitation of only the needed type of wave. This paper is devoted to the theoretical study of the main features of the propagation of A_0, SH_0, and S_0 waves in piezoelectric plates by the example of lithium niobate.

This problem was solved by a conventional method [5] based on the use of standard equations and boundary conditions. The material constants of lithium niobate used in this study are presented in [10]. We determined the velocity and the electromechanical coupling coefficient for the A_0, SH_0, and S_0 waves as functions of the direction of propagation for the main crystallographic cuts, *X*, *Y*, and *Z*. The square of the electromechanical coupling coefficient was determined for every mode in a regular way, namely, from the equation $K^2 = 2(V - V_m)/V$, where V and V_m are the wave velocities in a nonmetallized plate and in a plate metallized on one side, respectively. With the understanding that the appearance of higher types of waves is undesirable, the thickness h of the investigated plates was selected not to exceed half of the wavelength λ of the considered mode; i.e., the condition $h/\lambda \le 0.5$ was met.

Some specific features of the performed theoretical analysis should be pointed out:

(1) For the first time, the difference that occurs between the values of h/λ in metallized and nonmetallized plates because of the change in the wave velocity is taken into account. Obviously, this correction becomes more significant with an increase in the wave dispersion. For example, for an antisymmetric mode, the correction to the value of the square of the electromechanical coupling coefficient reaches 40%.

(2) For a number of directions in the range of values $0.25 \le h/\lambda \le 0.5$, the presence of higher types of waves with close values of velocities considerably complicates the determination of the values of V and V_m corresponding to the same fundamental mode. In this case, the structure of the wave cannot be a reliable criterion for the selection of the investigated mode and for prevention of jumping from one dispersion branch to another. This is associated with the fact that, in some cases, the metallization of the plate leads to essential changes in the wave structure. In such situations, we

1063-7710/00/4601-0033$20.00 © 2000 MAIK "Nauka/Interperiodica"

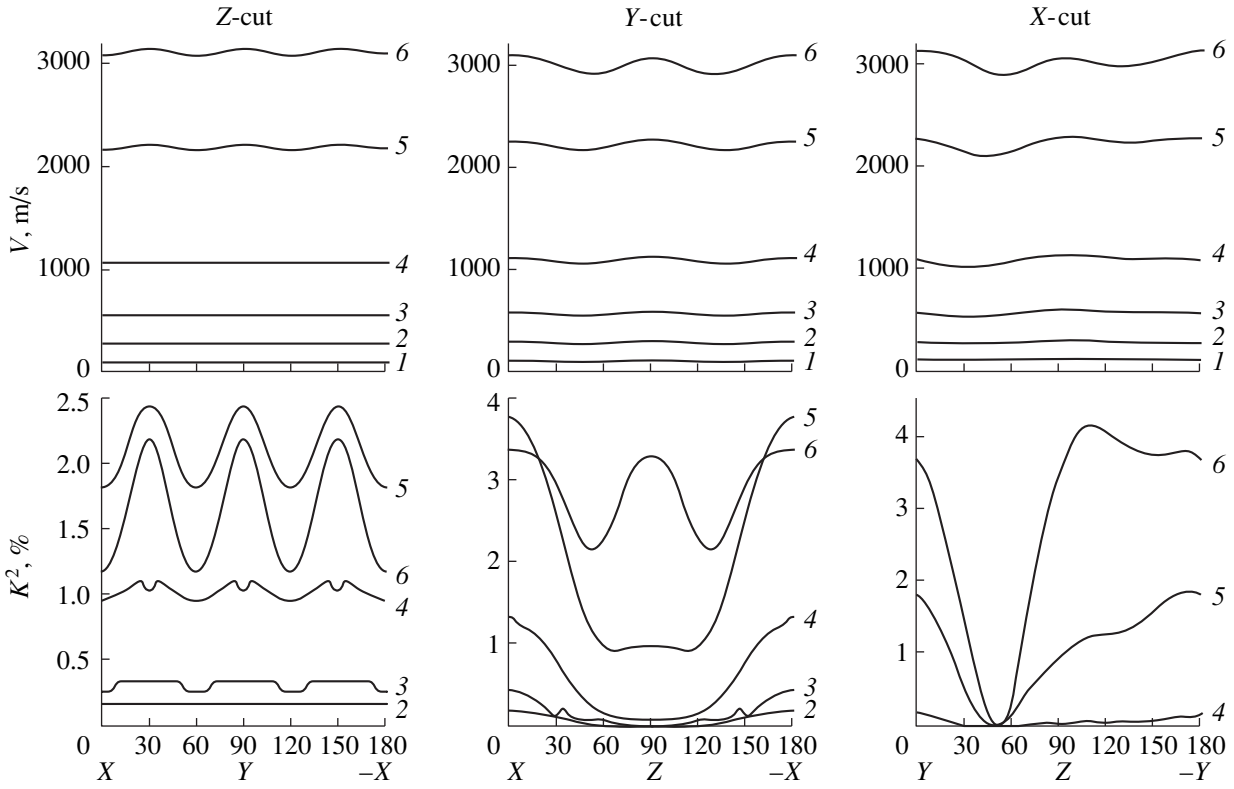

Fig. 1. Dependences of the velocity (upper row) and the square of the electromechanical coupling coefficient (lower row) on the direction of propagation for the A_0 antisymmetric mode in lithium niobate. h/λ = (*1*) 0.01, (*2*) 0.025, (*3*) 0.05, (*4*) 0.1, (*5*) 0.25, and (*6*) 0.5.

analyzed a piezoelectric plate with an ideally conducting electrode located at some distance from it. Changing the plate-to-electrode distance in the range (0–10)λ, we performed a smooth transition from the metallized to nonmetallized state. As a result, it was possible to follow the evolution of the analyzed mode and prevent the unwanted jumps.

The obtained dependences of the velocity and the square of the electromechanical coupling coefficient on the direction of propagation for the A_0, SH_0, and S_0 waves are shown in Figs. 1, 2, and 3, respectively. The analysis of these dependences reveals the following features of the investigated waves.

For the A_0 wave (Fig. 1), the velocity of the antisymmetric mode practically does not depend on the direction of propagation and the crystallographic cut and is mainly determined by the normalized thickness h/λ, i.e., this wave is characterized by a strong dispersion. This fact is related to the preferential orientation of mechanical displacements along the normal to the plate surface and to the absence of an elastic reaction of vacuum. On the other hand, the piezoelectric activity of this wave is characterized by a strong anisotropy, and the quantity K^2, represented as a function of the plate thickness, has an optimum lying in the range $h/\lambda = 0.2$–0.8. The maximum values of the square of the electromechanical coupling coefficient for the antisymmetric mode (~4%) and for a surface Rayleigh wave (~5%) in lithium niobate are commensurable. It is easily seen that the piezoactivity of the wave slightly increases the degree of dispersion.

For the SH_0 wave (Fig. 2), both the velocity and the electromechanical coupling coefficient exhibit a strong anisotropy. It is seen that the dispersion of this wave is determined by the level of its piezoelectric activity; i.e., the maximum dispersion corresponds to the maximum electromechanical coupling coefficient. For nonpiezoactive directions, the dispersion is totally absent. This conclusion is supported by the fact that, for the SH_0 wave, the electric boundary conditions are more significant than the mechanical ones [8, 9]. The nonpiezoactive directions of propagation of the SH_0 wave correspond to the directions of the peculiar bulk waves [11] for which mechanical stresses in the plane determined by the polarization vector and the wave vector always equal zero. Therefore, the presence of boundaries parallel to this plane does not affect the velocity and the structure of the propagating wave. In all cases, as the plate thickness grows, the electromechanical coupling coefficient of the SH_0 wave increases, reaches its maximum at $h/\lambda = 0.05$–0.15, and then decreases. For certain cuts and directions of propagation, the value of the square of the electromechanical coupling coefficient exceeds 30%, which is almost an order of magnitude greater than for the A_0 antisymmetric mode and the surface wave in lithium niobate.

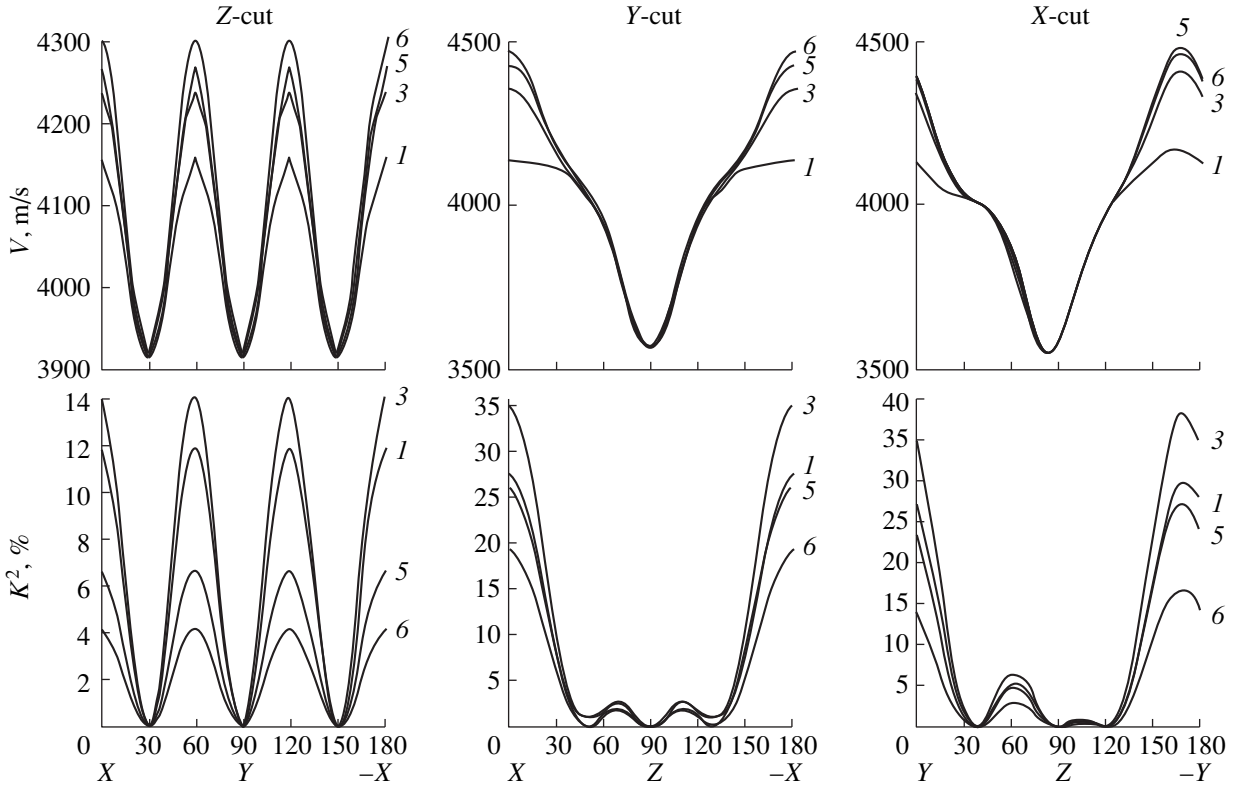

Fig. 2. Dependences of the velocity (upper row) and the square of the electromechanical coupling coefficient (lower row) on the direction of propagation for the SH_0 mode with transverse horizontal polarization in lithium niobate. h/λ = (*1*) 0.01, (*2*) 0.025, (*3*) 0.05, (*4*) 0.1, (*5*) 0.25, and (*6*) 0.5.

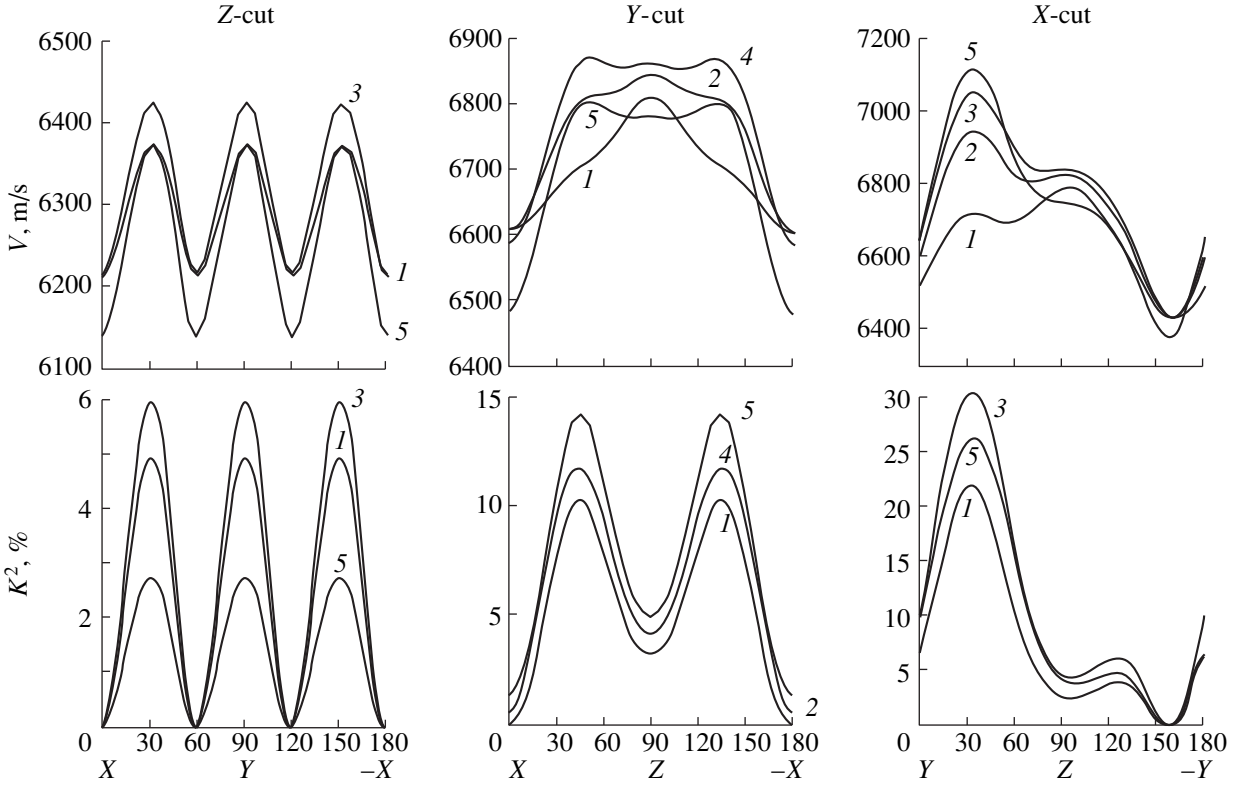

Fig. 3. Dependences of the velocity (upper row) and the square of the electromechanical coupling coefficient (lower row) on the direction of propagation for the S_0 symmetric mode in lithium niobate. h/λ = (*1*) 0.01, (*2*) 0.025, (*3*) 0.05, (*4*) 0.1, and (*5*) 0.25.

For the S_0 wave (Fig. 3), the velocity and the electromechanical coupling coefficient also strongly depend on the direction of propagation and the crystallographic cut. Similar to the SH_0 wave, the dispersion of the symmetric mode is determined by the level of its piezoactivity, and it is maximum where the electromechanical coupling coefficient is maximum. However, unlike the SH_0 wave, the dispersion does not disappear for nonpiezoactive directions of propagation, i.e., the electric and mechanical boundary conditions for the symmetric wave make commensurable contributions. As for the dependence of the electromechanical coupling coefficient on the plate thickness, it is similar to that for the A_0 and SH_0 waves, and the maximum of K^2 lies in the range $h/\lambda = 0.05$–0.25. For the X-cut and the direction of propagation $Y + 35°$, the square of the electromechanical coupling coefficient reaches a value as high as 30%.

Thus, the performed study revealed the main features of the propagation of fundamental waves of the types A_0, SH_0, and S_0 in thin piezoelectric plates. The data reported in the literature for specific cuts and directions of propagation of certain types of waves are in good agreement with the results of our study. These results may be useful in the development of devices for signal processing and sensors for different physical quantities, as well as for the development of chemical and biological instruments, on the basis of acoustic waves propagating in lithium niobate plates.

ACKNOWLEDGMENTS

This work was supported by the program "Federal Support of Integration of Higher Education and Basic Research for 1997–2000," project no. 696.3, and by the National Scientific Foundation of USA.

REFERENCES

1. S. W. Wenzel and R. M. White, IEEE Trans. Electron. Devices **35**, 735 (1988).
2. T. Giesler and J. Meyer, Sensors and Actuators A **36**, 113 (1993).
3. M. J. Vellekoop, G. W. Lubking, P. M. Sarro, *et al.*, Sensors and Actuators A **43**, 175 (1994).
4. F. Teston, G. Feuilard, L. Tessier, *et al.*, IEEE Trans. Ultrason. Ferroelec. Freq. Contr. **45,** 1266 (1998).
5. S. G. Joshi and Y. Jin, J. Appl. Phys. **70**, 4113 (1991).
6. Y. Jin and S. G. Joshi, Appl. Phys. Lett. **58**, 1830 (1991).
7. Y. Jin and S. G. Joshi, IEEE Trans. Ultrason. Ferroelec. Freq. Contr. **43**, 491 (1996).
8. B. D. Zaĭtsev, S. G. Joshi, and I. E. Kuznetsova, Smart Mater. Struct. **6**, 739 (1997).
9. B. D. Zaĭtsev, I. E. Kuznetsova, and S. G. Joshi, Ultrasonics **36**, 31 (1998).
10. G. Kovacs, M. Anhorn, H. E. Engan, *et al.*, in *Proceedings of IEEE Ultrason. Symp. 1990*, Vol. 1, pp. 435–438.
11. V. I. Al'shits, V. N. Lyubimov, N. F. Naumenko, *et al.*, Kristallografiya **30**, 213 (1985) [Sov. Phys. Crystallogr. **30**, 123 (1985)].

Translated by A.V. Svechnikov

Acoustical Physics, Vol. 46, No. 1, 2000, pp. 37–48. Translated from Akusticheskiĭ Zhurnal, Vol. 46, No. 1, 2000, pp. 47–59.

Long-Range Sound Propagation in the Greenland Sea

R. A. Vadov

Andreev Acoustics Institute, Russian Academy of Sciences, ul. Shvernika 4, Moscow, 117036 Russia

e-mail: bvp@akin.ru

Received November 10, 1998

Abstract—Experimental data on the long-range sound propagation in the Greenland Sea, in the presence of a well-defined underwater sound channel, are analyzed. A strong spatial variability of the propagation conditions is observed for the 350-km propagation path. This variability manifests itself in the reduced t/N–R/N diagram as noticeable deviations of the time structure of signals received at distances longer than 100 km from the time structure formed at the 100-km part of the path next to the reception point. At the distance about 100 km from the reception point, a local drop (by 3–5 dB) in the sound field level is observed along with changes in the shape of the terminal part of the received signals. The changes are related to the polar hydrological front, which crosses the propagation path at this distance. The experimental data are used to estimate the sound attenuation coefficient and its frequency dependence. © *2000 MAIK "Nauka/Interperiodica".*

In the late 1970s, a number of experiments were carried out in the deep-water part of the Greenland Sea with the aim to study the structure of the sound field and to determine the sound attenuation in the underwater sound channel. The experiments were carried out during the summer season. Here we report some results obtained by analyzing the data of the experiment in which explosive charges with pressure-sensitive detonators were used as the sound sources. With such detonators, the charges could be dropped from a vessel sailing at full speed, and the explosions occurred at predetermined depths.

The experiment was carried out in the southern region of the Greenland Hollow. Two research vessels were used. The receiving one drifted 170 n.m. northeast of the Yan Mayen Island. The transmitting vessel sailed West, a heading of 270°, away from the receiving one. The length of the propagation path was about 350 km. The echo sounding data obtained from the transmitting vessel provided sufficiently detailed information on the bottom relief along the propagation path. The depth of the sea varied within 2200–3200 m along the path, and it was about 2800 m near the receiving vessel. At a distance of 100–120 km from the reception point, a sharp bottom rise was detected: within an area 20 to 30 km in length, the sea depth decreased from 2800 to 2150–2250 m, then increased to 2650 m, and then increased up to 2750 m. At the 100-km part of the path measured from the receiving vessel, the depth differences reached 300–400 m with a mean periodicity of 25–30 km. The rest of the path exhibited smoother changes in the bottom relief. The path ran north of the North Yan Mayen Ridge and crossed its spurs.

In the Greenland Sea, the underwater environment is formed by the interaction of two currents: the cold East-Greenland current that carries arctic waters having a negative temperature and salinity of about 33‰, and the warm current that carries the Atlantic waters with a temperature higher than 8°C and salinity of about 34.7‰. These currents are separated by the polar hydrological front [1]. The propagation path was influenced by the Yan Mayen Current whose waters are formed as a result of the intermixture of the arctic and Atlantic waters. This current is a part of the cyclonic circulation that encompasses the water bulk of the Greenland Hollow.

Figure 1 shows the vertical sound speed profiles measured at different points along the path, immediately before and after the experiment. By the end of July, the underwater sound channel was fully developed with its axis lying at the depths 40 to 60 m. The sound speed difference was 18–20 m/s between the axis and the surface, and it was 40–50 m/s between the axis and bottom. The depth of the temperature discontinuity layer (with the sound speed gradient 2–3 1/s) varied from 25 to 50 m. In the middle of the path, the channel axis became slightly shallower (the axis depth decreased from 50–60 to 35–45 m), and the near-axis temperature increased from –1.5 to 0°C.

Down to the depth 25–30 m, a well-mixed sub-surface isothermic layer existed along the entire path (with the temperatures 4.2°C on the East and 3.3°C on the West of the region). At horizons deeper than 800–900 m, the water temperature remained constant (–1.0 to –1.1°C) all along the path.

At the depths 50 to 150 m, an interlayered water structure was observed at some parts of the path. The

1063-7710/00/4601-0037$20.00

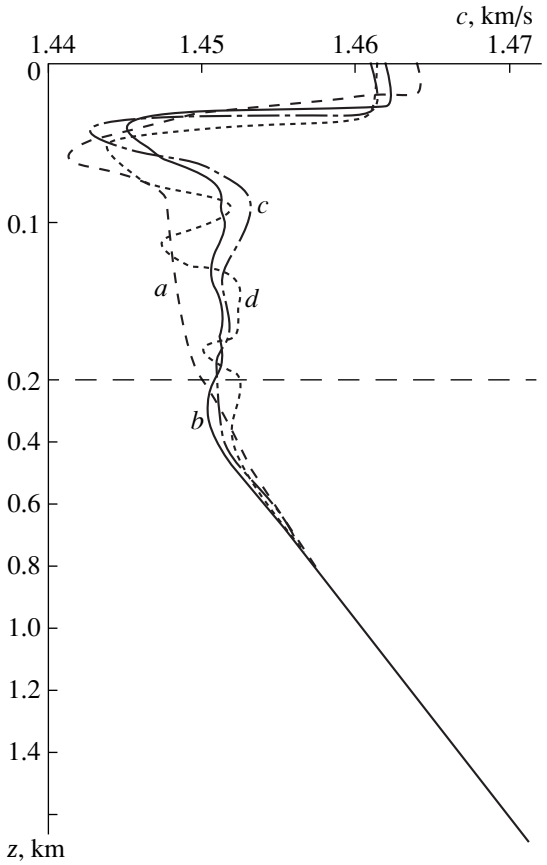

Fig. 1. Vertical sound speed profiles measured before and after the experiment at the distances (*a*) 0, (*b*) 100, (*c*) 180, and (*d*) 340 km from the receiving vessel.

interlayers differed in temperature and salinity. Such structure implies that, in addition to the main minimum of the sound speed, smaller ones exist in the profile $C(z)$. These sublayers were no thicker than 20–30 m, and the sound speed difference reached 4–5 m/s for the adjacent layers.

According to the published data [2], the bottom sediments of the Greenland Hollow mainly consist of terrigenic deposits; globygerinic and diatomic silts also occur.

During the experiment, north and east winds up to Beaufort 4 and seas of the same directions up to Beaufort 3 predominated. The air temperature varied from 5.5°C on the East to 3.5°C on the West of the region. Low clouds and fog restricted the visual range to 0.6–1.0 km. Individual ice-floes occured on the West. The receiving vessel drifted South, with a speed of 1.0–1.5 kn.

About 60 explosive charges were dropped from the transmitting vessel; they exploded at the depth 50 m. The distance between the vessels was determined by measuring the travel time of the sound signal. The explosion-generated sound signals were received by omnidirectional receiving systems at the depths 50 and 70 m.

The received sound signals were tape-recorded by a magnitograph. Then, in a laboratory, the recorded signals were reproduced, low-pass filtered with the 2.5-kHz cutoff frequency, and analog-to-digit converted with a sampling frequency of 10 kHz. For this purpose, a 12-digit analog-to-digit converter was used. The digitized received signals were stored in a computer memory. The stored data serve as a part of the data bank called Ocean Sound Propagation, which is now under development at the Acoustics Institute.

In the presence of a fully developed underwater sound channel, the most reliable information on sound attenuation can be obtained by positioning the source and receiver at the channel axis or near it. The same is true for the features of the sound field time structure.

Figure 2 shows the time structure of the signals received at the distances 1.6 to 15 km from the source (with steps varying with distance). All signals are normalized to their maximum levels. Up to the distance 20 km, the received signals exhibit a pronounced two-component structure which is a consequence of the two-pulse nature of the explosion-generated signals: the first pulse is caused by the shock wave, and the second one is caused by the gas-bubble fluctuation. These two components of the signal are time-separated by the fluctuation period T_0 that depends on the charge mass and the detonation depth; in our case, $T_0 = 100$ ms. The third pulse—the pulse of the second bubble fluctuation—is nearly undetectable. For this part of the path, the signal broadening due to the multiray propagation is less than 20–25 ms.

Figure 3 presents the signals that were received at ranges longer than 20–30 km. In the signals received from distances exceeding 95–100 km (Fig. 3a), the two-component structure of their tail parts is well pronounced, this structure being caused by the separation of the shock-wave pulse and the first bubble fluctuation. The near-axis signals are protracted only slightly. At these distances, the "classic" signal quartets which arrive ahead of the main signals are also visible. The quartets that are separately formed by the shock-wave pulse and the gas-bubble fluctuation are evident. On individual branches corresponding to the "classic" quartets, in addition to the "water" signals (traveling along the rays that do not touch the surface), the signals reflected from the sea surface manifest themselves. These signals are somewhat delayed with respect to the water ones. They are protracted in a reverberation manner. All the received multiray signals begin with the elementary ones that do not touch the surface in the course of their propagation.

The explosion-generated signals received at the distances 95–100 km and above (Fig. 3b) significantly differ in their shapes from those received at shorter ranges. Rather sharp terminations of the signals recorded at shorter distances are now replaced by smoothly decaying tails. (This change in the signal shape was observed in successive explosions at the distances

94.2 and 100.5 km from the source.) As the distance increases, the "classic" quartets are transformed into groups of unresolved signals—just as one can expect by analogy with other ocean regions (see, e.g., [3]). However, up to the longest distances, the signal groups corresponding to the shock-wave pulses and groups corresponding to the pulses of the first gas-bubble fluctuation remain separated.

When sound propagates in the underwater sound channel, the signal is protracted because of the multiray structure of the arrivals. Figure 4 shows the total duration of the received signals as a function of distance. To obtain the signal duration from the experimental data, we excluded the constant time duration of the elementary signal, i.e., the duration determined by the two-pulse (shock wave plus first bubble fluctuation) form of the signal. The rate of the monotonic (on average) increase in the signal duration was estimated for a 200-km part of the path and proved to be 0.0048 s/km. On the background of the smooth increase in the signal duration with distance, stepwise changes in this duration occur at the distances 43, 80, 120, 160, 200 km, and so on. These changes are caused by periodic fadings of the elementary-signal groups because of the surface cut-off of the rays that most widely deviate from the channel axis.

To describe the time structure of the sound field in the underwater sound channel, Ewing and Worzel [4] proposed the *t–R* diagram, where *t* is the travel-time advance for a signal propagating over an individual ray with respect to the signal that propagates along the channel axis, at the distance *R*. If the source and receiver are at the same depth, the *t–R* diagram is represented by a set of triplets of curves. The central curve of each triplet characterizes the *t–R* relation for the rays that produced an integer number of full cycles. The side curves characterize the rays that produced an integer number of cycles plus or minus a half-cycle. The neighboring triplets of curves differ by one full ray cycle from each other.

To compare the sound field structures for different ocean regions, we proposed a more compact, reduced *t–R* diagram that consists of a single curve describing a single full ray cycle [3, 5]. Such a curve does not allow one to estimate the time relations between the signals in the quartet. However, if appropriate scales (t/N, R/N) are chosen, this curve characterizes any ray producing an arbitrary number N of full cycles. It also determines the travel times for any "classic" signal quartet and the relative time delays between the adjacent quartets arriving at the receiver.

Based on the experimental data, we plotted a reduced t/N–R/N diagram that is characteristic for the Greenland Sea. For this purpose, we used five initial branches (N = 1, …, 5) corresponding to individual quartets. Figure 5 shows the values of t/N obtained for individual explosion-generated signals. For the two ini-

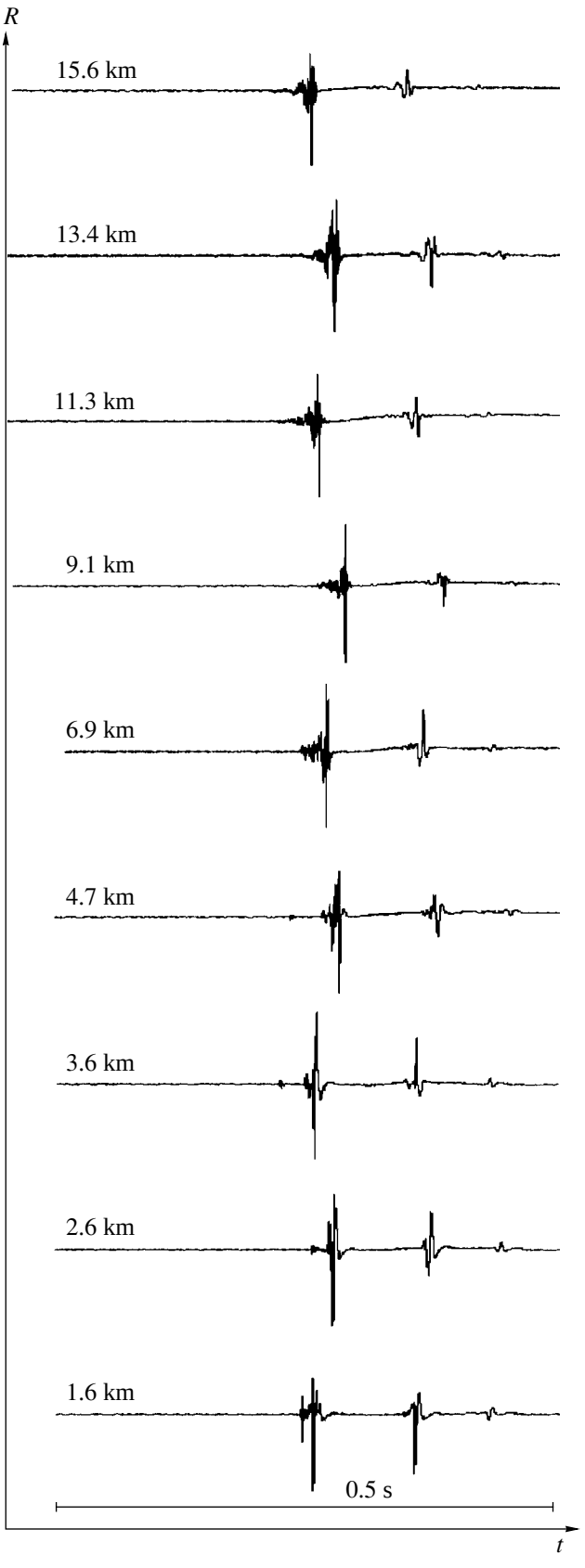

Fig. 2. Time structure of the explosion-generated signals received at short distances (< 20 km) from the source.

tial branches (N = 1, 2), the dependence of t/N (s) on R/N (km) can be described by the formula (Fig. 5a)

$$t/N = (aR/N)^n, \quad (1)$$

where a = 0.0141 and n = 2.3. However, for N = 3, 4, 5, as the distance R and the ordinal number N of the branch increase, the experimentally estimated values of t/N increasingly depart from the curve plotted for the two initial branches toward lower values (Fig. 5b). These changes in the t/N–R/N relations are governed by the changes in the propagation conditions, i.e., by the variations of the sound speed profiles along the

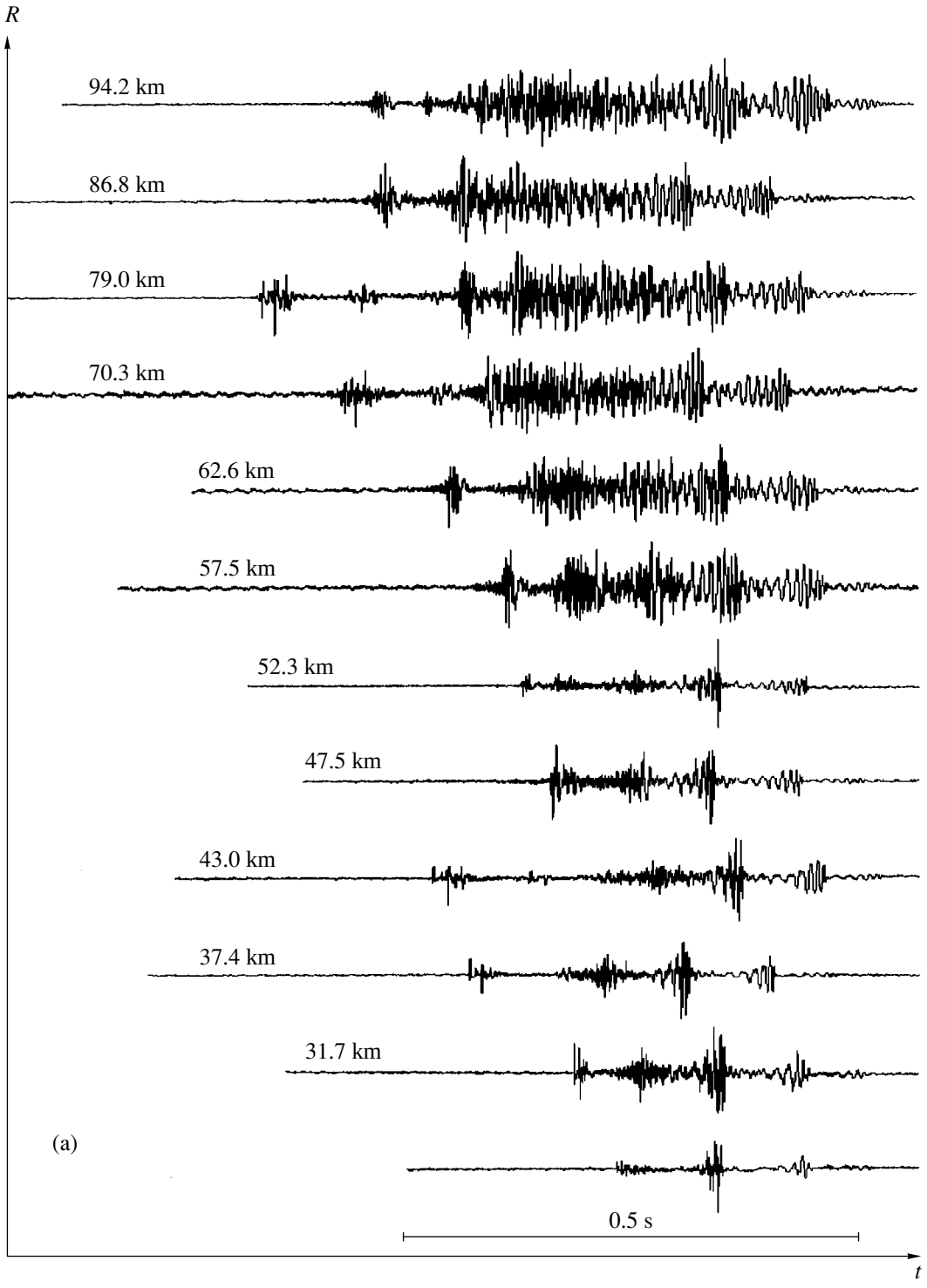

Fig. 3. Time structure of the explosion-generated signals received at long distances from the source: (a) 26–95 km; (b) > 100 km.

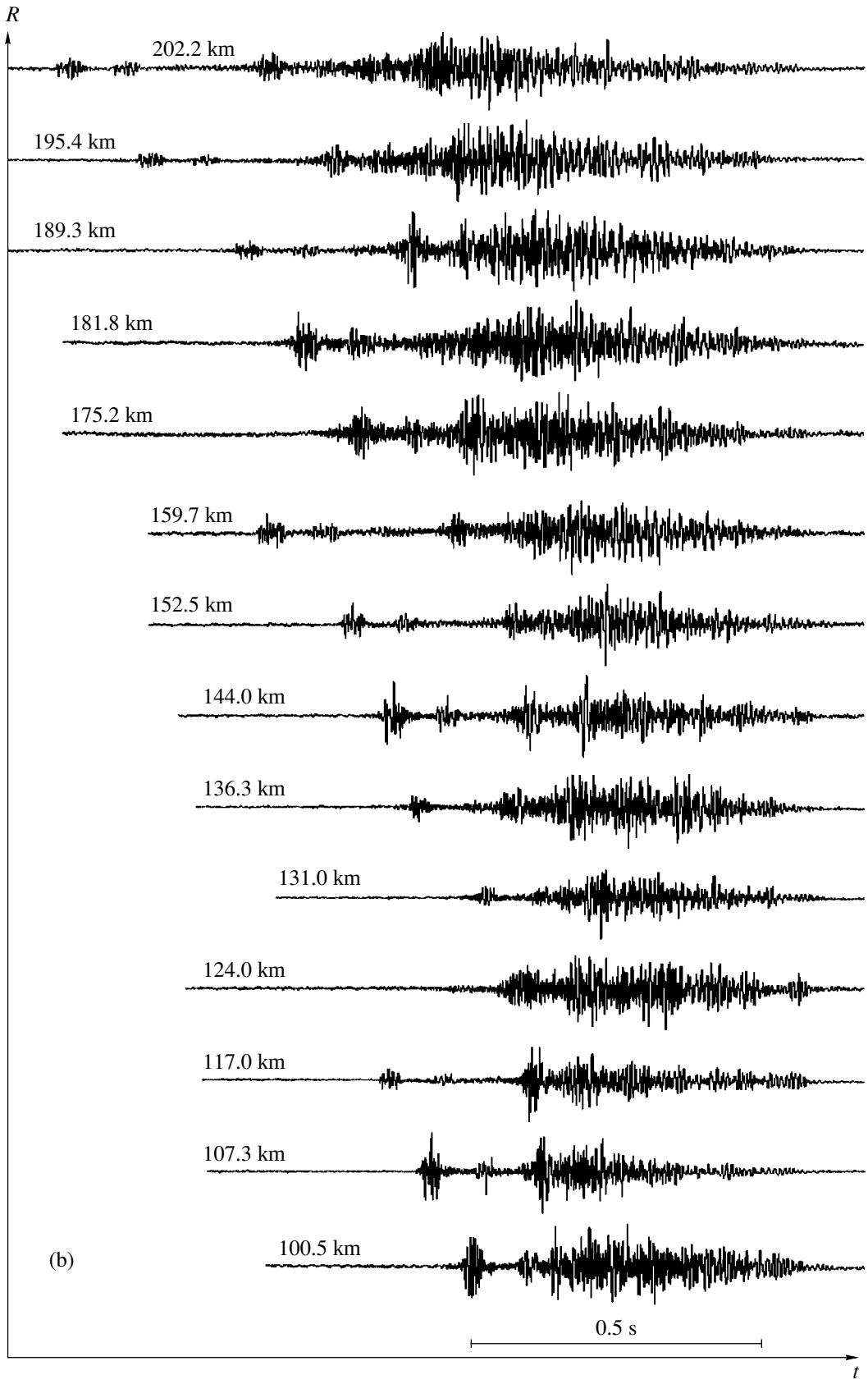
R
202.2 km
195.4 km
189.3 km
181.8 km
175.2 km
159.7 km
152.5 km
144.0 km
136.3 km
131.0 km
124.0 km
117.0 km
107.3 km
100.5 km
(b)
0.5 s
t

Fig. 3. (Contd.)

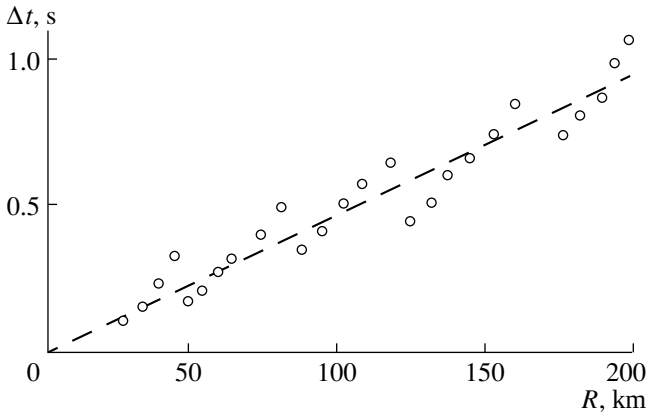

Fig. 4. Total duration of a multiray explosion-generated signal versus the distance from the source. The dashed line corresponds to the linear dependence with the slope 0.0048 s/km.

propagation path. Note that, for the two initial branches, the values of t/N were determined for the explosion-generated signals received at ranges less than 80 km, while for $N = 3, 4, 5$, the distances no less than 87 km were used. The t/N–R/N diagram was computed with the Tebyakin's [6] computer code which implies a horizontally stratified sea medium. The profile $C(z)$ measured at the reception point before the experiment was used in the computation. The computed values agree well with those experimentally estimated for the two initial branches ($N = 1, 2$) of the signal time structure. Thus, considerable changes in the propagation conditions most likely occurred at ranges longer than 80–100 km, while within the initial part of the path, i.e., within distances 80 to 100 km, the propagation conditions were fairly stable. Hence, one can consider the t/N–R/N relation obtained for the initial "unperturbed" 80-km path portion as a typical one for the eastern region of the Greenland Sea.

For the sake of comparison, Table 1 presents the values of the parameters a and n (see relation (1)), experimentally estimated for a number of ocean regions.

The Greenland Sea is not an exception to the rule established earlier [7]: the values of a are within the limits of the weak variations typical for other ocean regions. In its values of the exponent n, the Greenland Sea is closest to the Sea of Okhotsk and to the northwestern region of the Pacific Ocean.

The dispersion characteristics of the sound channel were analyzed on the basis of the experimental data. The signals received at different distances were filtered within 1/3-octave bands covering the frequency range 63–250 Hz. For the distances that are shorter and longer than 100 km, the dispersion relations are essentially different.

For instance, at the distance 79 km (Fig. 6a), the first mode is quite detectable in the filtered signal. As the frequency increases from 63 to 160–200 Hz, a slight decrease (by 1.5–2.0 m/s) in the group velocity of this mode is observed. With Galaktionov's computer code, which is an extension of the computation procedure described by Avilov *et al.* [8], the group velocities of the modes were calculated. The same profile $C(z)$ as for the reduced t/N–R/N diagram was used in the computation. The calculated group velocities of the first mode agree well with the experimental ones: the computed decrease about 2 m/s in the group velocity corresponds to the increase from 63 to 160 Hz in the frequency.

For the signals received at distances longer than 100 km, upon 1/3-octave filtering, no pulses or pulse groups could be attributed to individual modes (an example is shown in Fig. 6b for the distance 159.7 km).

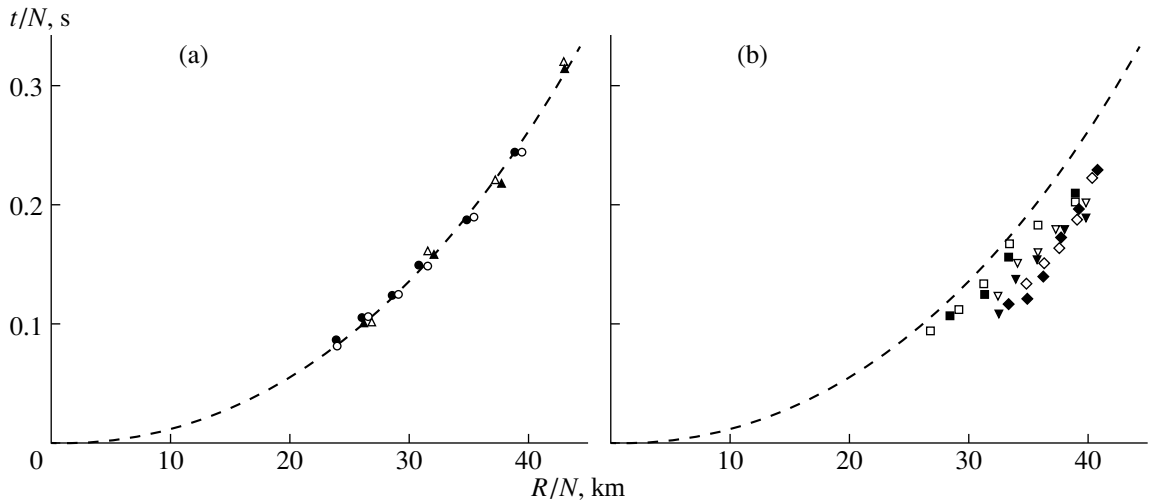

Fig. 5. Reduced t/N–R/N diagram for the explosion-generated signals received at the depths 50 m (empty circles) and 70 m (solid circles): (a) for $N = (\triangle)$ 1 and $(\circ)$ 2 and (b) for $N = (\square)$ 3, $(\triangledown)$ 4, and $(\diamond)$ 5. The dashed curve corresponds to formula (1).

For the 100–1000-Hz frequency band, the attenuation coefficients were estimated from the experimental data. It is common to determine the attenuation coefficient in the ocean by measuring the deviation of the experimental decay curve from the geometric cylindrical law of the sound field spread (strictly speaking, the latter law is valid for sound propagation in a horizontally stratified medium). With the explosion-generated signals, the following quantity is considered to be a characteristic of the sound field energy within the frequency band Δf:

$$E_f = \int_0^T p_f^2(t)dt,$$

where T is the duration of the explosion-generated signal and $p_f(t)$ is the sound pressure normalized to the frequency band Δf. In the computer signal processing, the equivalent quantity may be obtained from the power spectrum of the signal. To proceed with the power-spectrum analysis of the experimental data, a set of computer codes was developed. With these codes, it was possible to plot the experimental decay curves and to estimate the attenuation coefficients at individual frequencies. Upon processing the signals received at the depths 50 and 70 m, we obtained the range dependences of the sound field levels, and by estimating the deviation from the cylindrical law, we obtained the attenuation coefficients at different frequencies.

Figure 7 shows the experimental decays of the sound field levels, which are normalized to the cylindrical spread law, for the frequencies 100, 200, 400, and 630 Hz, and the receiver depth 50 m. At a distance of about 100 km, a noticeable drop (3 to 5 dB) in the sound field level occurs. At this distance, there is no such drop at high frequencies.

Table 2 shows the attenuation coefficients estimated from the deviations of the sound level decays from the cylindrical law. These estimates are obtained for the reception depths 50 and 70 m, at the distances 43–343 and 100–343 km, the latter part of the path being free of the aforementioned sound level drop.

For the sake of comparison, the right column of Table 2 shows the attenuation coefficients calculated according to the formula [9]

$$a = \frac{A_B f}{(f/f_{rB}) + (f_{rB}/f)} + \frac{A_{\mathrm{MgSO}_4} f}{(f/f_{r\mathrm{MgSO}_4}) + (f_{r\mathrm{MgSO}_4}/f)} + Kf^2, \quad (2)$$

where f is the sound frequency (kHz), $K = 1.42 \times 10^{[-8 + (1240/T)]}$ (dB/km × kHz^2), $f_{r\mathrm{MgSO}_4} = 1.125 \times 10^{[9 - (2038/T)]}$ (kHz), $A_{\mathrm{MgSO}_4} = 62.5ST \times 10^{-6}$ (Db/km × kHz), $f_{rB} = 37.9S^{0.8} \times 10^{(-780/T)}$ (kHz), $A_B = 16.5S \times 10^{[4 + 0.78\mathrm{pH} - (3696/T)]}$ (dB/km × kHz), S is the salinity (parts per thousand), T is the temperature (K), and pH is the pH value (more strictly, its effective value).

Table 1

Region	a	n
Black Sea	0.0147	1.7
Greenland Sea	0.0141	2.28
Sea of Okhotsk	0.0152	2.34
Northwestern Pacific	0.0141	2.48
Mediterranean Sea	0.0150	3.0
Sea of Japan	0.0156	3.6
Philippine Sea	0.0134	6.3

The first term in expression (2) characterizes the relaxation absorption associated with boron, the second term corresponds to the relaxation absorption associated with magnesium sulphate, and the third term determines the absorption in fresh water. The absorption coefficients calculated with the use of formula (2) for the Black and Mediterranean Seas and the Sea of Japan, whose waters widely differ in temperature and salinity, and for the northwestern region of the Pacific Ocean agree well with the experimental data obtained by the author.

For the Greenland Sea, the following water parameters were specified in the calculations: $T = 272.5$ K, $S = 33.5‰$, pH = 8.2. Within the entire frequency range at hand (100–1000 Hz), the attenuation coefficients estimated by the deviation of the experimental sound level decay from the cylindrical law far exceed the predicted values.

Note that in Table 2, the data on attenuation are roughly the same for the two reception depths 50 and 70 m: the difference of 20 m in the hozizons has nearly no effect on the slope of the sound field decay curve. The difference in the attenuation coefficients (0.01–0.005 dB/km) estimated for the path portions 43–343 and 100–343 km is also nearly constant and independent of both the reception depth and the frequency. This frequency independent difference is obviously governed by the relatively sharp drop in the sound field level at 100 km, this drop being distributed over the entire 43–343 km portion of the path in the estimation of the attenuation. This drop was visually undetectable in the decay curves at high frequencies but manifested itself in the estimates of the attenuation.

Presumably, in spite of the channel character of sound propagation, one can only tentatively speak of the cylindrical spread of the sound field, because the departure of the medium from the horizontally stratified one is quite substantial.

When the parameters of the medium vary along the propagation path, and one cannot accurately determine the law of the geometric spread, the “differential

method" [10] proposed in the mid-1950s should be used to estimate the attenuation coefficient. This method is based on two assumptions. The first one is that the geometric spread law is unknown, though the same for all the frequencies at hand. The second one is that the frequency dependence of the attenuation coefficient is described by an exponential function with a zero constant component. The decay of the sound field at an individual frequency is normalized to that at one selected frequency serving as a reference one. Thus, the unknown geometrical spread is excluded. From the normalized decay at each frequency, one determines the differential attenuation coefficient that is equal to the difference between the total attenuation coefficients at two frequencies—the frequency of interest and the reference one. By approximating the frequency depen-

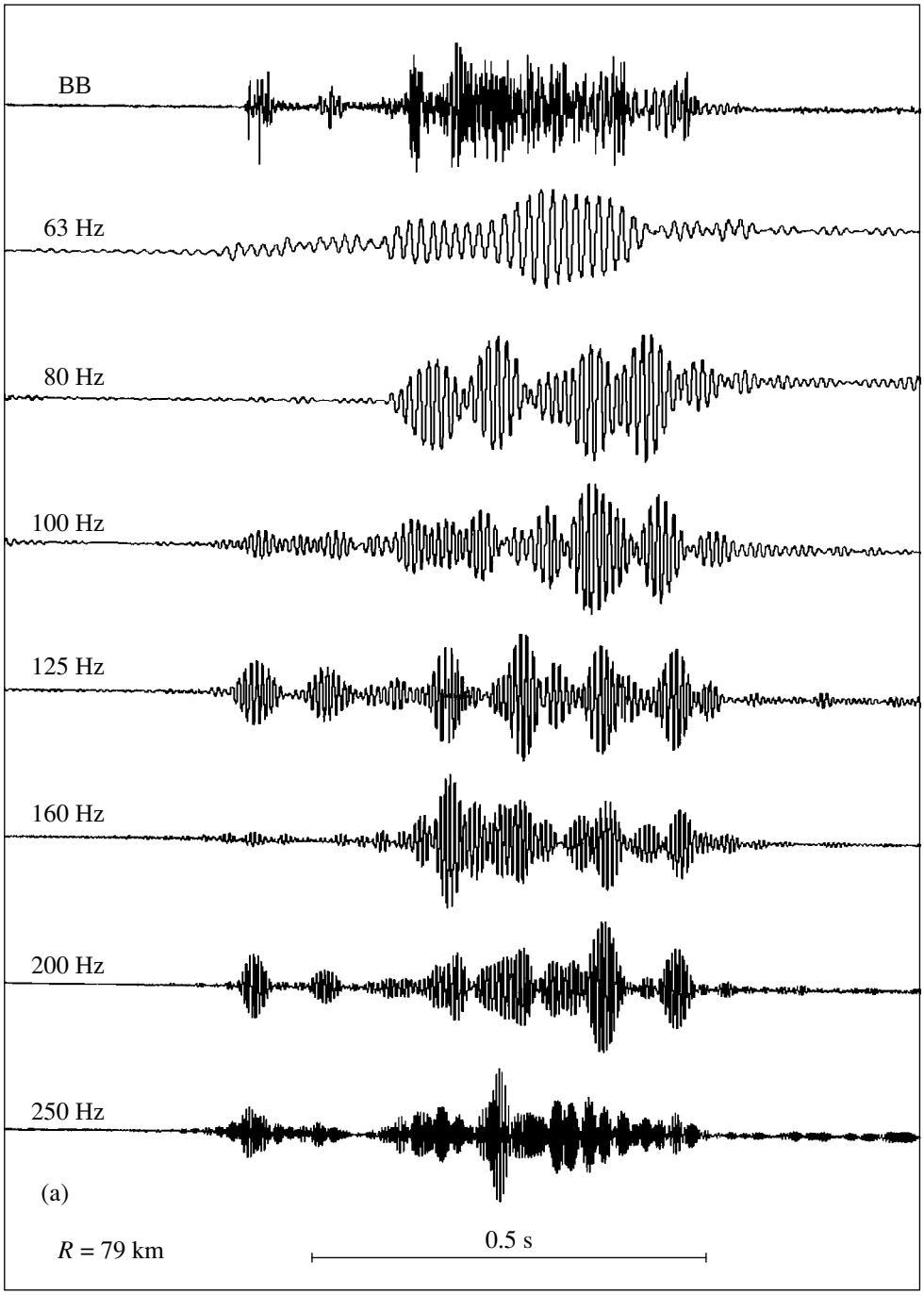

Fig. 6. Signals filtered within 1/3-octave bands with the central frequencies 63, 80, 100, 125, 160, 200, and 250 Hz and within the broad band (BB). The signals were received at the distances (a) 79 and (b) 159.7 km from the source; both the source and the receiver were at the depth 50 m.

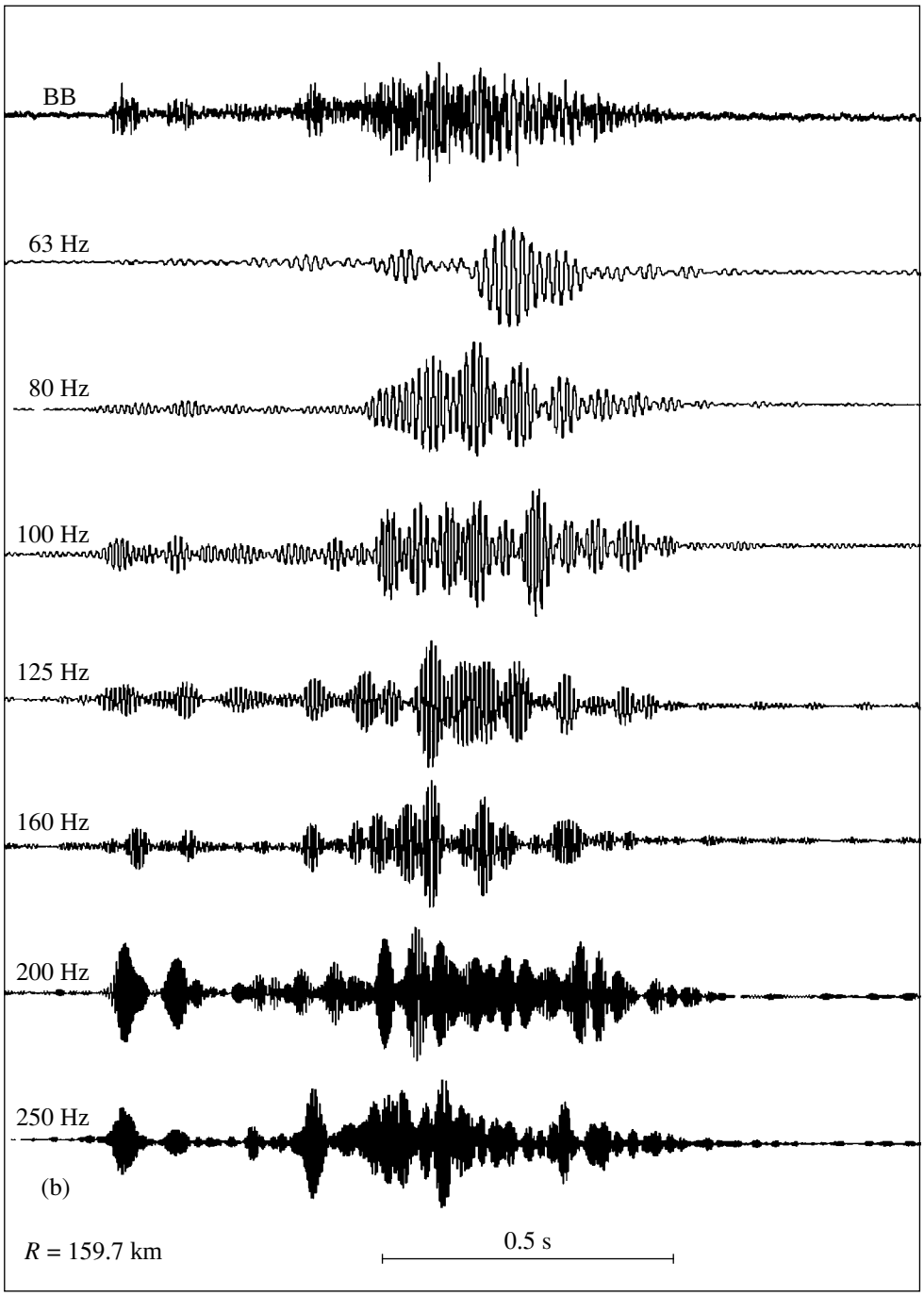

Fig. 6. (Contd.)

dence of the differential attenuation coefficient by an exponential function and omitting the free term, we obtain an explicit expression for the total attenuation coefficient:

$$\beta = af^n. \tag{3}$$

This method was implemented in the computer processing of the experimental data. The reference frequency was specified to be 250 Hz. The entire frequency band 100–800 Hz was analyzed. With the differential method, the differential attenuation coefficients were determined. The results are shown in Fig. 8 (Figs. 8a and 8b are for the reception depths 50 and 70 m, respectively). The exponential curves approximating the frequency dependences of the obtained attenuation coefficients are also shown in this figure. The method of least squares was used to estimate the parameters of these curves. It is easily seen how the differential attenuation

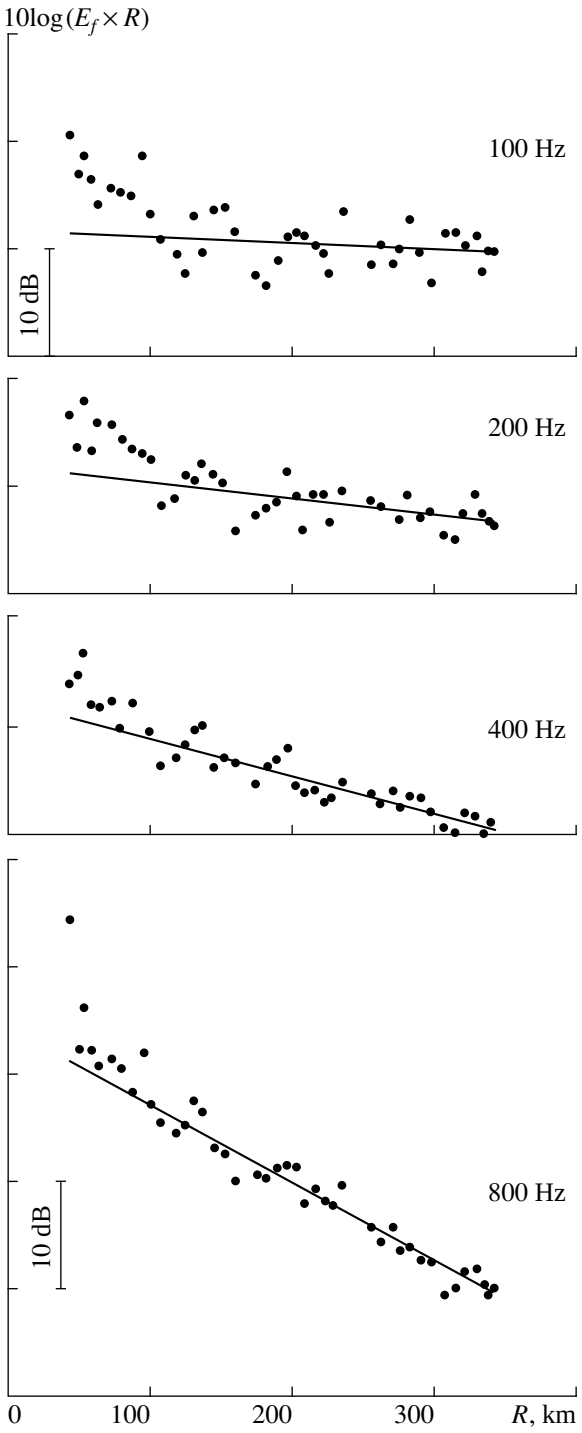

Fig. 7. Experimental sound field decay normalized to the cylindrical geometric spread at the frequencies 100, 200, 400, and 800 Hz. The source and receiver depths are both equal to 50 m. The solid curve is the regression line plotted for the signals received from the distances exceeding 100 km.

coefficients can be converted to the common ones by simply shifting the scale. With the frequency dependence of the attenuation coefficient described by expression (3) (frequency is in kHz and the attenuation is in dB/km), the following values of the parameters were obtained: $a = 0.092$, $n = 1.58$ and $a = 0.080$, $n = 1.59$ for the reception depths 50 and 70 m, respectively. The obtained expressions lead to close values of the attenuation coefficients which, nevertheless, are by a factor of 3–3.5 higher than the mean values typical for the world ocean [11].

The high attenuation coefficients are probably caused by sound scattering from inhomogeneities of thermic nature—maybe, the fine-structure ones. By analyzing a large body of experimental data on the water parameters of the northwestern region of the Pacific Ocean, Rostov [12] arrived at the conclusion that these inhomogeneities can be generated in the regions of sea currents. For such areas, the following values of the mean squared refractive index are typical: $\mu^2 \approx 10^{-5}$–10^{-7}. The author of this paper has no information on such generalizations for the Greenland Sea (or for the region of the Yan Mayen current). On the other hand, according to the calculations performed by Lysanov and Sazonov [13], the attenuation coefficients obtained by us at 800 Hz can be explained by specifying $\mu^2 = 1.4 \times 10^{-7}$. Currently, the fractal nature of the ocean fine-structure inhomogeneities is discussed [14]. The scattering from these inhomogeneities leads to an exponential dependence of the low-frequency attenuation. With certain fractal parameters, the values 1.58–1.59 of the exponent may be obtained, which is in good agreement with the experiment.

Thus, from the analysis of the experimental data, we can conclude that relatively sharp changes in the propagation conditions occurred at the distances 90–110 km from the reception point. A noticeable deformation of the signal was detected at these distances: a sharp termination of the signal was replaced by a smooth decay. Starting from 90–110 km, the t/N–R/N relations obtained for the path part nearest to the reception point began changing—the curve of the sound field decay with distance exhibited a sharp drop (by 3 to 5 dB). These changes can be associated with a relatively sharp bottom rise detected by echo sounding. This coincidence may be regarded as occasional, but one should remember that oceanologists [15, 16] have repeatedly emphasized the relation between the positions of the ocean fronts and the bottom relief. According to oceanographic data [1], at the distances 100–200 km from the receiver, the propagation path crossed the arctic front at an angle of 40°–60°. Unfortunately, our experiments had rather weak hydrological support, and the collected data were insufficient for the determination of the position and parameters of the front zone during the experiment.

Earlier, we reported on a hydrological survey carried out in summer, 80–100 n. miles north of our path, along the parallel 74°30′ [17]. The following parameters of the arctic front were obtained: the width of the front zone is 100 km and the depth of the lower boundary of the front waters is 850 m. According to the pro-

Table 2

f, Hz	Attenuation coefficient (dB/km), the receiver depth is 50 m		Attenuation coefficient (dB/km), the receiver depth is 70 m		Absorption coefficient (dB/km) calculated by formula (1)
	43–443 km	100–443 km	43–443 km	100–443 km	
100	0.0236	0.0107	0.0300	0.0161	0.0006
125	0.0243	0.0135	0.0327	0.0215	0.0009
160	0.0284	0.0175	0.0308	0.0184	0.0015
200	0.0289	0.0177	0.0331	0.0195	0.0023
250	0.0281	0.0223	0.0338	0.0264	0.0035
315	0.0337	0.0320	0.0377	0.0332	0.0053
400	0.0441	0.0371	0.0471	0.0372	0.0082
500	0.0528	0.0436	0.0552	0.0493	0.0120
630	0.0663	0.0611	0.0670	0.0606	0.0175
800	0.0853	0.0761	0.0823	0.0789	0.0250
1000	0.0947	0.0868	0.0949	0.0885	0.0343

files $C(z)$ measured along our propagation path, the main changes took place at the depths 300–400 m. In the middle of the path, the depth of the sound channel axis somewhat decreased (from 50–60 to 30–40 m), the profile $C(z)$ changed, and water interlayers of different temperatures appeared at the depths 50–150 m.

Such sharp changes in the parameters of the water column may be entirely responsible of the sound field features detected in the experiment. From the observed stability in the time structure and shape of the explosion-generated signals received at distances shorter than 100 km, a conclusion can be drawn that there were no significant changes in the propagation conditions within this part of the path. At ranges 100 km and longer, the decrease in the depth of the sound channel axis and the deviation of this depth from the reception horizon led to a decrease in the total duration of the multi-ray signal at the expense of the near-axis rays. The sharp drop in the axis depth caused a change in the sound field level at the distance 95–110 km from the reception point. The water interlayers, which are detected in the middle of the path and produced by mixing of the water masses of different nature in the front zone, give rise to a more complex ray structure of the sound field. This complexity manifests itself in the ray tracing with the use of the measured sound speed profiles.

All aforementioned features were considered theoretically in relation to the influence of the front zones on the sound field formation in the ocean (see, e.g. [18]). We observed these features in the experiment.

To conclude with, we emphasize that the obtained experimental data on the propagation of explosion-generated sound signals in the underwater sound channel of the Greenland Sea may serve to illustrate the main features of the sound field formation in this ocean region.

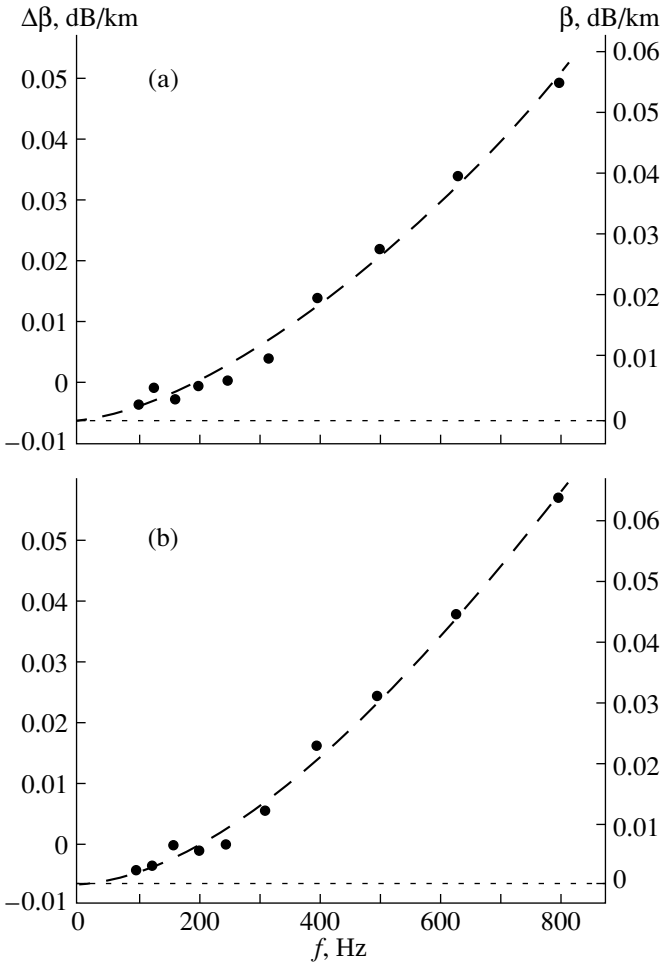

Fig. 8. Experimental values of the differential attenuation coefficient $\Delta\beta$ and its values recalculated to the total attenuation coefficient β for the signals received at the depth (a) 50 and (b) 70 m.

The t/N–R/N relation obtained at the initial "unperturbed" 80-km portion of the path complements the data available on the regional variability of the time structure of the sound field in the underwater sound channel. The changes in this relation, which were observed at longer distances (in the zone of water mixing), characterize the extent to which the polar front affects the sound field formation.

The analysis of the low-frequency sound attenuation in the Greenland Sea reveals the significant effect of sound scattering by the thermic inhomogeneities of the medium, which are produced by mixing of waters of different origin. In contrast to the Black and Mediterranean Seas, this effect is by a factor of 1.5–2.5 greater than that of sound absorption in the sea water (including the low-frequency relaxation processes associated with boron).

It is also worth mentioning that, in spite of the poor hydrological support of the acoustic measurements, a number of experimentally established features can be attributed to the zone of water mixing, which is typical for the polar front of the Greenland Sea. These features include the changes in the decay law and time structure of the sound field and the deformation of the shape of the explosion-generated signal received at the distance 80–90 km from the receiver.

REFERENCES

1. A. Zierhoffer, *Atlantic Ocean and Its Seas* (Panstwowe Wydawnictwo Naukowe, Warszawa, 1970; Gidrometeoizdat, Moscow, 1975).
2. V. F. Sukhovei, *Seas of the World Ocean* (Gidrometeoizdat, Leningrad, 1986).
3. R. A. Vadov, Akust. Zh. **44**, 601 (1998) [Acoust. Phys. **44**, 516 (1998)].
4. M. Ewing and J. Worzel, *Far-Range Sound Propagation* (Geol. Soc. Am., Mem. 27, 1948; Inostrannaya Literatura, Moscow, 1951).
5. R. A. Vadov, Akust. Zh. **40**, 930 (1994) [Acoust. Phys. **40**, 824 (1994)].
6. V. P. Tebyakin, *et al.*, *Raymod52: Basic Software Package for Calculating Sound Fields in a Stratified Inhomogeneous Ocean by the Ray Method* (Report of the Andreev Acoustics Institute, Moscow, 1990).
7. R. A. Vadov, Akust. Zh. **44**, 749 (1998) [Acoust. Phys. **44**, 651 (1998)].
8. K. V. Avilov, M. Yu. Galaktionov, and L. A. Ivanitskaya, in *Proceedings of the UDT-94 Conference, London, 1994*.
9. R. A. Vadov, Akust. Zh. **44**, 318 (1998) [Acoust. Phys. **44**, 265 (1998)].
10. M. J. Sheehy and R. Halley, J. Acoust. Soc. Am. **29**, 494 (1957).
11. R. A. Vadov, Itogi Nauki Tekh., Okeanologiya **3**, 179 (1975).
12. I. D. Rostov, Candidate's Dissertation in Geography (Pacific Inst. of Oceanology, Far East Division, Russ. Acad. Sci., Vladivostok, 1985).
13. Yu. P. Lysanov and I. A. Sazonov, Akust. Zh. **39**, 697 (1993) [Acoust. Phys. **39**, 366 (1993)].
14. Yu. P. Lysanov and L. M. Lyamshev, in *Proceedings of the Fourth European Conf. on Underwater Acoustics, Rome, 1998*, pp. 801–805.
15. K. N. Fedorov, *Physical Nature and Structure of Oceanic Fronts* (Gidrometeoizdat, Leningrad, 1983).
16. Yu. A. Kolmakov, in *All-Union Seminar "Oceanological Fronts of Northern Seas: Characteristics, Methods of Investigation, and Models", Moscow, 1989*, p. 15.
17. A. O. Shnaikher and V. N. Moretskiĭ, Okeanologiya (Moscow) **4**, 267 (1964).
18. E. C. Shang and Y. Y. Wang, J. Acoust. Soc. Am. **102**, Part 2, 3149 (1997).

Translated by E.A. Kopyl

Acoustical Physics, Vol. 46, No. 1, 2000, pp. 49–55. Translated from Akusticheskiĭ Zhurnal, Vol. 46, No. 1, 2000, pp. 60–67.

Internal Conical Refraction of Elastic Waves under Magnetic Field in Tungsten and Molybdenum

K. B. Vlasov and A. B. Rinkevich

Institute of Metal Physics, Ural Division, Russian Academy of Sciences,
ul. S. Kovalevskoĭ 18, Yekaterinburg, 620219 Russia
e-mail: rin@imp.uran.ru

Received December 22, 1998

Abstract—Measurements of the amplitude and phase of a beam of transverse ultrasonic waves propagating in tungsten and molybdenum crystals in the presence of magnetic field are performed. Under the conditions of the Doppler-shifted acoustic cyclotron resonance, a magnetically induced contribution to the phase of oscillations is observed, this contribution being even with respect to the magnetic field. Such a result testifies to the presence of the internal conical refraction that is caused by the magnetic field in the crystals under study. *© 2000 MAIK "Nauka/Interperiodica".*

This paper is devoted to the study of magnetoacoustic phenomena that accompany the propagation of ultrasound along the threefold symmetry axis of a cubic crystal magnetized along this axis and in an elastically isotropic magnetized crystal. In these two cases, the natural modes of the crystals correspond to circularly polarized waves. However, the plane perpendicular to the threefold axis is no mirror plane. This fact gives rise to the existence of the internal conical refraction of ultrasound (ICR), which manifests itself in the deflection of the energy flux from the wave normal toward the wavefront. One can expect that the internal conical refraction should also occur at the expense of the reduction in the crystal symmetry under magnetic field.

The aim of our studies was to obtain experimental evidence for the existence of the ICR induced by magnetic field. Since the expected deflection of the energy flux under the magnetic field was small, the best way to detect the presence of this type of conical refraction was to use an indirect method and to perform the measurements in resonance conditions. For this purpose, we observed the Doppler-shifted acoustic cyclotron resonance which occurs in ultrasonic beams with nonplanar wavefronts.

The ICR was observed earlier in the absence of magnetic field [1]. The effect of magnetic field on the direction of the energy flux was studied theoretically [2] for the case of wave propagation along the fourfold axis under a magnetic field directed normally to this axis. The specific features of the Doppler-shifted acoustic cyclotron resonance under the conditions of conical refraction were briefly reviewed in our earlier paper [3]. If we assume that an elastic wave is a plane harmonic one, the ICR will have little effect on the Doppler-shifted acoustic cyclotron resonance. Therefore, in the earlier experimental studies of the Doppler-shifted acoustic cyclotron resonance for the case of ultrasonic wave propagation along the [111] axis, the effect of the ICR was not observed [4–6]. The only researchers who mentioned the effect of the ICR were Jericho and Simpson [7]. They presented the results of the experiments on the ultrasonic wave propagation in a copper single crystal the length of which far exceeded its diameter. Because of the large angle of deflection of the energy flux (31° for copper), the beam emerged at the lateral surface of the crystal.

Our experiments were performed under the conditions of the ICR, but the beam did not touch the lateral surface of the crystal. The material under study was molybdenum. In molybdenum crystals, the angle of deflection of the energy flux is relatively small, and a considerable effect of magnetic field can be expected. The second object of our study was an elastically isotropic tungsten crystal. In such crystals, the ICR is virtually absent in the absence of magnetic field.

Specimens of approximately cylindrical shape with diameter 8–9 mm and length about 5 mm were cut out of molybdenum single crystals with the electric resistance ratio $\beta \equiv \rho_{273}/\rho_{4.2} = 29000$ and of tungsten single crystals with $\beta = 50000$. The normal to the plane surfaces was parallel to the [111] axis with an error not exceeding 1°. The error in the orientation of a specimen in magnetic field did not exceed 0.8°.

The acoustic measurements were performed at the frequencies $f = 40$–180 MHz. Using the technique proposed earlier [8], we determined the magnetically induced real $Re\Delta q^{\pm}$ and imaginary $Im\Delta q^{\pm}$ additions to the wave vector q for the natural waves of circular polarization (q is the wave vector in the absence of magnetic field). We also measured the rotation angle of the polarization plane φ. In an inclined magnetic field, the measurements were performed by the method described by Rinkevich [9].

1063-7710/00/4601-0049$20.00

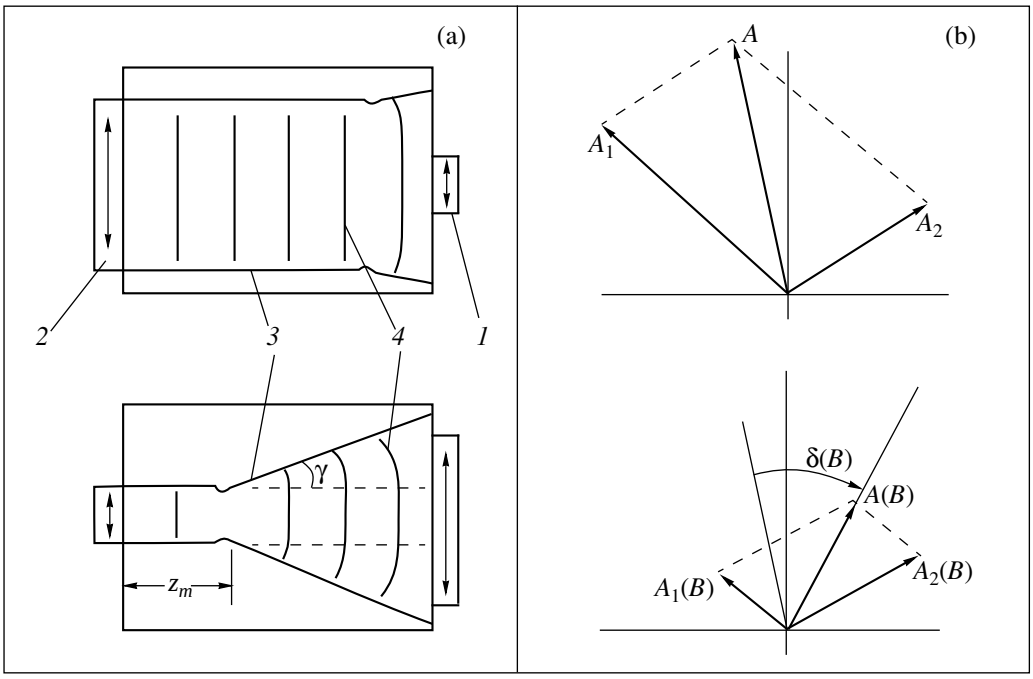

Fig. 1. (a) Schematic diagram of the experiment with transducers of different dimensions and (b) the interference of the signals $\vec{A}_1$ and $\vec{A}_2$ from two parts of the receiving transducer (top) in the absence and (bottom) in the presence of magnetic field. (a) The schematic diagram shows (*1*) the receiving transducer; (*2*) the transmitting transducer; (*3*) the beam; and (*4*) the wavefront.

For a beam with a nonplanar wavefront, the measured values were the insertion loss $L^{\pm} = Im(\Delta q^{\pm})z$ and the phase $\delta^{\pm} = Re(\Delta q^{\pm})z$ of elastic displacements, both quantities being averaged over the cross-section of the receiving transducer (here, z is the acoustic path length). The transducers were made of lithium niobate plates. Some of the experiments were performed with the transmitting and receiving transducers of different dimensions: one of them, transducer *1*, had the diameter 2.2 mm, and the second one, transducer *2*, was rectangular in shape with the dimensions 3×4 mm (Fig. 1a).

If the receiving transducer is smaller than the transmitting one (the upper figure), it receives the central part of the beam. As the distance of ultrasound propagation increases, the shape of the wavefront progressively deviates from a plane. The peripheral part of the beam becomes more distorted than its central part.

The experimental dependence of the insertion loss $L = L^{+} \approx L^{-}$ in molybdenum on the magnetic induction B exhibited some resonance peaks that were approximately identical in amplitude, shape, and positions for the clockwise and counterclockwise polarized waves. In similar experiments carried out for tungsten [6], the A and B resonances were observed; these resonances were interpreted as the manifestation of a doppleron-phonon resonance. We restricted our studies to weaker magnetic fields in which the changes in the parameters of elastic waves are caused mainly by the C resonances.

To verify the assumption that this resonance is a Doppler-shifted one rather than a doppleron-phonon resonance, we measured the dependences of the insertion loss on the magnetic induction at several frequencies (Fig. 2a). With increasing frequency, the positions of the resonance peaks on the magnetic field axis moved linearly toward higher magnetic fields (Fig. 2b). The dependence of the quantity α_{max}/f (α_{max} is the loss coefficient for the highest peak) on the parameter $(f\beta)^{1/2}$ proportional to $(ql)^{1/2}$ (l is the free path of electrons) is shown in Fig. 2c. For both molybdenum and tungsten, this dependence is a linear one. Such properties are characteristic of a Doppler-shifted acoustic cyclotron resonance, and the presence of a peak at $L^{\pm}$ indicates that the dominant mechanism of the interaction between the conduction electrons and ultrasound is related to the deformation of the material. The presence of almost identical peaks at L^{+} and L^{-} and the linear frequency dependence of the positions of the resonance peaks testify to the absence (or weakness) of the doppleron-phonon interaction component in the C resonances.

Having obtained the experimental data on the nature of the C resonances in molybdenum and tungsten, we consider the results of our measurements of the signal phase. Figure 3 presents the dependence of the phase $\delta^{\pm}$ of clockwise and counterclockwise polarized elastic displacements on the magnetic induction B near the C resonance of number $n = 1$ for different distances of propagation. One can notice the presence of the reso-

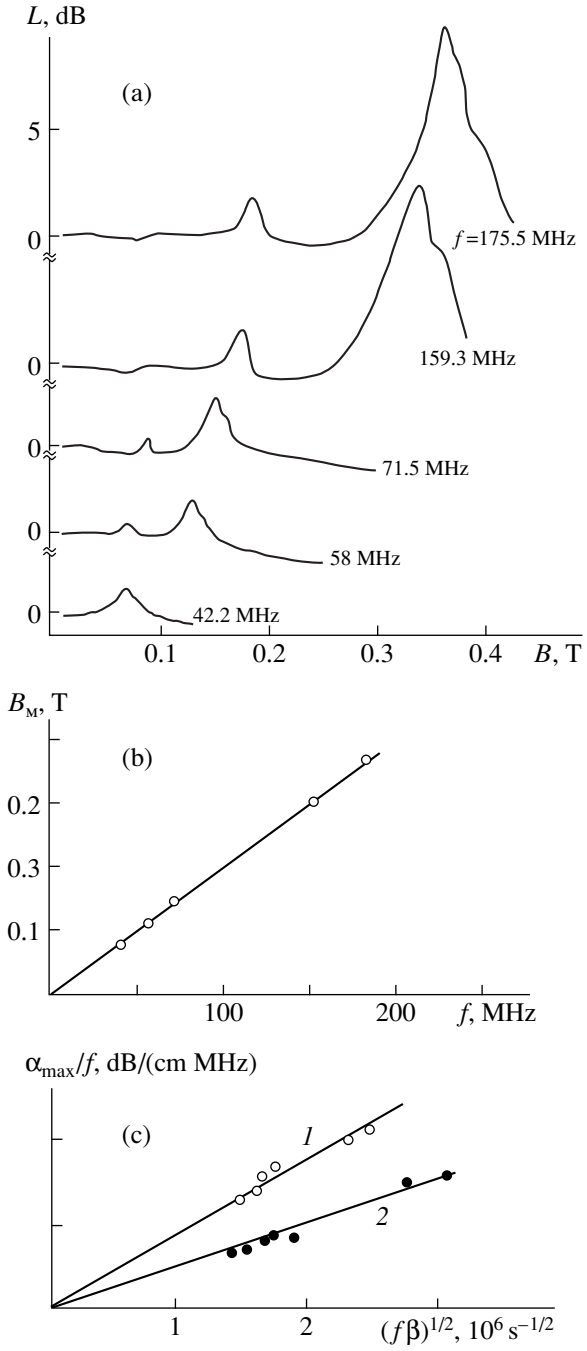

Fig. 2. (a) Doppler-shifted acoustic resonance in molybdenum at $q//B//[111]$; (b) magnetic induction corresponding to the *C* resonance as a function of the wave frequency; and (c) dependence of the ratio of the maximum absorption value to frequency α_{max}/f at the *C* resonance conditions on the parameter $(f\beta)^{1/2}$: (*1*) molybdenum and (*2*) tungsten.

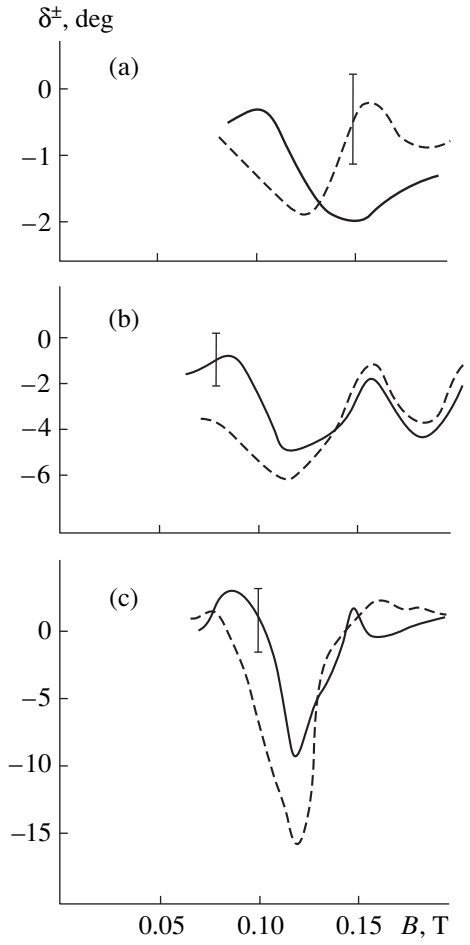

Fig. 3. Phase variations at the receiving transducer near the *C* resonance: solid curves correspond to δ^+ and dashed curves correspond to δ^-. The frequency is $f = 59.7$ MHz and the distance of ultrasound propagation is z = (a) 0.48, (b) 1.44, and (c) 2.4 cm.

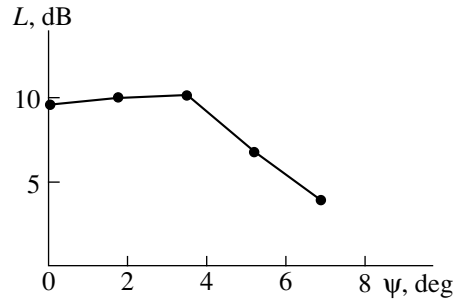

Fig. 4. Maximum value of the insertion loss under the *C* resonance conditions as a function of the angle ψ between the magnetic field direction and the [111] axis.

nance contributions of the same sign to the phases of both circular polarizations near the magnetic fields corresponding to the maximum absorption. Since a reversal of B is equivalent to the change of sign of the polarization of natural waves, + and –, it is reasonable to interpret this effect as an even contribution to the phase, i.e., a contribution that is even with respect to magnetic field.

For plane waves, the contribution to the phase $\delta^\pm = (Req^\pm - Req)z$ is proportional to the variation of the real part of the mode wave number. According to the theory of the Doppler-shifted acoustic cyclotron resonance

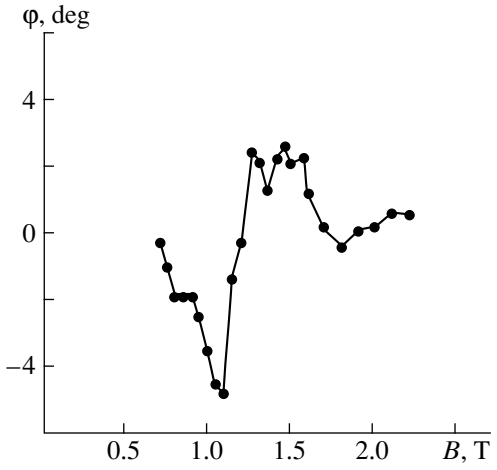

Fig. 5. Angle of rotation of the polarization plane near the *C* resonance in molybdenum: $f = 59.7$ MHz and $z = 1.4$ cm.

[10, 11], the behavior of the real part of the wave vector should differ from that shown in Fig. 3; namely, the theory predicts the relation $Re(q^+ - q) \approx -Re(q^- - q)$. In the vicinity of the Doppler-shifted acoustic cyclotron resonance, this relation is satisfied in both tungsten and molybdenum [12] at $q//B//[100]$ in similar experimental conditions but in the absence of the ICR.

The presence of the even contribution to the phase $\delta^\pm$ of the circular polarizations in the vicinity of the Doppler-shifted acoustic cyclotron resonance cannot be explained by the errors in the setting of the experiment, e.g., nonparallel or nonplanar end surfaces of the samples. Deviations of the vectors q and B from the [111] axis may in principle lead to the propagation of linearly polarized waves instead of the circularly polarized ones. However, the results presented in Fig. 3 cannot be interpreted as changes in the phase velocities of normal waves. The curves in Figs. 3a, 3b, and 3c were obtained for the distances of ultrasound propagation $z =$ 0.48, 1.44, and 2.4 cm. If we assume that the contribution to the phase is caused by the variations in the wave velocities, we should expect the aforementioned curves to be similar in shape with the only difference being in the scale along the ordinate axis. However, this is not the case. The even contribution to the phase sharply increases with increasing distance of propagation. This fact suggests the conclusion that the wavefront arriving at the receiving transducer is not a plane one. The factors that may be responsible for the curvature of the wavefront are the diffraction phenomena and the ICR.

Our experiments showed that the dependence of the maximum value of the insertion loss on the angle ψ lying between q and B is substantial in the vicinity of the *C* resonance (Fig. 4). The measurements of the rotation angle of the polarization plane φ at $q//B//[111]$ (Fig. 5) showed that the extremum values of this angle are much less than at $q//B//[111]$ [12, 13] in similar conditions. This difference was also observed in the earlier measurements of the rotation angle of the polarization plane in tungsten and aluminum single crystals [4, 5].

Similar measurements were performed on tungsten specimens. Their shape and dimensions were close to those of the molybdenum specimens, and the same transducers were used. Since tungsten is an elastically isotropic material, the ICR should be absent in it at $B = 0$ (because the elastic modulus is $c_{14} \approx 0$), while the diffraction phenomena should be approximately the same as in molybdenum. For tungsten, the results of measurements are shown in Figs. 6 and 7, where $f = 56$ and 172 MHz, respectively. One can see that at the lower frequency 56 MHz, the experimental dependences $L^\pm(B)$ and $\delta^\pm(B)$ obtained for tungsten (in contrast to molybdenum) agree well with the dependences predicted by the theory for the case of a small magnetically induced contribution to the ICR. This case corresponds to the relation $\delta^+ \approx -\delta^-$, and in these conditions, a nearly plane wavefront propagates in tungsten. With increasing frequency, the even contribution to $\delta^\pm$ becomes more evident (see Fig. 7).

The described experiments reveal the resonance dependence of the wavefront shape of a transverse wave on the magnetic field strength at $q//B//[111]$. The factors that may be responsible for the deviation of the wavefront from a plane are the diffraction phenomena and the ICR.

The measurements carried out with tungsten specimens show that, as the frequency increases, the even contribution to $\delta^\pm$ begins to manifest itself and grow. This does not correlate with the diffraction mechanism of the wavefront distortion: with increasing frequency, the angle of the diffraction divergence of the beam decreases. The estimated value of the angle of the diffraction divergence of the beam is $\gamma \cong \lambda/2a$, where λ is the wavelength and a is the transmitter radius. For the conditions of our experiment, this formula yields the value that is too small ($\gamma \sim 0.5°$) to noticeably affect the insertion loss. Judging from the data of Fig. 4, considerable changes of the insertion loss can be observed when the aforementioned angle exceeds 4°. Therefore, below, we analyze the possible effect of the ICR on the characteristics of the ultrasonic beam.

The effect of magnetic field can be described on the basis of some qualitative inferences. In the case of a nonplanar wavefront, the rays at the center of the beam are directed along the magnetic field B and the [111] axis of the crystal; the rays at the beam periphery are deflected from B. Let the central rays produce the signal A_1 at the receiving transducer, and the peripheral rays produce the signal A_2. A phase shift exists between these groups of rays (see top of Fig. 1b). If these rays are absorbed in the magnetic field in different ways, their interference at the receiving transducer will form an even contribution $\delta(B)$ to $\delta^\pm$ (see bottom of Fig. 1b),

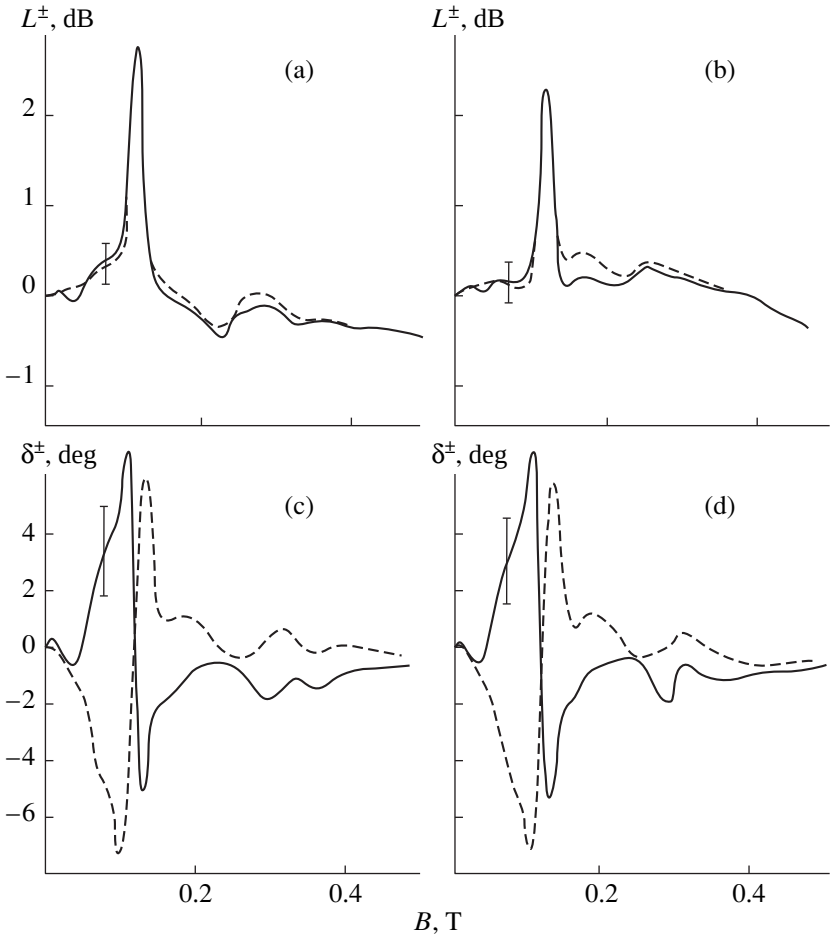

Fig. 6. Dependences of the (a, b) insertion loss coefficient $L^{\pm}$ and (c, d) phase $\delta^{\pm}$ of oscillations on the magnetic field near the *C* resonance in tungsten: f = 56 MHz; the transmitter and the receiver are transducers (a, c) *2* and *1*, respectively, and (b, d) *1* and *2*, respectively.

because the absorption under the conditions of the Doppler-shifted acoustic cyclotron resonance is an even function of the magnetic field at $\omega\tau \ll 1$ (ω is the circular frequency of the wave and τ is the relaxation time of electrons). From the above, it follows that an even contribution to the phase may arise only near the absorption peaks.

Waterman and Khatkevich [14, 15] mentioned a phenomenon that necessarily accompanies the ICR in an ultrasonic beam of finite dimensions. The polarization of oscillations is different in different points of the beam cross-section, while, in a given point, it is fixed. Therefore, one should expect that the rotation angle of the polarization plane under the magnetic field will be less in the presence of the ICR in the ultrasonic beam, as compared to the case without the ICR. This fact was confirmed in our experiments. Let us estimate the angle of the ICR under the conditions of the Doppler-shifted acoustic cyclotron resonance. The theory of ICR for plane waves at $q//B$ is described in our previous paper [16]. In a cubic crystal under a magnetic field, the components of the energy flux vector $P_i^{\pm}$ are as follows:

$$P_1^{\pm} = \mp\omega^2 c'_{14}\sqrt{\frac{\rho}{c'_{44} \pm c''_{45}}}(u^{\pm})^2 \sin 2\phi,$$

$$P_2^{\pm} = -\omega^2(c'_{14} \pm c''_{25})\sqrt{\frac{\rho}{c'_{44} \pm c''_{45}}}(u^{\pm})^2 \sin 2\phi, \qquad (1)$$

$$P_3^{\pm} = \omega^2\sqrt{\rho/(c'_{44} \pm c''_{45})}(u^{\pm})^2,$$

where $c_{ij} = c'_{ij} + ic''_{ij}$ represents the complex elastic modulus, ρ is the density of the metal, and $u^{\pm}$ is the amplitude of elastic displacements. The phase angle $\phi = qz - \omega t$ is measured with respect to the $[11\bar{2}]$ axis. Formulas (1) mean that with time the vectors of the instant energy flux $P^{\pm}$ describe conic surfaces. The bases of the cones are ellipses which differ for the waves of the "+" and "–" polarizations. If the magnetic field is zero, the imaginary components of the moduli

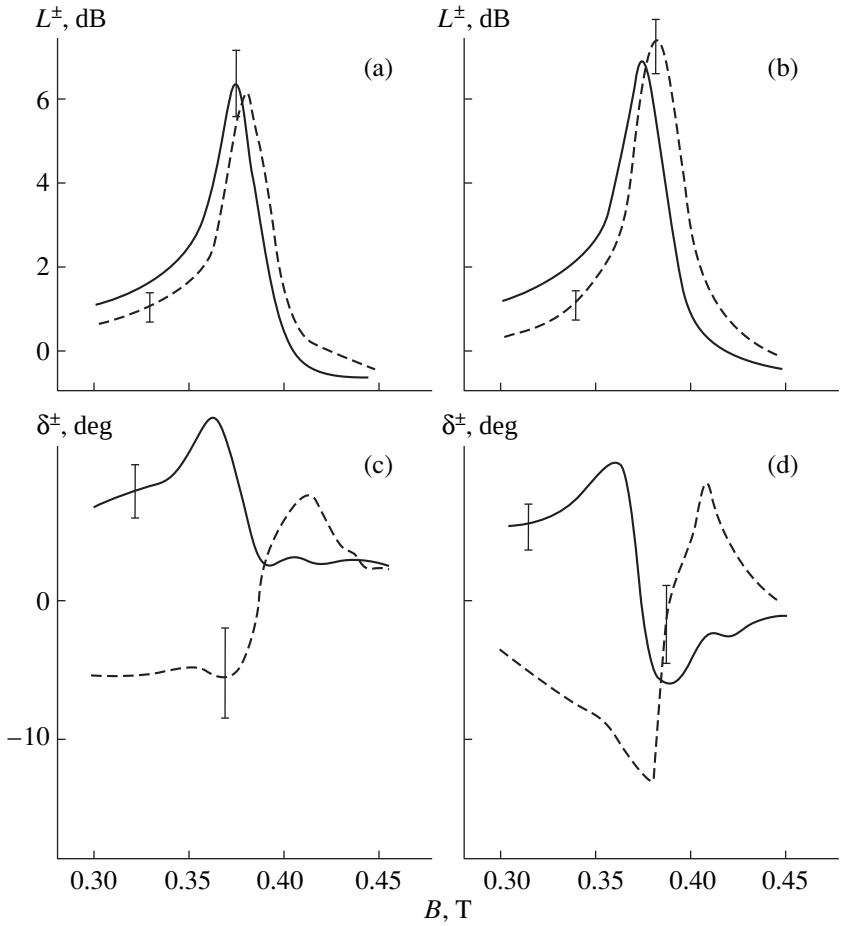

Fig. 7. Same as in Fig. 6 for f = 172 MHz.

c''_{25} and c''_{45} are zero. The cones of the ICR become circular and identical for both circular polarizations.

If c'_{14} is zero, which occurs in an elastically isotropic crystal, we obtain $P_1^{\pm} = 0$, and the cone of the ICR degenerates into a plane sector. Within the half-cycle of oscillations, a full cycle of the oscillations of the vector of the energy flux is completed.

To obtain the estimates, we need to know the values of the additions to the elastic moduli that appear under the conditions of the Doppler-shifted acoustic cyclotron resonance. The relative variation of the circularly polarized elastic moduli $\Delta c^{\pm}/c_{44}$ is coincident in order of magnitude with $Im\Delta q^{\pm}/q = L^{\pm}/zq$. From the data presented in Figs. 2, 6, and 7, we obtain the estimate $|\Delta c^{\pm}/c_{44}| \sim 10^{-4}$, and this value increases with increasing frequency of the ultrasonic wave. According to formulas (1), the magnetically induced addition to the angle of deflection $\Delta\theta$ is equal to $\Delta\theta = \Delta c_{14}/c_{44}$ when the angle of the ICR in the absence of magnetic field θ is small, $\theta \ll 1$. If the additions to the moduli $\Delta c^{\pm}$ and c_{14} are of the same order of magnitude, we obtain the addition for tungsten $\Delta\theta \sim 0.3°$. This estimate corresponds to the case of plane ultrasonic waves. Since the experiments are performed with a beam of finite dimensions, one should expect that a combined effect of diffraction and ICR will give rise to rays with greater angles of departure from the acoustic axis. The data reported in the literature on the distribution of the elastic field in the presence of ICR confirm this assumption. For example, in the studies of the ICR in a germanium crystal with the ICR angle $\theta = 14°$ [17], the angle of the diffraction divergence was estimated as $\gamma \cong \lambda/2a$ 1°. However, the experiments revealed elastic oscillations with the angles of deflection up to 20°, which far exceeds the quantity $\theta + \gamma$.

Now, we estimate the effect of the factors accompanying the divergence of the beam on the results of the experiments in magnetic field. For this purpose, we use the theory developed for the beams of electromagnetic waves of circular polarization [18, 19]. In our case, the increase in the beam radius is insignificant. Its relative increase S/S_0 with distance z is $S/S_0 = (1 + D^2)^{1/2}$, where $D = 2z/qa^2$, which at z = 2 cm, $q = 10^3$ cm^{-1}, and a = 0.1 cm makes several percent. The results of our measurements of the insertion loss in molybdenum are more strongly affected by the curvature of the wave-

front. The shape of the equiphase surface varies from a plane at $z \longrightarrow 0$ to a part of an ellipsoid of revolution at $z \gg z_m$, where z_m is the size of the near zone of radiation, $z_m = a^2/\lambda$. At $a = 0.1$ cm and $\lambda = 6 \times 10^{-3}$ cm, the distance z_m is approximately 2 cm. The phase difference $\Delta\varphi$ between the areas $r = 0$ and $r = a$ at the receiving transducer is determined by the expression

$$\Delta\phi = a^2/2\lambda R, \qquad (2)$$

where R is the wavefront curvature radius, $R = a\left(\frac{1 + D^2}{D}\right)^{1/2}$. Substituting the values of a, λ, and R, we obtain $\Delta\phi \sim 30°$. Such a phase difference is sufficient for the interference of signals, which leads to an even contribution to the phase with respect to magnetic field (see Fig. 1b).

Thus, on the basis of the analysis of experimental data on the insertion loss and the phase of circularly polarized elastic waves for different frequencies, different distances of acoustic propagation, and different dimensions of the transmitting and receiving transducers, as well as on the basis of theoretical estimates, it was found that in cubic crystals a magnetically induced contribution to the ICR is observed in compliance with the theoretical predictions [16]. This contribution exists in the case of the magnetization of the crystal along the [111] threefold axis and the propagation of transverse ultrasonic waves in the same direction.

The magnetically induced contribution to the ICR was observed in an elastically isotropic tungsten crystal (in which the ICR is absent because of the crystallographic anisotropy) and in an anisotropically elastic molybdenum crystal. The effect of magnetic field on the ICR was observed under the conditions of the Doppler-shifted acoustic cyclotron resonance, and this effect manifested itself in the resonance distortion of the wavefront of the ultrasonic beam.

ACKNOWLEDGMENTS

This work was supported by the Russian Foundation for Basic Research and the German Research Society (grant no. 98-02-04094).

REFERENCES

1. J. de Klerk and M. J. P. Musgrave, Proc. Phys. Soc. **68** (422B), Part 2, 81 (1955).
2. V. V. Filippov, Izv. Akad. Nauk Bel. SSR, Ser. Fiz.-Mat. **1**, 109 (1978).
3. K. B. Vlasov and A. B. Rinkevich, in *Proceedings of XI All-Union Acoustical Conference, Moscow, Russia 1991*, Part B, pp. 11–14.
4. S. W. Hui and J. A. Rayne, J. Low Temp. Phys. **12** (1/2), 49 (1973).
5. S. W. Hui and J. A. Rayne, J. Phys. Chem. Solids **33**, 611 (1972).
6. L. P. Volkova, L. T. Tsymbal, and A. N. Cherkasov, Fiz. Nizk. Temp. (Kiev) **11**, 290 (1985) [Sov. J. Low Temp. Phys. **11**, 158 (1985)].
7. M. H. Jericho and A. M. Simpson, Phil. Mag. **17** (146), 267 (1968).
8. V. V. Gudkov and K. B. Vlasov, Fiz. Met. Metalloved. **46**, 254 (1978).
9. A. B. Rinkevich, Metrologiya, No. 8, 36 (1982).
10. T. Kjeldaas, Phys. Rev. **113**, 1473 (1959).
11. J. Mertsching, Phys. Status Solidi **37**, 465 (1970).
12. K. B. Vlasov and A. B. Rinkevich, Fiz. Met. Metalloved. **54**, 668 (1982).
13. K. B. Vlasov, A. B. Rinkevich, and N. A. Zimbovskaya, Fiz. Met. Metalloved. **52**, 517 (1981).
14. P. C. Waterman, Phys. Rev. **113**, 1240 (1959).
15. A. G. Khatkevich, Kristallografiya **31**, 629 (1988) [Sov. Phys. Crystallogr. **31**, 371 (1988)].
16. K. B. Vlasov and A. B. Rinkevich, Akust. Zh. **41**, 67 (1995) [Acoust. Phys. **41**, 57 (1995)].
17. V. I. Anisimkin and A. I. Morozov, Fiz. Tverd. Tela (Leningrad) **17**, 3006 (1975) [Sov. Phys. Solid State **17**, 1994 (1975)].
18. A. Yu. Ardashev, V. A. Kashin, and G. V. Skrotskiĭ, Zh. Éksp. Teor. Fiz. **55**, 869 (1968) [Sov. Phys. JETP **28**, 451 (1968)].
19. M. B. Vinogradova, O. V. Rudenko, and A. P. Sukhorukov, *Theory of Waves* (Nauka, Moscow, 1979).

Translated by E.M. Golyamina

Acoustical Physics, Vol. 46, No. 1, 2000, pp. 56–61. Translated from Akusticheskiĭ Zhurnal, Vol. 46, No. 1, 2000, pp. 68–74.

The Effect of Water Stratification on the Spatial Fine-Structure Stability of the Sound Field Reflected from the Ocean Bottom

V. I. Volovov, A. I. Govorov, V. S. Gostev, and L. N. Nosova

Andreev Acoustics Institute, Russian Academy of Sciences,
ul. Shvernika 4, Moscow, 117036 Russia
e-mail: bvp@akin.ru

Received December 24, 1998

Abstract—The effect of the water stratification on the sound field reflected from the ocean bottom at normal incidence is considered in view of the new method of acoustic bottom mapping and its practical-purpose applications. The amplitude and phase distortions of the bottom-reflected signals received by a multielement planar array positioned horizontally near the ocean surface are estimated. Experimental data obtained on the fine (interference) spatial structure of the reflected sound field in deep ocean are presented.

Recently, the new methods of sea-floor mapping based on the use of the horizontal variability of the sound field reflected by the ocean bottom at normal incidence were proposed. The practical-purpose applications of these mapping methods in acoustics, navigation, and oceanology were also considered [1–6].

In general, depending on the specific situation, the maps may be either variable (synoptic ones) or stable (bathymetric ones) in time. The applications of the proposed methods (navigation, sea-floor surveying, searching for mineral resources) imply the stability of the obtained data, at least within the time interval required for solving the specific problem (comparison of two versions or portions of the maps). The parameters of the reflected signals, which serve as the starting data for acoustic mapping, are governed by the insonified bottom area (roughness of the micro- and mesorelief, sea-floor inhomogeneities), and this area is stable on the geological time scale. Hence, the acoustic parameters must be stable as well, their variability being solely caused by disturbing factors that act in the real ocean environment. The effects of these factors determine the feasibility and the quality of the acoustic sea-floor mapping. Therefore, it is advantageous to consider some of the aforementioned factors, namely, the parameters of the water column, that influence the most sensitive fine (interference) structure of the reflected sound signals. To obtain approximate estimates, we use a simplified model of the water column, which includes isotropic small-scale turbulent inhomogeneities of the sound speed, fine-structural inhomogeneities, mesoscale lenses, and general changes in the sound speed profile [7–9].

The turbulent small-scale inhomogeneities of the sound speed, or the microstructure of the water column, have scales less than 1 m. The field of the sound speed (or that of the refractive index) is nearly isotropic on these scales. The microstructural inhomogeneities are mainly located in the upper mixed layer of the ocean, 50–100 m in thickness, where they are represented in the form of clouds produced by breaking of the surface and internal waves [10, 11]. The sound speed fluctuations caused by the microstructure are characterized by the rms deviations of the refractive index, $(\overline{\mu^2})^{1/2}$, up to 5×10^{-5}–10^{-4} in the subsurface water layer, and, on average, they are by an order of magnitude less at deeper horizons [7].

The fine-structural inhomogeneities are strongly elongated in the horizontal direction and highly anisotropic, with vertical scales of several meters or several tens of meters and with the anisotropy coefficients (i.e., horizontal-to-vertical scale ratios) of 10^2–10^4. Their life times are several hours to several days: the larger the scale the longer the time. The fine-structural inhomogeneities are mainly located within the discontinuity layer and the main termocline, at depths of ~100 to ~1000 m. The maximum values of the parameter $(\overline{\mu^2})^{1/2}$, up to 5×10^{-4}–10^{-3}, correspond to the maximum sound speed gradient (the discontinuity layer). At deeper horizons, particularly, deeper than the axis of the underwater sound channel, the fine structure usually degenerates [7, 9].

The general changes in the sound speed profile are different for different ocean regions, because they depend on the seasonal variability of the water bulk and probable intrusions of foreign waters with different parameters, particularly, in the form of lenses that are caused by the synoptic eddies and meandering global

1063-7710/00/4601-0056$20.00

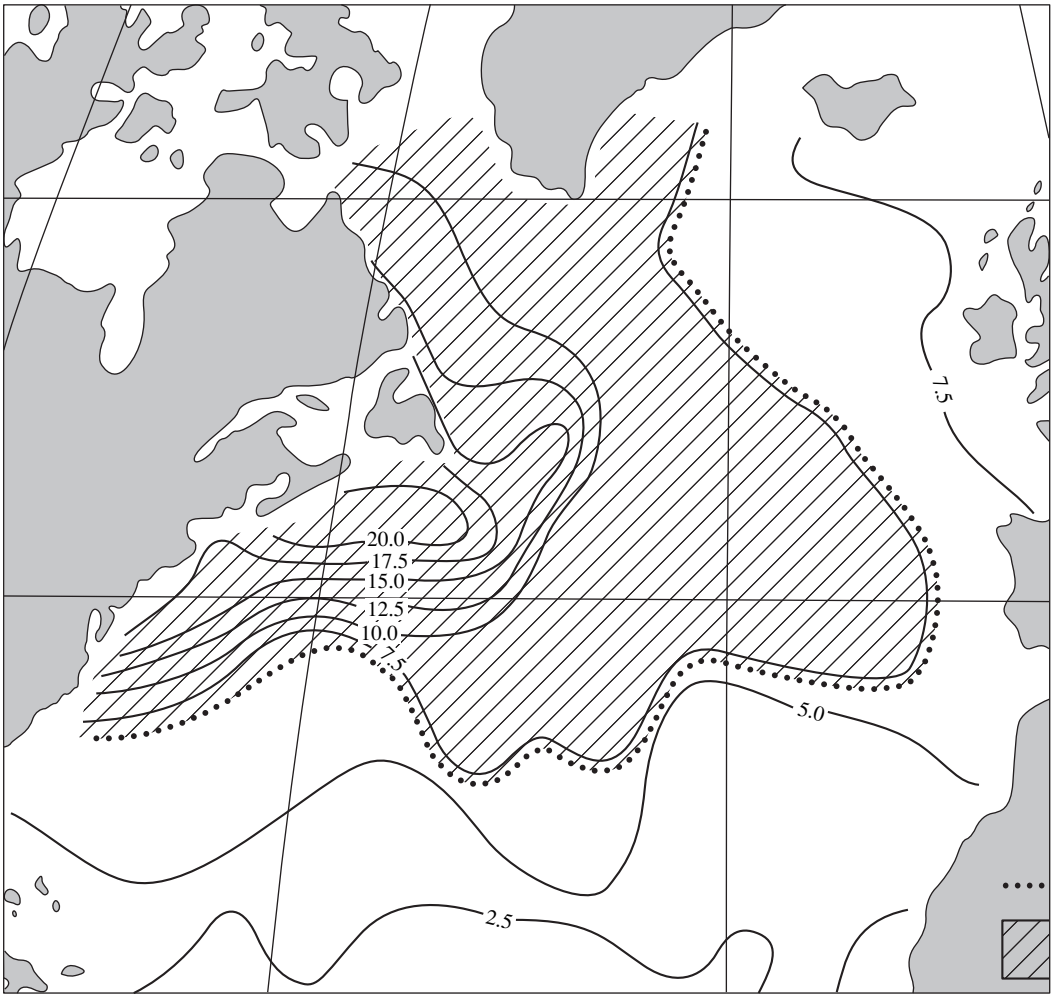

Fig. 1. Seasonal standard deviation of the surface sound speed (m/s) for the North Atlantic.

water currents. According to the generalized data [7, 12], the seasonal variability of the sound speed profile is mainly characteristic for moderate latitudes and subtropical regions. The highest seasonal changes, up to 15–20 m/s on average, naturally occur at the sea surface. This fact is illustrated by Fig. 1, which presents the standard deviation of the sound speed (in m/s) for the North Atlantic [12]. The maximum deviations correspond to the region where the Labrador Current and Gulf Stream converge. At the same time, the deviations are low for the near-equatorial zone. As the depth increases, the seasonal deviation monotonically decreases, by an order of magnitude, or more at the depths 300–500 m.

The variability of the sound speed profile, which is caused by the lenses in the Atlantic Ocean, is most pronounced in its north-western region where these variations are comparable with the seasonal ones. The sound speed disturbances caused by passages of the lenses, several tens of kilometers in size and several hundreds of meters in thickness, reach a value of 15–20 m/s. For instance, a lens observed in the region where the Mediterranean waters intrude into the Atlantic Ocean had a horizontal size of about 70 km and a thickness of ~600 m; the maximum disturbance of the sound speed, up to 18 m/s, corresponded to a depth of 950 m [13].

With the specified model of the water column, we may conclude that distortions of the sound signal reflected by the bottom and received near the ocean surface may have the following three forms: amplitude fluctuations caused by sound propagation within the water column; phase fluctuations of the elementary signals scattered by individual bottom areas under the influence of the column inhomogeneities, including the fine-structural ones and lenses; and changes in the phases of the elementary scattered signals because of the distortions of the sound speed profiles.

To consider the first mentioned factor, we compare the variation coefficient η of the signal amplitude received upon the bottom reflection and propagation through the water column with the variation coefficient η_1 caused solely by the reflection process. Earlier [3], it

was found that, under some realistic assumptions, these values may be specified as

$$\eta \cong (\eta_1^2 + \eta_1\eta_2 + \eta_2^2)^{1/2}, \quad (1)$$

where η_2 is the amplitude variation coefficient governed by the signal propagation through the inhomogeneous water column.

The estimations show that the propagation-caused amplitude fluctuations may be neglected, if the total variation coefficient is by a factor of 2.5–3 higher than the value η_2 caused by the propagation, and in this case $\eta \approx \eta_1$. According to the generalized experimental data [3], in the deep ocean, the amplitude variation coefficient of the bottom-reflected signal depends on the transmitted frequency and on the geomorphological zone of the ocean. For example, at the frequencies 2 and 10 kHz, the variation coefficient is 0.44–0.54 and 0.46–0.85, respectively, for highly rugged sea-floor areas; 0.32–0.46 and 0.49–0.58 for moderately rugged ones; and 0.13–0.34 and 0.31–0.47 for weakly rugged areas.

Let us estimate the amplitude variation coefficient η_2. If sound propagates in a randomly inhomogeneous medium over a distance L, and $L \gg L_0^2\lambda^{-1}$ (the usual case), the amplitude fluctuations of the reflected signal are known [8] to obey the following formula:

$$\eta_2 = [(\overline{\mu^2})k^2L_0L]^{1/2}, \quad (2)$$

where k is the wave number, L_0 is the spatial correlation length of the inhomogeneities, and λ is the wavelength.

By specifying $(\overline{\mu^2})^{1/2} = 10^{-4}$, $\lambda = 15$ cm, $L_0 \sim 1$ m, and $L \sim 100$ m, in view of the two-way sound transmission through the water layer, we obtain $\eta_2 = 0.04$, which is much less than the aforementioned value—the fact that has been experimentally confirmed. In particular, we [3] presented the experimental estimates for the depth of the amplitude fluctuations of the direct signal received in the subsurface layer of the deep ocean, for the vertical distance 250 m between the source and receiver, at a frequency of 12 kHz ($\lambda = 12.5$ cm). The amplitude variation coefficient proved to be less than 0.15, this value being overestimated because of the influence of other factors (roll and pitch of the transmitter and receiver, instabilities in the electronic circuits, etc.—see [3] for details). At the same time, the amplitude variation coefficient of the bottom-reflected signal was higher than 0.50. Similar data were obtained by us for the 4000-m reception depth.

Thus, the experimental data on the amplitude variability of the sound signals agree well with the theoretical estimates, the condition of the insignificance of the changes in the water-column parameters (this condition is determined by equations (1) and (2)) is satisfied, and, hence, the amplitude fluctuations of the reflected signal can be attributed to nothing but the reflection process [3]. Note that the above estimation does not imply a specific mechanism for the amplitude-phase interference forming the signal reflected by the real ocean bottom. The obtained estimates only show that the amplitude of the propagating signal remains stable with respect to the water inhomogeneities. The effect of other types of inhomogeneities on the amplitudes of individual components of the resultant signal can obviously be treated as small for the plane-layered ocean (we assume that such is the structure of the ocean under study), because no reflections by the water-layer boundaries arrive at the receiver in this case.

To proceed with considering the effect of water stratification on the bottom-reflected signal received near the ocean surface, we traditionally suppose that it is formed as a superposition of elementary signals scattered by the bottom roughness (irregularities). The situation is schematically illustrated in Fig. 2 for a case of two scattering bottom features [3]. The resultant received signal is evidently determined by the amplitudes of the two reflections and by their phase difference $\Delta\varphi = \varphi_1 - \varphi_2$, which is determined by the difference in the lengths of the paths S*1*R and S*2*R, as well as by the fluctuations of the refractive index on these paths. It is also evident that, even if the amplitudes of individual components remain unchanged (as above), the resultant reflected signal will change if the variation of the phase difference $\delta(\Delta\varphi)$ is considerable.

To consider the effect of the small-scale turbulent inhomogeneities on the sound field, we assume that the difference in the path lengths is constant. Let us estimate the fluctuations of the phase difference $\delta(\Delta\varphi)$, which are caused by random fluctuations of the refractive index. Such fluctuations manifest themselves in the random time variations of the phases of all elementary signals arriving at the receiver.

The phase fluctuations of each received signal are characterized by the rms value $[\overline{(\Delta\varphi_{1,2})^2}]^{1/2}$ determined in the same way as the variation coefficient in (2) [8]. In the worst case of fully uncorrelated phase fluctuations of all arrivals, the rms phase difference is as follows:

$$\delta(\Delta\varphi) = [2(\overline{\mu^2})k^2L_0L]^{1/2}, \quad (3)$$

and the fluctuations of the travel time along each ray are determined by the formula

$$[\overline{(\Delta t_{1,2})^2}]^{1/2} = [\overline{(\Delta\varphi_{1,2})^2}]^{1/2}/2\pi f, \quad (4)$$

where f is the transmitted frequency.

By using these formulas with the aforementioned parameters, we obtain $\delta(\Delta\varphi) \approx (6–7) \times 10^{-2}$ rad $\approx 4.0°$ and $[\overline{(\Delta t_{1,2})^2}]^{1/2} \approx 1$ μs. Thus, the effect of the small-scale turbulence on the phase structure of the reflected signal may be treated as weak, if one can neglect the phase difference up to 20° in the arrived signals, this

threshold value being primarily governed by the specifications of the experimental device and the phase stability of the channel circuits [14].

The fine-structural inhomogeneities may lead to an additional change in the phase difference of the individual signals that arrive at the receiver along different paths, because the change in the acoustic path length depends on the angle θ. To simplify our considerations, we assume that the fine-structural inhomogeneities are presented by plain-parallel layers with constant sound speed increments. Again, we consider the signal-forming mechanism of Fig. 2, and the phase difference $\delta(\Delta\varphi)$ is now governed by the difference in the acoustic paths of individual components of the resultant signal. As we will see later, the used estimation technique is also applicable to the lenses and the general changes in the sound speed profile.

With this approach, the travel time along the ray with the departure angle θ (Fig. 2), from the on-surface source to the ocean bottom located at depth H, is given by the formula [15],

$$t = \frac{1}{c_0}\int_0^H \frac{n^2(z)dz}{\sqrt{n^2(z) - \sin^2\theta}}, \tag{5}$$

where c_0 is the sound speed at the surface and n is the refractive index depending on the depth z.

As usual, we represent the squared refractive index in the form $n^2(z) = 1 + \varepsilon(z)$, where

$$\varepsilon(z) = -\frac{2\Delta c(z)}{c_0} + \left(\frac{\Delta c(z)}{c_0}\right)^2 \tag{6}$$

and $\Delta c(z) = c(z) - c_0$.

In accordance with the aforementioned generalized data, the value $\Delta c/c_0$ is approximately equal to 2×10^{-2}. Neglecting the value $(\Delta c/c_0)^2$ leads to the estimate

$$\varepsilon(z) \approx -2\Delta c(z)/c_0$$

and

$$t = \frac{1}{c_0}\int_0^H \frac{[1 + \varepsilon(z)]dz}{\cos\theta\sqrt{1 - [\varepsilon(z)/\cos^2\theta]}}. \tag{7}$$

Because the sea floor is surveyed with vertically oriented acoustic systems, and the reflecting bottom area has the angular half-width θ_0 less than 10° for most ocean regions (a broad directivity pattern [3]), we have $\varepsilon(z)/\cos^2\theta \ll 1$. Hence, we obtain

$$t = \frac{1}{c_0}\int_0^H \left[\frac{1 + \varepsilon(z)}{\cos\theta} - \frac{1}{2}\frac{\varepsilon(z)}{\cos^3\theta}\right]dz. \tag{8}$$

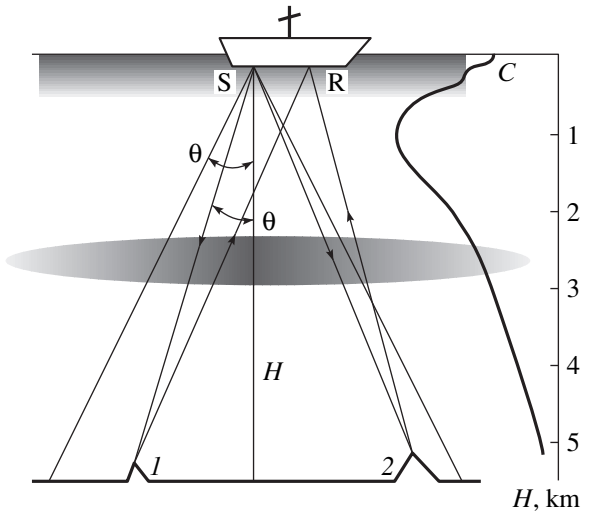

Fig. 2. Formation of the received signal reflected by two bottom features: (S) sound source; (R) receiver; (*1*) the first feature; and (*2*) the second feature.

At normal incidence ($\cos\theta = 1$), the travel time to the bottom is

$$t_0 = \frac{1}{c_0}\int_0^H \left[1 + \frac{1}{2}\varepsilon(z)\right]dz. \tag{9}$$

The travel time difference between the vertical ray and the ray with the departure angle θ is maximal and is determined by the expression

$$\Delta t = t - t_0 = \frac{1}{c_0}\int_0^H [f_1(\theta) + f_2(\theta)\varepsilon(z)]dz, \tag{10}$$

where

$$f_1(\theta) = \frac{2\sin^2(\theta/2)}{\cos\theta}; \quad f_2(\theta) = \frac{2\sin^2(\theta/2) - \tan^2\theta}{2\cos\theta}.$$

Let us estimate the variability of the quantity Δt depending on the change in the sound speed profile $\varepsilon(z)$. Let Δt_1 correspond to $\varepsilon_1(z)$ and Δt_2 correspond to $\varepsilon_2(z)$. Then, in the general case,

$$\delta(\Delta t) = (\Delta t_1 - \Delta t_2) = \int_0^H \left[\frac{f_1(\theta_1)}{c_{01}} - \frac{f_1(\theta_2)}{c_{02}} + \frac{f_2(\theta_1)\varepsilon_1(z)}{c_{01}} - \frac{f_2(\theta_2)\varepsilon_2(z)}{c_{02}}\right]dz. \tag{11}$$

In estimating the influence of the fine-structural inhomogeneities and lenses, the sound speed is $c_{01} = c_{02} = c_0$ at the surface, and the angle is $\theta_1 = \theta_2 = \theta$. Then, at small angles $\theta \le 10°$, in view of (6), formula (11) yields

$$\delta(\Delta t) = \frac{\theta^2}{c_0^2}\int_0^H \delta[\Delta c(z)]dz, \tag{12}$$

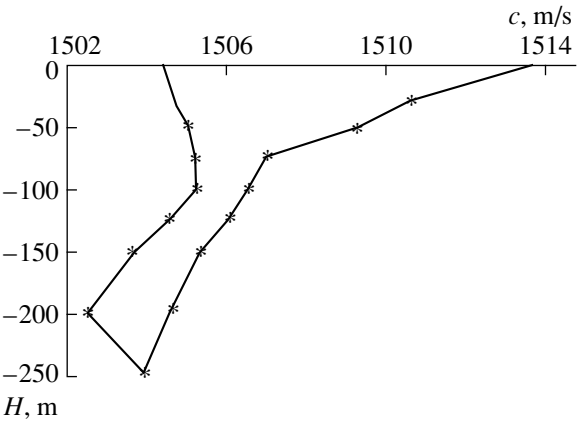

Fig. 3. Measured sound speed profiles for winter and summer seasons; moderate latitudes.

where $\delta[\Delta c(z)] = c_0[\varepsilon_1(z) - \varepsilon_2(z)]/2$ and

$$[\overline{(\Delta t_1 - \Delta t_2)^2}]^{1/2} = (H_T L_T)^{1/2}\sigma_{cT}\theta^2/c_0^2.$$

Here, H_T is the maximum depth of the fine-structural inhomogeneities ($H_T \approx 10^3$ m), L_T is their characteristic scale ($L_T \approx 10^2$ m), and σ_{cT} is the rms fluctuation of the sound speed in the fine-structural inhomogeneities ($\sigma_T \approx 0.7$ m/s) [9]. In this case, for $\theta = 10°$, we obtain $[\overline{[(\Delta t_1 - \Delta t_2)^2}]^{1/2} = 2.8$–$3$ μs, and we have $\delta(\Delta\varphi) \approx 10°$ at $f = 10$ kHz.

The obtained estimates show that neither small-scale nor fine-structural inhomogeneities of the water column can significantly distort the fine spatial structure of the reflected sound field. Hence, this structure must remain constant for a long time. This fact has been confirmed by successful operation of the correlation logs and arrays with synthesized apertures, i.e., the devices that make use of the stability of the sound field structure [3, 16–18]. In experiments, the stability of acoustic maps was observed at least on the time scales of several units to several tens of seconds. In particular, such time intervals are sufficient to implement the new high-sensitive method of measuring the displacement and speed of a vessel relative to the sea bottom [3, 4].

However, sometimes long-term acoustic mapping that is stable on large time scales, e.g., the seasonal ones, is required. This may be necessary for solving the problem of high-precision return of a vessel to the initial point, or for other purposes. In these cases, one should additionally consider the effect of the lenses and changes in the general sound speed profile.

To estimate the effect of a lens, formula (12) can be used. According to the aforementioned parameters of the lens, we can represent it as a linear deviation of the sound speed from its mean profile. We specify this deviation as a linear increase from $\delta[\Delta c(z)] = 0$ at the depth 650 m to $\delta[\Delta c(z)] = 18$ m/s at 950 m and as a linear decrease from the latter value to $\delta[\Delta c(z)] = 0$ at 1250 m. In this case, we have $\int_0^H \delta[\Delta c(z)]\,dz = 5.4 \times 10^3$ m^2/s and $\delta(\Delta t) = 2.4 \times 10^{-3}\theta^2$ s.

To consider the seasonal variability of the sound speed profile, we fix a point at the bottom. Then, in view of the change in the departure angle $\Delta\theta$, which is caused by the deformation of the sound speed profile, we derive the approximation from formula (11):

$$\delta(\Delta t) = \frac{H}{c_0}\left(\frac{\Delta c}{c_0}\frac{\theta^2}{2} - \Delta\theta\cdot\theta\right) + \frac{\theta^2}{2c_0^2}\int_0^H \delta[\Delta c(z)]dz\,. \quad (13)$$

Here, $\Delta c = c_{02} - c_{01}$ is the difference between the sound speeds at the surface and $\Delta\theta \cong \frac{1}{Hc_0}\int_0^H \delta[\Delta c(z)]\,dz \approx \frac{1}{2}\frac{\Delta c}{c_0}$ (H is the maximum depth reached by the seasonal variability, $H \approx 300$ m). Then, the first term of (13) may be neglected, and $\delta(\Delta t) = \frac{\theta^2}{c_0^2}\int_0^H \delta[\Delta c(z)]\,dz$. For the maximum seasonal deviation $\Delta c = 30$ m/s at the surface and $\delta[\Delta c(z)]$ uniformly decreasing down to zero at the depth 300 m, we have $\delta(\Delta t) \approx 2 \times 10^{-3}\theta^2$ s.

To estimate the quantity $I = \frac{1}{c_0^2}\int_0^H \delta[\Delta c(z)]\,dz$, we used the actual sound speed profiles measured in summer and winter (Fig. 3), at 42° N, 34.5° W [9]. The calculation yields $I \approx 3.5 \times 10^{-4}$ s. With the use of the modified Vagin's computer code to compute the travel time along the ray down to the bottom, the difference between Δt_1 and Δt_2 was found to be about 9 μs for $\theta = 10°$. Formula (3) yields 10 μs, which means that both approaches lead to equivalent results.

For a limiting case, when the maximum value of $\delta[\Delta c(z)]$ is equal to 30 m/s at the surface and zero at the depth 300 m (the seasonal variability usually never penetrates to deeper horizons), we have $I \approx 2 \times 10^{-3}$ s and $\delta(\Delta t) \approx 5.8 \times 10^{-5}$ s at $\theta = 10°$; these values correspond to $\delta(\Delta\varphi) \approx 200°$ for $f = 10$ kHz.

Figure 4 presents the angular dependences of the quantity $\delta(\Delta\varphi) = 360\delta(\Delta t)f$ (deg) for the frequencies $f = 1$, 3, and 10 kHz. The plots show that the calculated effect of the seasonal variability may be significant. In particular, at the frequency 10 kHz, the change in the phase difference is 100° or more, if the angular half-width of the reflecting bottom area exceeds 10°.

In the above estimations, a simplified situation was considered: the bottom was assumed to be flat and uniform. In such a situation, only the sea depth and the sound speed profile determine the difference in the arrival times Δt_1 and Δt_2, as well as the phase difference, for the signals that return to the receiver along different paths. However, one should take into account the bottom-surface roughness with heights that have the

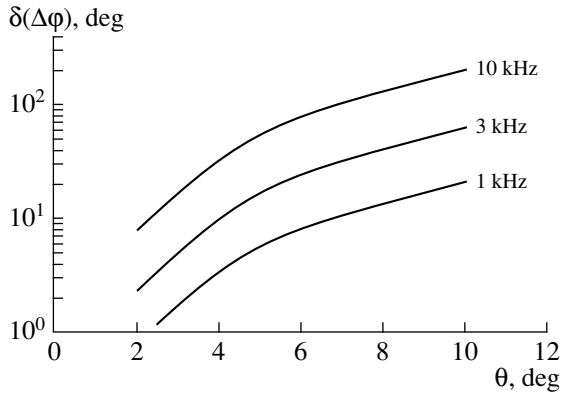

Fig. 4. Maximum difference that occurs in the phase advances of individual arrivals because of the seasonal variability of the sound speed profile (see Fig. 3) for the frequencies 1, 3, and 10 kHz.

same order of magnitude as the transmitted wavelength or higher (actually, it is the roughness that returns the reflected signal back to the receiver at $\theta \neq 0$). There is also an additional phase lag caused by scattering, and this quantity may differ for different rays. In view of these facts, another term should be added to the phase difference obtained from the quantities Δt_1 and Δt_2, this term being irregular in the general case. Nevertheless, the additional term does not violate the validity of the obtained results, because it has equal values for Δt_1 and Δt_2, and, in subtracting one of those from another according to (11), the effect vanishes.

The obtained estimates show that the effects of lenses and seasonal variability of the sound speed profile on the phase relations in the individual arrivals are of similar orders of magnitude and may be quite significant. However, for most ocean areas, the bottom is smooth or hilly (with $\theta_0 < 3°$–$4°$ [3]), the lenses are rare events, and the seasonal variability of the sound speed profile is nearly absent. Hence, the specified value of I is highly overestimated relative to the actual one, and we can conclude that the value of $\delta(\Delta\varphi)$ is in most cases lower than 10° for the frequencies at hand and can be neglected. Nevertheless, the proposed technique should be used to obtain the estimates for a specific situation.

Thus, the fine spatial (interference) structure of the bottom-reflected sound field, which manifests itself as the amplitude distribution over a horizontal plane near the ocean surface and, in particular, over the array aperture (the acoustic map of the bottom [3–5]), is actually rather stable to the effects of water stratification. This conclusion is important, because it testifies to the high stability of the acoustic bottom maps and confirms their applicability to navigation tasks. This is most true for the problems of measuring the displacements [3, 4] when the fine structure of the reflected sound field should remain unchanged for the time interval between successive measurements of the amplitude distributions. Because, in practice, this interval is less than several seconds, the effects of water stratification can be neglected.

ACKNOWLEDGMENTS

This work was supported by the Russian Foundation for Basic Research, project no 98-05-65096.

REFERENCES

1. A. V. Bunchuk, V. I. Volovov, and D. A. Zharinov, Akust. Zh. **36**, 599 (1990) [Sov. Phys. Acoust. **36**, 339 (1990)].
2. V. I. Volovov, Akust. Zh. **39**, 605 (1993) [Acoust. Phys. **39**, 317 (1993)].
3. V. I. Volovov, *Sound Reflection from the Ocean Bottom* (Nauka, Moscow, 1993).
4. V. I. Volovov, Akust. Zh. **40**, 142 (1994) [Acoust. Phys. **40**, 127 (1994)].
5. V. I. Volovov and A. I. Govorov, Akust. Zh. **43**, 476 (1997) [Acoust. Phys. **43**, 406 (1997)].
6. V. I. Volovov and A. I. Govorov, Akust. Zh. **43**, 849 (1997) [Acoust. Phys. **43**, 742 (1997)].
7. N. S. Ageeva, I. B. Andreeva, V. I. Volovov, *et al.*, in *Ocean Acoustics* (Nauka, Moscow, 1974), pp. 5–78.
8. S. D. Chuprov and R. F. Shvachko, in *Ocean Acoustics* (Nauka, Moscow, 1974), pp. 559–614.
9. V. S. Gostev and R. F. Shvachko, in *Problems of Ocean Acoustics* (Nauka, Moscow, 1984), pp. 153–164.
10. A. N. Serebryany, in *Proceedings of International Symposium "Ocean Cities'95", Monaco, 1995*, p. 376.
11. J. X. Zhon, X. Z. Zhang, and P. H. Rogers, in *Proceedings of IEEE "Oceans'96", 1996*, Vol. 1, pp. 1–8.
12. *Climate Characteristics of the Sound Speed in the Northern Part of the Atlantic Ocean* (Gidrometeoizdat, Moscow, 1984).
13. N. E. Mal'tsev, K. D. Sabinin, and A. V. Furduev, Akust. Zh. **36**, 86 (1990) [Sov. Phys. Acoust. **36**, 46 (1990)].
14. V. I. Volovov and A. I. Govorov, Akust. Zh. **43**, 328 (1997) [Acoust. Phys. **43**, 282 (1997)].
15. L. M. Brekhovskikh, in *Ocean Acoustics* (Nauka, Moscow, 1974), pp. 79–162.
16. A. V. Bogorodskiĭ, G. V. Yakovlev, E. A. Korepin, and A. K. Dolzhikov, *Underwater Apparatus for Investigation and Exploration of the Ocean* (Gidrometeoizdat, Leningrad, 1982).
17. V. S. Riyait, M. A. Lawlor, A. E. Adams, *et al.*, Int. Hydr. Rev. **72**, 115 (1995).
18. F. Ollivier, P. Cerbenka, and P. Alias, IEEE Proc. Radar, Sonar and Navigation **143**, 163 (1996).

Translated by E.A. Kopyl

Acoustical Physics, Vol. 46, No. 1, 2000, pp. 62–70. Translated from Akusticheskiĭ Zhurnal, Vol. 46, No. 1, 2000, pp. 75–83.

Acoustic Dark Field

V. A. Zverev

Institute of Applied Physics, Russian Academy of Sciences, ul. Ul'yanova 46, Nizhni Novgorod, 603600 Russia
e-mail: zverev@hydro.appl.sci-nnov.ru

Received January 20, 1999

Abstract—An acoustic dark field method is proposed. The method allows one to observe the signals scattered by moving inhomogeneities of the medium in the direction close to that of the illuminating field. The results of a full-scale experiment demonstrating the efficiency of the proposed method under reverberation conditions are presented. For the first time, the spatial distribution of the wave scattering from a rough water surface is observed individually for each side frequency of its spectrum. © *2000 MAIK "Nauka/Interperiodica".*

In optics, devices that allow one to observe small inhomogeneities in transmitted light are well known. In such devices, the direct light from the source does not reach the field of vision [1]. If the medium is homogeneous (without scatterers), the field of vision remains dark. This fact gave rise to the name of the corresponding method of observation—the dark field method. Once an inhomogeneity affecting the refractive index or the transparency of the medium occurs in the zone illuminated by an intense light source, this inhomogeneity is displayed as a shining object on the screen of the device. This method is used for the observation of perturbations introduced in the medium by acoustic waves and other inhomogeneities that cannot be distinguished against the light source.

Similar devices are badly needed in acoustics. They would allow one to observe ocean inhomogeneities, currents, and other objects. For such purposes, acoustic tomographic methods are developed [2, 3]. With tomographic methods, one can determine the location and the size of an inhomogeneity by measuring the fluctuations of the ray propagation times between many points of transmission and reception [2]. These methods require the solution of inverse problems. Such solutions are unstable. Moreover, under the conditions of a shallow sea, it is often impossible to resolve individual rays, and the acoustic tomography cannot be used [3].

The optical dark field method can be transferred to acoustics, for which purpose large-size acoustic antennas—the so-called focusable antennas—are necessary [4]. At low frequencies used for studying the oceanic inhomogeneities, a focusable antenna is a huge "Cyclopean" structure. Despite the fact that the success in building such a structure is guaranteed and verified in optics, the construction of such antennas (judging from the literature) is planned nowhere.

Earlier, we proposed an acoustic dark field method that allows one to darken the field of a source of intense radiation and to observe small perturbations of the medium against the signal of this source [5]. For the realization of this method, no large-size focusable antennas are necessary. It is sufficient to use any kind of antenna providing the required angular resolution of the observed inhomogeneities. However, this method is efficient only for small-angle spatial perturbations of the field [6, 7]. A special experiment carried out in shallow sea [6] showed that, along with the perturbations of interest, a noise halo covering the entire range of angles is present in the medium, the level of noise being 15–20 dB relative to the source level [8–10]. Under such conditions, the previously proposed dark field method [5] is inefficient.

In the cited method, the field of the source of intense radiation was suppressed by using the difference between the signals of complex amplitudes in neighboring elements of the antenna, which is practically equivalent to the subtraction of the appropriately phased values of the complex amplitudes of signals in neighboring elements of an antenna array [6]. In this paper, we propose a modified acoustic dark field method which is based on the subtraction of the values of the logarithms of the complex amplitudes at neighboring discrete instants of time. The subtraction of the values of signals at the neighboring instants of time is equivalent to filtering. A linear filtering is performed after taking the logarithms in the cepstral method of signal selection [11]. The frequency characteristic of a filter which produces the effect equivalent to the subtraction of signals within short time intervals linearly decreases with decreasing frequency. Such a frequency characteristic of the filter leads to the suppression of the constant component and attenuation of the low-frequency component of the field. As a result, the signals

1063-7710/00/4601-0062$20.00

scattered by moving inhomogeneities become prominent in proportion to their Doppler frequency.

The proposed method is studied by mathematical simulation and in full-scale experiments under the conditions of intense reverberation. In the experiment, the field of the direct fluctuating signal and the accompanying noise were suppressed by 60 dB relative to the direct field generated by the source and arriving at the array. We note that the best adaptive methods, including the aforementioned one [5], provide the suppression of the acoustic field of a source under intense reverberation by no more than 30 dB [6].

The essence of the method can be illustrated by a specific example. In an acoustic waveguide, we place a source of an intense monochromatic signal which illuminates the inhomogeneities of the medium. For the observation of these inhomogeneities, we place an acoustic array at some distance from the source. We consider a horizontal line array consisting of a set of equidistant receiving elements.

Let the complex field amplitude (a complex number whose magnitude and argument are respectively equal to the amplitude and phase of oscillation in the acoustic field [12, 13]) that occurs at the array element of number k at the instant of number n be $A_{k,n}$. The algorithm of the formation of an acoustic dark field includes the following operations on the complex field amplitudes received by individual receiving elements of the array:

$$S_{k,n} = \ln\left(\frac{|A_{k,n+1}|}{|A_{k,n}|}\right) + i(\arg(A_{k,n+1}) - \arg(A_{k,n})). \quad (1)$$

We first consider the effect of transformation (1) by using a mathematical model. As the simplest model, we select the observation of a single scatterer moving along a straight line and illuminated by a plane wave, as shown in Fig. 1. This model allows us not only to demonstrate the effect of transformation (1) but also to obtain the calibration signal necessary for the evaluation of the observed inhomogeneities. Consider a scatterer *4* moving with a constant velocity v along the path *3–3* between the source *1* and the receiving array *2–2* (see Fig. 1). Let us determine the complex amplitude of the scattered field produced by the moving scatterer at every element of the receiving array. We introduce the geometric parameters: the distance $R(x, t)$ from the scatterer to the point of reception (x is the coordinate of the receiving element of the array), the distance vt traveled by the scatterer along the path *3–3*, and the distance D from the scatterer trajectory to the array. Using the above notation and assumptions, we obtain the expression

$$R(x, t) = \sqrt{D^2 + (vt - x)^2}, \quad (2)$$

where t is time.

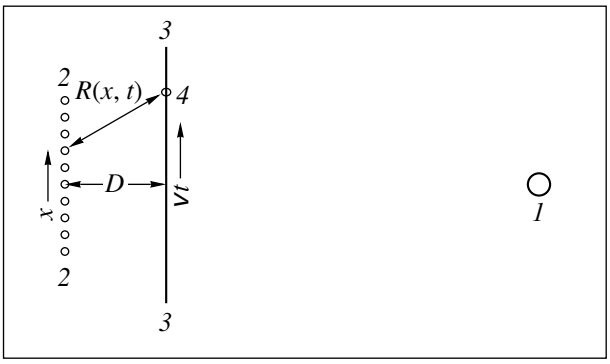

Fig. 1. Schematic diagram of the model experiment: (*1*) source; (*2–2*) receiving array; (*3–3*) path of the simulated moving scatterer; (*4*) scatterer; (D) distance from the path of the scatterer to the receiving array; and ($R(x, t)$) distance from the scatterer to every receiving element of the array.

Because of the variation of the distance $R(x, t)$, the phase of the signal arriving from the scatterer to every point of reception will depend on time according to the formula

$$\varphi(x, t) = \frac{2\pi}{\lambda} R(x, t), \quad (3)$$

where λ is the wavelength.

We assume that the source is sufficiently far from the array, so that, for the direct field, the phase difference between the neighboring array elements does not depend on the number of the array element (a consequence of the fact that the array is nonfocusable). Let this phase be time independent (the source and the array are fixed) and equal to zero for definiteness. The

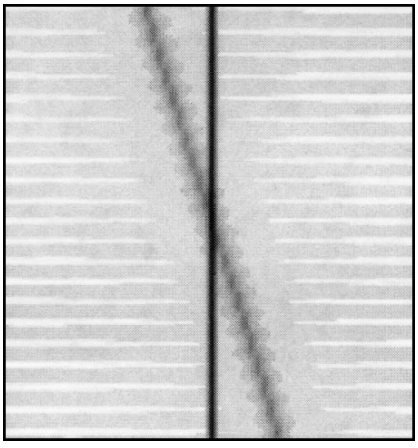

Fig. 2. Numerical model of the absolute value of the array response to the signal of the moving scatterer without darkening of the direct signal. The vertical axis shows the time, and the horizontal axis shows the spatial frequency (the angular spectrum (5)).

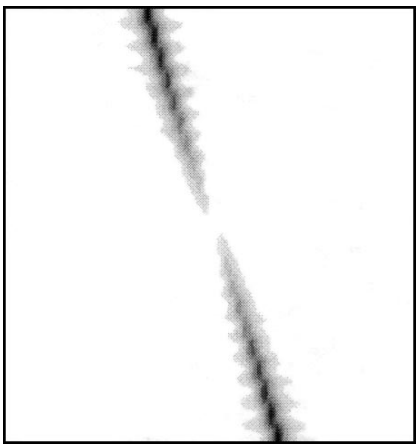

Fig. 3. Numerical model of the absolute value of the array response to the signal of the moving scatterer with the darkening of the direct signal. The axes are the same as in Fig. 2.

sought-for amplitude is obtained (accurate to a constant phase shift) in the form

$$A(x, t) = \exp(i\varphi(x, t)) + A_0, \quad (4)$$

where A_0 is the direct field of the source at the array.

Expression (4) was used in our studies for the mathematical simulation of a single scatterer moving in the zone of observation of the acoustic dark field.

Figure 2 shows the result of the observation of a moving scatterer by means of an array without using the acoustic dark field. In the case under consideration, this is possible because of the absence of reverberation. The signal processing consists of the determination of the spatial spectrum $A(x, t)$ specified by formula (4), the spectrum being determined along the array (as a function of the x coordinate only) as a function of time t [12, 13]. The relation between the spatial frequency U serving as the argument in the graphic representation and the scan angle θ of the array scanning over the zone of observation is as follows [13]:

$$U = U_{\max}\frac{\lambda}{2d}\sin(\theta), \quad (5)$$

where $U_{\max}$ is the maximum value of the spatial frequency (this value is equal to half of the total number of the points of the spectral Fourier expansion) and d is the distance between the receiving elements of the array. The simulation was performed for $2d = \lambda$. The interval of spatial frequencies shown in the graphs lies within $\pm U_{\max}$. In Fig. 2, the vertical line at the center, i.e., at $\theta = 0$, represents the source. The simulated scatterer is represented by the sloping line, because, according to formula (4), the direction toward the scatterer varies approximately in proportion to time.

Figure 3 shows the result of a similar signal processing with the use of an acoustic dark field. Here, the procedure is the same as in the case of Fig. 2, but it is performed for the signal $S(x, t)$ subjected to additional processing by formula (1) rather than for the signal $A(x, t)$. As a result, the signal of the source is invisible (the field is darkened), and the signal of the scatterer is observed at the same angles as in Fig. 2 with the intensity depending on the Doppler shift of its frequency at the corresponding instant of time.

The proposed algorithm of signal processing contains a nonlinear operation, namely, taking the logarithm. This is the only mathematical transformation that allows one to reduce the multiplicative noise to an additive one and to subject it to filtering in the latter form. The set of successive operations including taking of logarithm and filtering can be called nonlinear filtering. The efficiency of nonlinear filtering is demonstrated in the modern methods used for processing multiplicatively related signal spectra—the cepstral analysis [11]. The predominant effect of multiplicative noise is the specific feature of the propagation of acoustic monochromatic signals. An intense monochromatic sound radiation can be received in such a narrow frequency band that the effect of additive noise can be neglected. In this case, the noise is represented by the fluctuations of the level and phase of the illuminating acoustic signal. These fluctuations are multiplicatively related to the received signal.

Figure 4 shows an example of nonlinear filtering from the previous publication [14]. The initial signal whose spectrum is shown in Fig. 4a is phase modulated by an intense low-frequency signal. As a result, the spectrum of this signal takes the form shown in Fig. 4b. Figures 4c and 4d present the results of applying the nonlinear filtering to the initial signal and to the signal subjected to distortion. The procedure of nonlinear filtering is especially efficient in the situation described in our previous paper [15].

The full-scale experiment was carried out at the Sankhar lake—a picturesque lake of the Vladimir oblast. Schematically, the experiment corresponded to Fig. 1. The acoustic field was received by individual hydrophones of an array and processed; the processed data were stored.

The processing of the received signals included the following operations. First, the signals received by every microphone were filtered in the frequency band ± 3 Hz near every discrete frequency generated by the source. Second, the filtered signals were mixed with the signal of the generated frequency and formed signals of the difference frequency in two quadrature channels [12, 13]. In one quadrature channel, the signal had the form $A\cos(\varphi)$, and in the other channel it had the form $A\sin(\varphi)$, where A is the amplitude of the received signal and φ is its phase. The signals obtained from the two quadrature channels were recorded in digital form by a computer. The described preliminary signal processing provided the signal record in the form equivalent to the

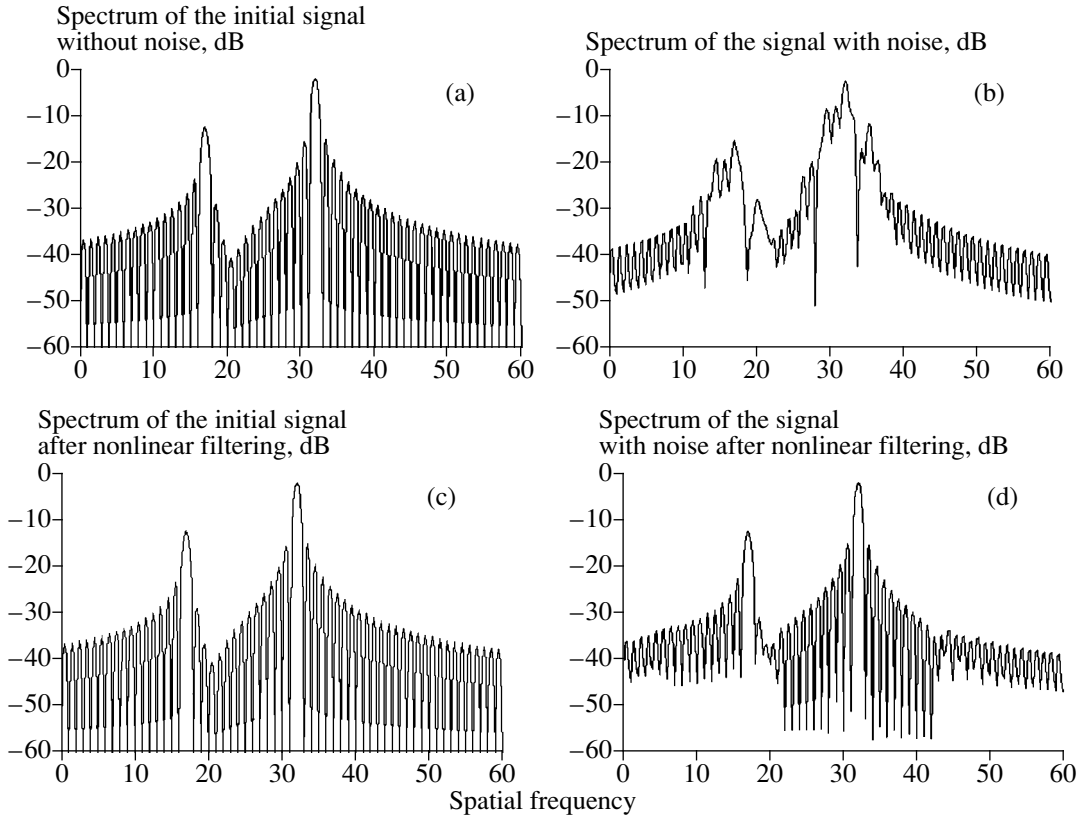

Fig. 4. Results of the numerical simulation of the application of nonlinear filtering to the signals received by the array [14]. The vertical axes show the level in dB. The horizontal axis represents the spatial frequency proportional to the sine of the arrival angle of the wave (see formula (5)). (a) Spectrum of the initial signal; (b) spatial spectrum of the initial signal distorted by phase modulation; and the results of the application of nonlinear filtering (c) to the initial signal and (d) to the distorted signal.

complex amplitudes considered before in [12, 13]. Such a record, i.e., a record of the total field or a hologram of the received acoustic signal, allows one, after subsequent processing, to obtain the same results as those provided by the corresponding processing of the directly received acoustic field.

In the experiment, the square of the lake depth (15–20 m) divided by the wavelength (~1 m) was approximately equal to the length of the acoustic path (~300 m). Such conditions are not exactly those of a shallow sea [15]. However, in these conditions, the number of reflections from the surface, banks, and bottom of the lake was sufficiently great to provide an intense reverberation of the signal. The aim of the experiment was to reveal the possibilities for the observation of natural factors that cause the scattering of the acoustic field. In our experiment, no objects were moving in the field of vision of the array, and only the source and the receiving array were in operation. Therefore, for the determination of the target strength of the scattered signals, a signal simulating the field of a scatterer was added to the signal received from the array in the course of its processing.

The simulation of the signal of a moving scatterer was performed by combining the signal received by the array with the same signal subjected to some modification; namely, the signal was attenuated (e.g., by 40 dB) and multiplied by a function of type (4) without its constant component. This operation is equivalent to the introduction of a Doppler shift proportional to the spatial frequency (angular displacement) into the signal in which the direct field of the source is dominant. As a result, in the additional attenuated signal, the direct field of the source with the introduced Doppler shift and angular displacement plays the role of a moving scatterer. Its level relative to the source is known. The method used in our experiments for the simulation of a moving scatterer allowed us to obtain the mathematical model of the scatterer with the known parameters and with the level and phase fluctuations that are identical to those of the direct field of the source under the conditions of our experiment.

We specify the aim of our experiment by using Fig. 5. This figure shows the time spectrum of acoustic signals received by individual hydrophones of the array. These spectra have the form similar to that of the spectra presented in the monograph [3, p. 214]. The

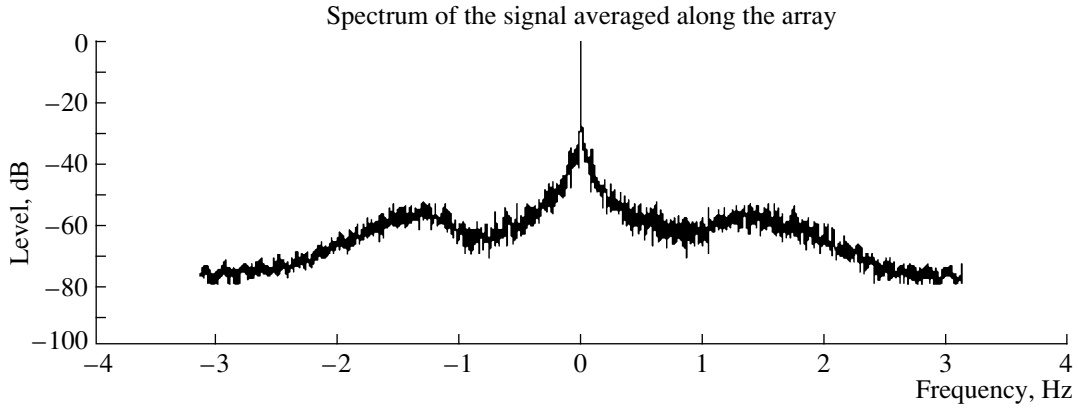

Fig. 5. Spectrum of the signal received by the hydrophones of the array.

spectrum exhibits a peak at zero frequency. By this frequency, the field of the source was shifted. In the graph, the frequencies higher than the source frequency are positive, and the frequencies that are lower than the source frequency are negative. The spectrum also has peaks at frequencies about ±2 Hz. For signals propagating in the sea, such peaks in their spectrum are explained by the wave scattering from the wind waves which modulate the signal and shift its spectrum [3]. In the cited monograph [3], a method of the diagnostics of the state of the sea surface on the basis of such spectra is considered. The specific aim of our experiment was as follows: with the help of the array, to observe the surface waves that modulate the signal of the source.

The results of the experiment are presented in the figures.

Figures 6 and 7 show the results of the signal processing for a signal received by the array. The black field corresponds to the maximum signal, and the white field corresponds to the minimum one. The processing consisted of the determination of the spatial spectra along the line passing through the receiving hydrophones of the array. The signals shown in Fig. 6 were subjected to additional processing. The darkening of the array field was performed by formula (1), and the signals were additionally filtered in time.

The experiment was performed at the frequency at which the condition $2d < \lambda$ was satisfied (see relation (5)). In this case, by virtue of relation (5), in the determination of the spectrum of spatial frequencies along the array, the whole range of real angles θ occupies only part of the full spatial spectrum shown in Figs. 6 and 7. In the region of imaginary angles, the acoustic waves are strongly attenuated [12, 13]. This region is displayed in the figures in the form of a white vertical band on each side of the plots. The fact that signals lying in the region of real angles θ prevail testifies to the absence of any noticeable noise of nonacoustic origin.

In Fig. 6a, the signal received by the array was processed in the entire band of temporal frequencies shown in Fig. 5. Figure 6b shows the result obtained by processing a filtered signal with the elimination of the two side frequencies exceeding (in magnitude) 1 Hz. By doing so, we suppressed to a considerable extent the signals caused by the scattering from wind waves [10, 13]. Thus, correlating Figs. 6a and 6b, we can reveal the contribution made by the scattering from the lake surface to the total scattered signal. For example, in Fig. 6a, the source is displayed in the form of an intense line, while in Fig. 6b it is barely visible. This means that the array can "see" the reflection of the source at the lake surface in the same way as we can see the "lunar" or "solar" track on a rough water surface. In Fig. 6a, one can see the angular distribution of the level of the signal scattered by the surface. Waves scattered by the rough lake surface are observed with confidence by the acoustic dark field method. In this case, the scattering from the surface forms a considerable part of the scattered signal. This is evident from the difference in the distinctness of the sloping line representing the result of adding the signal simulating the scatterer. In Figs. 6a and 6b, the distinctness of the simulated signal is noticeably different, although its level is the same.

Figures 6c and 6d show the results obtained with the elimination of only one side frequency—the lower one (Fig. 6c) or the upper one (Fig. 6d). In these figures, one can see the waves scattered by the surface either with an increase in the Doppler frequency or with a decrease in it. In this paper, the analysis of the spatial distribution of the acoustic signal scattering from wind waves with allowance for the sign of the Doppler effect is described for the first time.

Figure 7 shows the result obtained by processing the same signal as in Fig. 6 in the way we processed the signal shown in Fig. 2 (i.e., without using formula (1) producing the dark field). In the signal shown in Fig. 7, the simulation of a scatterer also takes place with its level

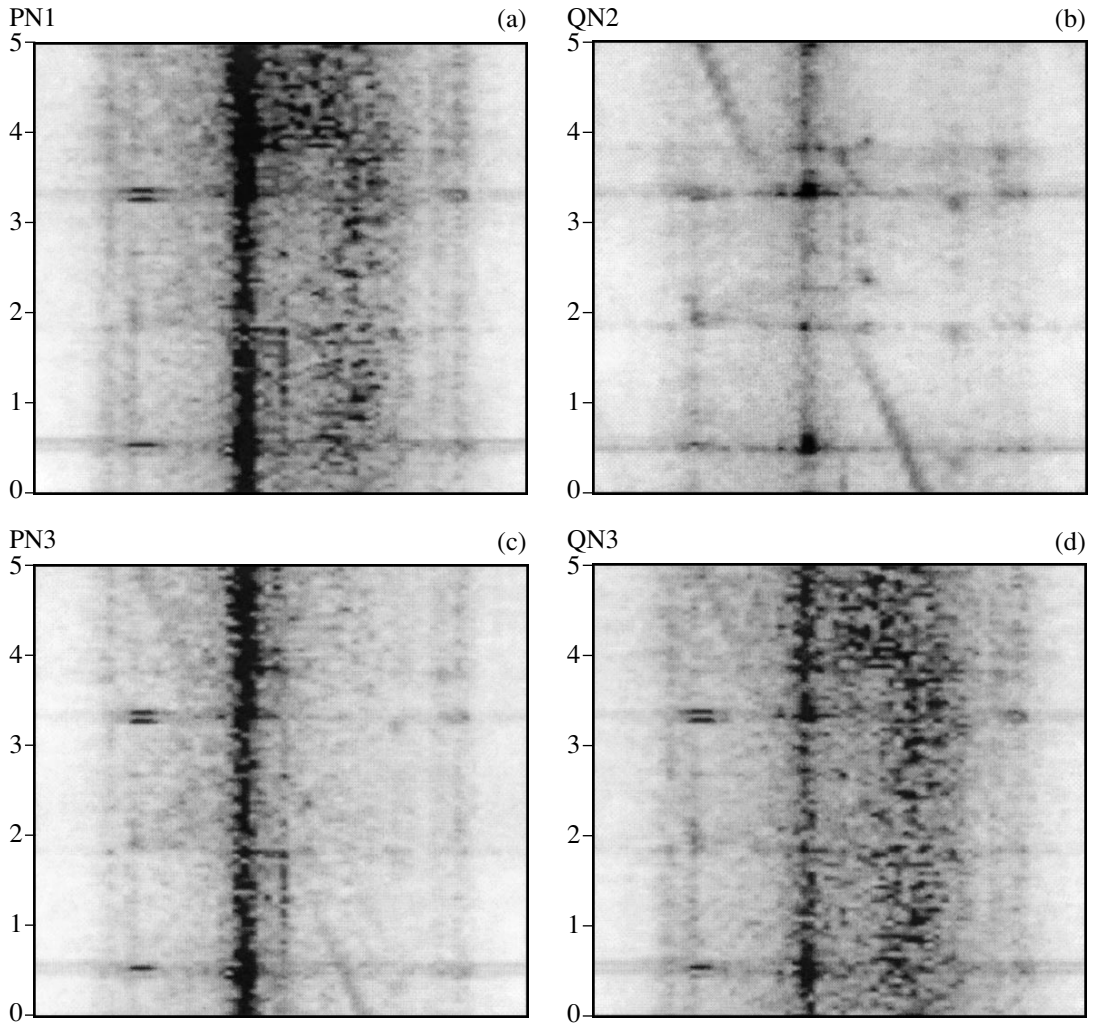

Fig. 6. Absolute value of the array response in the full-scale experiment with the darkening of the direct signal. A signal simulating the field of a moving scatterer (as in Fig. 1) is added with the level of the scattered signal being by 40 dB lower than the source field at the array. The vertical axis shows the time in minutes, and the horizontal axis corresponds to the spatial (angular) spectrum. (a) Array response in the entire frequency band shown in Fig. 5; (b) array response with the elimination of two side frequencies (exceeding 1 Hz in magnitude); and the field of vision of the array with the elimination of (c) only the lower side frequency and (d) only the upper one.

being 10 dB higher than that of the source. However, the scatterer cannot be distinguished in the figure. To make the simulated signal noticeable in this figure, it is necessary to increase its level by another 10 dB. The filtering of the Doppler components has also no effect on the pattern of Fig. 7. Thus, in the presence of reverberation, the localization of the centers of scattering from wind waves cannot be achieved without darkening the field of the array.

Figures 6 and 7 allow only qualitative estimates. They present distinct temporal variations of signals. However, they cannot be used for obtaining some quantitative data. For the latter purpose, Fig. 8 is more suitable. This figure presents the absolute values of the array response, i.e., the values shown in Figs. 6 and 7, for the same instant of time. From Fig. 8, one can see that the dark field method without additional filtering allows one to obtain the efficiency about 60 dB, and the subsequent temporal filtering provides about 10 dB extra.

In Fig. 8, we can see the response of the array to the signal simulating the scatterer: it is the maximum response in the thick line (the time section of Fig. 6b) at an angle slightly exceeding 20°. Its level is about –55 dB relative to the source signal, while it was set at –40 dB relative to this level. The difference is explained by the fact that the simulated signal moves too slowly, and, hence, even at the maximum angle, its Doppler shift is considerably reduced by the filter which darkens the field of vision of the array. From the time section of Fig. 7 that is shown in Fig. 8, one can see that the effect of reverberation on the shape of the array response is

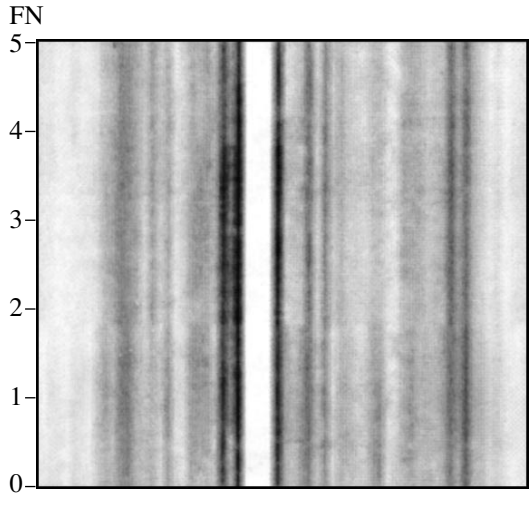

Fig. 7. Absolute value of the array response in the full-scale experiment. The direct field is not darkened, and the level of the signal simulating a moving scatterer is by 30 dB lower than the field of the source.

more substantial in the lake than in similar experiments in the sea [6]. This occurs because, the sea bottom is smoother and the reflections from the banks are absent. In Fig. 8, the reflections from the banks are well defined at angles close to 90°.

The efficiency of the acoustic dark field can also be demonstrated using the time spectra of signals shown in Figs. 9 and 10. Figure 9 presents the time spectrum of a signal at a single spatial frequency without an acoustic dark field. The spatial frequency (the angle of observation) is selected in such a way that the simulated signal at its maximum Doppler frequency fits into this spatial frequency. The level of the simulated signal is by 20 dB lower than the level of the source signal. In Fig. 9, the level of the simulated signal is by 30 dB lower than the source signal level, although, at this spatial frequency (this angle), the source signal is not maximum. The difference in the levels is related to the fact that, at this spatial frequency, the simulated signal is present in only a few realizations, while the source signal is accumulated in all 2048 temporal realizations in a coherent way and is enhanced by 66 dB.

Figure 10 shows the signal spectrum at the same spatial frequency as in Fig. 9 but with the use of the acoustic dark field. In this figure, the source signal is darkened despite its additional 66 dB. The comparison of Figs. 9 and 10 allows one to judge the efficiency of the proposed acoustic dark field method in full-scale conditions.

Thus, the results of the experiment show that, with the acoustic dark field method, the observation of the structure of the water surface and its variations is possible. One can localize the areas of intense surface waves and determine the wave velocities, the wind direction, and other parameters; it is also possible, by eliminating the Doppler frequencies related to the wind waves, to filter them out. In this case, one can observe the internal moving inhomogeneities and currents and see them in such a way as is possible with the array in use. A possibility arises to carry out an experiment that

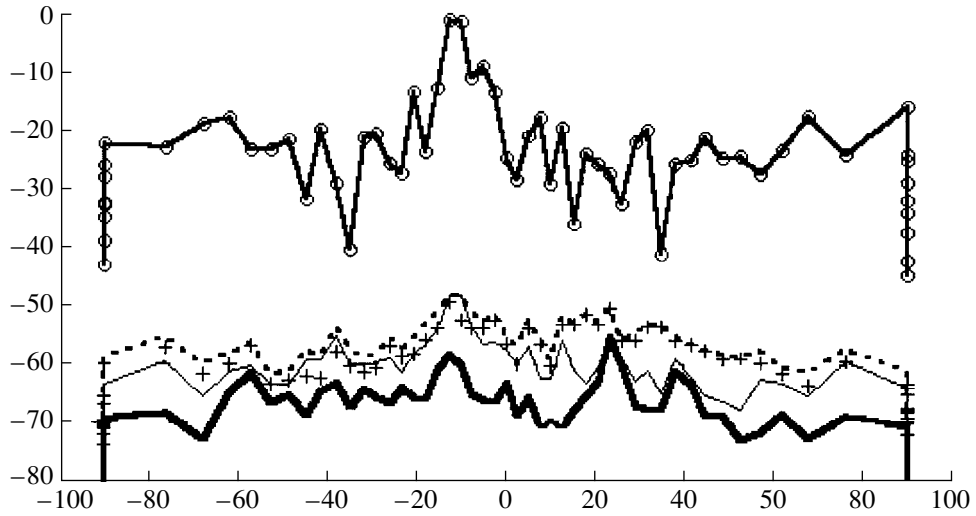

Fig. 8. Absolute values of the array response. The values are those shown in Figs. 6 and 7, and they correspond to the instant of time 15 s after the beginning of the experiment. The line with circles represents the array response without the darkening of the field (Fig. 7); the thick line shows the array response with the darkening of the field and the filtering of the signal (Fig. 6b); the dashed line shows the response with the darkening of the field within the entire frequency band (Fig. 6a); the thin line shows the response corresponding to one side frequency (Fig. 6c); crosses represent the response corresponding to the other side frequency (Fig. 6d). The horizontal axis represents the scan angle in degrees relative to the normal to the line of hydrophones, and the vertical axis shows the signal level in dB relative to the maximum response of the array without darkening.

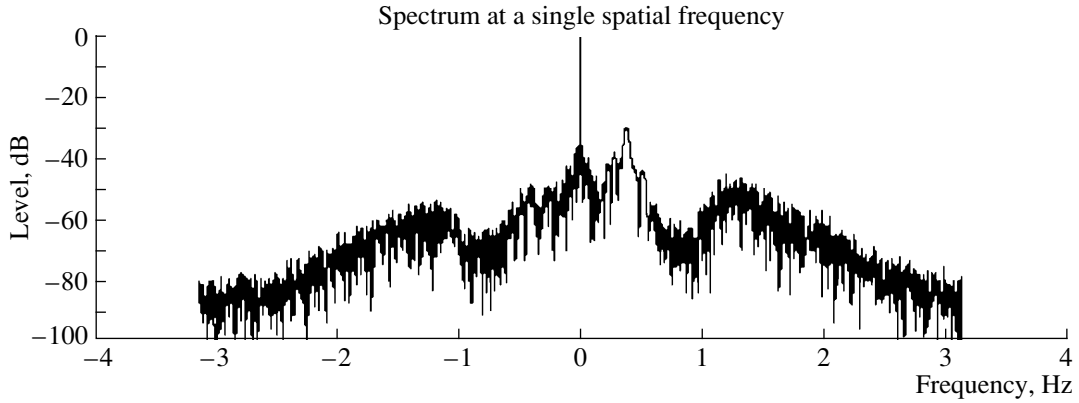

Fig. 9. Spectrum of the array response at a single spatial frequency (angular coordinate) corresponding to the maximum angular shift of the simulated scatterer (Fig. 6b). The direct field is not darkened.

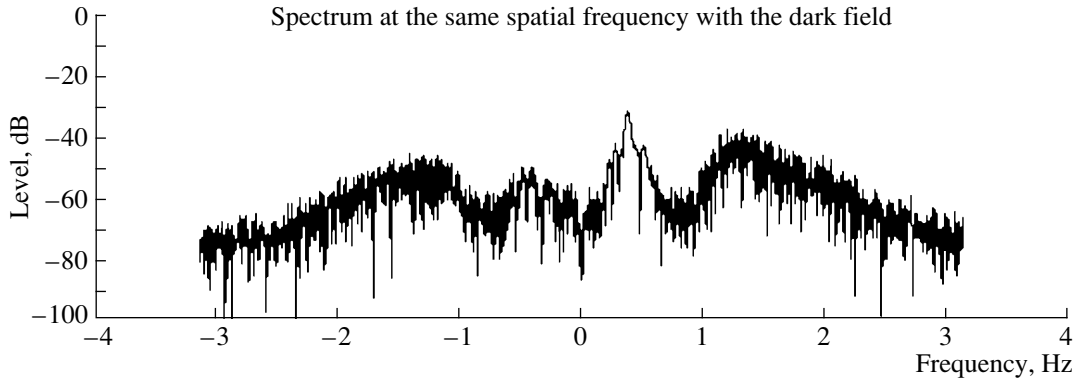

Fig. 10. Spectrum of the signal at a single spatial frequency with the darkening of the direct signal. Other parameters are the same as in Fig. 9.

would verify the calculations performed for the scattering from a rough ocean surface (e.g., [8, 17]). In connection with the proposed measuring technique, not only the solution of inverse scattering problems [18], but also the calculation of the direct forward scattering, which may be much stronger, becomes topical.

ACKNOWLEDGMENTS

I am grateful to B. M. Salin, V. I. Turchin, A. L. Matveev, and P. I. Korotin for the organization and performance of the experiment and the interest taken in this work; I am grateful to V. I. Talanov, A. L. Matveev, and the reviewer from the Editorial board of this journal for useful comments. The work was supported by the Russian Foundation for Basic Research (grant nos. 96-15-96603, 96-02-18621, and 97-02-17555).

REFERENCES

1. L. A. Vasil'ev, *Shadow Methods* (Nauka, Moscow, 1968).
2. W. Munk and C. Wunsh, Deep Sea Res. A **26**, 123 (1979).
3. V. V. Goncharov, V. Yu. Zaĭtsev, V. M. Kurtepov, *et al.*, *Acoustic Tomography of the Ocean* (Inst. of Applied Physics, Nizhni Novgorod, 1997).
4. V. A. Zverev, A. L. Matveev, M. M. Slavinskiĭ, *et al.*, Akust. Zh. **43**, 501 (1997) [Acoust. Phys. **43**, 429 (1997)].
5. V. A. Zverev, Akust. Zh. **40**, 401 (1994) [Acoust. Phys. **40**, 360 (1994)].
6. A. B. Gershman, V. I. Turchin, and V. A. Zverev, IEEE Trans. Signal Process. **43**, 2249 (1995).
7. V. A. Zverev, A. L. Matveyev, M. M. Slavinsky, *et al.*, Proc. I.O.A. **18**, Part 5, 85 (1996).
8. V. A. Zverev, Akust. Zh. **44**, 456 (1998) [Acoust. Phys. **44**, 389 (1998)].
9. V. A. Zverev and N. V. Litvak, Akust. Zh. (in press) [Acoust. Phys. (in press)].
10. V. A. Zverev, Akust. Zh. (in press) [Acoust. Phys. (in press)].
11. A. V. Oppenheim, R. W. Schafer, and T. G. Stockham, IEEE Trans. Audio and Electroacoust. **16** (3), (1968).
12. V. A. Zverev, *Radio-optics* (Sov. Radio, Moscow, 1975).

13. V. A. Zverev, *Physical Foundations of Image Formation by Wave Fields* (Inst. of Applied Physics, Nizhni Novgorod, 1998).
14. V. A. Zverev, in *Current Problems of Radiophysics* (Nizhni Novgorod State University, Nizhni Novgorod, 1996).
15. V. A. Zverev, A. L. Matveev, and V. V. Mityugov, Akust. Zh. **41**, 591 (1995) [Acoust. Phys. **41**, 518 (1995)].
16. B. G. Katsnel'son and V. G. Petnikov, *Acoustics of Shallow Sea* (Nauka, Moscow, 1997).
17. A. P. Rosenberg, J. Acoust. Soc. Am. **105**, 144 (1999).
18. J. A. Fawcett, W. L. J. Fox, and A. Maguer, J. Acoust. Soc. Am. **104**, 3296 (1998).

Translated by E.M. Golyamina

Acoustical Physics, Vol. 46, No. 1, 2000, pp. 71–75. Translated from Akusticheskiĭ Zhurnal, Vol. 46, No. 1, 2000, pp. 84–88.

Experimental Study of a Planar Active Noise Control System

E. V. Korotaev and V. V. Tyutekin

Andreev Acoustics Institute, Russian Academy of Sciences,
ul. Shvernika 4, Moscow, 117036 Russia
e-mail: bvp@akin.ru

Received April 7, 1999

Abstract—The general principles of the construction of planar active noise control systems are discussed. A flow chart of such a system based on the decomposition of sound fields into spatial harmonics is presented. An experimental noise control system suppressing the first two ($n = 0$ and $n = 1$) horizontal harmonics of a sound field is designed. Experiments performed in a hydroacoustic basin with this system are described. The soundproofing properties of the system are studied by comparing the sound levels measured behind the system with the latter being turned on and off. The frequency characteristics of the system efficiency are presented for different angles of incidence of plane sound waves in the frequency range 1–5 kHz. © *2000 MAIK "Nauka/Interperiodica".*

The problem of reducing the levels of noise fields or reflected sound fields is usually solved by applying sound-insulating, sound-absorbing, and other types of materials and structures. However, these methods are quite efficient at high frequencies, while at low frequencies (hundreds of hertz to several kilohertz), the necessary thicknesses of the aforementioned materials are too large. In the low-frequency range, better results can be achieved with the active methods of noise control, as evidenced by numerous publications (including the recent ones) concerned with this problem [1–7].

The most simple active noise control system that provides the suppression of sound fields in a given spatial region is the planar system described by Tyutekin [1]. For this system, a mathematical simulation was carried out with a relatively simple model of data processing: each receiver of the planar receiving array was connected through a controlled delay line with only one, opposite, radiator of the planar radiating array (the latter was parallel to the receiving one). The disadvantage of such a system is the presence of an amplification (rather than attenuation) of the arriving sound wave at the angles of incidence above 60°–65°.

Another approach to constructing active noise control systems including planar ones is the expansion of the primary and secondary sound fields in orthogonal spatial harmonics [8, 9]. This method uses the assumption that there exist some unidirectional receiving and radiating Huygens surfaces forming a coordinate surface in the orthogonal coordinate system (e.g., a plane, a cylinder, or a sphere). In the general case, the construction of an active noise control system with the use of orthogonal spatial harmonics was described by Boĭko and Tyutekin [2]. By analyzing the primary fields with the help of receivers to which certain weight coefficients are supplied, one can determine the complex amplitude for every harmonic. Supplying similar coefficients to the radiators, one can synthesize and radiate individual harmonics with given amplitudes and phases. Every "received" harmonic is related to the identical radiated harmonic by its middle block providing the suppression of this harmonic. The acoustic feedback between the receiving and radiating surfaces is absent, because the surfaces are unidirectional, and the coupling of harmonics is absent, because they are orthogonal to each other. The structure of such an active system is quite convenient for practical realization, because this system can be divided into independent "one-dimensional" channels. Approximate calculations show that the necessary number of harmonics is roughly equal to the number of receivers (radiators).

On the basis of the general concepts of constructing active systems using radiating and receiving Huygens surfaces with the decomposition of fields into orthogonal harmonics, a planar active noise control system was developed by Korotaev and Mazanikov [10]. This system is the most simple one in terms of the simplicity of the coordinate system in which the acoustic field is expanded in spatial harmonics. Some difficulties are caused by the fact that such a system can only be finite and hence cannot form a closed surface. The arrangement of the system in a screen presents a complicated technical problem; therefore, we did not use this method in our studies. The active system described below was developed in application to a water medium. In this case, the construction of radiating and receiving Huygens surfaces is best consistent with the theory, because the individual receiving and radiating elements can be represented by spherical piezoelectric transduc-

1063-7710/00/4601-0071$20.00 © 2000 MAIK "Nauka/Interperiodica"

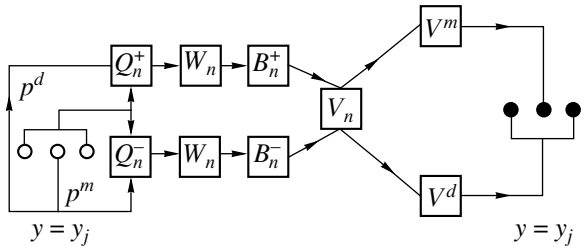

Fig. 1. Flow chart of a planar active noise control system (notations are given in the main body of text).

ers of size much less than the sound wavelength. We note that in contrast to this case, in aeroacoustics it is possible to use only microphones (receiving elements) and electrodynamic transducers (radiating elements) that do not fully comply with the theoretical model, at least because of the appearance of directivity with increasing frequency. In addition, the wavelength in water is approximately five times that in air; therefore, at equal frequencies, the necessary number of receiving and radiating elements in water is less than in air.

This paper is devoted to the development of active noise control systems on the basis of plane-parallel receiving and radiating arrays and to the study of their abilities to suppress the sound fields in a given spatial region, in a wide frequency range and a wide range of angles of incidence of external waves. Special attention is paid to the development of noise control systems that on the one hand are highly efficient and stable, and on the other hand have a practically reasonable number of radiators, receivers, and connections between them as well as sufficiently simple frequency characteristics of the electronic circuits and simple requirements on their tuning.

On the basis of the results obtained by Korotaev and Mazanikov [10], we designed an experimental model of an active noise control system. The model was tested in a hydroacoustic basin. In the experiment, we used two subsystems providing the suppression of the horizontal harmonics $n = 0$ and $n = 1$ in the presence of a plane vertical harmonic. We note that one can design a system of sound suppression for an arbitrary incidence of a plane wave on the array surface; in this case, it is necessary to expand the sound field in two-dimensional harmonics.

The structures of each of the subsystems suppressing the spatial harmonics of given numbers are also developed on the basis of the aforementioned paper [10]. These structures take into account the finite number of receivers and radiators of the "tripole" type (monopole + dipole) and their discrete arrangement in the planes of the receiving and radiating arrays.

Figure 1 shows the flow chart of the system. This flow chart illustrates the algorithm of the data processing. In the figure, $p^m(y_j)$ and $p^d(y_j)$ denote the sound pressures received by the monopole and dipole, respectively, at the point $y = y_j$ ($j = 1 \ldots N$). Other notations are as follows:

$$Q_n^+ = \sum_{j=1}^{N} (p^m(y_j) + a_n p^d(y_j)) \cos\frac{n\pi y_j}{D};$$

$$Q_n^- = \sum_{j=1}^{N} (p^m(y_j) + a_n p^d(y_j)) \sin\frac{n\pi y_j}{D};$$

$$a_n = (2i\sin(kl\cos\varphi_n))^{-1};$$

$$\cos\varphi_n = \left(1 - \left(\frac{n\pi}{kD}\right)^2\right)^{0.5}; \quad (1)$$

$$W_n = -\frac{ik\cos\varphi_n}{\omega}\exp(ikL\cos\varphi_n); \quad B_n^{\pm} = Q_n^{\pm} W_n;$$

$$V^{m,d}(y_j) = \frac{1}{2}\sum_{n=0}^{M}\left(B_n^+\cos\frac{n\pi y_j}{D} + B_n^-\sin\frac{n\pi y_j}{D}\right)q_n,$$

where $2l$ is the dipole size, D is the array width, L is the distance between the radiating and receiving surfaces, M is the number of harmonics, and q_n = {1 for the monopole radiator and $(ik\cos\varphi_a)^{-1}$ for the dipole radiator}. Here, $V^m(y_j)$ and $V^d(y_j)$ are quantities proportional to the voltages supplied to the monopole and dipole radiators, respectively.

The experimental results showed that the radiating and receiving arrays constructed according to the algorithm described above are unidirectional in a wide frequency band at a level no lower than –20 dB. The receiving and radiating surfaces were oriented so that the minima of their directional characteristics were directed toward each other for every harmonic. Therefore, the acoustic coupling of the arrays was no worse than –40 dB, which ruled out a self-excitation of the system. Structurally, each array consisted of vertical linear arrays containing six "tripole" elements each. In each plane, the elements were positioned at the points of a hexagonal lattice. The spherical transducers of diameter 3 cm were made of barium titanate. The central elements of "tripoles" were used as the monopole elements, and the two peripheral elements formed the dipole ones. The distances between the monopole elements satisfy the condition of a "dense" array, $d < \lambda/2$. The parameters have the following values: $d = 16$ cm, and $\lambda_b = 37.5$ cm is the wavelength at the upper frequency of the operating range 2–4 kHz. The linear dimensions of the system are as follows: $2D = 80$ cm, and the distance between the planes of the arrays is $L = 30$ cm. The measurements were performed using a

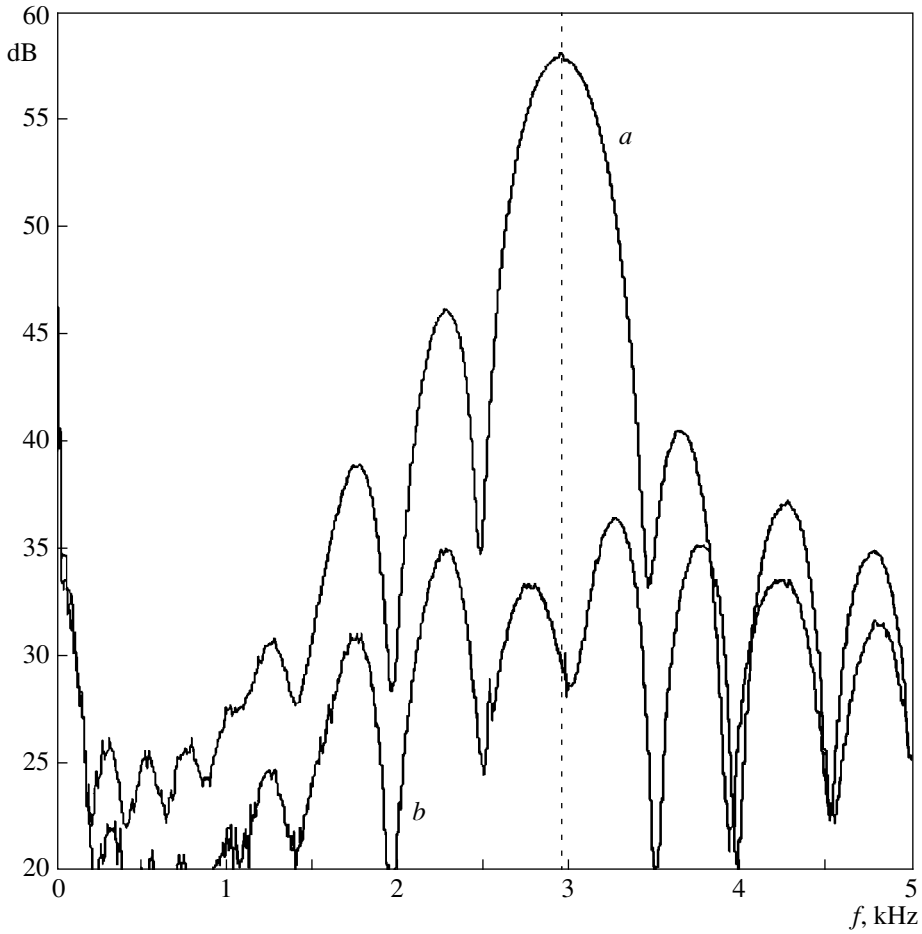

Fig. 2. Spectrum functions of the pulses transmitted through the system: the system is turned (*a*) off and (*b*) on.

pulse method in order to separate (in time) the signal transmitted through the system from the signals reflected (although attenuated) from the basin walls. A spherical source of the primary (incident) sound field was positioned before the receiving array at a distance $r > (2D)^2/\lambda_b$, which made it possible to consider the incident wave as a plane one.

The system was tuned to the mode of suppression of the incident waves by the readings of the control hydrophone placed behind the radiating array (in the shadow zone). The tuning was accomplished by varying the amplification coefficients (which were frequency independent) and controlling the phase-frequency characteristics of the delay lines W_0 and W_1. In this manner, it was possible to form a sufficiently dark shadow (efficient sound suppression) behind the radiating array.

Figure 2 presents the spectrograms of pulses transmitted through the system when the latter was turned off (a) and on (b), for the carrier frequency 3 kHz. The efficiency of the system at the "central" frequency was estimated by the difference in the corresponding sound levels at this very frequency. The efficiency values observed at the "side" frequencies were used for comparison or for illustration.

The experimental data characterizing the efficiency of the suppression of the zeroth and first harmonics as a function of frequency are presented in Fig. 3 (the

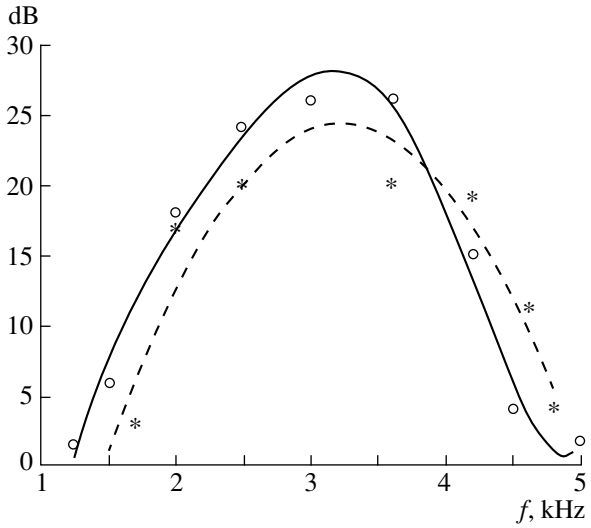

Fig. 3. Frequency dependences of the efficiency of the planar active system for the harmonics with (○) $n = 0$ and (*) $n = 1$.

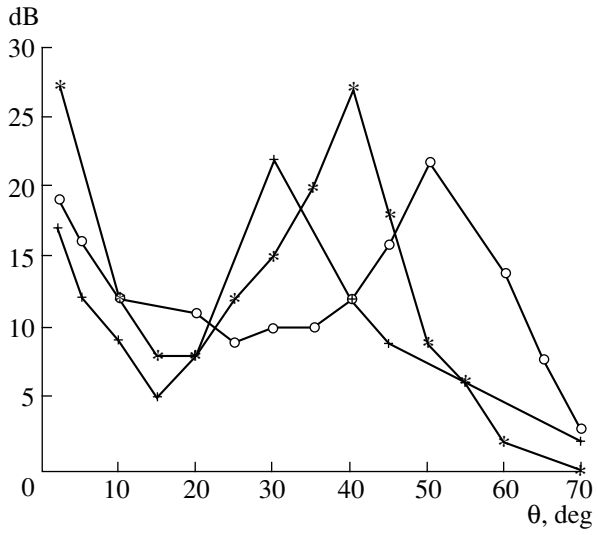

Fig. 4. Angular dependence of the efficiency of the planar active system (θ_0 is the angle of incidence of a plane wave) for the frequencies (+) 2.3, (∗) 3, and (○) 4 kHz.

curves are obtained by averaging over the experimental points). The control hydrophone was positioned at the center of the plane of the system, and the primary wave was incident on the system either normally ($n = 0$) or at the angle $\varphi \approx 38°$ ($n = 1$). From Fig. 3, we can draw the following inferences. The maximum efficiency in terms of sound insulation is achieved at the frequencies 3–3.5 kHz and reaches 24–28 dB for both harmonics. The frequency dependence is typical for this kind of system (the efficiency decreases with the frequency approaching the boundaries of the operating range) [11]. The whole frequency band is 1.5–5 kHz, the negative efficiency values are absent, and the system is resistant to self-excitation.

Figure 4 shows the experimental data on the efficiency of the system in the case of the simultaneous "operation" of the harmonics with $n = 0$ and $n = 1$ versus the angle of incidence of the primary field, for some frequencies of the operating frequency range. The solid lines connect the experimental points corresponding to the same frequency. Each of these curves has two efficiency maxima, which are caused by the fact that the conditions of total suppression are fulfilled for $n = 0$ at normal incidence, and for $n = 1$ at the angles of incidence determined by formula (1). For intermediate angles of incidence, these conditions are fulfilled only approximately, because, in the system under study, the complex coefficients W_n are independent of the angle of incidence.

For a real active system, the average efficiency over an angular interval increases with increasing number of harmonics (i.e., with increasing wave dimensions of the receiving and radiating arrays). In fact, the total number of harmonics N can be determined from the condition

$$\cos^2\varphi_N = 1 - (N/kD)^2 \geq 0.$$

Hence, we have $N \leq \frac{2D}{\lambda}$. Since the maximum efficiency is achieved at the angles $\varphi = \pm\varphi_n$ ($0 \leq n \leq N$), the number of such efficiency "peaks" increases with increasing N. At the intermediate angles, the efficiency of the system also increases.

In closing, we note that the "control" part of the system described above was based exclusively on analog methods. Judging from the numerous publications concerned with active noise control methods, one can expect that the employment of a computer control (specifically, in the tuning process) will lead to an increase in the efficiency of the system.

Thus, the data on the efficiency of the experimental model of a planar noise control system suggest the following conclusions:

1. The theoretical foundations of the development of active noise control systems based on the method of orthogonal spatial harmonics are justified by the experimental data on the efficiency of the model of a planar active noise control system.

2. The structure of the planar active noise control system considered above can be (with some modifications) extended to other forms of orthogonal spatial harmonics.

ACKNOWLEDGMENTS

This work was supported by the Russian Foundation for Basic Research (project no. 98-02-16231).

REFERENCES

1. V. V. Tyutekin, Akust. Zh. **43**, 238 (1997) [Acoust. Phys. **43**, 202 (1997)].
2. A. I. Boĭko and V. V. Tyutekin, Akust. Zh. **45**, 454 (1999) [Acoust. Phys. **45**, 402 (1999)].
3. J. Guo, J. Pan, and C. Bao, J. Acoust. Soc. Am. **101** (3) 1492 (1997).
4. Z. Wu, V. K. Varadan, and V. V. Varadan, J. Acoust. Soc. Am. **101**, 1502 (1997).
5. S. Uosukainen, ACUSTICA–Acta Acustica **63**, 105 (1997).

6. K. Wicker, and E. Arens, ACUSTICA–Acta Acustica **85**, Suppl. 1, S47 (1999).

7. C. R. Fuller and P. E. Cambou, ACUSTICA–Acta Acustica **85**, Suppl. 1, S102 (1999).

8. M. P. Zavadskaya, A. V. Popov, and B. L. Egel'skiĭ, Akust. Zh. **21**, 882 (1975) [Sov. Phys. Acoust. **21**, 541 (1975)].

9. A. A. Mazanikov, V. V. Tyutekin, and M. V. Fedoryuk, Akust. Zh. **26**, 759 (1980) [Sov. Phys. Acoust. **26**, 428 (1980)].

10. E. V. Korotaev and A. A. Mazanikov, Akust. Zh. **31**, 539 (1985) [Sov. Phys. Acoust. **31**, 323 (1985)].

11. A. A. Mazanikov, and V. V. Tyutekin, Akust. Zh. **24**, 788 (1978) [Sov. Phys. Acoust. **24**, 447 (1978)].

Translated by E.M. Golyamina

Acoustical Physics, Vol. 46, No. 1, 2000, pp. 76–79. Translated from Akusticheskiĭ Zhurnal, Vol. 46, No. 1, 2000, pp. 89–93.

Active Volume Sound Absorber

A. A. Mazanikov

Murmansk State Technical University, ul. Sportivnaya 13, Murmansk, 183010 Russia
e-mail: Alexander.Mazanikov@mstu.edu.ru

Received December 18, 1998

Abstract—A model of an active sound absorber whose efficiency is higher than the efficiency of a passive absorber of the same size is considered. Examples are provided in which the energy is predominantly absorbed on the rear (with respect to the incident acoustic wave) of the absorber. © *2000 MAIK "Nauka/Interperiodica".*

In essence, passive volume sound absorbers imitate black bodies, which completely absorb the energy of incident acoustic waves. It is well known [1] that complete absorption is only possible for bodies of infinite dimensions compared with the wavelength. There are several models of black bodies of finite wave dimensions [1] with different boundary conditions at the body surface. One of the possible versions is a body with an impedance surface (when a plane wave is normally incident on a plane surface with such properties, complete absorption occurs). This passive absorber can be implemented with a certain accuracy. The requirement that the absorber be passive imposes some constraints on the absorber characteristics. An active system (currently, active methods are being intensively developed [2–6]) is free from many of these constraints, which improves its efficiency and endows it with certain specific properties. We perform a comparative analysis of passive and active absorbers by the example of spherical absorbers subject to an incident monochromatic acoustic wave.

Consider a spherical absorber of radius R (Fig. 1) in the three-dimensional space (we use the spherical coordinates, the factor $\exp(-i\omega t)$ is omitted). For simplicity, we assume that the field is cylindrically symmetric, i.e., independent of the angle φ. Near the absorber, in the region free from other bodies and acoustic sources, the field can be represented in the form

$$p = p_0 + p_1 = \sum_{n=0}^{\infty} (A_n j_n(kr) + B_n h_n^{(1)}(kr)) P_n(\cos\vartheta), \quad (1)$$

where $j_n(z) = \sqrt{\frac{\pi}{2z}} J_{n+1/2}(z)$ and $h_n(z) = \sqrt{\frac{\pi}{2z}} H_{n+1/2}(z)$ are the Bessel and Hankel spherical functions and $P_n(z)$ are the Legendre polynomials. The fields p_0 and p_1 are created by the external sources and the absorber, respectively.

Representation (1) can be used to calculate the total energy flux through the absorber surface. Since the surface is absorbing, the flux is negative. As a criterion of the absorber efficiency, we use the ratio of this flux to the energy flux through the absorber geometric section $S = \pi R^2$.

The energy flux through a unit spherical surface of radius $r = R$ is [7]

$$W = (p^* v_r + p v_r^*)/4, \quad (2)$$

where the radial velocity v_r is expressed by the formula

$$v_r = \frac{1}{i\rho\omega}\frac{\partial p}{\partial r} = \frac{1}{i\rho c}\sum_{n=0}^{\infty} (A_n j_n'(kr) + B_n h_n^{(1)'}(kr)) P_n(\cos\vartheta), \quad (3)$$

where ρ is the medium density, and here and below, the derivatives of the Bessel functions are calculated with

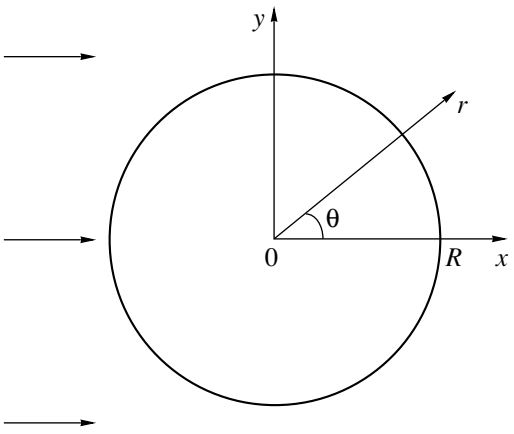

Fig. 1. Problem geometry.

1063-7710/00/4601-0076$20.00 © 2000 MAIK "Nauka/Interperiodica"

respect to the argument kr. Then, the energy flux through the surface of the sphere $r = R$ is

$$E = \frac{\pi R^2}{2}\int_0^\pi (p^* v_r + p v_r^*)\sin\vartheta d\vartheta. \quad (4)$$

Using the orthogonality relation for the Legendre polynomials

$$\int_0^\pi P_n(\cos\vartheta)P_m(\cos\vartheta)\sin\vartheta d\vartheta = \frac{2\delta_{nm}}{2n+1}$$

(δ_{ij} is the Kronecker delta) and formula for the Bessel function Wronskian $j_n(z)h_n^{(1)'}(z) - j_n'(z)h_n^{(1)}(z) = i/z^2$, after some algebra, we obtain

$$E = \frac{2\pi}{\rho c k^2}\sum_{n=0}^{\infty}\frac{1}{2n+1}\left(\left|\frac{A_n}{2} + B_n\right|^2 - \left|\frac{A_n}{2}\right|^2\right). \quad (5)$$

This expression shows that the maximum absorber efficiency (minimum negative energy flux through the absorber surface) is achieved at $B_n = -A_n/2$ (some results on the optimization of spherical active systems have been obtained in [8, 9]). Since $j_n(z) = [h_n^{(1)}(z) + h_n^{(2)}(z)]/2$, this absorber must produce the field that completely cancels the diverging waves of the external field so that the residual field in the space consists of only converging waves.

Compare the behavior of the passive and active absorbers by the example of absorption of the plane wave

$$p_0 = \exp(ikr\cos\vartheta) = \sum_{n=0}^{\infty} i^n(2n+1)j_n(kr)P_n(\cos\vartheta). \quad (6)$$

We will model the passive absorber by an impedance sphere on whose surface the boundary condition $p/v_r = -\rho c$ is satisfied. Since the boundary condition must be fulfilled for any incident field, it must be met for all numbers of harmonics in expressions (1) and (3). Then, the coefficients B_n in (1) can be expressed as

$$B_n = -\frac{j_n'(kR) + ij_n(kR)}{h_n^{(1)'}(kR) + ih_n^{(1)}(kR)}A_n. \quad (7)$$

At $n \ll kR$, we use the short-wave asymptotics of the Bessel functions to obtain $B_n \approx -A_n/2$, i.e., the converging low-index harmonics are almost completely absorbed. At $n \gg kR$, the Hankel functions rapidly increase in absolute value, while the Bessel functions decrease; therefore, $B_n \longrightarrow 0$ so that the impedance sphere exerts almost no effect on the high-index harmonics. This behavior is typical of not only the impedance absorber, but also any other passive scatterer that imitates the black body [1]. The absorbed energy can be determined by substituting coefficients (7) into (5) and taking into account that for a plane wave, $A_n = i^n(2n+1)$.

As a model of the active absorber, we consider an active system similar to the one described in [10], which contains acoustically transparent surfaces composed of monopole and dipole receivers and radiators. The outer surfaces $r = R_3$ and $r = R_4$ are occupied by the radiators, and the inner surfaces $r = R_1$ and $r = R_2$ carry the receivers (we assume that $R_1 < R_2 < R_3 < R_4 = R$). The active system must use the results of measurements to find the amplitudes A_n of the external field harmonics and radiate diverging waves with the harmonic amplitudes $B_n = -A_n/2$ into the external space in such a manner that the field is not radiated inside the sphere $r = R_3$ (in this case, the active system does not affect its own receivers). The radiation problem has been solved in [10]: if we denote the input actions applied to the radiators (for example, electric voltages) by $U(R_j, \vartheta)$, $j = 3$, 4, and assume that the electroacoustic conversion factors are equal to unity, we obtain

$$U_n^4 = \frac{iA_n h_n^{(1)}(kR_3)}{2(kR_4)^2(j_n(kR_3)h_n^{(1)}(kR_4) - j_n(kR_4)h_n^{(1)}(kR_3))},$$
$$U_n^3 = -\left(\frac{R_4}{R_3}\right)^2\frac{h_n^{(1)}(kR_4)}{h_n^{(1)}(kR_3)}U_n^4, \quad (8)$$

where

$$U_n^j = \frac{2n+1}{2}\int_0^\pi U(R_j, \vartheta)P_n(\cos\vartheta)\sin\vartheta d\vartheta. \quad (9)$$

The reception problem can be solved similarly to [10]: the coefficients A_n are calculated from the data obtained by the receivers $U(R_j, \vartheta)$, $j = 1$, 2, (at unity conversion factors) by the formula

$$A_n = \frac{U_n^1 h_n^{(1)}(kR_2) - U_n^2 h_n^{(1)}(kR_1)}{j_n(kR_1)h_n^{(1)}(kR_2) - j_n(kR_2)h_n^{(1)}(kR_1)}. \quad (10)$$

One of the problems that arises in developing active systems is to refer the data obtained on the receiving surfaces to the radiating surfaces. Omitting the related formulas, note that the phase characteristics of the obtained transfer functions monotonically increase with frequency, which basically allows one to implement such an active absorber in an arbitrarily wide frequency range.

The active absorber can be implemented only for a finite number of harmonics not only because a processor for an infinitely large body of information cannot be created, but also due to the specific behavior of the Bessel functions with increasing order at a fixed argument: the absolute value of the Hankel function rapidly increases, while that of the Bessel function rapidly decreases. As a result, when implementing the active system according to formulas (8)–(10), one has to deal

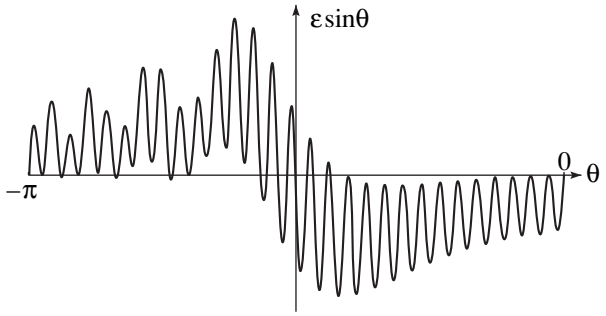

Fig. 2. Absorbed energy distribution over the surface of the active absorber.

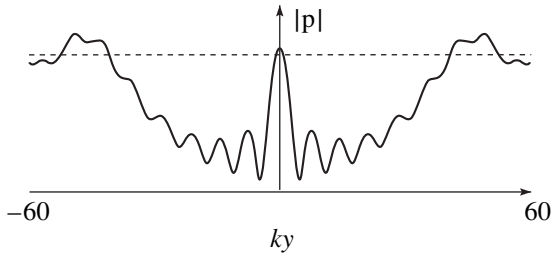

Fig. 3. Field distribution in a plane behind the absorber, outside its effective volume.

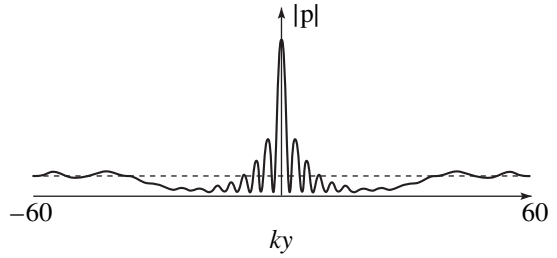

Fig. 4. Field distribution in a plane behind the absorber, inside its effective volume.

with very small (when receiving) and very large (when radiating) quantities. Even in computer simulations of an active absorber (the results are discussed below), serious problems arise with the word length when $n - kR > 25$.

Below, we assume that the active system absorbs the harmonics of the external field with indices up to $n = N - 1$ (the number of absorbed harmonics is N). In this case, the absorbed energy of the incident plane wave can be exactly calculated from formula (5):

$$E = \frac{2\pi}{\rho c k^2}\sum_{n=0}^{N-1}\frac{1}{2n+1}\left(-\left|\frac{A_n}{2}\right|^2\right) = -\frac{\pi}{2\rho c k^2}\sum_{n=0}^{N-1}\frac{(2n+1)^2}{2n+1} = -\frac{\pi N^2}{2\rho c k^2}. \quad (11)$$

All results of simulations provided below are given for the normalized (by the energy flux of the plane wave through the absorber cross-section) quantity $\tilde{E} = E/(\pi R^2/2\rho c)$. At $N = kR$, this normalized quantity is exactly equal to –1.

In addition to the total absorbed energy, we calculated the absorbed energy density as a function of the angle ϑ and the energies $\tilde{E}^+$ and $\tilde{E}^-$ absorbed by the left and right hemispheres (Fig. 1). When a plane wave is incident on a perfect black body of infinite wave dimensions ($kR \longrightarrow \infty$) from the left, all its energy is absorbed by the left hemisphere, while the right one is in the shadow zone, where the field and consequently the energy flux are zero.

Figure 2 shows the absorbed energy density ε as a function of the angle ϑ for the active system with the wave dimension $kR = 20$ and suppressing the harmonics with indices up to $N = 30$. The angle ϑ is represented by the abscissa (for convenience, the plot is reversed so that its extreme left point corresponds to the extreme left point of the sphere in Fig. 1). The plot shows that unlike the perfect black body of infinite wave dimensions, the energy is absorbed mostly by the right hemisphere rather than by the left one that radiates energy. The energy radiation and absorption per unit surface are maximum at the extreme left and extreme right points of the sphere (in Fig. 2, the energy density is multiplied by $\sin\vartheta$; the plot of the energy density has only two narrow peaks at the extreme points). Calculations performed for other values of N show that when N is slightly greater than kR, the absorption and radiation regions exist on the left and right hemispheres. As N increases, the absorption regions on the left hemisphere shrink and disappear; on the right hemisphere, an opposite process evolves.

At a distance $kr > N$ from such an active absorber, the field is almost the same as the field of a passive absorber of the dimension $kR = N$. Figure 3 shows the field amplitude in the cross-section perpendicular to the plane wave propagation direction and located at the distance $kx = 60$ behind the sphere for $N = 30$. The central region represents the shadow zone whose width corresponds to the cross-section of a sphere with $kR = 30$ (the actual absorber dimension is $kR = 20$). At the center of the shadow zone, one can see a peak known as the Poisson spot. At the distances $kR < kr < N$ from the active absorber, the field looks quite different. Figure 4 shows a plot similar to the previous one for $kx = 25$. The central part of the plot corresponds to the near-field region of the active absorber, where the field is much stronger than the unit incident field. The effect of the active absorber on the total field actually manifests itself in the shadow-lobe radiation, its width corresponding to an antenna with the wave radius N, rather than to the actual dimension of the radiator kR. In antenna theory, this phenomenon is called the supergain.

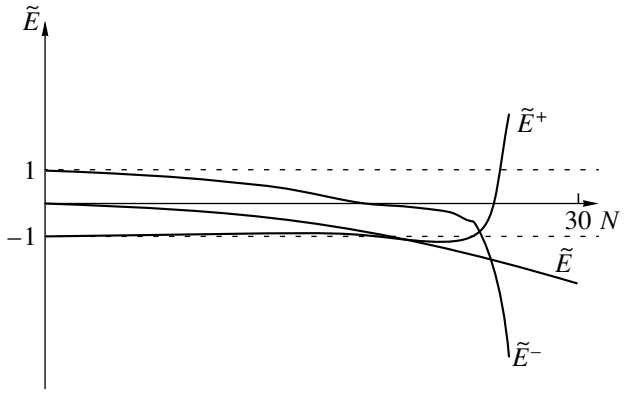

Fig. 5. Absorbed energy against the absorber effective dimension.

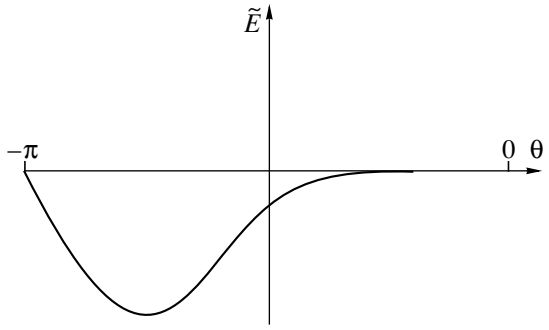

Fig. 6. Distribution of the absorbed energy over the surface of the impedance sphere.

Figure 5 shows the total absorbed energy $\tilde{E}$ and the energies $\tilde{E}^+$ and $\tilde{E}^-$ absorbed by the left and right hemispheres, respectively, calculated at $kR = 20$ as a function of the number of absorbed harmonics N. At small N, the left hemisphere absorbs the incident energy almost completely, but the right one reradiates almost the same amount, so that the plane wave does not notice such an absorber with a small effective dimension. As N increases up to kR, the absorption on the left remains almost unchanged, while the radiation on the right significantly decreases, so that the total absorbed energy increases. As N increases further, the absorption behavior becomes reversed: the left hemisphere starts radiating and the right one starts absorbing; the total absorbed energy corresponds to formula (11).

Figure 6 shows a plot similar to the one in Fig. 2 for an impedance sphere with $kR = 20$; the plot is obtained using formula (7). As could be expected, the major part of the energy is absorbed by the left hemisphere, though a low absorption exists on the right due to the energy diffracted into the shadow zone. Note that this plot hardly differs from the similar plot for the active absorber with $N = kR = 20$.

Thus, the active absorber allows one to increase the effective absorption cross-section. Theoretically, this increase can be made arbitrarily large, though, in practice, it is limited by the difficulties associated with near fields. The distribution of absorption and radiation regions on the absorber surface is also of interest. In view of the above note that it is possible to design a wideband absorber whose operation does not contradict the causality principle, the increase in the effective cross-section and absorbtion by the rear surface of the sphere mean that if a wave packet passes by the absorber so that the major part of its energy crosses the effective absorber cross-section, but does not cross its physical cross-section, this packet will be captured by the absorber and absorbed by the right hemisphere. This behavior is somewhat similar to the astrophysical black hole.

ACKNOWLEDGMENTS

This work was supported by the Russian Foundation for Basic Research, project no. 98-02-16231.

REFERENCES

1. L. N. Zakhar'ev and A. A. Lemanskiĭ, *Wave Scattering by Black Bodies* (Sov. Radio, Moscow, 1972).
2. S. Uosukainen, ACUSTICA–Acta Acustica **83**, 105 (1997).
3. V. V. Tyutekin, Akust. Zh. **43**, 238 (1997) [Acoust. Phys. **43**, 202 (1997)].
4. G. C. Laichle, J. R. MacGillivray, and C. D. Swanson, J. Acoust. Soc. Am. **101**, 341 (1997).
5. P. Kokowski and R. Makarewich, J. Acoust. Soc. Am. **101**, 360 (1997).
6. J. Guo, J. Pan, and C. Bao, J. Acoust. Soc. Am. **101**, 1492 (1997).
7. M. A. Isakovich, *General Acoustics* (Nauka, Moscow, 1973).
8. I. A. Urusovskiĭ, Akust. Zh. **30**, 267 (1984) [Sov. Phys. Acoust. **30**, 155 (1984)].
9. I. A. Urusovskiĭ, Akust. Zh. **32**, 560 (1986) [Sov. Phys. Acoust. **32**, 354 (1986)].
10. A. A. Mazanikov, V. V. Tyutekin, and M. V. Fedoryuk, Akust. Zh. **26**, 759 (1980) [Sov. Phys. Acoust. **26**, 428 (1980)].

Translated by A.D. Khzmalyan

Acoustical Physics, Vol. 46, No. 1, 2000, pp. 8–14. Translated from Akusticheskiĭ Zhurnal, Vol. 46, No. 1, 2000, pp. 13–20.

Creating Virtual Sound Objects

A. V. Agranovskiĭ and G. E. Evreinov

Spetsvuzavtomatika State Design Bureau, Gazetnyi 51, Rostov-on-Don, 344007 Russia
e-mail: asni@ns.rnd.runnet.ru

Received February 24, 1997

Abstract—How is an auditory contour pattern perceived? What additional attributes must be adjusted to stabilize the perception of the boundaries of a virtual sound pattern in order to form an auditory perception isomorphous to the visual one? A possibility to correct the perception of subjective patterns through controlling the parameters (the frequency deviation and the duration at the critical points) of virtual sound patterns created by the illusion of the apparent motion of acoustic sources is discussed. *© 2000 MAIK "Nauka/Interperiodica".*

Unlike the voluntarily fixable visual attention, for a sound pattern created by the apparent motion of virtual sound sources, it is necessary to efficiently control the parameters that can be used to keep attention of the auditory system continuously focused on the sound sequence developing in time. The attention-control process is quite complicated and insufficiently studied until now.

How is a sound contour pattern perceived? What additional attributes must be adjusted to stabilize the perception of the boundaries of the virtual auditory pattern in order to form an auditory perception isomorphous to the visual one?

We create virtual sound patterns with the help of a vector audio display [1–3]. The device consists of a single-piece acoustic module controlled via a special-purpose interface, which operates four electrodynamical acoustic sources supplied with settings that limit the insonified sector to 90°. The sources are placed at the corners of a square with sides 0.46 m in length and at a 0.6-m distance from the auditory channels of the subject, whose head is free (no limitations are placed on the motion) and eyes are closed. The 0.46-m distance was accepted as the base and height of the acoustic plane. The programmable interface creates graphic objects on a monitor screen and then makes a sound pattern of them by moving one or more sound cursors (virtual acoustic sources) formed by controlling the space position of an interference maximum of the sound signal created by these four acoustic sources by the rule

$$A_1 + A_2 + A_3 + A_4 = B = \text{const} \tag{1}$$

or

$$\begin{aligned} &AX(1-Y) + A(1-X)(1-Y) \\ &+ AXY + A(1-X)Y = B, \end{aligned} \tag{2}$$

where A is the signal amplitude, X and Y are the current coordinates in the interval [0, 1] with the origin at the lower left point of the image plane, and B is the subjectively perceived volume of the acoustic source. Therefore, a subjective sound pattern described by the subject can be compared to the real image on the monitor screen. The virtual acoustic plane was additionally simulated by a sheet of paper, on which the tested person reproduced one's subjective impression with a soft-tip pen immediately after observing the presented sound objects while keeping one's eyes closed.

The general view of the part of the interface concerned with creating graphic objects is shown in Fig. 1a. It consists of Windows 95 software modules written in Visual Basic 4.0. The module that creates the graphic objects uses a fixed workspace of $M \times M = 128 \times 128$ points. In a sense, it is similar to the matrix of virtual sound sources [4–6], but has an eight times higher spatial resolution and provides the necessary continuous insonification without applying special interpolation methods to the sound signal between the points. Interpolation is used only for drawing the image.

The toolbar serves to create standard graphic objects, namely, straight lines (a segment or polygonal line), arc, circle, ellipse, rectangle, and arbitrary curve, and to copy and arbitrarily move them within the workspace. The control panel can be used for editing the sound attributes of the graphic objects. An additional panel provides the pointwise editing of the image fragments. This function includes marking the critical points (end points or intermediate ones) that are necessary to control the perception process and adjust an arbitrary number of silent points.

The general view of the sound-control part of the programmable interface is shown in Fig. 1b. The sound frequency can be changed within 100–5000 Hz, though, in our experiments, it was no higher than 800 Hz. The built-in oscillators and attenuators of the acoustic module are controlled with 8-bit analog-to-digital converters to provide a wide choice of sound frequencies and volumes. A relatively wide band of the sound signal was provided by its almost rectangular envelope. The frequency deviation (D_x and D_y) was controlled as a

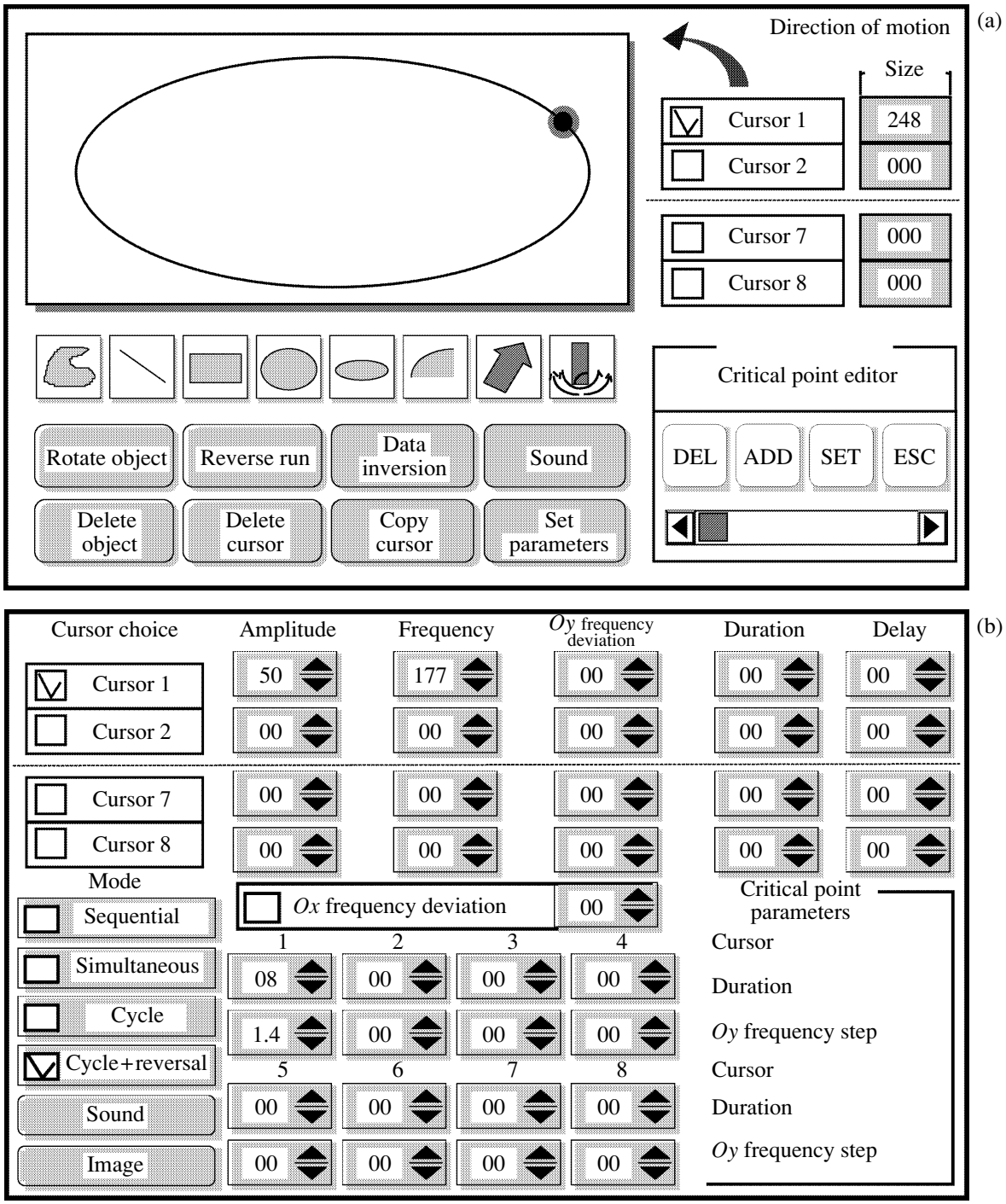

Fig. 1. (a) Creation of graphic objects and (b) sound parameter control.

function of the image point coordinates (X, Y): in the Oy axis, independently for each cursor and, in the Ox axis, simultaneously for all cursors. The initial frequency F_0 was associated with $X = 0$, $Y = 128$, i.e., the frequency decreased when the point moved downwards and increased when it moved from the left to the right, so that the lowest frequency is adjusted at the lowest left position of the virtual plane, while the highest frequency is at its upper right point.

Additionally adjustable parameters are the sound duration and the frequency step at the critical points (end or intermediate ones) of each fragment of the sound pattern.

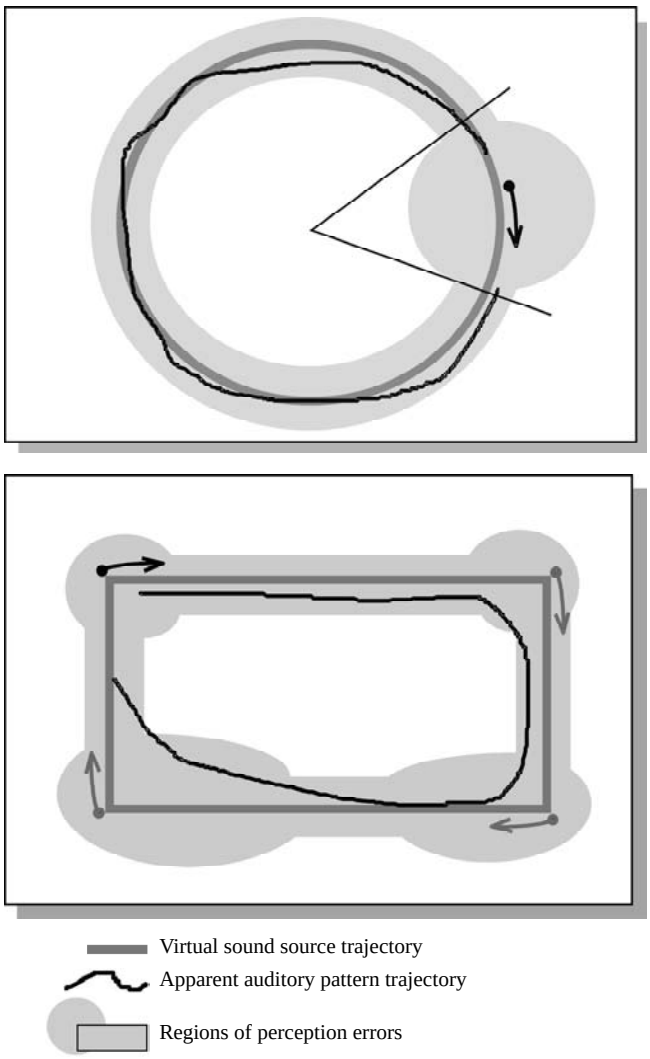

Fig. 2. Virtual sound pattern perception with no critical point marking.

The time parameters are adjusted individually for each cursor with a 1-ms quantum. One should distinguish between the parameter indicated as the *duration*, which determines the rate of changing the current coordinates of the given cursor (which is equivalent to the sound duration at the current point of the array), and the parameter marked as the *delay*, which controls different time parameters depending on the mode of creating the sound pattern. When the sound cursors are presented sequentially, the *delay* function introduces a lag in activating the first point of the next fragment with respect to the last point of the previous one. When the sound cursors are activated simultaneously, the *delay* parameter shifts the beginning of activating the first point of the presented sound pattern with respect to the moment of pushing the *sound* button by a given interval. The sound duration at the critical points is determined as a multiple of the sound duration at the current point plus 4 ms.

Fragments of the sound pattern created by the related sound cursor can be presented sequentially or in parallel with synchronized start moments, or asynchronously for each cursor: in a single run with possible reversal or in cycles.

The software interface provides a standard set of functions for managing the created files.

Let us study the perception of a fragment of a sound pattern. For better visualization, we use closed contours, in particular, a circumference and a rectangle. Figure 2 shows original graphic objects and their subjective auditory images from graphic reports of the tested persons after a single presentation, without special attributes used to indicate the initial point of the pattern. For the circumference, a sector can be shown around the start point, in which an uncertainty in localizing the trajectory causes significant errors in the perception of the presented sound pattern. The extent of this sector depends on the velocity of the virtual source, radius of the circumference, and signal spectral parameters. Distortions in the perception of the rectangular pattern are minimum near the points where the motion changes its direction, i.e., whose parameters require an additional processing time from the sensor system.

If at a certain time moment, the first (or any other critical) point of the sound pattern appears in the virtual acoustic plane, the new stimulus activates the orientation reaction, which is functionally characterized as the selective attention [8]. The orientation reaction has an excitation threshold and a latent period, which depend on the gradient of the physical parameters of the stimulus and on the initial activation level of the sensor system at the moment when the stimulus is presented. Therefore, the moment of subjective indication of the beginning of the sound pattern not necessarily coincides with the first sound point. The further development of the reaction and perception of the sound sequence substantially depends on the dynamics of the sound stimulus parameters and on such specific parameters of the auditory system as the minimum audible movement angle of the sound source [9]. When the stimulus parameters come to a steady state and stop changing, the attention dissipates. Any change in the stimulus keeps the indicated point in focus and concentrates the attention.

Let us use one sound cursor to represent a trajectory equivalent to a horizontal straight line of 100 points (0.36 m) placed in the central region of the virtual acoustic plane symmetrically relative to its side borders. Set the fundamental frequency on the sound control panel at 305 Hz. Set the frequency deviation along the *Ox* and *Oy* axes and the parameters of the additional critical point markers to the inactive state. Then, the subjective perception of the length of the given segment in a single run depends on the time interval within which the sound is emitted by 100 points (sequentially excited virtual sources).

Set the amplitude of the sound cursor at 50 dB. At a 4-ms sound duration at each point, the power of the virtual source (at 305 Hz) may appear to be insufficient to reliably locate the beginning of the segment, which may require the activation of several points. The same effect can be observed when insonifying the whole segment, in particular, at its end point. Therefore, the length estimation of the presented sound segment in the experiment stated in this manner is inefficient. The variance of the trajectory length in subjects' reports can be comparable with the length of the segment at any recording technique, and the number of points within the segment, as well as the fundamental frequency, is of small significance.

Note that the quantization of the virtual trajectory (stepwise changes in amplitudes of the four sources each 4 ms) can cause the *vibrato* sensation. However, this effect can be observed only with tone signals and the number of points $M < 64$ [3], and when the amplitudes of the tone and modulation are comparable. The stepwise changes in the level of the rectangular signal (at a rate of 250 Hz) that accompany the motion of the sound cursor (305 Hz) are less than 0.5 dB (at $M = 128$). Interference of these signals is insignificant, because the difference frequency is at the edge of both the auditory perception and the frequency band of the used acoustic systems. Therefore, no special measures are needed to provide a continuous shape of the sound signal at $M \geq 128$.

Experiments on recognizing alphanumeric symbols have also shown that it is necessary to highlight the first point of each sound pattern [6]. In this case, the experiment provided 60–90% of correct answers. It is even more significant to highlight the critical points when several sound cursors interact within a single sound pattern (Fig. 6). An increase in the duration of sounding a point from 5 to 16 ms changes the subjective perception of the segment length (100 points) by a factor of two. Increasing the duration leads to a diffuse perception of the edge points; decreasing, to the degeneration of the impression of an extended object to a diffuse pattern.

In the first experiments, we marked the critical points by the sound duration using the repetitive sounding (at a fixed space position) a given number of times. However, this particular solution proved to have a low efficiency for more complex and faster presented sound patterns. The sound duration at critical points that is sufficient for stabilizing the attention was from 40 to 200 ms. For a 100-point segment, the edge points sounded up to 50% of the total time.

Since, in future experiments, we planned to study a possibility to form quasistatic virtual patterns (cursor, scale rules, window borders, and other attributes of the graphic interface), the mode of cyclic presentation of the sound pattern with an opportunity of the reverse presentation was introduced to the sound part of the software interface. The optimum values of certain frequency and time parameters that stabilize the perception of a sound pattern were determined in the cyclic mode using the direct and reverse runs, the result being tested in a single run. For example, at the given frequency and a 4-ms point sounding, when the critical points were not specially highlighted, the cyclic presentation of a straight segment caused a sensation of acoustic beats; however, the effect of horizontal motion was experienced by only a part of subjects (8 persons). When the sound duration at the end points increased to 40 ms, two diffuse regions could be clearly resolved between which the sound motion was perceived. At a 60-ms duration of the edge points, the impression of the motion of the virtual source became more clear, but the variance in perceiving the edge positions increased (it decreased as the sound duration at each point increased to 8 ms).

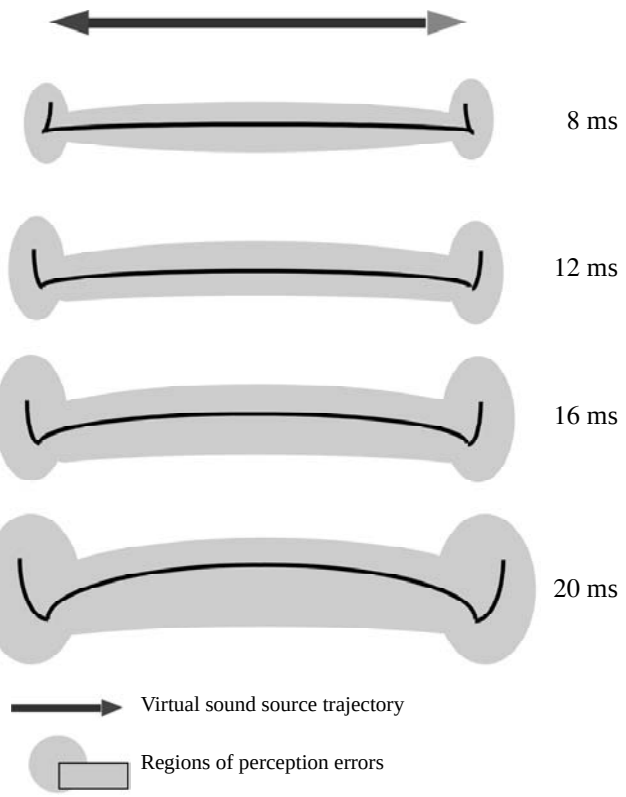

Fig. 3. Subjective images of a straight segment at different critical point durations.

Therefore, we decided to study a possibility of marking the critical points by simultaneously changing their sounding time and applying a deviation to the fundamental frequency (a stepwise frequency change at the critical point).

Under the same conditions (100 points, 305 Hz), the edge positions of the straight horizontal segment, the minimum sound duration at the critical points was adjusted at 8 ms, while the sound frequency was changed for this time from 305 to 725 Hz in a stepwise manner. This value was much higher than the one nec-

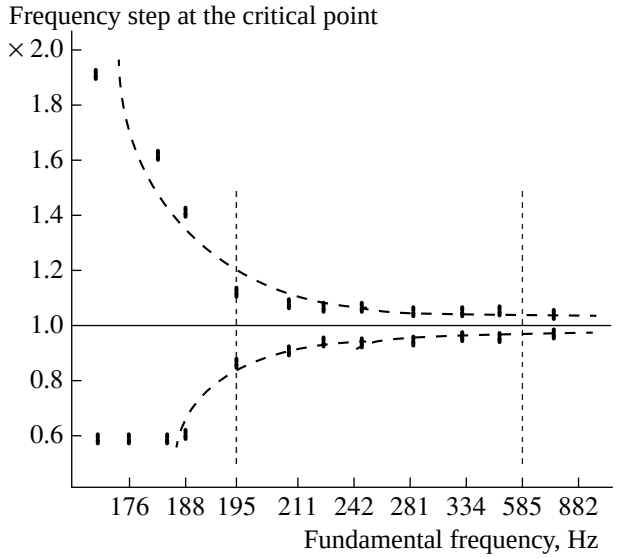

Fig. 4. Frequency step necessary for the efficient ($P > 90\%$) critical point localization in space against the fundamental frequency F_0 of the horizontally moving cursor (averaged over 8 subjects).

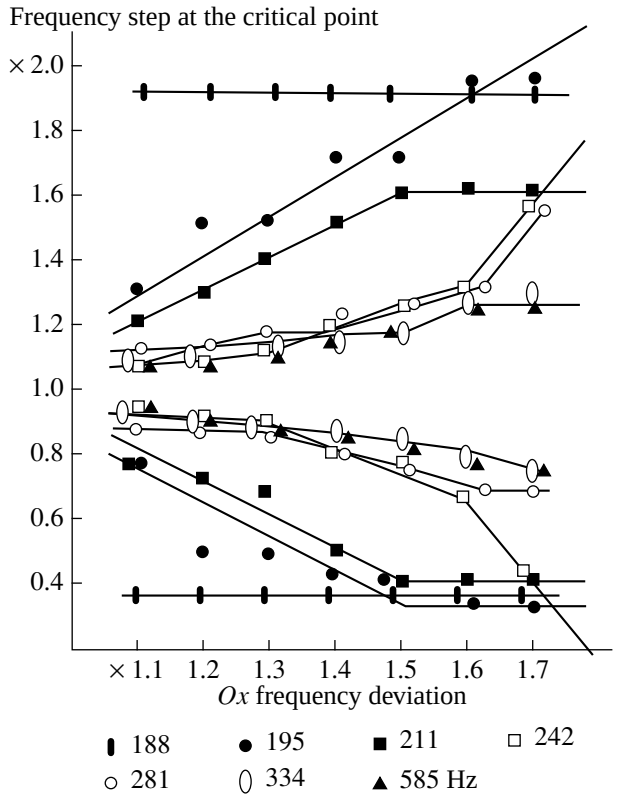

Fig. 5. Frequency step that is necessary to occur at a critical point for its efficient ($P > 90\%$) localization against the *Ox* frequency deviation with the fundamental frequency F_0 as the curve parameter for a horizontally moving cursor (averaged for one subject).

essary for the perception and efficient localization of the critical point in space at the chosen sound duration and produces a stable and almost identical sensation in all subjects.

It was found that, when the sound duration at the end point of the segment increased (from 8 to 20 ms and longer) and the frequency simultaneously changed, a significant deviation of the segment shape from the linear one was observed. Figure 3 schematically shows a subjectively perceived sound model of a straight segment for different sound durations at the critical points for the frequency deviation $D_y = 1.3$.

Since a 8-ms duration of the frequency step was sufficient to satisfactorily localize the point (with the detection probability $P > 90\%$), we decided to study the necessary frequency step at the end point versus the frequency of the fundamental tone of the moving horizontal cursor in the absence of the fundamental frequency deviation in both axes: $D_y = 1.0$ and $D_x = 1.0$. This problem was solved by measuring the subjective threshold of perceiving a short-time change in the frequency of the moving virtual source of the rectangular signal at the given frequency, velocity, and also duration and localization of the change at the given point of the trajectory in the virtual acoustic plane. In essence, it was necessary to determine a set of parameters of the virtual sound source in the vicinity of the critical points that facilitate the sensory fixation of the respective position and simultaneously do not mask the neighboring points. These requirements were fulfilled with the source parameters increased by a factor of two with respect to their threshold values. These settings reduced the variance in the test results associated with subjects' individual auditory properties. Our results had much greater magnitudes than those obtained in [7] and in audiometric studies of the differential thresholds in resolving the frequency of overlapping tones and impulse sources cited in [10]. The frequency step necessary for the efficient localization of the critical points in space as a function of the fundamental frequency of the horizontally moving sound cursor averaged over tests in 8 subjects is plotted in Fig. 4. Three regions of the fundamental frequency are clearly seen: below 200 Hz, from 200 to 500 Hz, and above 500 Hz. Respectively, in the first region, the effective frequency step is higher than 1.2; in the third one, no higher than 1.02; and, in the intermediate one, it changes within 1.02–1.2. However, these conditions were acceptable when no frequency deviation was applied to the sound cursor in the *Ox* and *Oy* directions. For arbitrary sound patterns, these parameters are higher and vary from 1.05 to 1.6. Consequently, it was no less important to determine the relationship between the necessary frequency step at the critical point and the frequency deviation of the sound cursor within the virtual acoustic plane relative to the fundamental tone. The experiments used seven fundamental frequencies (F_0): 188, 195, 211, 242, 281, 334, and 585 Hz, and a frequency deviation along the *Ox* axis from 1.1 to 1.7 for the moving sound cursor.

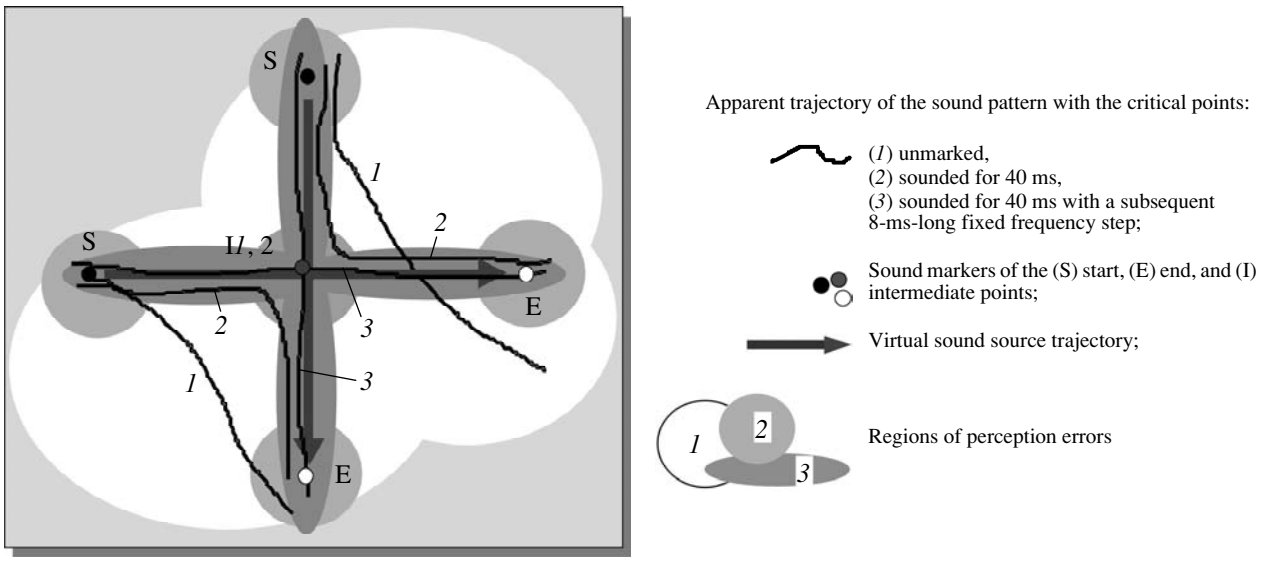

Fig. 6. Perception of a virtual sound pattern formed by the simultaneous motion of several sound sources: apparent trajectory of the sound pattern with the critical points.

The test results for one of the subjects are given in Fig. 5. The practically significant D_x is within 1.05–1.6 and depends on the fundamental frequency. The *Ox*-axis frequency deviation shifts the right end points upwards with respect to the left end point proportional to D_x, the frequency step with respect to $F_0 \times D_x$ for the right end point remaining unchanged.

Of course, a more thorough study of the perception process at the critical points of a linear segment, in particular, when the sounding procedure is cyclically reversed, can reveal the differences associated with changing the sign of the frequency step and the *Ox* axis fundamental tone deviation. However, this effect is of no practical importance because the frequency variation at the critical point is substantially greater than the threshold in perceiving the frequencies at two adjacent points. The sign of the frequency deviation at the critical point is much more important, and this sign should be associated with the ordinate of the virtual acoustic plane, because the fundamental frequency deviation is also dependent on this parameter [11, 12]. As a result of the analysis of the experimental data and the refining tests, the critical point parameters for the fundamental tone above 200 Hz (see Figs. 4, 5) were defined by the following conditions:

(1) The virtual acoustic plane is divided into two segments at a point with the ordinate *K*.

(2) If the critical point ordinate is equal to or less than *K*, the deviation increases the given point frequency by a factor of *H*.

(3) If the critical point ordinate is greater than *K*, the deviation decreases the given point frequency by a factor of *L*.

The empirical values of these quantities for the fundamental tone no higher than 550 Hz were found to be $H = 1.2$, $L = 1.2$, and $K = 43/128$ with the lower left point of the virtual acoustic plane taken as an origin. These rules, which control the parameters of the straight horizontal virtual segment were tested in similar experiments with the segment placed vertically in the acoustic plane. No additional correction or substantial change in the control parameters of the acoustic cursors were necessary.

The frequency deviation (stepwise change) at the critical points of the virtual sound pattern proved to be an efficient control parameter. In the case of a deficiency of time, this parameter is convenient for marking the points necessary for switching the attention of the audio display user.

Figure 6 plots the apparent trajectories of a sound pattern formed by the simultaneous motion of two sound sources when the critical points are (*1*) not marked, (*2*) sounded for 40 ms, and (*3*) sounded for 40 ms and experience a fixed 8-ms-long frequency step. The contraction of the region of uncertain space localization of the perceived virtual sound source trajectory is clearly seen. Unlike the familiar model of interaction between two sound fluxes [13], in which the time factor is the main one for merging and splitting, our model introduces the frequency marking of the critical points to control the subject's attention.

By dividing the functions switching the attention to a region that requires the space localization into the stepwise frequency change and fixing the attention through a longer sounding of the critical point at the initial frequency, we substantially decreased the sound duration at the critical points and stabilized the perception of the virtual sound pattern borders. The proposed technique provides new means for controlling the space parameters of patterns in virtual acoustic media.

ACKNOWLEDGMENTS

We are grateful to the editorial board and the reviewer for useful remarks, attention, and comprehensive analysis, which helped us in improving the paper.

The work was carried out under the project "Applied Software Package for Transforming a Graphic Image into Structured Acoustic Field for Blind PC Users" (state registration no. 01.960.010307) supported by the State Science and Technology program "Informatization of Russia."

REFERENCES

1. A. V. Agranovskiĭ, G. E. Evreinov, and A. S. Yashkin, in *Proceedings of the 5th International Conference ICCHP'96 on Interdisciplinary Aspects in Computers Helping People with Special Needs, Linz, Austria, 1996* (Linz, Austria, 1996), p. 539.
2. G. E. Evreinov and S. A. Kurkin, Akust. Zh. **42**, 629 (1996) [Acoust. Phys. **42**, 555 (1996)].
3. A. V. Agranovskiĭ and G. E. Evreinov, RF Patent No. 96105192/14 (008800) (19 March 1996).
4. A. J. Hollander, *Master's Thesis* (Human Interface Technology Lab., Washington State University, 1994).
5. K. Itoh and Y. Yonezawa, J. Microcomput. Appl. **13**, 117 (1990).
6. S. Lakatos, Perception **22**, 363 (1993).
7. E. Zwicker, *Psychoakustik* (Springer, Berlin, 1982).
8. R. Floru, in *Neuron Mechanisms of the Orientation Reflex* (Moscow State Univ., Moscow, 1970) pp. 346–360.
9. T. Z. Strybel, C. L. Manligas, and D. R. Perrott, Human Factors **34**, 267 (1992).
10. A. Shik, in *Psychological Acoustics in Noise Control*, Ed. by N. I. Ivanov (Baltic State Tech. Univ., St. Petersburg, 1995), p. 34.
11. A. V. Agranovskiĭ and G. E. Evreinov, in *Proceedings of the International Conference on New Technologies in the Education of the Visually Handicapped, Paris, France*, 1996, Vol. 2, pp. 28–30.
12. A. V. Agranovskiĭ and G. E. Evreinov, in *Proceedings of the Fourth International Congress on Sound and Vibration, St. Petersburg, Russia*, 1996, Vol. 1, pp. 301–304.
13. R. M. Ruff and E. Perret, Percept. Mot. Skills **55**, 155 (1982).

Translated by A.D. Khzmalyan

Acoustical Physics, Vol. 46, No. 1, 2000, pp. 80–86. Translated from Akusticheskiĭ Zhurnal, Vol. 46, No. 1, 2000, pp. 94–101.

Complex Matched Filtering of Diffraction Sound Signals Received by a Vertical Array

A. L. Matveev and V. V. Mityugov

Institute of Applied Physics, Russian Academy of Sciences, ul. Ul'yanova 46, Nizhni Novgorod, 603600 Russia

e-mail: matveyev@hydro.appl.sci-nnov.ru

Received December 22, 1998

Abstract—Theoretical foundations of the use of complex matched filtering in the processing of the diffraction-shadow sound signals received by a multielement vertical array are discussed. The theoretical predictions are compared with the experimental data obtained in a natural water basin. © *2000 MAIK "Nauka/Interperiodica".*

INTRODUCTION

In our previous publications [1, 2], we developed a theory for describing the acoustic diffraction signals observed in a shallow-sea sound channel and carried out a computer simulation of the received sound field on the background of interfering fluctuations. For the diffraction-shadow method of observing ocean objects, high inhomogeneity and nonstationary state of the vertical sound field structure are characteristic, these features being caused by the multimode sound propagation. That is why using a vertical receiving array is advantageous: it allows one to significantly depress the effect of unpredictable amplitude-phase variations of the signals received by individual array elements when multichannel processing is implemented.

An important stage of successive signal processing is the filtering matched to the expected Fresnel-zone structure of the diffraction signal. Mathematically, such a signal transformation is identical to the procedure of the source reconstruction from its holographic image in coherent optics. The analogy is so full that our computer procedures used for the detection of the "sharpened" diffraction response are accompanied by difficulties that are typical of optical holography.

In practice, the amplitude algorithm of the matched filtering is the simplest to be implemented. Such filtering uses envelopes of the received signals and is insensitive to variations in the current phase. Our simulations [2] showed that this algorithm increases the signal-to-noise ratio by 10–14 dB, depending on the parameters of the screen, which causes the signal diffraction, and on the characteristics of its motion. We [3] applied the amplitude matched filtering to the records of the acoustic diffraction observed in a fresh-water basin. The phenomenon was observed with the signal-to-noise ratio 20 dB. In these measurements, by full analogy with the optical case, the sharpened peak of the signal was observed on a background of a broad "basement" of relatively high level. Similarly, in amplitude optical holography, the reconstructed image of a point source is inevitably surrounded by an aberration spot that can be eliminated by nothing but phase holography [4].

The objective of this paper is to test the efficiency of the complex amplitude-phase matched filtering of the diffraction signals received in full-scale experiments. For processing, we used the experimental records obtained in a natural water basin. The comparison with the full-scale observations in the sea [5] showed that in our experiments, the interfering noise was rather close to that typical of a shallow sea in its space and time features.

FORMATION OF THE DIFFRACTED SIGNALS

Consider an acoustic path, L in length, in a shallow-water channel of depth $H \ll L$ (H is the thickness of the water layer). The vertical receiving array consists of N equidistant hydrophones and covers the entire channel, from its surface to bottom. At the other path end, at depth z_s, a sound source is located that emits a cw signal of frequency f. By analogy with our previous papers [2, 3], all lengths and distances here are expressed in a dimensionless form, i.e., normalized to the sound wavelength $\lambda = c/f$ (c is the mean sound speed in the channel).

In the absence of shadowing and variations of the medium parameters, the kth single hydrophone located at the depth z_k receives a time-independent signal whose amplitude and phase (apart from the electroacoustic convertion factor) are determined by the dimensionless transfer coefficient

$$K_k(z_k, z_s) = \sum_n (\chi_n L)^{-\frac{1}{2}} U_n(z_k) U_n(z_s) e^{i\chi_n L}. \qquad (1)$$

Here, the mode eigenfunctions $U_n(z)$ and the mode wave numbers χ_n are conventionally [6] found by solving the wave equation with the given sound speed profile $c(z)$ and appropriate boundary conditions at the surface and the bottom. Computer algorithms and codes that implement such calculations are well known (see, e.g., [7]).

1063-7710/00/4601-0080$20.00

In experiments, the channel parameters are nonstationary; hence, the amplitude and phase of the received signal significantly fluctuate in time. The analysis of the experimental data shows that, in the informative frequency range, the governing mechanism of signal fluctuations is the long-wavelength oscillations of the water surface (the so called seiches). The characteristic scale of these oscillations is of the same order of magnitude as our test path, or higher. To the first approximation, the effect of this phenomenon can be estimated by simply considering the variations of the channel depth H that is a parameter of formula (1). In coherent multimode interference summation (1), the changes in the wave numbers χ_n due to the changes in H lead to a high sensitivity of the received signals to the mentioned variations [8]. As a result, these variations prove to be the main source of interfering noise in diffraction observations.

In addition, there are other factors that lead to variations of the signals received in the channel. Particularly, rapid amplitude and phase fluctuations can be caused by sound reflection from the rough water surface. The analysis of experimental records obtained on lake paths and the comparison of those with the data of sea experiments [9] show that fluctuations caused by the wind-generated surface waves are relatively high-frequency ones and may be filtered out by signal processing with reasonable parameters of the screen and its motion. Additional amplitude-phase distortions of the sound field can be caused by sound reflections from the bottom roughness and from the lake banks. Such distortions are slowly time-dependent and nearly do not influence the result of our processing.

Let us consider the resultant time changes in the received signals influenced by both the mentioned interference fluctuations and the diffraction shadowing caused by the moving screen. Represent the current complex amplitude $x_k(t)$ of the signal received by the kth hydrophone as the sum

$$x_k(t) = x_k^{(s)}(t) + \delta x_k(t), \tag{2}$$

where $x_k^{(s)}(t)$ is the fluctuating direct signal from the source and $\delta x_k(t)$ is the effect of the diffraction shadowing of the array by the moving screen.

We assume the following kinematic scheme of the screen motion [1]. Let the screen move at a constant speed v, at a constant depth, perpendicularly to the acoustic path (i.e., to the source–receiver line) and cross the path at the instant t_0, at a distance R from the receiving array. Then, according to [1, 2], we have

$$\delta x_k(t) = |\delta x|_{\max} D(t) \exp[-i\pi v^2 (t - t_0)^2/h + \delta\varphi_k], \tag{3}$$

where h is the reduced distance of the screen, which is determined by the formula

$$\frac{1}{h} = \frac{1}{R} + \frac{1}{L - R}. \tag{4}$$

The factor $D(t)$ is the aperture envelope that depends on the screen shape. Particularly, for a rectangular screen, it has a canonic form: $\sin a(t - t_0)/a(t - t_0)$. To construct the algorithm for the screen of unknown shape, we assume the Gaussian form for the quantity $D(t)$ [2]:

$$D(t) = \exp[-2v^2 l^2 (t - t_0)^2/h^2], \tag{5}$$

where l is the horizontal screen size.

Computer simulations and full-scale experiments showed that the initial phase of the diffraction disturbance, φ_k in formula (3), significantly depends on the depth, and its values may noticeably differ even for the adjacent array elements. Therefore, possible patterns of the diffraction-shadowing envelopes may considerably vary [1, 10]. In particular, the "inverse" diffraction had been repeatedly observed in experiments: at some of the hydrophones, the signal envelope exhibited a typical rise instead of the expected diffraction shadowing.

Strictly speaking, the factor $|\delta x|_{\max}$ in (3) should also have a subscript—the hydrophone number k. Similarly to the initial phase, the disturbance amplitude significantly depends on the depth and is governed by many factors: the sound speed profile, the bottom relief, and the depth of the screen towing. However, for subsequent estimations, it is convenient to use the value of the factor $|\delta x|_{\max}$ averaged over the array elements and depths of the screen motion. One should also note that the multimode sound propagation in the shallow-water waveguide somewhat increases the disturbance amplitude as compared to the "refined" two-dimensional (cylindrical) diffraction scheme. In view of these considerations, we use the model semi-empirical estimate (see [1]) for the amplitude of the shadowing disturbance (relative to the mean amplitude of the direct signal):

$$\frac{|\delta x|_{\max}}{|x^{(s)}|} = \mu \frac{\sigma}{H\sqrt{h}}, \tag{6}$$

where $\mu > 1$ is the gain of the shadow due to the multimode propagation and σ is the screen area. The computer simulation for the conditions close to those of the experiments described below yields the value $\mu \approx 1.4$.

PROCESSING ALGORITHMS

Let us represent the current received complex signals $x_k(t)$ in the form

$$x_k(t) = X_k(t) e^{i\varphi_k(t)}. \tag{7}$$

As the first stage of the preliminary processing, we form the normalized amplitude and phase variables:

$$Y_k^{(a)}(t) = \frac{X_k(t)}{\tilde{X}_k(t)} - 1, \tag{8}$$

$$Y_k^{\varphi}(k) = \varphi_k(t) - \tilde{\varphi}_k(t), \tag{9}$$

where $\tilde{X}_k(t)$ and $\tilde{\varphi}_k(t)$ are the moving-smoothed variables $X_k(t)$ and $\varphi_k(t)$ is obtained by linear window-filtering with the transfer function

$$g(t) = \begin{cases} \tau^{-1} & \text{for } |t| \le \tau/2 \\ 0 & \text{for } |t| > \tau/2. \end{cases} \quad (10)$$

The time τ of smoothing is chosen from the *a priori* considerations to be somewhat greater than the expected time of passing the diffraction obstacle. This time is estimated from the angular width of the diffraction lobe and the expected speed of the screen.

Note that the procedure of amplitude normalization (8) is nonlinear. Its repeated utilization showed that this procedure is also efficient for nonstationary sound propagation when the theory of linear filtering, which is developed for stationary and ergodic random processes, is inadequate and cannot lead to useful conclusions.

The next step of signal processing consists of using the matched filtering. The simplest amplitude algorithm of the matched filtering [2, 3] includes the transformation of the variable $Y_k^{(a)}(t)$ according to the formula

$$F_k^{(a)}(t) = \left| \int Y_k^{(a)}(t')\Phi(t-t')dt' \right|, \quad (11)$$

where

$$\Phi(t) = C\exp\left[-\frac{v^2}{h}\left(i\pi + \frac{2l^2}{h} \right) t^2 \right] \quad (12)$$

is the transfer function of the filter matched with the aforementioned model for the diffraction disturbance. The normalization factor C will be discussed below.

The algorithm for detecting the sharpened diffraction peak is similarly constructed by the matched filtering of the phase variable:

$$F_k^{(\varphi)}(t) = \left| \int Y_k^{(\varphi)}(t')\Phi(t-t')dt' \right| \quad (13)$$

with the same transfer function $\Phi(t)$ as in (12). The computer simulation and processing of the experimental records show that the diffraction peaks extracted by procedures (11) and (13) from the amplitude and phase components of the received signal are nearly identical. In both cases, the signal peak overlies a broad basement, which is well known from amplitude optical holography. The aforementioned identity of the peaks is a consequence of the fact that, for a small diffraction disturbance (relative to the direct signal), the variables $Y_k^{(a)}(t)$ and $Y_k^{(\varphi)}(t)$ are simply the quadrature components of a complex disturbance of type (3). The latter statement can be confirmed by substituting the signal representation (2), in view of (3), into expressions (8) and (9). Neglecting the fluctuations of the direct signal and specifying $\tilde{X}_k = \overline{|x_k^{(s)}|}$, we obtain the following form in the linear approximation with respect to $|\delta x_k|$:

$$Y_k^{(a)}(t) = \frac{|\delta x|_{\max}}{\overline{|x_k^{(s)}|}} D(t) \times \cos[-\pi v^2 (t-t_0)^2/h + (\delta\varphi_k - \tilde{\varphi}_k)], \quad (14)$$

$$Y_k^{(\varphi)}(t) = \frac{|\delta x|_{\max}}{\overline{|x_k^{(s)}|}} D(t) \times \sin[-\pi v^2 (t-t_0)^2/h + (\delta\varphi_k - \tilde{\varphi}_k)]. \quad (15)$$

Note that the quantity $|\delta x|_{\max}/\overline{|x_k^{(s)}|}$ is equal to several percent for the experiments described below.

In spite of the mentioned similarity in the purely amplitude and purely phase algorithms, it is much more difficult to deal with the phase variable. One should use auxiliary algorithms to resolve an ambiguity in the phase within its domain of definition, to compensate for the phase drops in the domains of abnormally low amplitude, etc. In addition, even after all possible computer processing, the resultant phase fluctuations subjected to the appropriate normalization may exceed the amplitude ones.

Similar difficulties, in their optical-mechanical version, were known in early optic holography. Then, the amplitude holograms were obtained by relatively simple means, with rather imperfect and unstable sources of radiation. To obtain the amplitude-phase holograms, considerable and specific efforts were required: the use of independent basements for the optical systems, the experiments during the most quiet night hours, etc.

The complex matched filtering of the brightness-shadow sound signals is carried out as follows. Let us form the linear combinations $Y_k(t) = Y_k^{(a)}(t) + iY_k^{(\varphi)}(t)$ of the amplitude and phase variables. Then we apply the transform to them:

$$F_k(t) = \left| \int Y_k(t')\Phi(t-t')dt' \right|, \quad (16)$$

where $\Phi(t)$ is the transfer function given by expression (12). Note that, with the diffraction disturbance (14), (15), the complex procedure (16) increases the amplitude by a factor of $\sqrt{2}$. Therefore, the normalization constant C of (12) should be chosen from the conditions

$$\int |\Phi(t)|^2 dt = \begin{cases} 2 & \text{for } F_k^{(a)},\ F_k^{(\varphi)} \\ 1 & \text{for } F_k. \end{cases} \quad (17)$$

The analysis shows that, with the chosen normalization, formula (6) can be used to estimate the diffraction cross-section σ from the experimental data in all three cases at hand. Note that, just at this stage of matched fil-

tering (16), the fluctuations governed by the surface waves are mainly eliminated.

The next step of the multichannel processing of the transformed diffraction responses consists of their incoherent accumulation over the vertical array:

$$F(t) = \frac{1}{N}\sum_{k=1}^{N} F_k(t), \tag{18}$$

where N is the number of array elements to be summed. In addition, for the experiments discussed below, the summation over several emitted frequencies was also used. Denote these frequencies as f_j ($j = 1, 2, \ldots, M$; M is the number of operating frequencies), and label the functions (11), (13), (16), and (18) with the frequency subscript j: $F_{kj}^{(a)}(t)$, $F_{kj}^{(\varphi)}(t)$, $F_{kj}(t)$, and $F_j(t)$, respectively. We do not renormalize the filter parameters (12) to the varying wavelength λ_j, because the difference between the adjacent frequencies is about several percent in our case. With these notations, we write down the result of the complex matched filtering in the form

$$F(t) = \frac{1}{M}\sum_{j=1}^{M} F_j(t). \tag{19}$$

The experimental equipment allowed us to use up to five frequencies simultaneously. The minimum frequency separation was chosen in such a manner that the signals of the adjacent frequencies could be treated as statistically independent, up to a practical-purpose accuracy. Particularly, additional tests showed that a frequency separation of several percent was sufficient for the amplitude fluctuations of the received cw signals to have a correlation coefficient of about 0.1.

The signal fluctuations were also weakly correlated at different array elements. According to the measurements, the amplitude and phase fluctuations of the single-frequency signals received by individual hydrophones separated by $\lambda/2$ in the vertical can be treated as nearly independent (the actual hydrophone separation was slightly less than $\lambda/2$ in the array used in the experiment).

The aforementioned considerations show that the efficiency of the incoherent accumulation (18) over the array elements and the frequency accumulation (19) is fairly high, which is confirmed by the experimental data.

EXPERIMENTAL DATA

The experiment was carried out in a natural freshwater basin (lake), with a depth of about 14 m and a relatively smooth bottom. The length of the propagation path was about 480 m. The sound source was located near the bottom. The receiving vertical array consisted of 64 elements and covered nearly the entire channel depth. The sound field was excited by a monopole-type ceramic transducer, simultaneously at five frequencies around 3 kHz, with a separation of 40 Hz between the adjacent frequencies. The vertical temperature profile of the channel was characterized by a near-surface warm layer, with a temperature of about 20°C and thickness up to 4 m. At lower horizons, the water temperature sharply decreased and reached 6–7°C near the bottom. The temperature profiles, the surface state (at wind speeds of 3–5 m/s), and the relative fluctuations (about 0.1–0.2) of the received direct signal were compared with the corresponding parameters of the shallow-sea experiment [9]. The comparison showed that these two experiments were qualitatively and order-of-magnitude quantitatively similar.

The diffraction screen with a cross-section of 0.5×2.5 m was towed at different speeds across the propagation path in the vicinity of its midpoint. The depth of towing was constant. For the subsequent analysis, the experimental record that was obtained at the towing speed $v \approx 0.3$ m/s was used.

We start with discussing the sequence of the numerical procedures used in the signal processing based on the purely amplitude algorithm of the matched filtering. The complex signals received by each array channel at each frequency of the five ones were numerically filtered within a narrow band of about 1 Hz to eliminate local acoustic and electric noise. At all frequencies, the envelope samples $X_k(t)$ are detected and then subjected to normalization (8) with a characteristic time $\tau = 60$ s by the rectangular filter (10), to amplitude matched filtering (11), and to incoherent accumulation (18). After that, frequency averaging (19) is performed over the five frequencies. The result of the amplitude filtering is presented in Fig. 1.

The aforementioned aberration basement is clearly visible in the plot, this basement serving as a background for the diffraction-shadow peak sharpened by procedure (11) (compare with [2]). The numbers that are shown in the upper left corner of the figure have the following meaning:

max = 0.0377—height of the highest peak;

snr = 15.4360—signal-to-noise ratio;

ave = 0.0153—mean interference-noise basement;

rms = 0.0015—standard deviation of the remaining noise fluctuations.

The above values are presented for the linear amplitude scale. Note that, after procedure (8), all quantities are normalized to the amplitude of the direct signal: the corresponding dimensionless data are plotted along the ordinate axes of all four figures. The statistical parameters of the remaining noise (ave and rms) are calculated for the signal segments that are free from the peak, the aberration basement, and the boundary effects of the level decrease, which are characteristic of this processing technique.

A simple analysis shows that, for the experimental estimate of the diffraction cross-section σ by formula (6), the quantity $|\delta x|_{\max}/\overline{|x^{(s)}|}$ should be specified to be equal to the difference (max) – (ave). For the data of

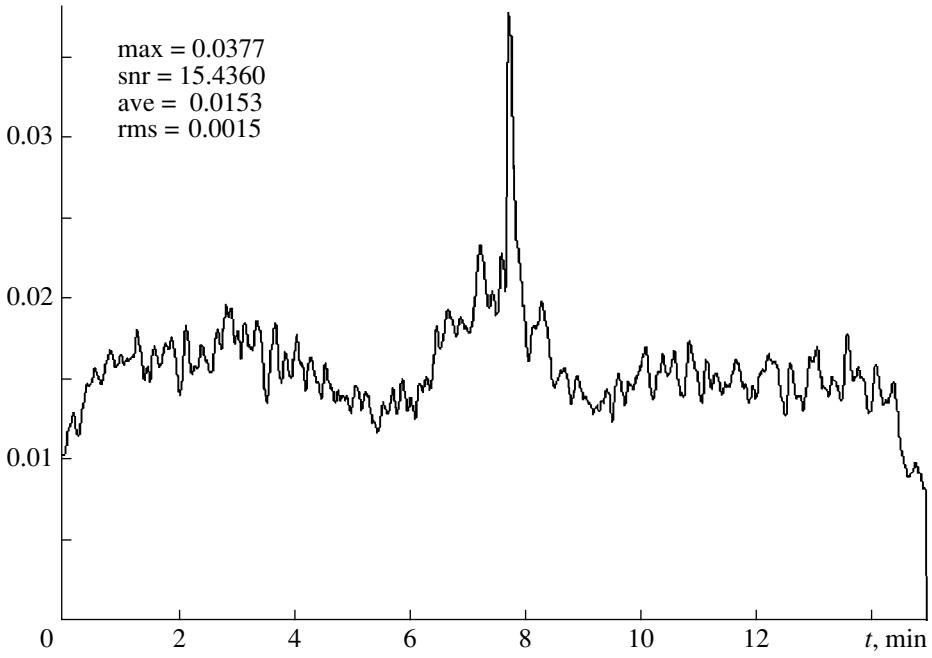

Fig. 1. Amplitude filtering.

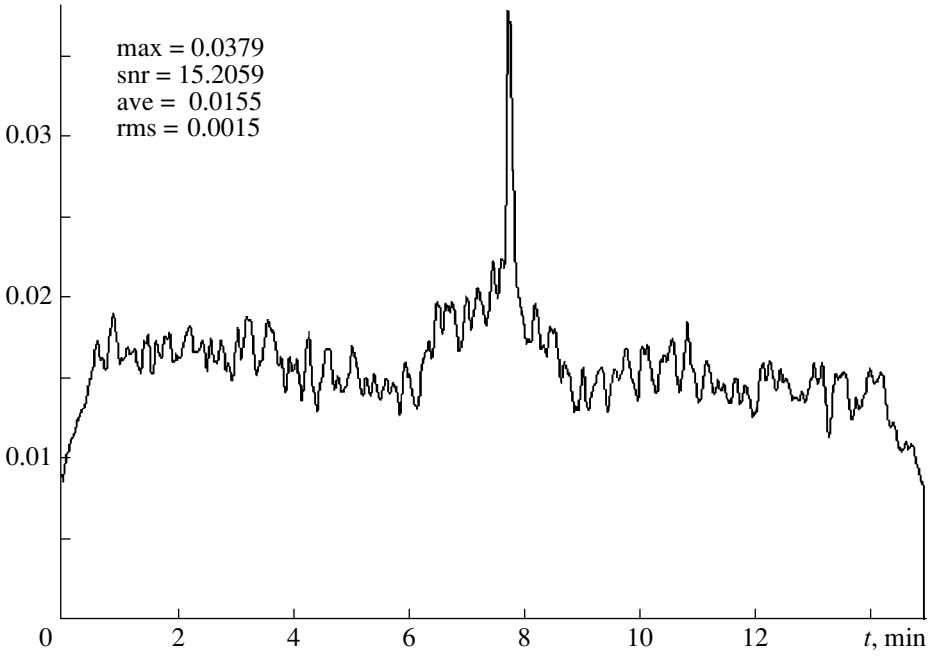

Fig. 2. Phase filtering.

Fig. 1, we have (max) – (ave) ≈ 0.022. Compare this value with the estimate yielded by formula (6). By substituting $\sigma = 5$, $H = 30$, $h = 240$, and $\mu = 1.4$, we obtain (max) – (ave) ≈ 0.014, i.e., we obtain a good agreement in the order of magnitude.

Comparison with a large number of similar experiments shows that, on average, formula (6) leads to somewhat underestimated values. The most probable reason for this discrepancy is the existence of a considerable temperature inhomogeneity (temperature discontinuity) in the subsurface water layer. We [1] neglected this phenomenon in estimating the factor μ by the computer simulations. Physically, it is evident that the heated subsurface water layer (6–8 sound wavelengths in thickness for the experiment at hand) decreases the efficient depth H of the channel in which

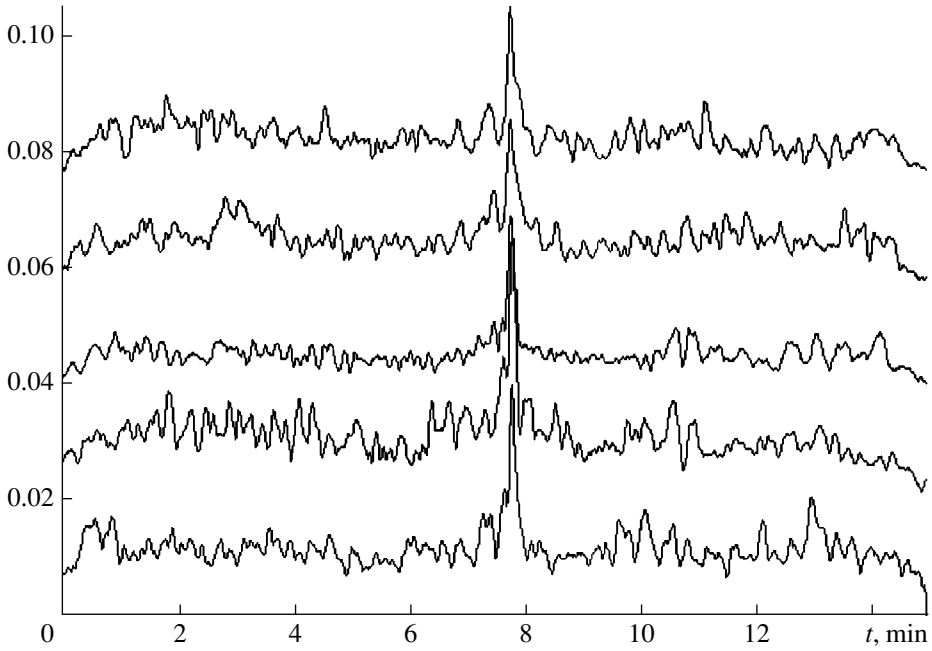

Fig. 3. Complex filtering for five frequency channels.

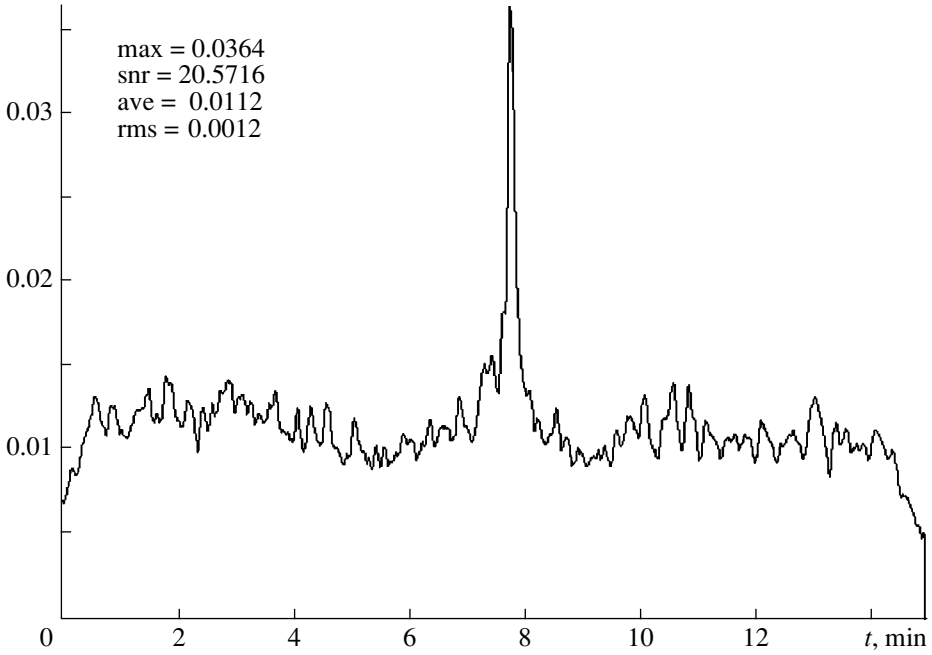

Fig. 4. Frequency averaging.

the main sound energy is concentrated. The tests showed that the appropriate empirical correction nearly eliminates this systematic error in estimating the height of the diffraction peak.

Figure 2 shows the similarly processed phase components $Y_k^{(\varphi)}(t)$, upon performing all aforementioned accumulation procedures. The comparison confirms the nearly complete similarity of the resultant curves for purely amplitude and purely phase processing. As above, the aberration basement is well pronounced, its shape being somewhat masked by the remaining interfering noise.

The next step of the analysis consists in the complex matched filtering (16). Figure 3 shows the processed data after accumulation (18) over the array elements for

all five frequencies (for illustrative sake, the curves are shifted along the vertical axis; hence the ordinates are true only for the lower curve). By the visual study of the curves, one can guess that the noise overshoots are uncorrelated with each other. It is this uncorrelation that yields the considerable noise suppression in the procedure of frequency accumulation. On the other hand, the diffraction peaks sharpened by matched filtering look quite similar at different frequencies.

Figure 4 is obtained by averaging (19) the curves shown in Fig. 3. In accordance with the theory [2] and with the optical-holography analogy, the aberration basement of the diffraction peak proves to be eliminated by the complex matched filtering. The comparison with Figs. 1 and 2 shows a considerable gain in the signal-to-noise ratio with respect to the purely amplitude and purely phase procedures of matched filtering.

Thus, the complex matched filtering of the diffraction-shadow signals, along with other processing procedures typical of a vertical receiving array, proves to be an efficient method for the observation of moving inhomogeneities in a shallow-water channel.

ACKNOWLEDGMENTS

We are grateful to P. I. Korotin, B. M. Salin, and the staff of the Institute of Applied Physics for the organization and performance of the experiment.

This work was supported by the Russian Foundation for Basic Research, project nos. 97-02-17555 and 99-02-16401.

REFERENCES

1. S. M. Gorskiĭ, V. A. Zverev, A. L. Matveev, *et al.*, Akust. Zh. **41**, 223 (1995) [Acoust. Phys. **41**, 190 (1995)].
2. V. A. Zverev, A. L. Matveev, and V. V. Mityugov, Akust. Zh. **41**, 591 (1995) [Acoust. Phys. **41**, 518 (1995)].
3. A. L. Matveev, V. V. Mityugov, and B. M. Salin, in *Ocean Acoustics: Proceedings of the Advanced-Study School of Academician Brekhovskikh L. M.* (Geos, Moscow, 1998), pp. 151–156.
4. M. Françon, *Holography* (Paris, Masson, 1969; Mir, Moscow, 1972).
5. B. G. Katsnel'son, L. G. Kulapin, A. A. Migulin, *et al.*, Akust. Zh. **38**, 308 (1992) [Acoust. Phys. **38**, 164 (1992)].
6. L. M. Brekhovskikh, *Waves in Layered Media* (Nauka, Moscow, 1973; Academic, New York, 1980).
7. M. B. Porter, *The KRAKEN Normal Mode Program* (SACLANT Undersea Research Center, 1991).
8. J. Tabrikian, J. L. Krolik, and H. Messer, J. Acoust. Soc. Am. **101**, 241 (1997).
9. A. L. Matveev and V. V. Mityugov, *Report on the 7th Expedition of the AKADEMIK SERGEĬ VAVILOV Research Vessel* (Inst. of Oceanology, Academy of Sciences of the USSR, Moscow, 1990), Chap. 7.
10. V. A. Grigor'ev and V. M. Kuz'kin, Akust. Zh. **41**, 410 (1995) [Acoust. Phys. **41**, 359 (1995)].

Translated by E.A. Kopyl

Acoustical Physics, Vol. 46, No. 1, 2000, pp. 87–95. Translated from Akusticheskiĭ Zhurnal, Vol. 46, No. 1, 2000, pp. 102–111.

Effect of the Sound Speed Field Inhomogeneities on the Propagation over a Continental Slope

A. V. Mikryukov and O. E. Popov

Andreev Acoustics Institute, Russian Academy of Sciences,
ul. Shvernika 4, Moscow, 117036 Russia
e-mail: bvp@akin.ru

Received November 25, 1998

Abstract—Results obtained by processing the data of an experiment on the propagation of explosion-generated sound signals from the deep ocean to the coastal wedge are presented. The propagation path, 275 km in length, passes areas with inhomogeneities of the sound speed field, including the front zone. The effects of these inhomogeneities on the sound field formation are analyzed for different parts of the path. The frequency band of the analysis covers 25–400 Hz. It is shown that after the path crosses the boundary of the front zone, the dispersion curves of the first and second modes nearly coincide. The signals of these modes are not resolved in time, and as the distance increases, they cause pronounced modulation of the level in the signal tail at low frequencies (25–50 Hz). Therefore, to separate the effect of sound interaction with the inclined bottom, i.e., the effect that determines the increase in the sound level over the coastal slope, it is necessary to perform a detailed analysis of the mode content of the received signals. © *2000 MAIK "Nauka/Interperiodica".*

To solve various problems of applied and general underwater acoustics, a detailed knowledge of the specific features of sound propagation from deep-water ocean areas to shallow-water coastal ones is required. One of such features is the repeatedly observed increase in the sound field level, which occurs over the continental slope.

This increase is caused by the interaction of the sound field, which propagates in the deep-water sound channel, with the rising bottom of the continental slope. That is why investigators closely study the relief features and geophysical parameters of the sea floor in the continental slope areas [1, 2]. On the other hand, the sound speed field is commonly discussed with relation to the depth of the underwater sound channel, because the interaction of the channeled sound energy with the inclined bottom begins to manifest itself exactly in the vicinity of this depth. Of course, the source and receiver positions relative to the channel axis are also important.

In the numerical modeling of the sound propagation over the continental slope, the sound speed profile $C(z)$ in water is usually assumed to be constant all along the path [2, 3]. Such approximation is fully justified for most ocean regions where the depth of the channel axis is within 800–1200 m. However, in a number of regions with shallower axis depths (50–400 m), sub-surface currents exist that produce front zones separating warm waters of the open ocean and cooler over-slope waters and rings. In such regions, the effect of the horizontal inhomogeneity of the sound speed field on the sound field formation becomes substantial and should be studied in detail.

With the use of experimental data, we will show that the interaction of sound waves, which propagate from the deep ocean to coastal areas, with disturbances of the sound speed field can almost completely mask the effect of the relief and geoacoustic parameters of the bottom. Without thorough and detailed analysis of all mechanisms participating in the sound field formation over the continental slope, one can easily arrive at the wrong conclusions.

The experiment was carried out in the northwestern part of the Pacific Ocean, near the coast of the Kamchatka Peninsula. The Kuril-Kamchatka Current crossed the path of sound propagation from the ocean to the coastal shelf, this current being cold and highly unstable in both space and time.

The sound signals propagated along a path 275 km in length. The path began in the deep ocean and ended at an edge of the coastal shelf where the sea depth was 270 m. At the continental slope, the path was nearly normal to the isobaths. The receiving vessel with a hydrophone submerged to a depth of 130 m drifted at the starting point of the path, in the deep ocean region. The transmitting vessel sailed along the path, from its terminal point at the coastal shelf toward the receiving vessel. As the sound sources, pressure-sensitive detonators (0.38 kg in mass) were used. They were dropped from the transmitting vessel sailing at full speed and exploded at the depth 270 m. The explosions were separated by different time intervals, depending on the changes in the bottom relief. The initial nine charges were dropped with 0.6–0.7-km separations in distance, in an area with the depth varying from 270 to 1150 m. The next nine charges had 1.6–1.7-km separations,

1063-7710/00/4601-0087$20.00

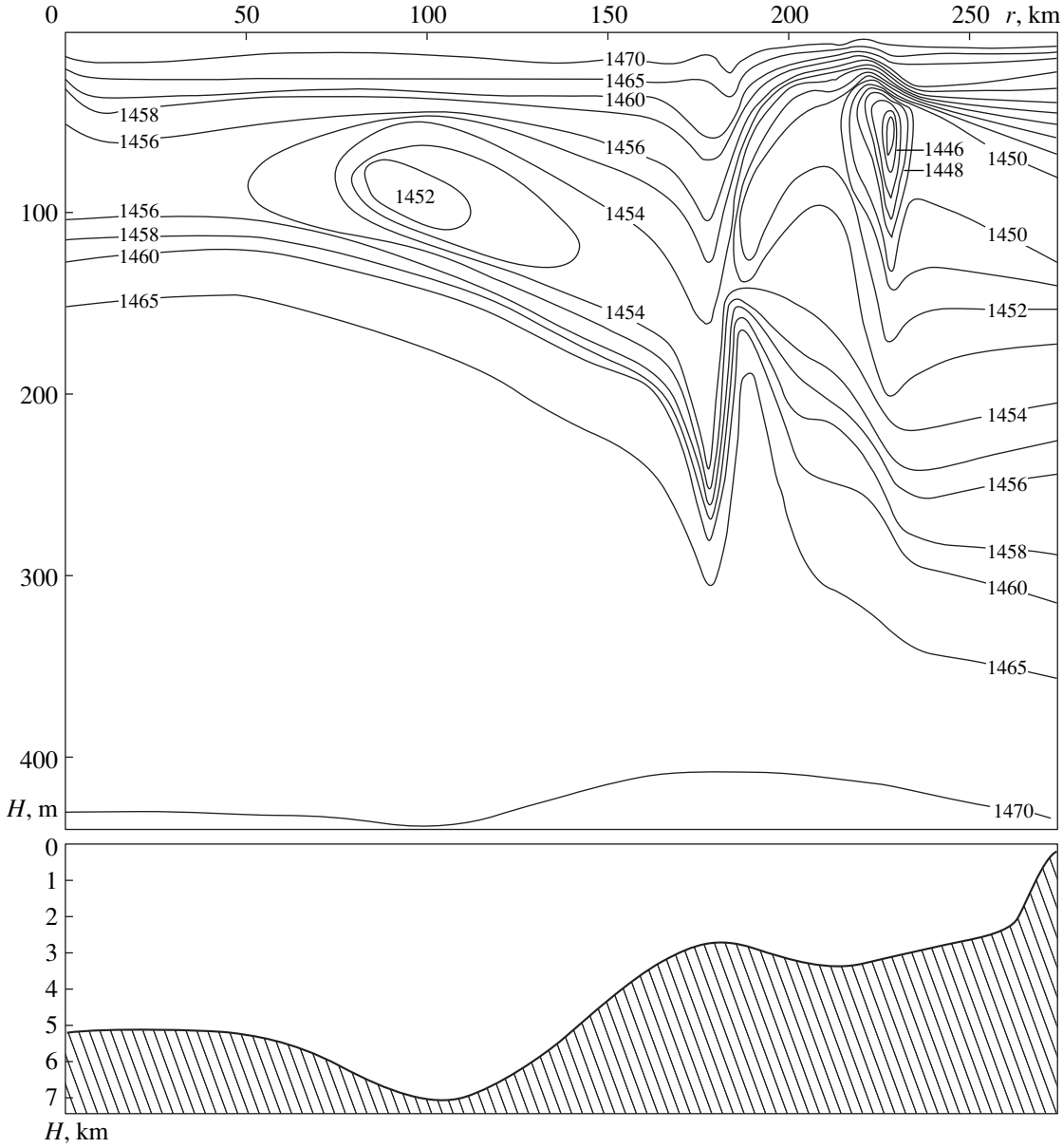

Fig. 1. Sound speed field and bottom relief along the propagation path.

with the depth varying from 1180 to 2800 m. The remaining twenty explosions were spaced at 10-km intervals. The last charge exploded at 55 km from the receiving vessel, eleven hours after the beginning of the experiment. Such a distribution of the explosions was expected to yield reliable estimates for the determination of both the sound field decay law characterizing the propagation in the deep ocean and the deviation from this law over the rising bottom of the continental slope [1].

In Fig. 1, the sound speed field reconstructed from the measured profiles and the data of echo-sounding along the path are shown. One can see that the sound speed field is inhomogeneous in distance. Note that the depth of the channel axis smoothly increases within the first part of the path, while pronounced changes in the sound speed field occur within the second path portion. At the distance 180 km from the starting point, a front zone governed by the boundary of the cold current is observed. At the 225-km distance, the cold water core occurs with a minimum sound speed of 1446.0 m/s at the depth as shallow as 50 m. By the end of the path, the sound channel is nearly smeared out, and the minimum in $C(z)$ is fairly weak. The acoustic energy that was concentrated within the narrow sound channel in the deep ocean is now spread over a much thicker water layer. As a consequence, this energy begins to interact with the rising bottom at greater depths and longer distances from the shelf edge as compared to the case of a

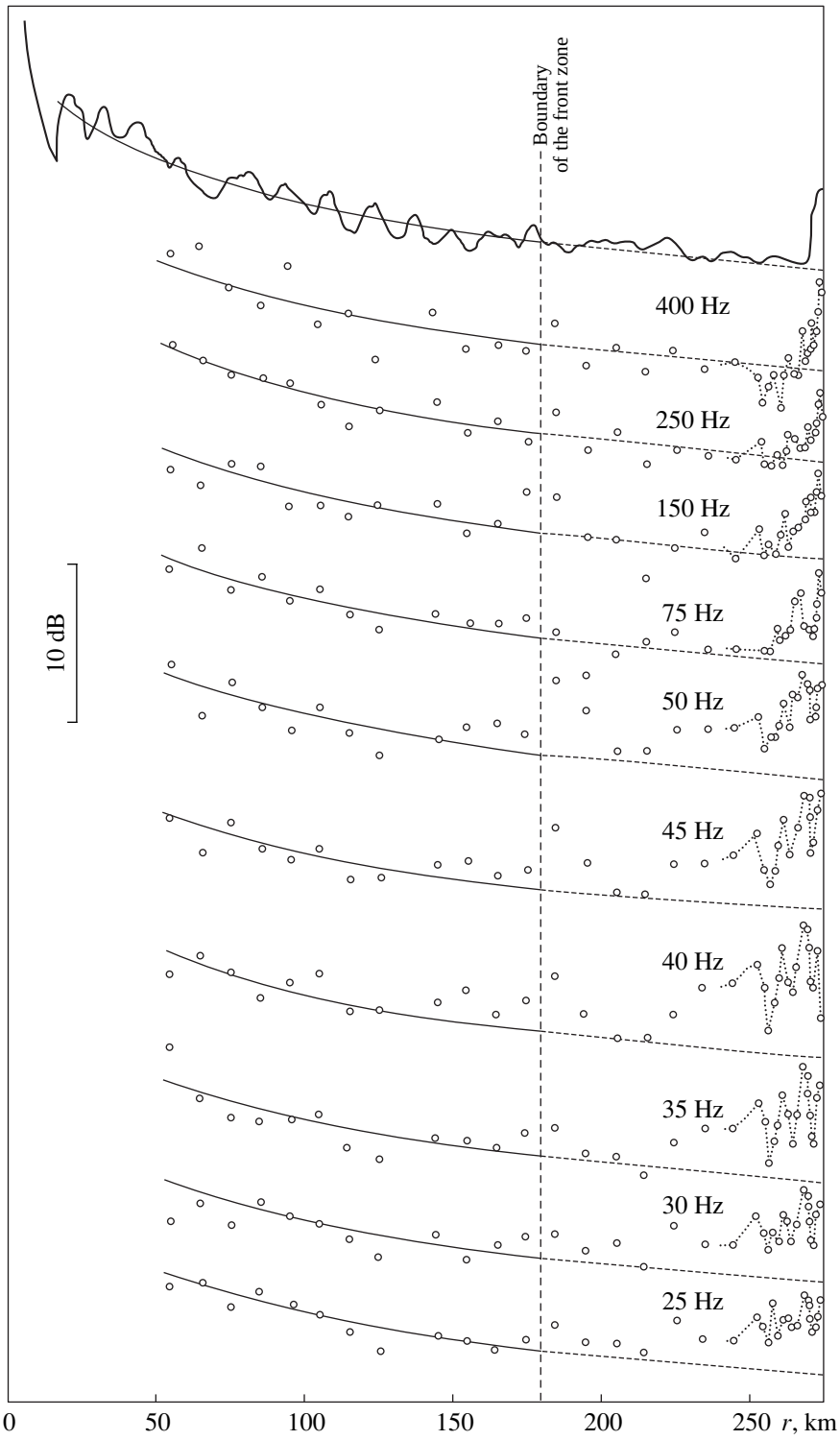

Fig. 2. Calculated (top) and experimental sound levels versus the range. Bandwidth of the filter is 10 Hz for all frequencies. Solid curves and their dashed extensions present the cylindrical decay law estimated for the first half (50–185 km) of the path.

constant $C(z)$ along the path. Note that all changes in the sound speed field occur solely in the upper subsurface water layer, 20 to 300 m, while the sound speed remains nearly range independent in deeper water layers.

Figure 2 shows the range dependence of the sound level for a number of frequencies. In the signal processing, a bandwidth of 10 Hz (at the –3-dB level) was obtained by using a filter with the output pulse response in the form of a squared Hanning window. The estimate

obtained with the geometric-acoustics approximation is also shown in Fig. 2. It is known that the ray parameters are most sensitive to changes in the sound speed in the vicinities of their turning points. In our case, these points correspond to depths shallower than 30 m and deeper than 270 m, while the main transformations of the sound speed field occur at intermediate depths. Therefore, the calculation results shown in the upper part of the figure exhibit only a weak effect of the $C(z)$ disturbances on the sound field decay law. The cylindrical spread law was plotted by using the least-squares approximation for calculating the sound level up to the front zone, for the first part of the path (the solid curve in Fig. 2). This law was extended up to the end of the path (the dashed curve). The plotted curves approximate well the experimental decay of the sound level all over the path. According to the calculation for a perfectly reflecting bottom, the slope-caused increase in the sound level should begin at the distance 265–270 km where the sea is deeper than 1500 m. In this slope area, up to the shelf edge, the bottom inclination is about 7°.

The experimental data are somewhat more sensitive to the features of the sound speed field than one can expect according to the ray calculations. A pronounced rise in the sound level occurs when the path crosses the boundary of the front zone. At longer distances, the sound level is somewhat higher with respect to the cylindrical law corresponding to the experimental parameters of the first half of the path. At the same time, at frequencies higher than 75 Hz, a sharp rise in the sound level takes place starting from nearly the same distances as in the ray calculations.

The change in the range dependence of the sound level at frequencies lower than 50 Hz, which occurs after the path crosses the front boundary, is somewhat unexpected at first glance. At these frequencies, after a pronounced increase in the sound level at the boundary of the front zone, the sound level continuously rises starting from the distance 215 km up to the path end. The rate of this rise increases as the frequency decreases; it reaches its maximum value at frequencies of 35–45 Hz. After that, the sound level decreases. Owing to small separations of the explosions at the last 30 km of the path, one can see that at this part of the path, the range dependence of the sound level exhibits an interference behavior with a characteristic period of about 8 km. At frequencies lower than 50 Hz, this behavior complicates the evaluation of the distance after which the sound level should increase because of the sound propagation over the inclined bottom.

To understand the origin of the observed phenomenon, one should separate the effects of the sound speed field and the sea bottom. For this purpose, we consider the time structure of the received explosion-generated signals. In Fig. 3, the circles show the transformation of the signal time structure as a function of distance along the path. These data were calculated in the geometric-acoustics approximation with the use of all information available on the sound speed field, bottom relief, and sea-floor parameters. The abscissa axis represents the quantity $\Delta T = T - r/1.45$, where T is the total travel time along the ray up to the receiver, which is at the distance r from the source. The inset in Fig. 3 presents the record of the signal received at the distance 105 km, in a broad frequency band. Lower in the inset, the signal time structure that was computed in the ray approximation for the same distance is shown. Both signal representations shown in the inset are synchronized relative to the arrival time of the initial four "water" rays which leave the source at highest angles. For these rays, the travel times are most stable—both in space and in time [4]. By synchronizing the beginning of the experimental signal with the corresponding calculated arrival time of the most steep water rays, one can reliably predict the difference in the times of individual arrivals in the initial part of the signal. All other received signals were also synchronized in the same manner. In Fig. 3, the solid circles show the arrival times for the time-separable individual arrivals in the initial part of the signal.

The duration of the experimental signals is higher than that calculated in the ray approximation. As was mentioned in a number of papers, when the source and receiver are offset from the channel axis in the vertical direction, the geometric-acoustics approximation often fails to explain the fact that, in the tail part of the signal, acoustic energy exists that arrives with group velocities close to the sound speed near the channel axis. Nevertheless, if the signal is received at a horizon lying below the channel axis, the experimental signal duration may be nearly equal to that obtained with the source and receiver positioned at the channel axis (this effect is governed by the frequency and sound speed gradients above and below the axis). The observed difference in the durations of the experimental and ray-calculated signals is caused by several effects. For example, Spiesberger and Tappert [5] used the data of the experiments carried out in eastern and northeastern regions of the Pacific Ocean to obtain the following quantitative estimate for the frequency 250 Hz: if the receiver is positioned 100–200 m below the axis, the difference in the experimental and calculated durations may be attributed to the diffraction effects at caustics and turning points; if the receiver lies 300 m below the axis, the effects of internal waves may predominate; if the receiver is 800–1000 m below the axis, sound scattering by large meso-scale inhomogeneities should be taken into account.

In our previous paper [6], we explained the observed phenomenon by considering the diffraction effects for a specific signal. Hence, we do not discuss the details below. The only important fact we mention here is that the geometric-acoustics approximation yields a reliable

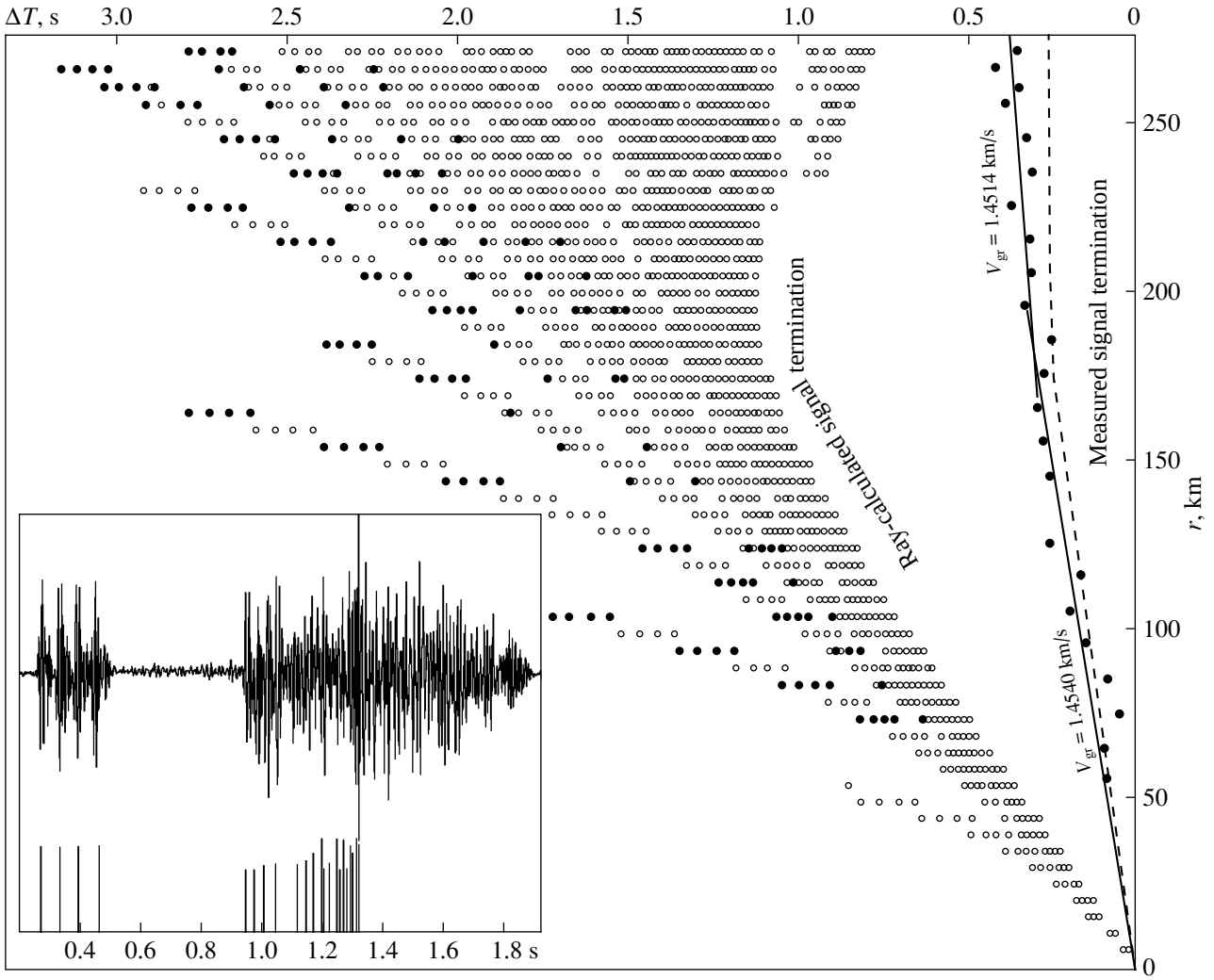

Fig. 3. Changes in the duration of the calculated (circles) and measured (dots) signals versus the distance. The dashed curve shows the terminal part of the signal calculated for the source and receiver positioned at the channel axis. The inset shows the signal recorded at the distance 105 km and its ray-calculated durations.

time estimate for the initial part of the signal, thereby allowing us to obtain absolute travel times from the experimental signal.

According to the real-time spectral analysis of our signals, the minimum group velocity of the tail arrivals corresponds to a frequency of 40 Hz, all over the path. Thus, by measuring the total signal duration, from the signal beginning that is reliably detected in a broad frequency band to the tail filtered within a narrow band around the central frequency 40 Hz, we can estimate the change in the group velocity of the tail arrivals (i.e., of the first mode) for the frequency at hand. This procedure can be performed for all distances, up to the path end, and the resulting values can be compared with the calculated ones.

As Fig. 3 shows, the group velocity of the first mode at a frequency of 40 Hz remains nearly constant up to the boundary of the front zone: it is equal to 1.4540 km/s (the calculated value is 1.4545 km/s for the profile $C(z)$ measured at the beginning of the path). Beyond the front zone and up to the path end, the group velocity of the first mode becomes slightly lower at this frequency: it reaches 1.4514 km/s (1.4505 km/s is the velocity calculated with the profile $C(z)$ corresponding to the terminal point of the path). A similar behavior is observed for the range dependence of the signal duration calculated in the ray approximation with the source and receiver depths both equal to 90 m, i.e., the depth of the channel axis at the starting point of the path (the dashed curve in Fig. 3).

Figure 4 shows the records of the signals received at the distances 55–185 km (before the front zone) and filtered within a band of 10 Hz around the central frequency 40 Hz. These records are presented in a successive manner, from top to bottom. The inset shows the dispersion curves. According to these curves, the group

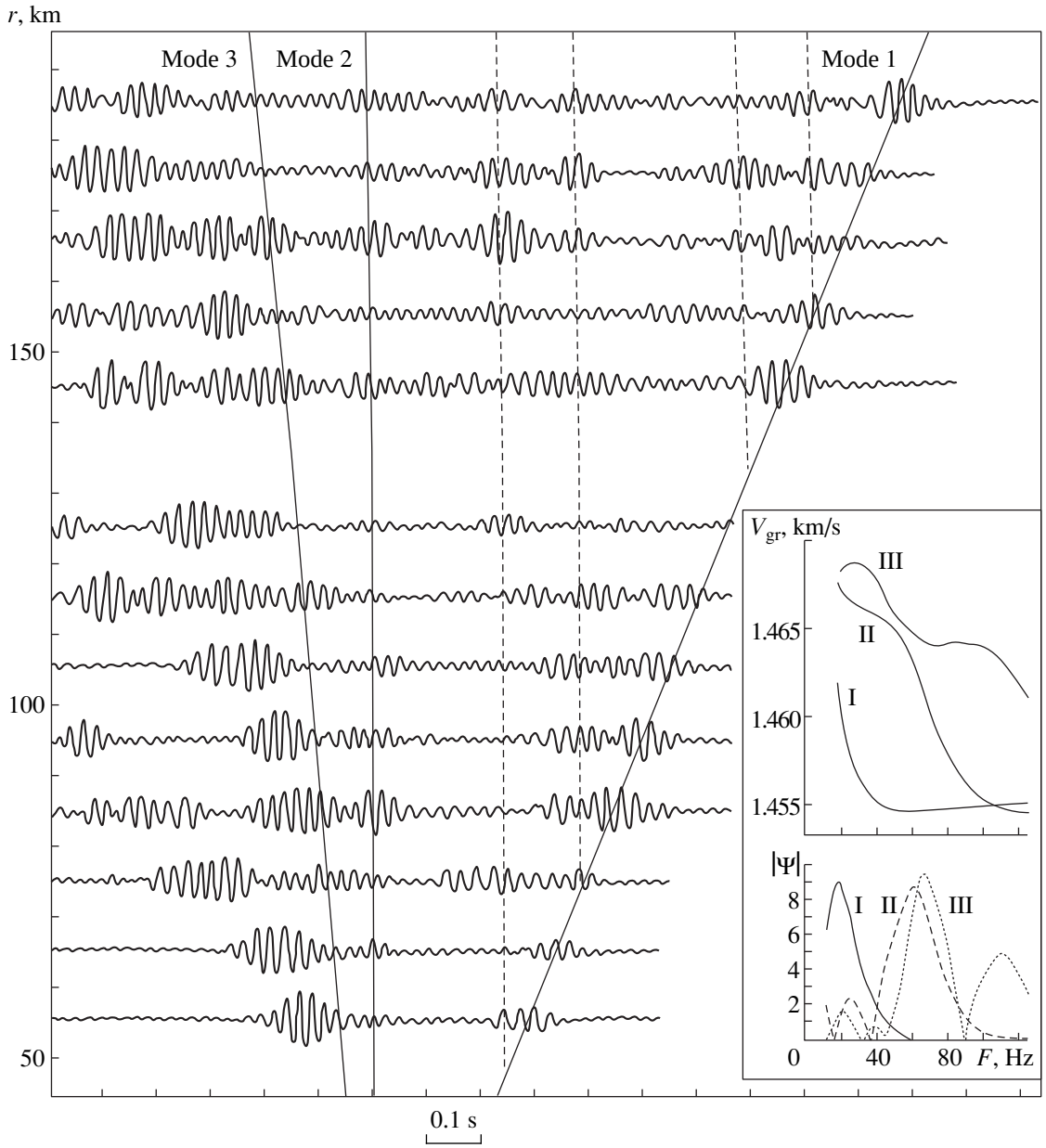

Fig. 4. Records of the signals received within the first half of the path. The filter bandwidth is 10 Hz, and the central frequency is 40 Hz. The solid lines show the arrival times of the three initial modes, the dashed lines show the arrival times of the initial local modes. The inset presents the dispersion curves and the frequency dependences of the amplitudes of the three initial modes at the reception horizon for the profile $C(z)$ of the path origin.

velocities V_{gr} of the initial three modes are significantly different: 1.4545, 1.4654, and 1.4676 km/s, respectively. Hence, the time structure of the signal tail can be reliably analyzed, because the arrivals of individual modes are fully resolved in time. Within the path portion at hand, the degree of excitation of these modes at 40 Hz is not high because of the 270-m explosion depth chosen in the experiment. The lower part of the inset shows the calculated frequency dependences for the initial three modes $|\psi|$ at the reception point. Higher frequency cannot be chosen for the analysis because of the lesser difference in the group velocities of the initial two modes. In addition, one cannot observe the actual termination of the signal, because the amplitude of the first mode sharply decreases with increasing frequency (see inset in Fig. 4). Even with the frequency 40 Hz selected for the analysis, the existence of the initial three modes can be rather guessed than established. Nevertheless, we [6] have shown that the measured and calculated group velocities of these modes are nearly equal for this part of the path, which significantly sim-

plifies the identification of the mode arrival times in the experimental records (Fig. 4).

For the reasons explained below, the records were time-synchronized relative to the arrival time of the second mode. Between the pulses of the first and second modes (solid curves in Fig. 4), a number of additional pulses can be seen. Some of them have amplitudes higher than those of the identified modes. These arrivals are most lively to be a consequence of the mode interaction caused by internal waves and meso-scale inhomogeneities of the sound speed. Unfortunately, with the 50-km interval used for measuring $C(z)$ in this part of the path, one can estimate neither the parameters of internal waves nor the positions of the boundaries of large sound speed inhomogeneities. Within the interval between the arrivals of the first and second modes, the arrival times of the most pronounced pulses were closely studied at the frequency 40 Hz and the nearest frequencies. The time separations of these pulses from the pulse of the second mode (vertical dashed lines in Fig. 4) proved to be nearly range independent at all frequencies. This independence shows that (at least during the experiment) the inhomogeneities of the sound velocity field had time-invariable boundaries that caused mode interactions when they were crossed by the sound waves. The constancy of the time intervals relative to the arrival time of the second-mode pulse implies that the mode interaction at the boundaries of these inhomogeneities leads mainly to the energy transfer from the second mode to the first one that has a lower group velocity.

We estimated the boundaries of the sound speed inhomogeneities to be at about 60, 80, 145, and 175 km from the path origin. The fact that the energy is transferred from higher modes to lower ones is not unexpected. Colosi and Flatte [7] described such a mechanism for the case of the mode interaction caused by internal waves. The signals produced by the energy transfer from the first mode to higher ones is not quite pronounced in the records, which can be explained by a weak excitation of the first mode.

At this part of the path, the main energy is associated with the initial part of the signal, i.e., it is carried by higher modes. According to computations, with the profile $C(z)$ being constant along the path, we should observe a pronounced rise in the 40-Hz signal level near the continental slope, at the same distances as at higher frequencies. However, the front zone existing in the second half of the path radically changes the conditions of the formation of the low-frequency sound field at these distances.

Computations performed with the profile $C(z)$ of the path end point show that at low frequencies (20–50 Hz), only the first and second modes are strongly excited because of the increase in the depth of the weakly pronounced minimum in the sound speed. At frequencies

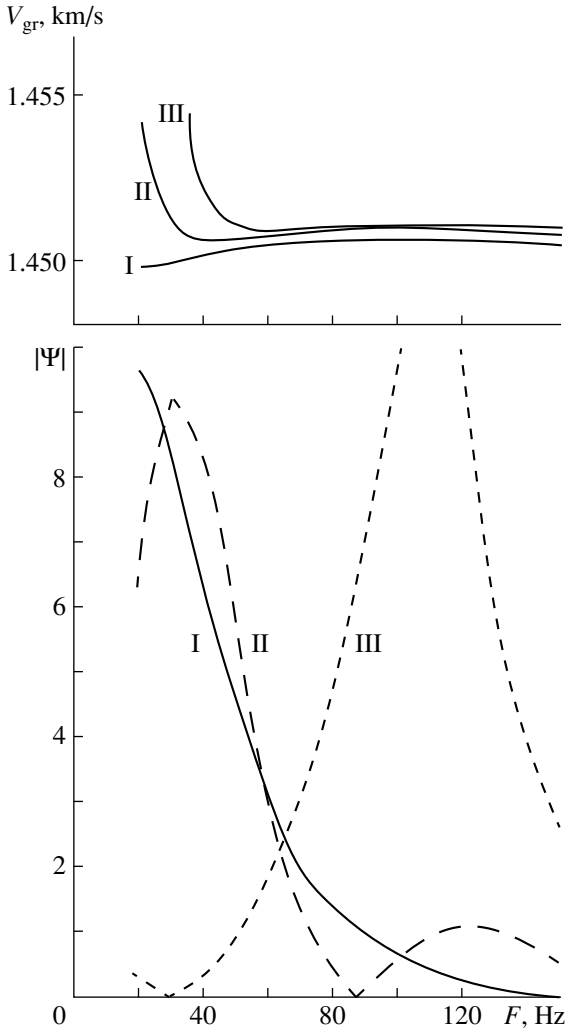

Fig. 5. Dispersion curves and frequency dependences of the amplitudes of the three initial modes at the reception horizon for the profile $C(z)$ of the path end.

higher than 30 Hz, the group velocities of these modes prove to be quite close to each other: the difference is 4 m/s at 40 Hz (Fig. 5). The small difference in the group velocities makes it impossible to resolve in time the two initial modes at the path portion at hand. As a result, at these distances, the signal records exhibit strong modulation of the signal level in the signal tail, this effect being accompanied by an extremely weak generation of the pulses corresponding to higher modes. The interference period estimated for the first and second modes at 40 Hz is 7.6 km, which agrees well with the observed modulation period of the signal tail at the terminal 30-km portion of the path. For this part of the path, Fig. 6 shows the range dependences of the total signal energy (the solid curve), the energy of the signal tail (the dashed curve), and the energy of the signal without the tail (the dotted curve) for the signals narrow-band-filtered at 40 Hz. The records are also shown for the signals received at the distances corre-

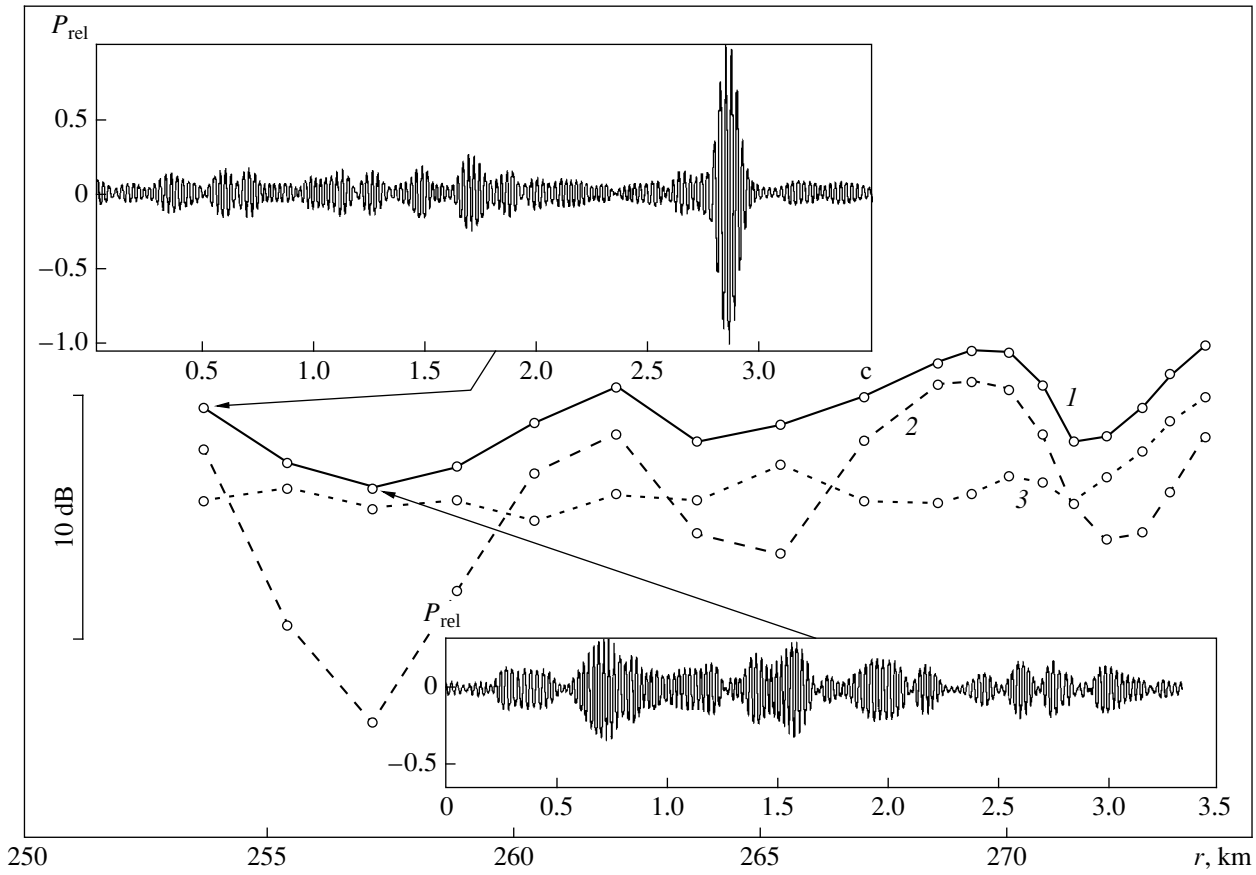

Fig. 6. Changes in the energy of (*1*) the total signal, (*2*) the signal tail, and (*3*) the tail-free signal versus the distance for the terminal part of the path. The filter bandwidth is 10 Hz, and the central frequency is 40 Hz.

sponding to the maximum and minimum in the sound interference pattern. It is seen that the modulation of the total sound field is completely produced by the interference between the pulses of the first and second modes that arrive at the end of the signal and are not resolved in time. At the same time, the range dependence of the tail-free signal level proves to be similar to that at higher frequencies. A noticeable rise in the signal level begins from the distance where, according to the ray theory, the interaction of the channeled sound with the inclined bottom begins, i.e., in the area of the continental slope.

The presented data of the experiment on the sound propagation from the deep-water region of the northwestern Pacific to coastal areas show the importance of the inclusion of all environmental parameters in the analysis of the received signals. Among these parameters, the sound speed field of the actual ocean is crucial. The same is true for the sound propagation in a deep ocean where changes in sound speed are usually weaker, and, at first glance, it is sufficient to measure the profiles $C(z)$ at points separated by longer distances (50 km in our case). The experimental signal records exhibit pronounced pulses of local modes whose nature may be studied only indirectly because of the large spacings between the measured profiles $C(z)$. At the same time, the knowledge of the formation mechanisms and arrival times of these local modes—the so-called signal interfering noise—is very important for the correlation processing the received signals. The detailed information on the sound speed field becomes even more important for the continental slope region, if there exists a coastal current that forms a clearly defined boundary between the cold over-slope waters and warmer waters of the deep ocean. Significant changes in the mechanism of sound propagation may occur after the propagation path crosses the boundary of the front zone. If no detailed analysis of these changes is performed, incorrect conclusions may be drawn. For example, in our case, wrong estimates may be obtained for the distance at which the sound level begins to increase due to the bottom inclination, and one can get a false impression that this distance strongly depends on the frequency.

ACKNOWLEDGEMENTS

This work was supported by the Russian Foundation for Basic Research, project no. 96-02-19021.

REFERENCES

1. R. A. Vadov, Akust. Zh. **43**, 606 (1997) [Acoust. Phys. **43**, 521 (1997)].
2. K. V. Avilov, A. V. Mikryukov, and O. E. Popov, Akust. Zh. **42**, 149 (1996) [Acoust. Phys. **42**, 129 (1996)].
3. R. A. Koch, S. R. Rutherford, and S. G. Payne, J. Acoust. Soc. Am. **74**, 210 (1983).
4. P. F. Worcester, B. D. Cornuelle, J. A. Hildebrand, *et al*., J. Acoust. Soc. Am. **95**, 3118 (1994).
5. J. L. Spiesberger and F. D. Tappert, J. Acoust. Soc. Am. **99**, 173 (1996).
6. A. I. Belov, A. V. Mikryukov, and O. E. Popov, Akust. Zh. **45**, 157 (1999) [Acoust. Phys. **45**, 127 (1999)].
7. J. A. Colosi and S. M. Flatte, J. Acoust. Soc. Am. **100**, 3607 (1996).

Translated by E.A. Kopyl

Acoustical Physics, Vol. 46, No. 1, 2000, pp. 96–99. Translated from Akusticheskiĭ Zhurnal, Vol. 46, No. 1, 2000, pp. 112–115.

Optical Excitation of Transverse Acoustic Waves in a Photorefractive Crystal Plate under a Transverse Electric Field

P. A. Pyatakov

Andreev Acoustics Institute, ul. Shvernika 4, Moscow, 117036 Russia
e-mail: slpapyat@cityline.ru

Received December 9, 1998

Abstract—Photoacoustic phenomena arising in the case of a pulsed optical excitation of transverse waves of horizontal polarization in a $Bi_{12}GeO_{20}$ photorefractive crystal plate under an external transverse electric field are studied. © *2000 MAIK "Nauka/Interperiodica".*

Many photosensitive dielectrics and high-resistance semiconductors belong to photorefractive crystals. These crystals have a set of optical and electroacoustic properties that provide an opportunity to observe many optoacoustic effects in them [1–5]. One of these effects is the photoacoustic effect with memory, which was first observed by Deev and Pyatakov [3]. Several versions of this effect are known. The excitation of surface waves of the Rayleigh type [3] and purely bulk transverse waves [6] were observed.

This paper studies the photoacoustic effect with memory in a $Bi_{12}GeO_{20}$ photorefractive crystal plate with the crystallographic orientation and the boundary conditions that allow the existence of a purely transverse surface wave of the Gulyaev–Bleustein type. The photorefractive effect with memory has not yet been observed under conditions where a transverse surface wave can substantially contribute to the radiation field. As compared to our previous paper [6], a new experimental detail is the orientation of the external electric field; namely, the field is transverse with respect to the propagation direction of the excited transverse waves. As is demonstrated below, with such a geometry, the acoustic signal is observed at any polarity of the external electric field. It is interesting that, in the case of a reversal of the electric field, the region of the generation of acoustic signal is shifted from one surface of the plate to another.

The purpose of this paper is to describe the experimental observations of the photoacoustic effect with memory in a photorefractive piezoelectric crystal plate under an external transverse electric field and to discuss the specific features of the optical excitation and propagation of transverse waves near the surface.

The optoacoustic cell used for the experiments (Fig. 1) was made of a bismuth germanate crystal ($Bi_{12}GeO_{20}$) cut in the shape of a plate with dimensions $60 \times 20 \times 1.5$ mm^3. The large face of the plate was parallel to the (110) crystallographic plane, and the long rib coincided with the $[\bar{1}10]$ crystallographic axis. A purely transverse piezo-active bulk wave can propagate along this direction in the bulk of a bismuth germanate crystal with the displacement vector of this wave being parallel to the (110) plane. An aluminum film was deposited on one of the large faces of the plate. This electrode was grounded. Another electrode of the cell, i.e., the electrode to which the voltage was delivered, was made in the form of a transparent conducting film of SnO_2 on a glass substrate. The glass plate with the transparent electrode was pressed to the crystal through a liquid layer (a solution of glycerol in water). The thickness of the liquid layer was ~10 μm. A transverse-wave laminated transducer made of $LiNbO_3$ was positioned at the end of the bismuth germanate plate (see Fig. 1), at its upper face. The resonance frequency of the transducer was ~90 MHz, and its sensitivity range was 20–160 MHz. The transducer dimensions were 0.5 mm in depth and 8 mm in width.

The bismuth germanate crystal was illuminated through the transparent electrode with laser pulses of length 20 ns with the wavelength $\lambda = 0.53$ μm. The

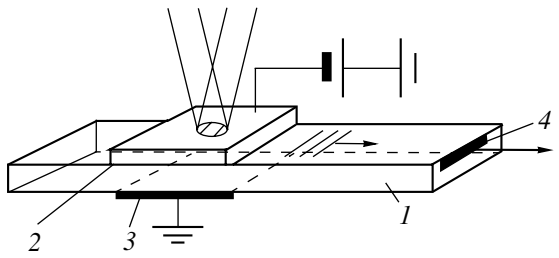

Fig. 1. Schematic diagram of the experiment: (*1*) a $Bi_{12}GeO_{20}$ crystal, (*2*) a transparent SnO_2 electrode on a glass substrate, (*3*) an aluminum film, and (*4*) an end transducer.

1063-7710/00/4601-0096$20.00 © 2000 MAIK "Nauka/Interperiodica"

intensity distribution in the light spot represented either an interference pattern with the period equal to the acoustic wavelength (in this case, the pattern was formed by the interference of two light beams of equal amplitudes) or a spot homogeneous in space. In the latter case, one of the interfering beams was shut by a shutter.

Photoacoustic effects of two types were observed: an instantaneous photoacoustic response and a photoacoustic response with memory. The carrier frequency of acoustic pulses was $f \approx 30$ MHz. In the case of an instantaneous response, the acoustic signal was excited by a periodically inhomogeneous illumination. In the case of a photoacoustic response with memory, the acoustic signal was a response to a homogeneous illumination under the condition of preliminary recording, i.e., a preliminary exposure to an inhomogeneous illumination. The experimental results are given in the form of plots in Figs. 2–4. Let us indicate the main characteristic properties of the observed effects.

As one can see from Fig. 2, the first instantaneous response for all exposures to illumination is relatively small. The subsequent signals noticeably exceed the first one and reach their maximum values when the total exposure from the first illumination to the one corresponding to the maximum acoustic signal is $\sum(W_i) \sim 0.1$ mJ/cm^2.

The acoustic signal is observed in the cases of an instantaneous response and a photoacoustic response with memory (Fig. 3) for both negative and positive polarities of the external acoustic field. In the case of the negative polarity of the external field, the amplitude of the acoustic signal is considerably greater than in the case of the positive polarity.

The dependence of the photoacoustic response on the exposure to illumination (Fig. 4) obeys the same rule for different polarities of the external electric field: first, an increase according to the law $\sim W^{0.5}$ and, then, saturation and decrease.

We note that, under a transverse electric field, the time of memory is much longer than in the case of a longitudinal field: $\tau_m = 10^3$–10^4 s and $\tau_m = 10$–10^2 s, respectively.

The indicated features of the effects may be explained qualitatively on the grounds of the following physical model. We assume that the electrodes at the upper and lower faces of the photorefractive crystal form blocking contacts, i.e., they do not conduct electric current at least in one direction. Let a negative potential of the electrical field be fed to the upper face of the plate. Then, in the case of periodically inhomogeneous illumination of the crystal, a periodic charge structure will be formed at the upper electrode, because the photoinduced carriers in bismuth germanate are electrons.

In the case of a positive potential of the upper electrode, the blocking properties of the lower electrode

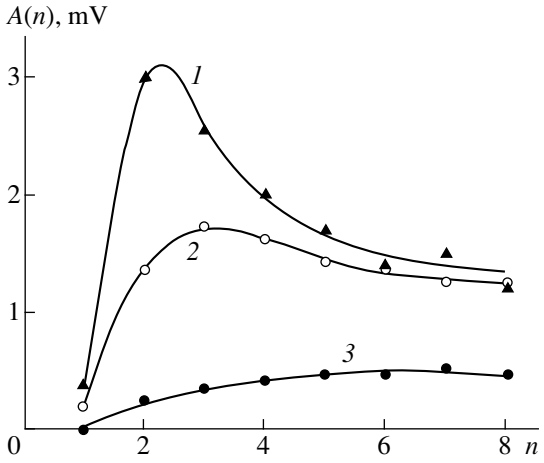

Fig. 2. Instantaneous photoacoustic response as a function of the order number of laser pulse. The voltage is $U = -600$ V. The exposure in the pulse is (*1*) 70, (*2*) 20, and (*3*) 10 μJ/cm^2.

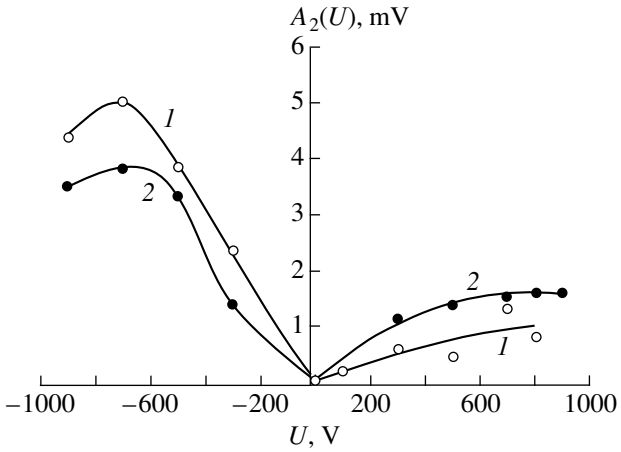

Fig. 3. Photoacoustic response with memory (curve *1*) and the second-in-order instantaneous photoacoustic response (curve *2*) as functions of the external electric field. The recording exposure is $W_m = 70$ μJ/cm^2. The reading exposure is $W_r = 200$ μJ/cm^2. The exposure in the case of the second instantaneous response is $W = 70$ μJ/cm^2.

are essential, and, correspondingly, the space-charge region is formed close to the lower electrode.

Two time scales should be distinguished in the evolution of the charge structure.

At the first stage of relatively short duration about the half-period of the acoustic wave (~16 ns), a relatively small increase in the amplitude of the periodic charge structure occurs. However, just this charge increase is responsible for the excitation of the acoustic wave the source of which is the mechanical stress arising due to the piezoelectric effect. The overall formation of the charge structure induced by a single laser pulse occurs within the time in the order of the life time of conduction electrons (in the case of bismuth germanate, $\tau = 10^{-4}$–10^{-6} s). A positive charge region is

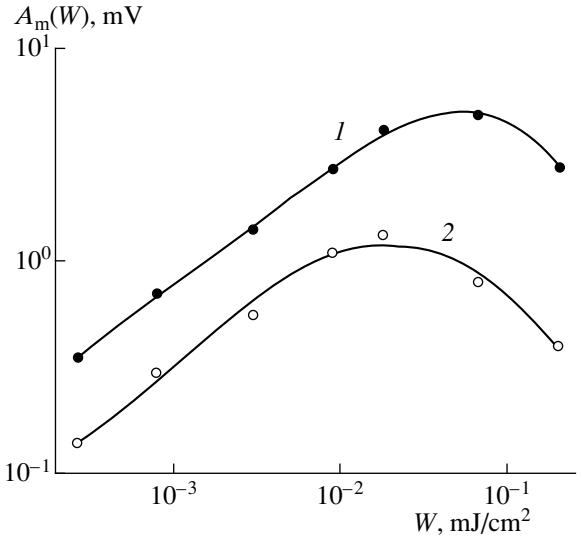

Fig. 4. Photoacoustic response with memory as a function of the recording exposure. $U = -800$ V. Curve *1* corresponds to the negative potential of the upper electrode, and curve *2* corresponds to the positive potential.

already formed at the surface of the blocking electrode by the moment of the action of the second laser pulse. The effective thickness of the sample layer where voltage drop occurs decreases down to the thickness of the charge layer, and, therefore, the electric field strength increases in the space-charge region. The generation of the second pulse, as well as of the subsequent pulses, takes place at a higher electric field strength than the generation of the first pulse, and, therefore, their amplitudes are higher. An increase in the total exposure above a certain optimum value leads to no further increase in the amplitude of the photoacoustic response, since it causes a compression of the spatial charge to a thickness less than the corresponding dimension of the receiving transducer.

A photoacoustic signal with memory is the reaction of the recorded charge structure to a homogeneous erasing illumination. The change in the internal electric field in the process of erasing produces an acoustic wave pulse. An acoustic memory signal, as well as an instantaneous response, is radiated either from the upper surface region of the crystal in the case of the negative polarity of the external field or from the lower surface region in the case of the positive polarity.

It is easy to explain the difference in the signal amplitudes corresponding to different polarities of the external electric field, if one notices that the receiving transducer is positioned asymmetrically with respect to the upper and lower faces of the plate. In fact, the transducer is shifted toward the upper face. It is useful to estimate the ratio of the amplitudes of two signals numerically. We note that photoacoustic signals are short pulses of transverse waves excited along the boundaries. The pulse length is $\Delta t = d/v_t \approx 1$ μs, where $d \approx 2$ mm is the length of the illuminated area and $v_t \approx 1.7$ mm/μs is the velocity of acoustic waves. The pulse length is so small that we can ignore the second boundary while treating the diffraction field and consider the field in the halfspace, since the signals directly transmitted and reflected from the boundary are separated in time.

The conditions at the boundaries and the short-circuiting of electric fields through the electrodes leads to the appearance of surface waves in the spatial spectrum of the radiation field. These waves penetrate to the depth 10–20Λ, where Λ is the wavelength. Surface waves localize the energy at the surface, which causes a decrease in the diffraction spreading of energy away from the boundary. After the waves come out from under the electrodes, the spectrum of the free halfspace is restored, and the total field is diffracted in a regular way. Therefore, in order to estimate the ratio of the signal amplitudes, we assume that the field has such a form as it would have in the case of purely transverse waves under a free boundary, and we take into account the effect of transverse waves under the electrodes by introducing the effective track length $l < l_0$, where l_0 is the true distance from the receiver to the place of generation. The numeric estimation of the diffraction integral is conducted using the approximation of preset force sources. We assume that the function of the source distribution in depth has the form

$$F(y) = F_0(1 - |y_1|/h), \text{ if } -h \le y_1 \le h$$
$$\text{and } F(y_1) = 0, \text{ if } -h \ge y_1 \ge h,$$

i.e., real sources are set in the layer $0 \le y_1 \le h$, while imaginary sources are set in the layer $-h \le y_1 \le 0$. The ratio of the signal amplitudes m is calculated as the ratio of two integrals I_1/I_2, where

$$I_{1,2} = \int_{b_{1,2}}^{H} dy_2 \int_{-a}^{a} dx_1 \int_{-h}^{h} F(y_1) e^{ikr}/r\, dy_1,$$

$r = \sqrt{l^2 + (x_1 - x_2)^2 + (y_1 - y_2)^2}$, x_1 and y_1 are the coordinates in the plane of sources, y_2 is the coordinate in the plane of the receiver, $H = 0.5$ mm is the receiver size in depth, $a = 1$ mm is the half-thickness of the illuminated area, l is the distance from the sources to the receiver, $b_1 = 0$, $b_2 = 1$ mm, and k is the wave number of the acoustic wave.

The ratio m is presented in Fig. 5 as a function of thickness of the source layer h for three values of l. The comparison of the plots with the experimental data ($m \approx 1.5$–2.5 in Fig. 3) yields the estimate of the layer thickness $h \approx 0.6$ mm. The estimated value of h seems reasonable. It is close to the receiver size in depth, which corresponds to the condition of the observation of the maximum photoacoustic response.

We note that, for a smaller receiver size in depth, one should expect a smaller thickness of the photoacoustic source layer corresponding to the best condi-

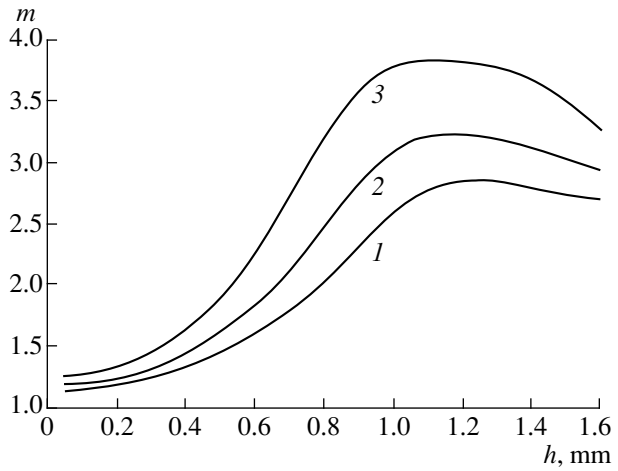

Fig. 5. Dependence of the ratio m on the thickness of the layer of the spatial charge h. Curve *1* corresponds to the distance $l = l_0 = 40$ mm, curve *2* corresponds to $l = 30$ mm equal to the distance from the receiver to the electrode, and curve *3* corresponds to $l = 35$ mm.

tions of excitation. However, in this case, the necessary value of the preliminary exposure providing the optimum operation mode of the cell increases.

Thus, an experimental study of pulsed optical generation of transverse waves of horizontal polarization in a photorefractive piezoelectric under a transverse electric field is conducted. Signals of photoacoustic responses were observed for both polarities of the external electric field. The specific features of the effects are explained with the help of the assumptions on the blocking properties of the electric contacts and the displacement of the region of the photoacoustic sources under a change of polarity of the external field. The localization depth of the spatial charge providing the maximum photoacoustic response is estimated.

ACKNOWLEDGMENTS

This work was supported by the Russian Foundation for Basic Research (project no. 97-02-17671).

REFERENCES

1. N. J. Berg, B. J. Udelson, and J. N. Lee, Appl. Phys. Lett. **31**, 555 (1977).
2. D. E. Oates, P. G. Gottschalk, and P. V. Wright, Appl. Phys. Lett. **46**, 1125 (1985).
3. V. N. Deev and P. A. Pyatakov, Pis'ma Zh. Tekh. Fiz. **11**, 76 (1985) [Sov. Tech. Phys. Lett. **11**, 30 (1985)].
4. O. V. Bystrov and A. V. Golenishchev-Kutuzov, Pis'ma Zh. Éksp. Teor. Fiz. **61**, 128 (1995) [JETP Lett. **61**, 135 (1995)].
5. L.-A. Montimorillon, P. de Delage, J.-C. Lannay, *et al.*, J. Appl. Phys. **82**, 5913 (1997).
6. V. N. Deev and P. A. Pyatakov, Akust. Zh. **34**, 621 (1988) [Sov. Phys. Acoust. **34**, 358 (1988)].

Translated by M.L. Lyamshev